

Guanosine-7 tRNA methylation regulates
Prostate Cancer progression through protein
reprogramming via tRNA-derived fragments
biogenesis



VNiVERSIDAD
D SALAMANCA

Ph.D Thesis

Raquel García Vílchez

Salamanca, December 2022

Biosciences: Cancer biology and treatment and translational medicine

Centro de Investigación del Cáncer

Instituto de Biología Molecular y Celular del Cáncer (IBMCC)


CSIC-Universidad de Salamanca

La **Dra. Sandra Blanco Benavente**, Científica Titular del Consejo Superior de Investigaciones Científicas y del Instituto de Biología Molecular de Salamanca

CERTIFICA

Que el trabajo de tesis titulado **“Guanosine-7 tRNA methylation regulates Prostate Cancer progression through protein reprogramming and tRNA-derived fragments biogenesis”**, presentado por **D^a Raquel García Vílchez** para optar al Grado de Doctor por la Universidad de Salamanca, ha sido realizado bajo mi dirección en el Centro de Investigación del Cáncer de Salamanca (USAL/CSIC). Considerando que cumple con las condiciones necesarias, autorizo su presentación a fin de que pueda ser defendido frente el tribunal correspondiente.

Y para que conste a efectos oportunos, expido y firmo el presente certificado en Salamanca a 07 de Diciembre de 2022.



Fdo: Dra. Sandra Blanco Benavente

It's the questions we can't answer that teach us the most. They teach us how to think. If you give a man an answer, all he gains is a little fact. But give him a question and he'll look for his own answers

Las preguntas que no podemos contestar son las que más nos enseñan. Nos enseñan a pensar. Si le das a alguien una respuesta, lo único que obtiene es cierta información. Pero si le das una pregunta, él buscará sus propias respuestas

- Patrick Rothfuss -

ABSTRACT

Prostate Cancer (PCa) is the most common tumour and the third cause of death by cancer in European men. Although important advances have been made in early stages of the disease and most of the tumours respond to hormone deprivation therapy, many patients develop Castration Resistant Prostate Cancer (CRPC) which lacks effective therapeutic options. One of the major drawbacks for PCa treatment is the high intratumoural heterogeneity and the lack of reliable biomarkers of disease progression. During the last years, several studies have highlighted the importance of RNA chemical modifications in the progression and therapy response of several tumours. Thus, manipulation of the epitranscriptome might be a potential therapeutic target to specifically eliminate those cancer cell resistant to conventional treatments. Thereby, this thesis focuses in deciphering the epitranscriptomic landscape of PCa in order to identify altered epitranscriptomic regulators that may control tumour proliferation and survival capacities.

In silico analysis demonstrated that the tRNA methyltransferase METTL1 was overexpressed in primary and advanced PCa tumours, being increased expression correlated with poor prognosis. Altered expression of the methyltransferase was confirmed in primary tumours samples from both patients and from *Pten*KO PCa mouse model. For functional characterization of METTL1 molecular role, cells over-expressing, silenced and knocked out for the methyltransferase were generated in distinct PCa cell lines. In consequence, lack of *METTL1* resulted in accumulation of 5'TOG tRNA-derived fragments, which lead not only to a global inhibition of protein synthesis but also to an alteration of the translational programme. As a result, *METTL1* deletion resulted in impaired cell proliferation and self-renewal capacity in cell cultures and reduced tumour formation and proliferation in both xenografted and *Pten*KO PCa *in vivo* murine models. Impaired self-renewal capacity is observed in a human PDXs-derived model upon the enzyme depletion. In addition, cells lacking *METTL1* exhibited impaired autophagy termination, which lead to accumulation of protein aggregates, ROS and DNA damage, resulting in an hypersensitivity to stress conditions. Altogether, this thesis demonstrates that METTL1 regulates tumoural cells capacity to respond to stress stimuli and inhibition of its methyltransferase activity ultimately leads to an increase sensitivity to traditional therapeutic agents.

This study concludes that METTL1 is overexpressed in PCa and higher expression correlates with poor prognosis. METTL1 is essential for 7-guanine methylation in tRNAs and lack of the methylation results in protein synthesis alterations, which results in a deregulation of essential cellular processes as proliferation and self-renewal. Whether METTL1 can be used as a therapeutical target needs further validation.

RESUMEN

El cáncer de Próstata (CaP) es el cáncer más común y la tercera causa de muerte por cáncer de hombres en Europa. Aunque recientemente se han hecho grandes avances para el tratamiento de las fases tempranas de la enfermedad y la mayoría de los tumores responden a terapia de deprivación androgénica, muchos pacientes desarrollan Cáncer de Próstata resistente a la Castración, con reducidas opciones terapéuticas. Unos de los mayores problemas para el desarrollo de tratamientos efectivos para el CaP es la gran heterogeneidad intratumoral y la falta de biomarcadores fiables de la progresión de la enfermedad. En los últimos años, distintos estudios han destacado la relevancia de las modificaciones del ARN en la progresión tumoral y la respuesta a tratamiento de distintos tipos de cáncer. Así, la manipulación del epitranscriptoma podría ser una potencial diana terapéutica para eliminar de manera específica aquellas células tumorales resistentes a tratamientos. El objetivo de esta tesis es descifrar el epitranscriptoma del CaP con el fin último de identificar modificadores epitranscriptómicos reguladores de la capacidad proliferativa y de supervivencia de los tumores.

Análisis *in silico* han demostrado que la metiltransferasa de ARNts METTL1 está sobreexpresada en tumores de próstata primarios y avanzados, existiendo una correlación directa entre mayores niveles de expresión y peor pronóstico. La alteración de los niveles de la proteína se validó en muestras de tumor primario de pacientes, así como en el modelo murino de CaP *Pten*KO. Para la caracterización funcional del papel molecular de METTL1, se generaron distintas líneas de CaP con sobreexpresión, silenciamiento o ausencia total de la enzima. En consecuencia, la ausencia de *METTL1* produjo una acumulación de fragmentos 5'TOG derivados de ARNts, lo que no sólo condujo a una inhibición de la síntesis global de proteínas sino también a una alteración del programa traduccional. Como resultado, la delección de *METTL1* dio lugar a un deterioro de la capacidad proliferativa y de autorrenovación de líneas celulares y a una reducción de la formación y proliferación de tumores tanto en modelos murinos de xenotransplantes como de CaP. La capacidad de autorrenovación de un modelo humano derivado de PDXs se vio disminuida tras la depleción de la enzima. Además, las células que carecen de la metiltransferasa mostraron una alteración de la terminación de la autofagia, que conduce a una acumulación de agregados de proteínas, ROS y daño al DNA, lo que se traduce en una hipersensibilidad a condiciones de estrés. En conjunto, esta tesis demuestra que METTL1 regula la capacidad de las células tumorales para responder a los estímulos de estrés y la inhibición de su actividad metiltransferasa conduce en última instancia a un aumento de la sensibilidad a los agentes terapéuticos tradicionales.

Este estudio concluye que METTL1 está sobreexpresada en CaP y que una mayor expresión se correlaciona con un mal pronóstico. METTL1 regula la metilación de guanina-7 en ARNts y la falta de esta modificación altera la síntesis proteica, lo que se traduce en una desregulación de procesos celulares esenciales como la proliferación y la capacidad de autorrenovación. El potencial terapéutico de METTL1 precisa de un análisis más detallado.

FUNDING

The research performed during this Ph.D thesis has been supported by:

- I. The student fellowship “Ayudas para contratos predoctorales para formación de doctores, FPI” BES-2017-080-530, funded by the Spanish Ministry of Science and Innovation and the State Research Agency MCIN/AEI.
- II. Funding from the “Programa Estatal de Investigación, Desarrollo e Innovación Orientada a los Retos de la Sociedad” SAF2016-78667-R and PID2019-111692RB-100 by the Spanish Ministry of Science and Innovation and the State Research Agency MCIN/AEI.
- III. Funding from “Ramon y Cajal programme” RYC-2014-16550 by the Spanish Ministry of Economy and Competitiveness MINECO.
- IV. Funding from “Regional strategy for research and innovation (RIS3)” CLC-2017-01 funded by the regional government of Castilla y León 2014-2020, co-financed by the Ministry of Education of the Regional Government of Castilla y León and the European Regional Development Fund.
- V. Funding from “Proyectos prueba de concepto” funded by ProteoRed and Carlos III Health Institute (ISCIII).
- VI. Funding from “Proyectos de la Junta de Castilla y León” CSI264P20 funded by the Regional Government of Castilla y León.

TABLE OF CONTENTS

LIST OF FIGURES	2
LIST OF TABLES	4
TABLE OF ABBREVIATIONS	6
INTRODUCTION.....	12
1. Prostate Cancer	12
1.1. Anatomy of the prostate	12
1.2. Prostate tumour formation.....	13
1.3. Treatment of PCa.....	14
1.4. Molecular characteristics of PCa.....	15
1.1.1. PCa mouse models	16
1.1.2. Patient Derived Xenografts Organoids.....	18
2. Epitranscriptomics	20
3. tRNA modifications.....	20
3.1. Regulation of protein translation by modifications deposition at anticodon loop.....	22
3.2. Regulation of tRNA-derived fragment formation by RNA modifications.....	23
3.3. tRNA fragment biogenesis regulates protein translation.....	24
3.4. Interconnection between tRNA fragments biogenesis, translation inhibition and stress response.....	26
3.5. tRNA modifications in cancer.....	27
3.6. m ⁷ G tRNA modification.....	29
3.6.1. m ⁷ G detection	29
3.6.2. m ⁷ G function in physiological and pathological conditions.....	31
4. Deregulated protein synthesis triggers UPR.....	32
5. Autophagy as a stress response mechanism.....	34
5.1. Autophagic process and its molecular regulation.....	35
5.2. RNA modifications and autophagy regulation.....	36
5.3. Autophagy dual role in cancer.....	37
OBJECTIVES.....	42
RESULTS.....	46
1.1. <i>METTL1</i> is upregulated in human and murine PCa and associated with poor prognosis	46
1.2. <i>METTL1</i> expression is regulated via PI3K pathway	49
1.3. <i>METTL1</i> is upregulated during PCa progression and highly expressed in luminal cells in PCa murine model.....	52
2. Identification of METTL1 targets at single-nucleotide resolution	55
2.1. tRNAs are the main METTL1 targets	55
2.2. Identification of METTL1 deposition sites at single nucleotide resolution	57
2.3. 7-guanine methylation regulates tRNA stability by preventing tRNA-derived fragments biogenesis.....	59

2.4.	METTL1-dependent tRNA fragments biogenesis inhibits translation initiation	63
3.	Phenotypic characterization of <i>METTL1</i> depletion	65
3.1.	METTL1 regulates tumour growth and self-renewal capacity <i>in vitro</i> and <i>in vivo</i>	65
3.2.	METTL1 specifically controls translation of stress response-related proteins	69
4.	Evaluation of METTL1 role in stress response pathways	72
4.1.	Loss of METTL1 alters cell proteostasis without triggering UPR.....	72
4.2.	METTL1 is essential for maintaining a basal autophagic flux.....	73
4.3.	METTL1 loss results in ROS accumulation and increased stress sensitivity.....	77
5.	Characterization of <i>Mettl1</i> role <i>in vivo</i>	80
5.1.	Generation of a PCa mouse model with <i>Mettl1</i> deletion in prostatic epithelium.....	80
5.2.	<i>Mettl1</i> depletion in murine PCa restores cell composition towards a healthy tissue ...	81
5.3.	METTL1 regulates chemotherapy response <i>in vivo</i>	84
6.	Generation of organoids from a Patient-derived xenograft model depleted for <i>METTL1</i> expression.....	86
DISCUSSION		92
CONCLUSIONS		102
GRAPHICAL SUMMARY		104
MATERIALS AND METHODS.....		108
2.	Cloning and site directed mutagenesis	108
3.	Cell culture procedures.....	110
3.1.	Cell lines and culture conditions	110
3.2.	Lentivirus production and generation of stable cell lines.....	111
3.2.1.	Generation of <i>METTL1</i> knock-out cell lines by CRISPR-Cas9 technology	113
3.2.2.	gDNA extraction and CRISPR-Cas9 editing validation	113
3.2.3.	Generation of <i>METTL1</i> knock-down cell lines	113
3.2.4.	Generation of catalytic dead mutant cell lines	114
3.3.	Transitory <i>METTL1</i> silencing in U2OS-GFP cell lines	114
3.4.	Transfection of synthetic 5'TOG and anti-TOG oligonucleotides.....	115
3.5.	Transitory transfection of GFP-LC3 plasmid.....	115
3.6.	Cell proliferation assay.....	115
3.7.	Cell survival assay.....	116
3.8.	Soft agar colony formation assay	116
3.9.	Single-cell spheroids generation	116
3.10.	Organoid culture and proliferation assay	117
3.10.1.	Organoid derivation.....	117
3.10.2.	Organoid lentiviral infection	117
3.10.3.	Expansion of xenografted LAPC9 in NSG mice.....	117
3.10.4.	Organoid formation capacity quantification.....	118
3.11.	PI3K pathway inhibition and DHT treatment	118
4.	Molecular and cell biology techniques.....	118

4.1.	Assaying autophagy dysregulation.....	118
4.1.1.	Evaluating autophagy flux under normal and autophagy-inducing or blocking conditions	118
4.2.	Flow cytometry analysis.....	119
4.2.1.	Apoptosis quantification.....	119
4.2.2.	Measurement of global protein synthesis by O-propargyl-puromycin incorporation	119
4.2.3.	Cell cycle analysis	120
4.2.4.	ROS measurement	120
4.3.	Cell Immunofluorescence.....	120
4.3.1.	Quantification of protein aggregates	121
4.4.	Immunohistochemistry	121
4.5.	Western Blot.....	122
5.	Analysis of global and specific protein synthesis	125
5.1.	Total proteome analysis.....	125
5.2.	Capture of nascent polypeptides.....	125
5.3.	Mass spectrometry analysis of global and nascent proteome.....	126
5.4.	Polysome profiling	126
5.5.	Biotinylated 5'TOG oligonucleotides pulldown	127
5.6.	Cap Binding assay	127
6.	RNA methods.....	128
6.1.	RNA extraction and quantitative real-time PCR (RT-qPCR)	128
6.2.	Total RNA extraction	130
6.3.	tRNA extraction	131
6.4.	tRNA-seq m ⁷ G identification at single nucleotide resolution by high-throughput sequencing or Bo-seq	131
6.2.	Quantification of m ⁷ G levels by Northdot blot	132
6.3.	LC/MS-MS quantification of m ⁷ G tRNA levels	133
6.4.	tRNA <i>in vitro</i> cleavage assay	133
6.5.	Transcriptomic analysis in PC3 cell lines.....	133
6.6.	Northern blotting	134
7.	Mouse lines and <i>in vivo</i> assays.....	135
7.1.	Ethical statements.....	135
7.2.	Xenograft generation in immunodeficient mice.....	135
7.3.	Prostate Cancer mouse model deficient for Mettl1 in prostate epithelium	135
7.4.	Prostate dissociation for analysis of prostate cell populations	137
7.5.	mRNA expression in PCa mouse model	137
8.	PCa patient samples	138
9.	<i>In silico</i> analysis of gene expression and mutation load data from human prostate tumour data sets	138

LIST OF FIGURES

Figure 1. Estimated number of new cases and 5-year prevalent cases in 2020 in men worldwide, from a total of 10,065,305 and 24,828,480 patients respectively.....	12
Figure 2. Graphical representation of normal prostate.....	13
Figure 3. Schematic representation of prostate cancer progression and development of metastasis.	14
Figure 4. A) Cloverleaf structure of the general structure of tRNAs. B) L-shaped three-dimensional representation of the yeast Phenylalanine tRNA.....	21
Figure 5. Schematic representation of an average tRNA molecule.....	22
Figure 6. tRNA-fragments derived from mature tRNAs with the known ribonucleases implicated in their biogenesis.....	24
Figure 7. Schematic representation of normal active protein synthesis and the inhibition mediated by Ψ -5'mTOG.....	26
Figure 8. Schematic representation of METTL1/WDR4-dependent m ⁷ G modification in human tRNAs.....	29
Figure 9. Schematic representation of the workflow followed for all the NaBH ₄ -based m ⁷ G detection methods.	30
Figure 10. Schematic representation of the three different branches of the UPR pathway.....	33
Figure 11. Schematic representation of the autophagic flux and the main regulators of the pathway.	36
Figure 12. <i>METTL1</i> is upregulated in human and mouse Prostate Cancer.....	47
Figure 13. Expression of distinct RMPs in PCa.	48
Figure 14. Assaying <i>METTL1</i> expression in PCa patient samples and cell lines.	49
Figure 15. <i>METTL1</i> expression regulation is dependent of PI3K pathway but AR independent....	51
Figure 16. Human and murine prostate cancer progression correlates with higher METTL1 levels..	52
Figure 17. <i>Mettl1</i> is overexpressed in prostate invasive carcinoma..	53
Figure 18. <i>Mettl1</i> is highly expressed in luminal cells from murine prostates.....	54
Figure 19. tRNAs are METTL1 preferred targets.	56
Figure 20. Generation of PCa cell lines with reduced <i>METTL1</i> expression.	57
Figure 21. Development of a new variation of NaBH ₄ -based m ⁷ G detection method: Bo-seq.....	58
Figure 22. Validation of METTL1-dependent tRNA methylation at position 46.....	59
Figure 23. METTL1-mediated m ⁷ G deposition protects tRNA from endonucleolytic cleavage	60
Figure 24. tRNA cleavage in the absence of m ⁷ G ₄₆ is enhanced upon stress conditions.....	62
Figure 25. Lack of METTL1 m ⁷ G-dependent mark results in global protein translation inhibition by displacement of the translation initiation complex through 5'TOG formation.....	64

Figure 26. <i>METTL1</i> depletion decreases prostate cancer cell proliferation <i>in vitro</i>	66
Figure 27. Depletion of <i>METTL1</i> impairs tumour growth capacity <i>in vivo</i>	67
Figure 28. <i>METTL1</i> methylating activity promotes cell growth.	69
Figure 29. Loss of <i>METTL1</i> -mediated m ⁷ G deposition alter normal translational programme.	70
Figure 30. <i>METTL1</i> -mediated 5'TOG biogenesis induces translation of specific transcripts.....	71
Figure 31. Loss of <i>METTL1</i> enhances misfolded protein accumulation but does not activate UPR..	73
Figure 32. <i>METTL1</i> deletion enhances autophagic flux.....	74
Figure 33. Loss of <i>METTL1</i> impairs autophagosome maturation.....	76
Figure 34. <i>METTL1</i> depletion impairs redox balance within the cell increasing oxidative stress sensitivity.	78
Figure 35. Loss of <i>METTL1</i> diminishes cells proliferation upon autophagy induction and PCa chemotherapeutic agents treatment.	79
Figure 36. Generation of a prostate cancer mouse model with conditional <i>Mettl1</i> deletion.....	81
Figure 37. Characterization of <i>Mettl1</i> depletion effect on mice prostate tumours.	82
Figure 38. <i>Mettl1</i> regulates tumour cell survival in mouse PCa	83
Figure 39. Depletion of <i>METTL1</i> increases sensitivity to chemotherapeutic agents <i>in vivo</i>	85
Figure 40. Evaluation of the proliferative effect of <i>METTL1</i> silencing in prostate cancer PDX- derived organoid model.....	86
Figure 41. Schematic representation of the molecular mechanism identified in PCa cell lines after <i>METTL1</i>	104
Figure 42. Schematic workflow used for protein synthesis evaluation under stress conditions.. .	120

LIST OF TABLES

Table 1. Summary of tRNA modifying proteins alterations associated with cancer.	28
Table 2. Tumours associated with aberrant <i>METTL1</i> expression levels.	32
Table 3. Primers used for the cloning and sequencing of the indicated human and plasmid sequences.	110
Table 4. Description of the plasmids used for the generation of both stable and transient cell lines	112
Table 5. Sequences or references of the siRNAs and synthetic oligonucleotides transiently transfected in cell lines.	114
Table 6. List of antibodies with the working dilutions used for cell immunofluorescence.	121
Table 7. Antibodies used for IHC staining of paraffin embedded tissue. Antigen retrieval conditions and dilutions are indicated for each antibody.....	122
Table 8. List of antibodies used for Western blot protein visualization. Host species and working dilution are specified.	124
Table 9. Oligonucleotides designed for RT-qPCR amplification of the specified human genes by SYBR green.....	129
Table 10. Sequences of oligonucleotides used for RT-qPCR quantification of mouse samples. ..	130
Table 11. List of Taqman and UPL probes used for RT-qPCR of human and mouse samples.....	130
Table 12. Sequences of the synthetic oligonucleotides used for in vitro assessment of Cys-CGA fragmentation.	133
Table 13. List of probes used for tRNA fragmentation analysis by Northern blot.....	134
Table 14. Sequences of the oligonucleotides synthesized for the generation of edited <i>Mettl1</i> ^{fllox/fllox} mice.	136
Table 15. Primary and secondary antibodies used for flow cytometry sorting of mouse prostate populations. The host specie, dilution and reference of the product are indicated.....	137

TABLE OF ABBREVIATIONS

3D	Three-dimensional	DLP	Dorsolateral prostate
3-MA	3-methyladenine	DMEM	Dulbecco's Modified Eagle Medium
5-FU	5-Fluorouracil	Dox	Doxycycline
ADAT	tRNA adenosine deaminases	DPX	Dibutylphthalate polystyrene xylene
ADT	Androgen deprivation therapy	DSBs	Double-strand breaks
AGO	Argonaute	DTT	Dithiothreitol
AlkAniline	Alkaline hydrolysis and aniline	ECL	Enhanced
-Seq	cleavage sequencing		Electrochemiluminescence Reagent
ALKBH5	Alpha-ketoglutarate-dependent	EGF	Endothelial Growth Factor
	dioxygenase homolog 5	EGFR	Endothelial growth factor receptor
AML	Acute myeloid leukemia	ER	Endoplasmic reticulum
AMPK	Adenosine monophosphate-		Endoplasmic reticulum -associated
	activated protein kinase	ERAD	degradation
AP	Anterior prostate		Oesophageal squamous cell
		ESCC	carcinoma
AR	Androgen Receptor	eV	Empty vector
ATF6	Activating transcription factor 6	FACS	Fluorescence activated cell sorting
ATG	Autophagy-related genes	FBS	Fetal bovine serum
BC	Bladder cancer	FC	Fold change
BoRed-seq	Borohydride reduction	FDA	Food and Drug administration
	sequencing	FSC	Forward scatter
Bo-seq	Borohydride-sequencing	FTO	Fat mass and obesity-associated
bp	Base pairs		protein
BPE	Bovine Pituitary Extract	GBM	Glioblastoma
BPH	Benign prostatic hyperplasia	GCN2	General control non-derepressible-2
BRCA	Breast Cancer		kinase
CC	Colon cancer	gDNA	Genomic DNA
CDFH-DA	2'7'-Dichlorofluorescin	GEMMs	Genetically engineered mouse
	Diacetate (models
CHX	Cycloheximide	Gm	2'-O-methylguanosine
CK8	Cytokeratin 8	GSTP1	Glutathione S-transferase P
Cm	2'-O-methylcytidine	H&E	Haematoxylin and eosin
CMA	Chaperone-mediated autophagy	HCC	Hepatocellular carcinoma
CQ	Chloroquine	HGF	Hepatocyte growth factor
CRISPR	Clustered Regularly Interspaced	HGPIN	High grade prostatic intraepithelial
	Short Palindromic Repeats		neoplasia
CRPC	Castration resistant prostate	hm5C	5-hydroxymethylcytidine.
	cancer		
CTCF	Corrected total cell fluorescence	HNSCC	Head and neck squamous cell
			carcinoma
DAB	3,3'-diaminobenzidine	HPLC	High performance liquid
			chromatography
DCHF-DA	2'7'-Dichlorofluorescin	I	Inosine
	Diacetate	IHC	Immunohistochemistry
DFS	Disease free survival	OP-puro	O-propargyl-puromycin
DKC1	Dyskerin 1		

int-tRFs	Internal-derived tRNA fragments	ORF	Open reading frame
IRE1α	Inositol requiring enzyme-1	PABPC1	Polyadenylate-binding protein 1
IRES	Internal Ribosome-Entry Sites	PAGE	Polyacrylamide gel electrophoresis
IRF9	Interferon regulatory factor 9	PAM	Protospacer adjacent motif
		PAR-CLIP	PhotoActivatable-Ribonucleoside-enhanced Cross-Linking ImmunoPrecipitation
ISG15	Interferon-stimulated gene	PARP	Poly ADP-ribose polymerase
ISR	Integrated stress response	PAS	Phagophore assembly sites
ITAFs	IRES trans-acting factors	PCa	Prostate Cancer
KO	Knock-out	PDXs	Patient derived xenografts
K-SFM	Keratinocyte Serum Free Medium	PE	Phosphatidylethanolamine
LC3B	Protein light chain 3 beta	PERK	RNA activated protein kinase-like endoplasmic reticulum kinase
LC-MS/MS	Liquid chromatography with tandem mass spectrometry	PFA	Paraformaldehyde
lncRNA	Long-noncoding RNA	PGE2	Prostaglandin E2
M	Metastatic tumour	PI3K	Phosphatidylinositol-3-kinase
m¹A	N1-methyladenosine	PI3P	Phosphatidyl inositol triphosphate
m¹G	1-methylguanosine	PIN	Prostatic intraepithelial neoplasia
m²G	N2-methylguanosine	piRNA	Piwi-interacting RNAs
m⁵C	5-methylcytosine	PKR	Protein kinase RNA
m⁵U	5-methyluridine	polyHEMA	Poly-2-hydroxyethyl methacrylate
m⁶Am	N6,2'-O-dimethyladenosine	PSA	Prostate specific antigen
m⁷G	7-methyl guanosine	PT	Primary tumour
m⁷G-MeRIP-seq	m ⁷ G-methylated RNA immunoprecipitationsequencing	PTEN	Phosphatase and tensin homolog
m⁷GTP	7-methylguanosine triphosphate	Q	Queosine
MAB	Maximum androgen blockade	RBP	RNA Binding Protein
mcm⁵s²U	5-methoxycarbonylmethyl-2-thiouridine	RMP	RNA modifying proteins
mcm⁵U	5-methoxycarbonyl-methyluridine	RNA	Ribonucleic acid
mCRPC	Metastatic Castration resistant prostate cancer	RNA-seq	RNA-sequencing
METTL1	Methyltransferase-1	ROS	Reactive oxygen species
miRNA	micro-RNA	RPMs	Reads per million
mRNA	messenger RNA	rRNA	Ribosomal RNA
ms²t⁶A	2-methylthio-N6-threonylcarbamoyladenine	RT-qPCR	Real time-quantitative polymerase chain reaction
mTOG	mini-5' terminal oligoguanine	NKX3.1	NK homeobox 3 1
mTOR	;ammalian target of Rapamycin	NSG	NOD/scid/gamma mice
NC	Normal conditions	SAM	S-adenosylmethionine
ncm⁵U	5-carbamoylmethyluridine	SD	Standard deviation
ncm⁵Um	5-carbamoylmethyl-2'-O-methyluridine	SEM	standard error of the mean
ncRNA	non-coding RNA	SG	Stress granules
NSG	NOD/scid/gamma mice	TCGA	The Cancer Genome Atlas
OD	Optical density	tiRNAs	Stress-induced tRNAs
sgRNAs	Single-guide RNAs	tracrRNA	Trans-activating CRISPR RNA
shRNA	Short-hairping RNA		

SIP1/2	Site-1/2 proteases	TRAC-seq	tRNA reduction and cleavage sequencing
siRNAs	Small-interfering RNAs	TRAMP	Transgenic Adenocarcinoma Mouse Prostate
SNARE	Soluble-N-ethylmaleimide-sensitive factor attachment protein receptor	tRFs	tRNA-derived small fragments
sncRNA	Small noncoding RNA	tRMPs	tRNAs Modifying proteins
SPF	Specific pathogen free	tRNA	transfer RNA
SQSTM1/p62	Sequestosome-1	Um	2'-O-methyluridine
ssODN	Single-stranded oligodeoxynucleotides	UPR	Unfolded protein response
t6A	N-threonylcarbamoyladenosine	VEGF	Vascular endothelial growth factor
TCA	Trichloroacetic acid	VP	Ventral prostate
TCGA	The Cancer Genome Atlas	WDR4	WD Repeat domain 4
TE	Translation efficiency	WT	Wild type
TOGs	5' terminal oligoguanine	yW	Wybutosine
t6A	N-threonylcarbamoyladenosine	Ψ	Pseudouridine
TCA	Trichloroacetic acid		

INTRODUCTION



INTRODUCTION

1. Prostate Cancer

Prostate Cancer (PCa) is the second most commonly diagnosed cancer type and the first in terms of prevalence in men worldwide¹. Every year, an estimation of 1,414,2059 new cases of the disease are diagnosed, which causes 375,304 deaths worldwide (Figure 1). Age comprises the fundamental risk factor for the disease development, since higher PCa incidence and mortality are observed in elderly men (>65 years of age). Race and family history are also linked with higher PCa probability, and certain diseases and conditions such as obesity and Lynch disease (reviewed in²).

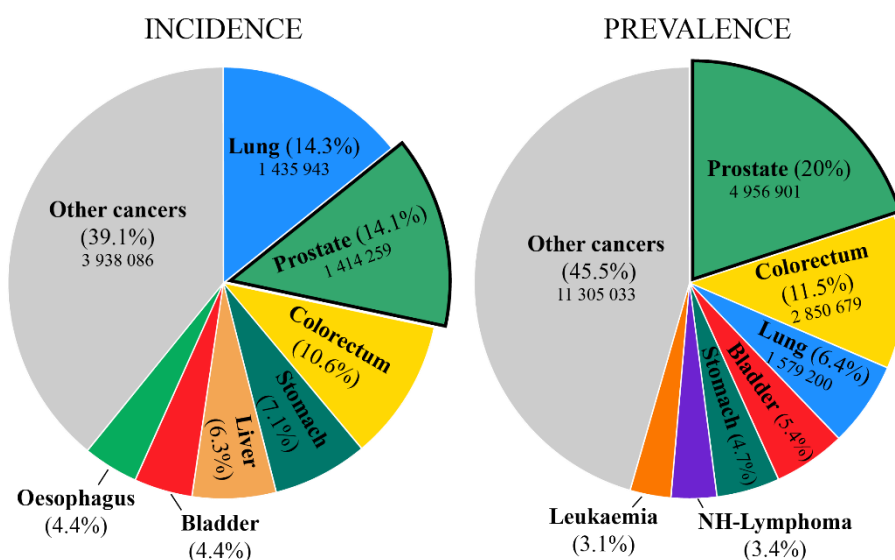


Figure 1. Estimated number of new cases and 5-year prevalent cases in 2020 in men worldwide, from a total of 10,065,305 and 24,828,480 patients respectively. Modified from ¹

1.1. Anatomy of the prostate

The prostate is a small muscular gland, part of the male reproductive system, whose main function is the production of the seminal fluid. There are anatomical differences in the prostate between species. Human prostate consists in a single structure divided in three zones: peripheral zone, where most of the tumours are formed, the central and the transition zone³. In comparison, mouse prostate is divided into paired lobes: the anterior prostate (AP), the ventral prostate (VP) and the dorsolateral prostate (DLP)⁴ (Figure 2). At cellular level, human and mouse prostates are comprised by a pseudostratified epithelium constituted by three different cellular types^{4,5}:

- Luminal cells. Responsible of production of secretory proteins. Characterised by expression of cytokeratin 8 (CK8) and 18 (CK18), androgen receptor (AR) and NK homeobox 3.1 (NKX3.1).
- Basal cells. Their function remains unclear. They are thought to regulate luminal cell biology and serve as structural barrier to maintain prostate tissue homeostasis⁶. Distinguished by high expression levels of CK5, CK14, p63, Sca-1 and Trop2, and low levels of AR.

- Neuroendocrine. Small cell population located within the basal cell layer. Express neuroendocrine markers such as synaptophysin.

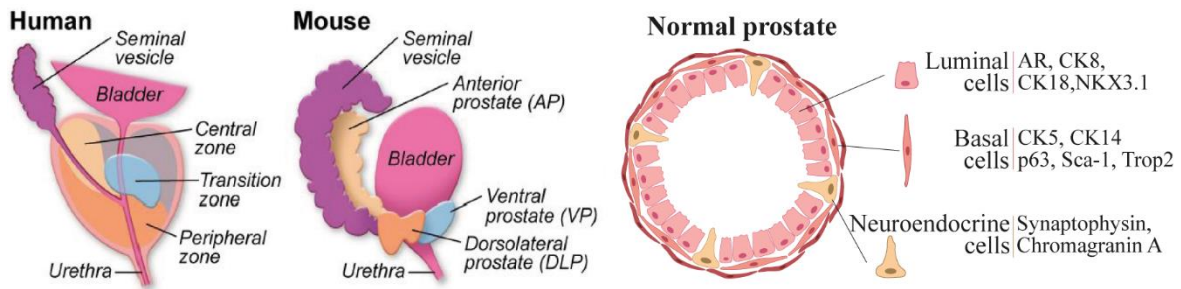


Figure 2. Graphical representation of normal prostate. Anatomical comparison of human and mouse prostates and schematic description of the different cell types that comprise the prostatic epithelium. A summary of the characteristics markers for every cell type is also indicated. Modified from⁷.

1.2. Prostate tumour formation

Prostate tumour formation initiates with the appearance of a prostatic intraepithelial neoplasia (PIN), characterised by neoplastic proliferation of luminal cells within pre-existing benign ducts⁷. This event is the beginning of a multistep process that progress to *in situ* adenocarcinoma, which can further develop into invasive prostate cancer, characterised by an invasion through the basal lamina. The last step of prostate transformation is the metastatic prostate cancer, in which the tumoural cells metastasises first to draining lymph nodes and then to distant organs such as bones, liver and lungs^{8,9} (Figure 3).

The identification of the cell of origin for prostate cancer is one of the unanswered issues of the field since prostate tumours exhibit both luminal and basal phenotypes. Understanding the cells of origin of cancer would provide crucial information about tumour initiation and evolution, as well as molecular features that would help to identify new markers for early cancer detection and treatment⁶. Traditionally, basal cells have been established as the preferred cell-of-origin of PCa, mainly due to the technical limitations of luminal cells culture. However, advances in 2D and 3D culture systems are enlarging the knowledge about the role of luminal cells in PCa initiation¹⁰⁻¹². Several published studies exhibit that either luminal-^{13,14} or basal-derived^{15,16} prostate tumours are more aggressive and carry a worst prognosis, but no consensus has yet been reached. Which has been clearly proved is that both stem-like and differentiated cells have tumorigenic potential¹⁷. The main luminal composition of prostate tumours¹⁸ together with the increased susceptibility of luminal cells to oncogenic transformation^{17,19} establish luminal cells as potential candidates to be cell of origin of prostate tumours^{12,13,17,20,21}. Nevertheless, further research is needed to clarify the nature of the cell-of-origin of PCa, In addition, other cell types comprising prostate epithelium such as fibroblast, muscle cells, endothelial cells and immune cells, can influence biology and clinical outcome of the tumour²².

1.3. Treatment of PCa

After PCa detection, the suitable treatment choice would depend on the tumoural characteristics of each patient. Initial prostatic specific antigen (PSA) levels, clinical TNM stage, Gleason's score together with the presence of potential risk factors such as comorbidities, are the principal prognosis factors considered for specific treatment application²³. For patients with localised disease and low risk PCa, the standard treatment consists in active surveillance, total or partial prostatectomy, cryotherapy and radiotherapy. The most common radiation therapies used in PCa are brachytherapy and external beam radiation²⁴. Androgen deprivation therapy (ADT) is used in patients with advanced localised PCa with the main aim of producing maximum androgen blockade (MAB) due to the dependency of PCa on testosterone levels²⁵. First-generation anti-androgens such as flutamide and bicalutamide are commonly used at this stage. However, after prolonged AR blockade, castration resistance by genomic mutations in AR gene is commonly developed, progressing to metastatic castration resistant prostate cancer (mCRPC) characterised by its poor prognosis²⁶. For years, the standard treatment for mCRPC was Docetaxel, with an overall survival improvement of 3 months²³. Recently, a new subset of second-generation AR inhibitors has been developed, as abiraterone^{27,28} and enzalutamide²⁹ with promising results in naive or post-Docetaxel treatment of mCRPC (Figure 3). Moreover, Cabazitaxel is a second generation taxane approved by the Food and Drug Administration (FDA) in 2010 for the treatment of Docetaxel resistant mCRPC³⁰ with modest efficacy results. More recently, the radioactive calcium mimetic radium-223 dichloride has been accepted for the treatment of bone metastases in mCRPC, which are present in 80-90% of the cases. Radium-223 has been shown to significantly improve survival and recovery of patients with mCRPC²³.

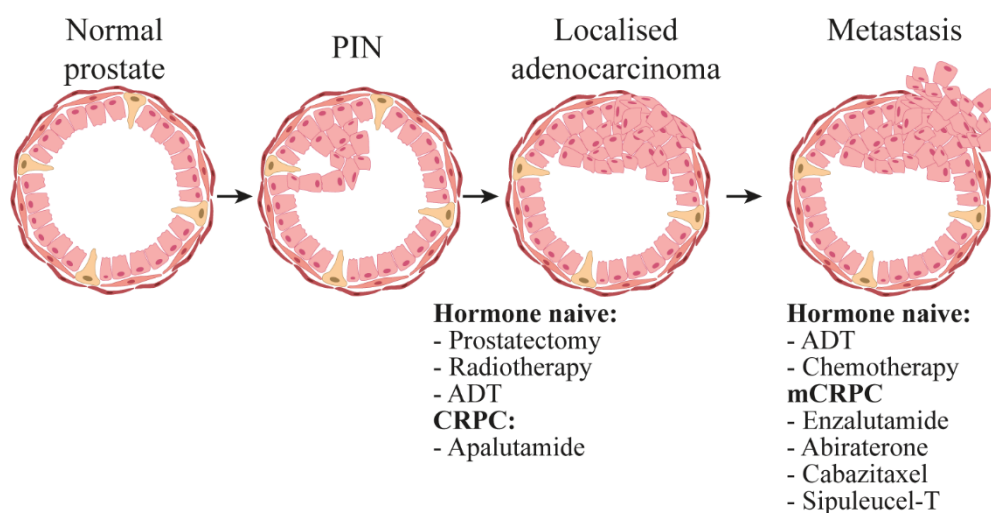


Figure 3. Schematic representation of prostate cancer progression and development of metastasis. The most common treatments used in every phase are indicated. Adapted from⁷.

Conversely, although PCa is characterised by its low immunogenic capacity, the immunotherapeutic agent Sipuleucel-T, which is an autologous dendritic cell-based immunotherapy, was approved in

2011 as a first-line treatment of patients with asymptomatic advanced and metastatic PCa with resistance to hormone therapy³¹. Due to the high heterogeneity of PCa tumours, a rising interest in the development of precise medicine treatments is emerging. For example, tumours with mutation in *BRCA1* and *BRAC2* related genes are suitable for treatment with poly-ADP ribose polymerase (PARP) inhibitor olaparib³², meanwhile anti-PD-1 agent pembrolizumab exhibited high response in tumours with mismatch repair deficiencies³³.

Thus, due to its major androgen dependency, ADT is one of the first lines of action to hamper tumour growth³⁴. However, the high percentage of patients that acquire hormone therapy resistance limit these treatments application. Although several new therapeutic agents have been recently developed, the survival improvement obtained is of around 3-4 months. Thereby, the development of new effective therapies to target mCRPC is still a pending task.

1.4. Molecular characteristics of PCa

With the aim of further deciphering the molecular characteristic underlying the disease progression, several large-scale genomic studies in primary tumours and mCRPC have been performed during the last years³⁵⁻⁴². Altogether, these data picture both primary prostate tumours and mCRPC to exhibit a low mutational load in comparison with other tumours. However, prostate tumours are characterised by a marked increase of genome-wide copy number alterations, genomic rearrangements, and gene fusions^{36,43-48}. The most commonly genetic altered pathways in PCa are Androgen Receptor (AR), Phosphatidylinositol-3-kinase/phosphatase and tensin homolog (PI3K-PTEN), DNA repair and cell cycle components^{40,49}. Thus, amplifications of *MYC* have been detected in 50% of prostate tumours^{48,50}, meanwhile activating mutations of AR pathway are usually correlated with castration resistance^{44,51}. One of the most common genes that is deleted in PCa is *PTEN*, correlated with a more aggressive tumour and increased metastasis⁵² and being detected in approximately 23% of high-grade prostatic intraepithelial neoplasia (HGPIN), in the 69% of localised PCa⁵³, and 86% of mCRPC⁵⁴. *NKX3.1*, which plays an essential role in urogenital development and function, has been reported as a tumour suppressor gene linked with prostate carcinogenesis initiation⁴⁷. In addition, mutations in *BRCA* genes and other DNA repair related genes as *ATM*, increase predisposition for PCa development and are associated with poorer prognosis, being detected in ~30% of mCRPC tumours^{36,55}.

But not only genetic alterations are important in PCa evolution. Aberrant DNA methylation has been widely proved to contribute to oncogenic transformation either by hypermethylation of tumour suppressor genes promoters, which lead to silencing of gene expression, or by generating genome instability through global hypomethylation⁵⁶. mCRPC and tumours insensitive to AR treatments have been described to be enriched in alterations of epigenetic master regulators (reviewed in³⁵). Thus, deregulation of DNA methyltransferases such as DNMT1⁵⁷, histone modifiers (*AXL1*, *KMT2A*, *KMT2D*, *UTX*), chromatin remodelers (*ARID* family)^{40,43} and proteins of polycomb group

(EZH2)^{58,59} have all been associated with PCa progression and castration resistance. For example, DNMT1 has been shown to act as a tumour suppressor gene at early stage PCa and an oncogene in later stages⁵⁷. However, the most-widely studied alteration is the hypermethylation of *glutathione S-transferase P (GSTP1)* promoter, which leads to gene silencing in early stages during prostate carcinogenesis⁶⁰. GSTP1 protein modulate distinct signalling pathways associated with cell proliferation, differentiation and apoptosis⁶¹ and has been proposed as potential prognostic biomarker⁶². Other PCa key genes have been also described to present DNA methylation alteration, since inactivating hypermethylation of AR promoter is described in up to 30% of CRPC⁶³. In addition, hypermethylation of *PTEN* promoter CpG islands is a frequent cause of the gene silencing, while hypermethylation of the tumour suppressor gene p16 is associated with cell cycle acceleration which leads to increased proliferation and disease progression⁶⁴. Moreover, hypomethylation and consequent upregulation of several genes as heparanase and urokinase plasminogen activator (uPA) has been reported to contribute to metastasis and tumour invasion⁶⁵, and several methylation signatures have been proposed as molecular biomarkers of PCa progression⁶⁶.

To summarize, even though important advances has been made in PCa research, its elevated prevalence, therapy resistance and the high inter-patients and intratumoural heterogeneity, comprise major milestones that still require further investigation. New therapeutic approaches and specific prognostic biomarkers are essential for facing a significant medical problem that affects a high percentage of the population.

1.1. *In vivo* PCa models

1.1.1. PCa mouse models

Reliable mouse models that accurately mimic patient conditions are crucial tools to unravel and study the behaviour, development, and progression of a disease, and thus, address different treatment approaches. As so, a huge effort has been made in the development of genetic engineered mouse strains that resemble human prostate cancer. The major idea that must prime when choosing a specific mouse model is that it has to be representative of the disease under examination. As so, distinct mouse model have been engineered to express many oncogenic elements (*Myc*, *ERG*) or to delete tumour suppressor genes that can either initiate (*Pten* or *Nkx3.1*) or promote (*smad4*, *Trp53*) PCa progression in combination with other tumour suppressors or oncogenes⁵⁶. Usually, these Genetically Engineered Mouse Models (GEMMs) use prostate-specific promoters to selectively regulate the gene edition by Cre expression in the prostatic tissue, such as the ARR₂PB (*Probasine*) promoter⁶⁷ or regulatory elements from *PSA*, *Nkx3.1*, *Hoxb13* and *TMPRSS2* genes⁶⁸. The use of *Pb* promoter allowed the generation of more accurate mouse model. Besides to regulate specific expression in prostatic epithelium, *Pb* promoter is androgen responsive, which results that gene expression is induced after puberty (at age of 7 weeks), once the prostate is completely formed⁶⁷.

The first PCa mouse model developed was the Transgenic Adenocarcinoma Mouse Prostate model or TRAMP⁶⁹, which is based in the expression of the viral oncogene Simian Virus 40 (SV40) under the control of *Pb* promoter. SV40 encodes for *Large T* and *Small T* tumour antigens, resulting in cancer development since *Large T* antigen bind and inhibit p53 and Rb tumour suppressors⁷⁰. These mice display hyperplasia at 8 weeks and PIN from 18 to 24 weeks of age. Adenocarcinoma can arise at 28 weeks of age, and ultimately develop metastases by 30 weeks, primarily to lungs and lymph nodes⁶⁹. As one of the first developed models, TRAMP mice have been widely used for validation of PCa oncogenic role of specific genes⁷¹ as well as for development of new chemotherapeutic approaches⁷².

The LADY model is a variation of TRAMP mice. In this case, the *Pb* promoter drives the expression of only *Large T* antigen of SV40, since *Small T* antigen has been described to target a wide subset of intracellular proteins. These mice develop dysplasia and PIN by 10 weeks of age and undifferentiated adenocarcinoma in 20 weeks-old mice. After 33 weeks of age, several metastases with neuroendocrine characteristics are developed. Distinct LADY models have been established in the last years (reviewed in⁷³), all of them characterised by a rapid progression of the disease⁸.

Due to the differences with the human disease of these firstly generated models, a second generation of GEMMs was established with the aim of targeting genetic lesions observed in human PCa in murine prostates⁷³. Based in this approach, mice with mutant *Nkx3.1*, *Pten*, *p53* or *Rb* successfully developed epithelial hyperplasia and dysplasia.

PTEN is one of the most common driver genes of PCa development, being deleted in approximately 23% of HGPIN, 69% of PCa and 86% of metastatic CRPC)⁷⁴. The first *Pten* edited mice consisted in heterozygous *Pten* knockout (*Pten*^{+/-}), which developed lymphomas, endometrial hyperplasia, PIN and thyroid neoplasm⁷⁵. However, mice exhibited adenocarcinoma between 40 and 65 weeks of age. For accelerating PCa development, combination of *Pten*^{+/-} with *Nkx3.1*^{-/-} was performed, with 60% of the mice exhibiting HGPIN at 26 weeks and adenocarcinoma at week 52 with 100% penetrance⁷⁶.

However, one of the most extended models for invasive localised PCa adenocarcinoma is the *PB-Cre4 x Pten*^{fllox/fllox} mouse model developed by Professor Pandolfi⁷⁷. This model is based on the conditional deletion of *Pten* in prostatic epithelium⁷⁴. Thus, a genetic engineered mouse with *Pten* exons 4 and 5 flanked by *loxP* sites was generated by Trotman *et al.*⁷⁷. For prostate specific deletion, *Cre* recombinase gene expression is under the control of ARR₂PB promoter, that induces *Cre* expression at high levels and high penetrance⁷⁸. This provides an essential benefit, since any possible developmental effect that could be caused by *Pten* inactivation during prostate organogenesis is avoided⁷⁷. Therefore, *PB-Cre4 x Pten*^{fllox/fllox} mouse is characterised by developing at HGPIN at 12 weeks in all three prostate lobes and 100% penetrance, that progresses to invasive cancer after 4-6 months latency. No metastasis has been detected even in mice up to 130 weeks of aging⁷⁹. Thus, this

model can be widely used for deciphering the tumorigenic role of specific genes of interest by evaluating how its presence/absence affects prostate tumour development.

Variations of these model have also been developed, as *Pten^{flox/flox}/Nkx3.1-Cre^{ERT2}* with ablation of one allele of Nkx3.1. These mice constitute the best model for CRPC since, after castration, there is a tumour regression that progress to microinvasive adenocarcinoma with nuclear AR⁸⁰. Another interesting variant of the model is the *Pten^{flox/flox}/Nkx3.1^{ERT2}* coupled with oncogenic Ras *Kras^{LSL-G12D/+}*) developed by Aytes *et al.*⁸¹, which besides aggressive adenocarcinomas also develop metastasis with 100% penetrance in lung and liver. Thus, this model is a potent tool for studying the most advanced stage of PCa.

Lastly, another commonly used PCa model is based in the overexpression of the *c-Myc* oncogene. *c-Myc* is overexpressed in PCa, being higher the expression towards tumour stage progression. Two distinct models with different expression models depending on the used promoters have been generated: Lo-Myc with small *Pb* promoter, and Hi-Myc, with ARR₂PB promoter⁸². Hi-Myc mice develop PIN at 13 weeks which progress to invasive adenocarcinoma by week 26, while Lo-Myc progress slower, with a delayed adenocarcinoma appearance at 30 weeks-old mice. The main limitations of these models are that they do not become castration resistance after castration and no metastasis have been detected⁸².

In summary, the generation of PCa mouse models is an expanding field but due to the differences in human and mouse prostates, the search of a model that accurately represents the disease is still ongoing. In fact, one of the main disadvantages of working with PCa mouse model is the long time needed for disease generation and the difficulties in reproducing metastatic phenotypes specially bone dissemination. Thus, further research of target genes is still needed.

1.1.2. Patient Derived Xenografts Organoids

A novel *in vitro* model that is gaining interest over the years is the use of Patient Derived Xenografts (PDXs)-derived organoids. PDX-derived organoids are 3D *in vitro* models generated from patient tumour tissue expanded in murine models, or in other words, are *in vitro* models derived from an *in vivo* PDX⁸³.

Due to the elevated complexity of human tumours, cancer cell lines often fail in recapitulate some of their biological characteristics. Thus, although a high number of anti-cancer compounds tested for clinical safety in Phase I studies progress to the efficacy testing in Phase II, most of these drugs fail in Phase II or Phase III of examination of clinical response due to the vast differences between the pre-clinical models and the patients⁸⁴. With the aim of overcoming the limitations of cancer cell lines and enhance the correlation with human tumours, the establishment of surgically derived primary clinical tumour samples that are grafted into mice or PDXs was performed⁸⁵. PDXs are powerful tools that allow the study of intra-tumour characteristics and drug response in a more reliable and

accurate manner than two-dimensional cell culture since consist in a more realistic representation of the original tumour⁸⁵. For tumour engraftment, immunodeficient mice such as NOD/SCID/IL2R γ ^{null} are necessary to increase efficiency⁸⁶. PDXs models have been established in a broad variety of cancers, including colorectal⁸⁷, pancreatic⁸⁸, breast⁸⁹, lung⁹⁰, skin⁹¹, head and neck⁹², prostate⁹³ and ovarian cancer⁹⁴. However, several limitations arise when working with PDXs. Limited engraftment rates of PDXs remain a major challenge and is highly variable between cancers. Orthotopic transplantation in the organ of interest has been described to provide a more physiological engraftment than heterotopic (e.g. subcutaneous), even leading with invasive growth and metastases⁹⁵, but reduced viability is also observed. In addition, accumulation of copy number alterations and genomic instability after serial transplantations reduce the accuracy of the model^{96,97}. It has been described that human stroma is subsequently replaced by murine stroma over engraftment passages, resulting in a deviation of the PDXs from the original tumour over time⁹⁸. Additionally, when using PDXs to evaluate the effect of specific drugs, it is crucial to take into account that drug metabolism and pharmacokinetics differ from mouse to human, which may influence in the treatment response⁸³.

To address some of these restrictions, PDXs-derived organoids arise as an optimal alternative, since they recapitulate tumour features such as phenotype, heterogeneity, drug response and overall complexity, while providing an alternative to animal model^{83,99}. Due to its origin from cancer stem cells, PDXs-derived organoids faithfully recapitulate the histopathology properties of the PDX tumour. Moreover, numerous studies have shown that the concurrent genetic profile and pharmacological response observed in organoids may accurately predict the clinical outcome^{100,101}. The growth of PDX-derived organoids in highly enriched conditions allows the generation of three-dimensional multicellular structures that mimic patient tumour with high stability and genomic integrity. Thereby, organoid cultures are a potent *in vitro* tool to evaluate therapy response of certain patients subgroups and decipher the underlying cause⁸³. However, the use of PDX-derived organoids also entails several limitations, as the low proliferation rates of PCa organoids which results in the need of mouse expansion step, and the limited availability of material¹⁰¹. In addition, organoid cultures cannot mimic vasculature and tumour-stroma interactions. Tough, the establishment of distinct bone metastatic PCa PDXs models as BM18¹⁰² and LAPC9¹⁰³ improves material availability, as well as allow genetic manipulation to address the effect of specific genes in a human preclinical model. So far, large scale drug screening on primary PCa organoids have not been yet performed and the extent to which PCa organoids can model key features of therapy resistance and drug response needs further investigation, but patient-derived tumour organoids are a promising tool for distinct translational applications^{83,101}.

2. Epitranscriptomics

During the last years, numerous studies have highlighted the high relevance of non-mutational mechanisms, such as epigenetic marks, on prostate cancer development and progression³⁵. In this scenario, RNA modifications or epitranscriptomics arise as a new layer of information/regulation with an important role in maintaining essential biological processes and regulating different tumour-initiating events (reviewed in¹⁰⁴⁻¹⁰⁷).

Epitranscriptomics has emerged as the study of all the changes at which RNA is subjected once the transcription is over, in terms of chemical modification or sequence alterations (known as RNA editing). Currently, more than 170 different known RNA modifications compose the epitranscriptome, containing most RNA species one or multiple chemical modifications that can be present in all four RNA bases and the ribose sugar¹⁰⁸. Although their existence has been known for decades, until the development of sufficiently sensitive tools and high-resolution genome-wide techniques their identification and study have been hampered, especially of those present in low-abundant RNA species¹⁰⁹. Thus, despite their abundance, the lack of specific and sensitive techniques has maintained the epitranscriptome out of the focus of study for years, being their function still widely unknown. Nevertheless, even the limited characterisation performed so far has highlighted numerous essential biological functions regulated by RNA modifications, such as cell self-renewal, differentiation, migration or stress response^{110,111}. The epitranscriptome, indeed, arises as an area as complex and extensive as epigenetics^{112,113}. Similar to DNA, RNA modifications can be dynamically and reversibly regulated by specific enzymes named as readers, writers and erasers¹¹⁴. Epitranscriptomic writers are defined as the enzymes responsible for deposition of RNA marks, while erasers arise as the proteins in charge of their removal. Readers are proteins that selectively recognise and bind to specific RNA chemical modifications to perform various functions¹¹⁵. Some examples of writers are the methyltransferases from METTL, NSUN, TRMT or ALKBH8 families, or non-methyltransferases as DKC1, NAT10 and TRIT1, that mediate pseudouridine (Ψ), N4-acetylcytidine and N6-isopenenyladenosine, respectively¹¹⁵. The first eraser discovered that led to the coining of the epitranscriptome as a dynamic event was the fatmass and obesity-associated protein (FTO), that demethylates N6-Methyladenosine (m⁶A) in both DNA and RNA¹¹⁶. Another example of m⁶A eraser is the alpha-ketoglutarate-dependent dioxygenase homolog 5 (ALKBH5)¹¹⁷. Regarding readers, the most well-known family of RNA readers is the YTH domain proteins¹¹⁸, which bind to m⁶A-mRNA and perform distinct functions. YTHDF1 was described to increase translation efficiency in a m⁷G cap-independent manner. In contrast, the extensively studied reader ALYREF specifically recognises m⁵C-modified mRNA promoting its nucleus-to-cytosol export¹¹⁹.

3. tRNA modifications

Among all RNA species, transfer RNAs (tRNAs) are the most extensively modified, with more than 90 different types of modifications identified so far¹⁰⁸. Despite its non-coding RNA (ncRNA) nature,

tRNAs are essential elements of the translational machinery, being the molecules responsible of carrying the amino acids required to form the nascent peptides at the ribosome¹²⁰. Molecularly, tRNAs exhibit a characteristic double-strand clover leaf secondary structure with five major domains (Figure 4)¹²¹:

- Acceptor stem, to which the specific amino acid is attached.
- D-loop, together with acceptor stem, is involved in amino acid recognition and charge on to the acceptor stem.
- Anticodon loop is responsible for mRNA codon recognition.
- Variable loop regulates three-dimensional structure by interacting with D-loop and T-loop.
- T-loop and TΨC arm are implicated in the ribosome-tRNA interaction essential for efficient translation.

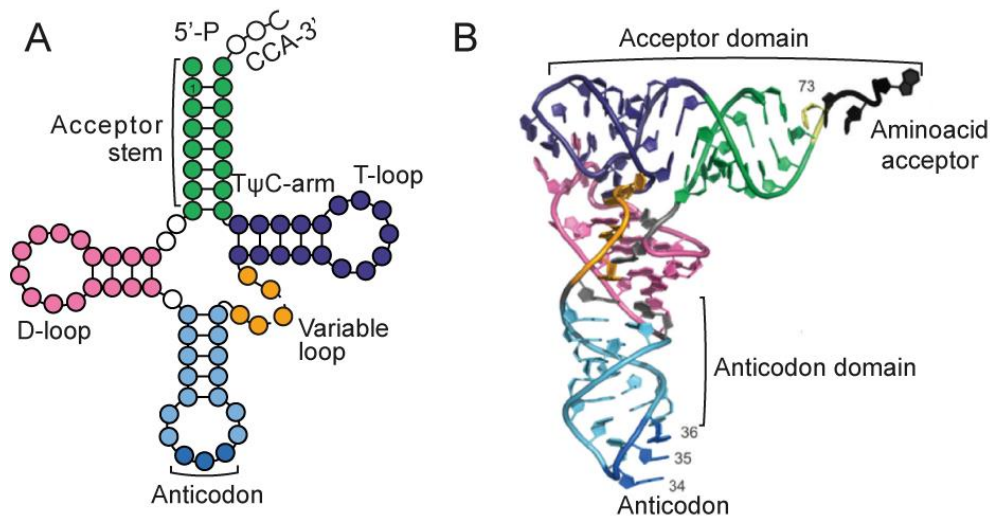


Figure 4. A) Cloverleaf structure of the general structure of tRNAs. B) L-shaped three-dimensional representation of the yeast Phenylalanine tRNA. Colours label the same structures within both representations. Adapted from¹²².

It is largely known that tRNAs are multiple and versatile molecules capable to regulate gene expression, being RNA modifications crucial in this process. All tRNAs isotypes carry chemical modifications distributed along the cloverleaf structure, however, the number of modifications in individual tRNAs can vary between organisms, tissues, organelles and tRNA species. The standard length of the majority of eukaryotic tRNAs isoforms is of 76 nucleotides, with an average of 13 different modifications per molecule. This entails that approximately 20% of the nucleotides that comprise a tRNA molecule carry a modification¹²³ (Figure 5). Mitochondrial tRNAs exhibit an average of 5 modifications per molecule, being some of them exclusive^{123,124}.

tRNA modifications are highly diverse, being pseudouridylation (Ψ) the most abundant and conserved modification followed by methylation (m^5C , 5-methylcytosine; m^7G , 7-methylguanosine; m^5U , 5-methyluridine; m^1A , N1-methyladenosine...). Other complex multistep modifications such as N6-threonylcarbamoyl-adenosine (t^6A) and 5-methoxycarbonylmethyl-2-thiouridine (mcm^5s^2U) also decorate the tRNA structure¹⁰⁴ (Figure 5).

A wide variety of functions of tRNA modifications have been described, being dependent of the location within the molecule and its chemical nature. The anticodon loop hosts complex modifications involved in regulating strength and specificity of codon recognition as well as optimization and maintenance of reading frame^{104,125,126}. Modifications in this region are highly conserved in eukaryotes due to its high relevance in regulating translation fidelity. In fact, the highest variability in chemical deposition occurs at the wobble position (position 34), with more than 30 distinct modifications identified to date¹⁰⁸. Wobble modifications control base pairing and codon usage, regulating the diversity of codon recognition properties of the tRNA^{125,127}.

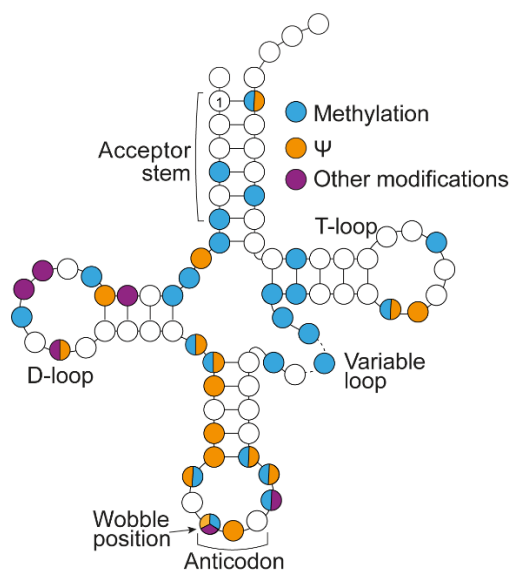


Figure 5. Schematic representation of an average tRNA molecule. The distinct parts are indicated. Coloured circles represent the type of modification present in that position: blue for methylations, orange for Ψ , and in purple other less common modifications are indicated. Among methylations, the modifications included are: m^1A ; ms^2t^6A , 2-methylthio-N6-threonylcarbamoyladenine; m^1G , 1-methylguanosine; Gm, 2'-O-methylguanosine; m^7G ; Cm, 2'-O-methylcytidine; m^5C ; m^5U ; m^2G , N2-methylguanosine; Um, 2'-O-methyluridine; m^6Am , N6,2'-O-dimethyladenosine. Other modifications are composed by: yW , wybutosine; I, inosine; mcm^5U , 5-methoxycarbonylmethyluridine; mcm^5s^2U , 5-methoxycarbonylmethyl-2-thiouridine; ncm^5U , 5-carbamoylmethyluridine; ncm^5Um , 5-carbamoylmethyl-2'-O-methyluridine, hm^5C , 5-hydroxymethylcytidine. Adapted from^{104,105}.

Modifications deposited within the structural D- or T-loops of the tRNA are necessary for tRNA stability and proper folding¹²⁸, and its absence is linked to tRNA degradation¹²⁰ and impaired processing^{110,129,130}. Besides, modifications on the tRNA structure are arising as key regulators of tRNA-derived RNA fragments formation, small noncoding RNA molecules produced by tRNA cleavage. Although initially considered as degradation products, a growing interest in the study of these tRNA fragments is emerging due to its role in regulating gene expression at both transcriptional and translational levels^{110,131}.

3.1. Regulation of protein translation by modifications deposition at anticodon loop

Due to tRNAs function as mRNA decoders, modifications located at the functional sites of the molecule, the anticodon loop, are crucial for the modulation of protein synthesis by regulating tRNAs capacity to interact with mRNA. As previously mentioned, the most relevant effect is produced by those modifications localised at the wobble position, which is the most heavily modified region of the tRNA and the responsible to optimise codon usage during gene-specific translation by restricting or expanding the decoding capacity of the molecule¹⁰⁴. The most known modification is the adenosine deamination to Inosine (I, A-to-I), which occurs in at least eight different tRNAs isoacceptors. This modification permits a single tRNA to decode up to three distinct codons for the

same amino acid, being essential for the codon degeneracy¹³². Thus, this change is catalysed by tRNA-adenosine deaminases (ADATs)¹³³, being I34 able to wobble with adenine, cytosine and uridine¹³⁴. Alterations on A-to-I editing due to ADAT3 mutations are associated with intellectual disability and strabismus¹³⁵. Moreover, guanosines or cytosines at position 34 are susceptible of being modified by 2'-O-methylation catalysed by FTSJ1, which has been previously described to enhance codon-anticodon interaction of the ribosome¹³⁶. Mutations on *FTSJ1* are linked with intellectual disability¹³⁷. Complex modifications such as 5-carbamoylmethyl (ncm⁵) or 5-methylaminomethyl-2-thiouridine (mcm⁵s²U) have been identified at U34 of the wobble base of tRNA^{UUU}, tRNA^{UUC}, tRNA^{UUG} and tRNA^{UCU} isoacceptors. These complex wobble modifications require the joint action of several RNA modifying proteins (RMPs) and are essential for improving base pairing and protein translation of mRNAs enriched for the corresponding codons^{127,138}, since their loss pause translation of specific codons at the ribosomes¹³⁹. Another modification of the wobble position is queosine (Q), which has been described to increase, together with m⁵C at C38, translational speed and fidelity. Alteration of Q levels results in accumulation of unfolded proteins that triggers endoplasmic reticulum stress response¹⁴⁰.

Other modifications that occur at the position 37 adjacent to the anticodon, such as N-threonylcarbamoyladenine (t⁶A) help to stabilise codon:anticodon interaction and prevent translational frameshifting^{141,142}. While m⁵C at position 38 regulates translation fidelity, since its loss cause to *DNMT2* alteration results in impaired discrimination of Asp and Glu codons, causing codon-specific mistranslation and dysregulation of haematopoiesis¹⁴³.

3.2. Regulation of tRNA-derived fragment formation by RNA modifications

Due to their important role in the post-transcriptional regulation of gene expression in physiological and pathological conditions, small noncoding RNAs (sncRNAs) have been widely investigated during the last years. High-throughput sequencing technologies have included tRNAs-derived RNA fragments to the growing list of sncRNAs composed by the largely known small-interfering RNAs (siRNAs), microRNAs (miRNAs) and piwi-interacting RNAs (piRNAs) among others¹⁴⁴⁻¹⁴⁶. These fragments can originate from both precursor and mature tRNAs, and their production can be either constitutive or induced under certain circumstances, such as developmental stage, proliferative status, stress or viral infection^{147,148}. Their high conservation between organisms together with their specific cleavage ends rule out their origin as random tRNA degradation products¹⁴⁹.

tRNA-derived fragments classification is usually based on their length, tRNA domain of origin and function. Those fragments derived from tRNAs can be divided into two major types: tRNA halves (stress induced tRNAs or tiRNAs) and tRNA-derived small fragments (tRFs) (Figure 6). tiRNAs are produced by the specific cleavage of the mature tRNA at the anticodon loop obtaining two distinct fragments: 30-35 nucleotide (nt) 5'tiRNAs and 40-50 bases 3'tiRNAs. Under normal conditions,

small amounts of these fragments can be found in human cells¹⁵⁰; however, their production is usually stress-induced (oxidative stress, heat shock or UV irradiation) by angiogenin ribonuclease¹⁵¹. 5'tiRNAs derived from tRNA^{Ala} and tRNA^{Cys} have been described to specifically inhibit protein translation and to promote stress granule (SG) assembly^{151,152}.

Conversely, tRFs are 13-30 nucleotides fragments produced by endonucleolytic cleavage of either mature (5'tRFs and 3'tRFs) or pre-tRNAs (tRF-1)^{153,154}. 3'tRFs and 5'tRFs derive from tRNA cleavage at the T or D-loop respectively, being the cleavage produced by DICER or other ribonucleases such as angiogenin or RNase Z^{148,155,156}. tRFs have been shown to be essential in regulating protein translation and, in particular, gene expression via association with argonaute (AGO) proteins and RISC complex^{157,158}.

tRNA fragment biogenesis appears to be heavily dependent on tRNA modifications.

Thus, modifications such as queuosine, 2'-O-methylation, m⁵C or m¹G have been described to protect tRNAs from cleavage in human cells¹⁵⁹⁻¹⁶¹. For example, m⁵C deposition at the variable loop prevents 5'tiRNAs-angiogenin-dependent formation, and its deregulation impairs cells survival under stress conditions¹⁶². In contrast, other modifications as PUS7-mediated pseudouridylation have been shown to mark tRNAs for its cleavage in human embryonic stem cells (hESCs)¹³¹. The formation of 5' terminal oligoguanine short fragments (mTOGs), which are essential for hESCs correct differentiation, depends on this modification. In summary, whether targeting or protecting tRNAs from its cleavage, it is evident that tRNA modifications are critical for tRNA-fragments formation, and their deregulation compromises crucial biological processes. In fact, a growing interest in tRNA-derived fragments is emerging since they seem to accumulate in different tumours and play important roles in cancer by regulating of cell proliferation, invasion, and metastasis^{153,156,163}. Furthermore, the aberrant expression of tRNA-derived fragments in cancer may serve as diagnostic biomarkers or therapeutic targets¹⁶⁴.

3.3. tRNA fragment biogenesis regulates protein translation

Regulation of translation rates through tRNA-derived fragments has raised an especial interest in the area. Since only a small portion of the tRNAs (<5%) within a cell are susceptible of being cleavage through the processes previously described, the consequently reduction of the pool of mature tRNAs

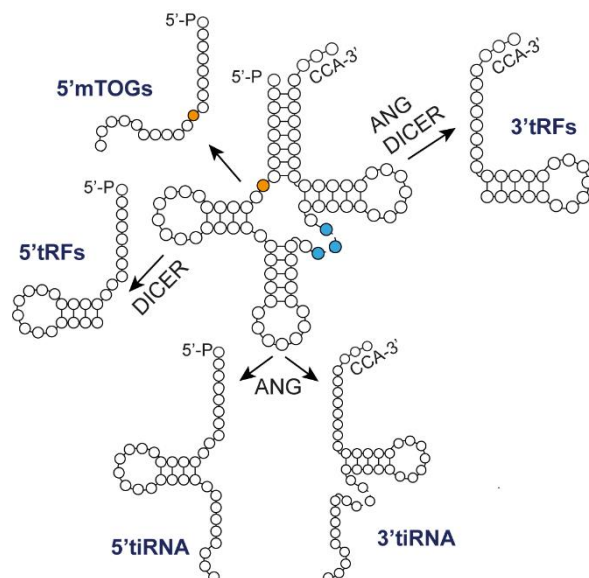


Figure 6. tRNA-fragments derived from mature tRNAs with the known ribonucleases implicated in their biogenesis. Adapted from^{184,185}.

would not be significant to affect protein synthesis. Thus, in the last years distinct mechanisms have been identified to be responsible of translation inhibition (reviewed in¹⁵⁶).

The importance of tRNA-derived fragments on translation regulation was first elucidated after Thompson *et al.* revealed that stress induced 5'tiRNAs but not 3'tiRNAs inhibited protein synthesis¹⁶⁵. This result not only introduced the specificity of tRFs function but also discarded the idea that the mere tRNA cleavage was the cause of protein inhibition. In the following years, several studies have shed light to the process.

One of the most studied translation inhibition mechanisms is based in the presence of tRNA-fragments containing 4 to 5 guanine residues at the 5' end (5'end terminal oligoguanine or TOG motif). Specific 5'tiRNAs and 5'tRFs fragments derived from tRNA^{Ala} and tRNA^{Cys} have been described to meet these qualities^{131,166}. The oligoguanine nature of these fragments confers a hairpin-like three-dimensional conformation that interferes with the assembly of the canonical translation initiation complex eIF4F. TOG-containing 5'tRFs can be either 35 nucleotide long (5'TOGs) or mini-TOGs (mTOGs), 18 nucleotide length TOGs fragments and pseudouridinylated at the eighth position of tRNAs^{131,166,167}. This phenomenon was first described by Ivanov *et al.*, demonstrating that the guanosine-containing 5'tiRNAs specifically displaced translation initiation factors eIF4G/eIF4A from capped mRNA and also bound to the translational repressor YB-1, which lead to global translation inhibition^{166,167}. Moreover, this study also linked this translation inhibition as a response to stress signal, since the 5'tiRNA fragment biogenesis was induced upon the stress-induced angiogenin ribonuclease activation¹⁶⁷. More recently, a new type of shorter oligoguanine-containing tRNA-derived fragments was described in hESCs¹³¹. Thus, Ψ-modified mTOGs were found to displace eIF4A/G from actively translated capped-mRNAs by specifically binding to polyadenylate-binding protein 1 (PABPC1) (Figure 7)¹³¹. PABPC1 is one of the factors that conform the translation initiation complex and binds to eIF4G allowing the complex formation and enhancing translation. In addition, Guzzi *et al.* also showed that mTOGs-binding capacity is dependent of the modification state of the fragments, since synthetic unmodified oligonucleotides preferentially bound to YB-1, which acts as a translation repressor responsible for storage of mRNAs on a silent state. Thus, tRFs inhibit global protein synthesis rates by impairing the formation of the translation initiation complex¹³¹.

The underlying mechanism of TOG translational inhibition together with its alteration in cancer, attract attention as a potential prognosis and therapeutic approach.

Besides 5'TOG dependent translation inhibition, other mechanisms have been also reported. Thus, YB-1 has been also described to bound to tRNA^{Glu}, tRNA^{Asp}, tRNA^{Gly} and tRNA^{Tyr}-derived tiRNAs fragments and downregulate translation of specific mRNAs in breast cancer cells¹⁶⁸. Moreover,

3'tRF fragments derived from tRNA-Leu-CAG were proved to enhance the translation of mRNA codifying for ribosomal proteins, regulating ribosome biogenesis in hepatocellular cancer cells^{169,170}.

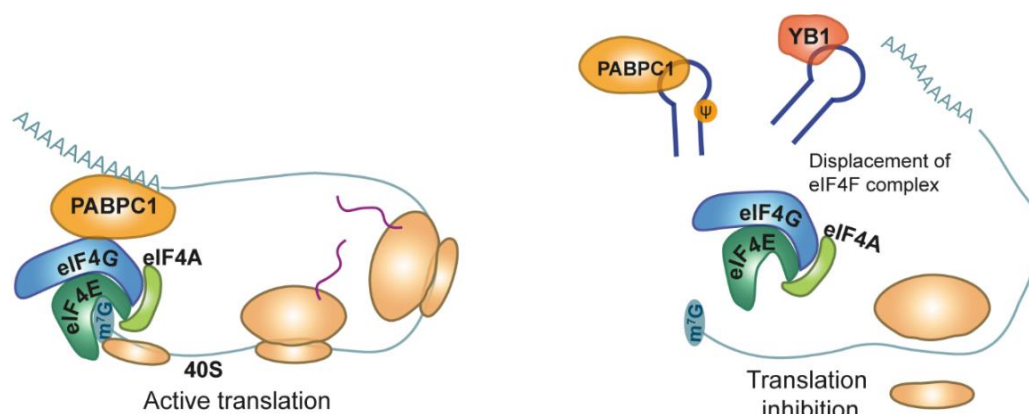


Figure 7. Schematic representation of normal active protein synthesis and the inhibition mediated by Ψ -5'mTOG. Adapted from^{131,156}

Thus, although the molecular insights regulating these processes needs further investigation, it is clear that tRNA-derived fragments regulate essential cellular processes as protein synthesis in a fragment-specific manner.

3.4. Interconnection between tRNA fragments biogenesis, translation inhibition and stress response

As stated before, biogenesis of most of tRNA-derived fragments described are highly dependent on stress conditions, being mainly cause by the stress-mediated activation of the human ribonucleases that mediate the process, such as angiogenin and RNase L¹⁵¹. tRNA-fragment formation via angiogenin activation is one of the best characterised processes, being described its activation by a large variety of stresses such as oxidative, heat shock or viral infection^{151,171}. For example, NSUN2-mediated m⁵C modification has been widely proved to protect tRNAs from angiogenin-mediated cleavage¹⁶². Depletion of NSUN2 results in 5'tiRNAs accumulation which leads to global inhibition of protein translation by displacing translation initiation factors from tRNAs¹⁶⁶ and activation of stress pathways measured by the accumulation of stress granules (SG) in the cytoplasm¹⁶². Remarkably, although global translation inhibition was detected upon tRNA fragmentation due to *NSUN2* depletion, an enhanced translation of the cell cycle inhibitor p21 was detected¹⁷², indicating a specific inhibition of cell proliferation. Several studies have highlighted that accumulation of 5'tiRNAs due to increased angiogenin expression drive the cells into a state of stress hypersensitivity¹⁵¹ due to a reduced capacity to rapidly adapt to environmental changes. In the context of cancer research, this eventually results in increased therapy sensitivity.

Thereby, as demonstrated by increasing data, global translation inhibition is a common response to most types of stress. This is produced as an energy saving action and to prevent the synthesis of unwanted proteins¹⁷³. However, it has been widely proved that stress-induced translation reduction is often accompanied by an enhanced selective translation of proteins involved in stress response¹⁷⁴.

Attenuation of global translation upon stress may be caused by tRNA-fragments accumulation by any of the mechanism previously described or by stress-mediated phosphorylation of the eukaryotic translation initiation factor 2 α (eIF2 α)¹⁷⁵. However, the mechanisms that govern preferential translation of specific mRNAs are still being elucidated.

eIF2 α is a component of the translation initiation complex essential for translation initiation that mediates the binding of tRNA^{Met} to the 40S ribosomal subunit. Its inactivation by phosphorylation is mediated by four distinct protein kinases: the heat sensor haem-regulated inhibitor kinase (HRI); protein kinase RNA (PKR) activated by double-stranded RNA; the sensor of ER stress PKR-like endoplasmic reticulum kinase (PERK); or the general control non-derepressible-2 (GCN2) kinase that is activated upon amino-acid starvation¹⁷⁴. Besides global translation inhibition, phosphorylation of eIF2 α also activates the translation of specific transcripts. For example, it has been described that eIF2 α phosphorylation mediated by PERK activation upon ER stress not only inhibit translation of most mRNAs but also induce the translation of *ATF4* mRNA, resulting in activation of the unfolded protein response (UPR) pathway¹⁷⁶.

Another alternative for cap-independent translation of specific transcripts is through the Internal Ribosome-Entry Sites or IRES. Briefly, ribosomes can directly recruit specific mRNAs that present discrete sequence elements in the 5'UTR in a cap and eIF4F complex independent manner¹⁷⁷. This process is mediated by some cellular proteins known as IRES *trans*-acting factors (ITAFs)¹⁷⁸, and was firstly described for viral mRNAs but its regulation is still being clarified. Thus, no common features of IRES sequences have been detected, but they have been reported in mRNAs characterised for exhibiting long 5'UTRs with high GC content and an extensive predicted secondary structure. Similarly, several ITAFs have been implicated in IRES-dependent translation but its requirement seems to be IRES specific¹⁷⁸. One mRNA described to harbour IRES-mediated translation is that encoding vascular endothelial growth factor (VEGF), that promotes angiogenesis¹⁷⁴.

Finally, another potential mechanism that would explain differential translation would be angiogenin-mediated direct cleavage of specific mRNAs or production of tRFs that target certain mRNAs and produced its degradation together with argonaute proteins¹⁷³.

Thus, biologically, tRNA modifications allow protein synthesis regulation through two distinct processes: by modulating tRNA biogenesis via modifications within the structural backbone or either by regulating codon pairing and translation speed of specific genes through anticodon modifications.

3.5. tRNA modifications in cancer

Thereby, tRNA modifications are key regulators of essential physiological processes. In fact, during the last years numerous lines of evidence remark that dysregulation of epitranscriptomic pathways may contribute to the appearance or progression of different human pathologies, including cancer^{106,109}

Gene symbol	Type of enzyme	Modification	Cancer type	Expression in cancer	Ref.
ALKBH3	Eraser	m ¹ A	Prostate Cancer	No change	179
			Hepatocellular cancer	No change	180
ALKBH8	Writer	m ⁵ hmU	Bladder cancer	Upregulated	181
CTU1 and CTU2	Writer	m ⁵ S ² U	Melanoma	Upregulated	182
			Breast cancer	Upregulated	183
DNMT2	Writer	m ⁵ C	AML treatment	No changes	184
			Glioblastoma treatment	No changes	185
			Myeloid Leukaemia	Upregulated	186
			Breast cancer	Upregulated	186
ELP1 and ELP3	Writer	cm ⁵ U	Melanoma	Upregulated	182
			Breast cancer	Upregulated	183
			Colorectal cancer	Upregulated	187
NAT10	Writer	ac ⁴ C	Colorectal cancer	No change	188
NSUN2	Writer	m ⁵ C	Squamous cell carcinoma	Upregulated	189
			HNSCC	Upregulated	190
			Bladder cancer	Upregulated	191
			Skin, breast and colon cancer	Upregulated	192
			Gastric cancer	Upregulated	193
			Gallbladder carcinoma	Upregulated	194
			Oesophageal squamous cell carcinoma	Upregulated	195
			Ovarian cancer	Upregulated	119
NSUN3	Writer	Mitm ⁵ C	Metastasis HNSCC	-	196
			AML treatment	-	184
			Glioma	Upregulated	197
			LUSC	Upregulated	198
NSUN6	Writer	m ⁵ C	Pancreatic cancer	Downregulated	199
TRMT2A	Writer	m ⁵ U	Glioblastoma treatment	No change	200
			ccRCC	Downregulated	198
TYW2	Writer	yW	Breast cancer	Upregulated	201
PUS7	Writer	ψ	Colon cancer	Downregulated	202
			Breast cancer	Upregulated	203
PUS10	Writer	ψ	AML	Loss	131
PUS10	Writer	ψ	Prostate cancer	No change	204
			Lung cancer	Genomic alterations	205

Table 1. Summary of tRNA modifying proteins alterations associated with cancer. AML: Acute Myeloid Leukaemia, HNSCC: Head and Neck Squamous Cell Carcinoma; ICC: Intrahepatic cholangiocarcinoma; LUSC: Lung Squamous Cell Carcinoma; ccRCC: clear cells Renal Cell Carcinoma.

Aberrant deposition of distinct tRNA modifications has been described to regulate cancer cell proliferation, invasion, and self-renewal as well as treatment response^{105,106}. Therefore, many tRNA

modifying proteins (tRMPs) have been found to be involved in the development, progression and survival of various tumour types (Table 1). For example, the m⁵C tRNA methyltransferase NSUN2 has been described to protect tRNAs from angiogenin cleavage under stress conditions and maintain normal translation programs. Its loss results in tRNA cleavage and low translation rates, which is translated in an increased proliferation of tumour initiating cells but that exhibit increased sensitivity to 5-Fluorouracil (5-FU)^{162,189}. Similarly, the demethylase ALKBH3 has been described to regulate prostate cancer by production of tRNA-derived small RNAs that alter translation by regulation ribosome assembly and prevent apoptosis through binding with Cyt-c¹⁷⁹.

3.6. m⁷G tRNA modification

N⁷-methylguanosine (m⁷G) is one of the most common tRNA modifications in human and is observed in distinct prokaryotes, archaeas and eukaryotes species²⁰⁶. The deposition process was first described in yeast, where the Trmp8/Trmp82 heterodimeric complex catalyses the S-adenosylmethionine (SAM)-dependent modification at the variable loop of more than 10 tRNA species²⁰⁷. Although this modification is not essential for yeast survival under normal culture conditions, Trm82 mutant yeasts show increased sensitivity to heat stress²⁰⁸. In humans, the catalytic ortholog methyltransferase-1 (METTL1) and the regulatory unit WD Repeat Domain 4 (WDR4) are the responsible for the methylation of the 7-guanosine at position 46 of several tRNA species^{209,210} (Figure 8).

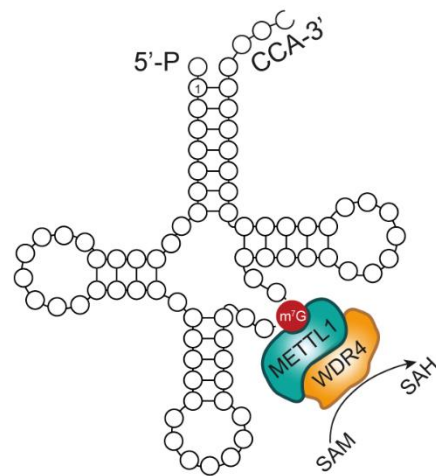


Figure 8. Schematic representation of METTL1/WDR4-dependent m⁷G modification in human tRNAs. S-adenosylmethionine (SAM) donates the methyl group transforming into S-adenosylhomocysteine. Adapted from^{208,352}.

3.6.1. m⁷G detection

One of the major drawbacks that have limited the study of RNA modifications was the lack of reliable and sensitive methods that allow their accurate detection. This restriction is exacerbated when working with specific chemical modifications, such as m⁷G, since its chemical nature does not impair Watson-Crick base complementarity, hampering its detection²¹¹. As consequence, m⁷G does not interfere during reverse transcription being unable to be directly detected by standard sequencing technologies. Thus, over the last years distinct techniques exploiting the increased sensitivity that methylated guanosines present under chemical treatment have been developed in order to overcome the sequencing limitations, but some difficulties still arise. These new developed techniques have detected internal METTL1-dependent m⁷G modification in miRNAs, mRNAs and rRNA²¹¹⁻²¹⁴, besides the well-known tRNA substrate. However, excepting tRNAs which specificity has been widely demonstrated, some targets fail to be reproducible and need further validation.

For quantitative detection of RNA modifications, the most broadly used method is liquid chromatography with tandem mass spectrometry (LC-MS/MS). Its high cost and technical difficulty are outweighed by its high reliability and reproducibility. However, this technology retrieves information about the percentage of nucleosides modified within a sample, but not about its deposition location²¹⁵.

For detection of m⁷G deposition sites at single nucleotide resolution, several approaches have been developed, but all of them exploit the increased sensitivity that m⁷G group presents when treated with sodium borohydride (NaBH₄). This reaction produces a reduction of 7-methylguanosine under alkaline conditions, that results in the formation of an abasic site that can be subsequently cleaved and detected with deep sequencing²¹⁶ (Figure 9). This chemical principle is the basis of distinct methods like AlkAniline-Seq (alkaline hydrolysis and aniline cleavage sequencing)²¹⁷, m⁷G-MaP-seq (m⁷G Mutational Profiling sequencing)²¹³, BoRed-seq (Borohydride Reduction sequencing)²¹¹ and TRAC-seq (tRNA reduction and cleavage sequencing)²¹⁸. A variation of these methods relies on using m⁷G-specific antibodies to enrich samples for m⁷G-modified, such as m⁷G-MeRIP-seq (m⁷G-methylated RNA immunoprecipitation) method. This technique identified m⁷G deposition at mammalian tRNAs and mRNAs by combining m⁷G immunoprecipitation with next-generation sequencing in a non-quantitative manner²¹².

All the described methods allow the identification of m⁷G deposition sites at single-nucleotide

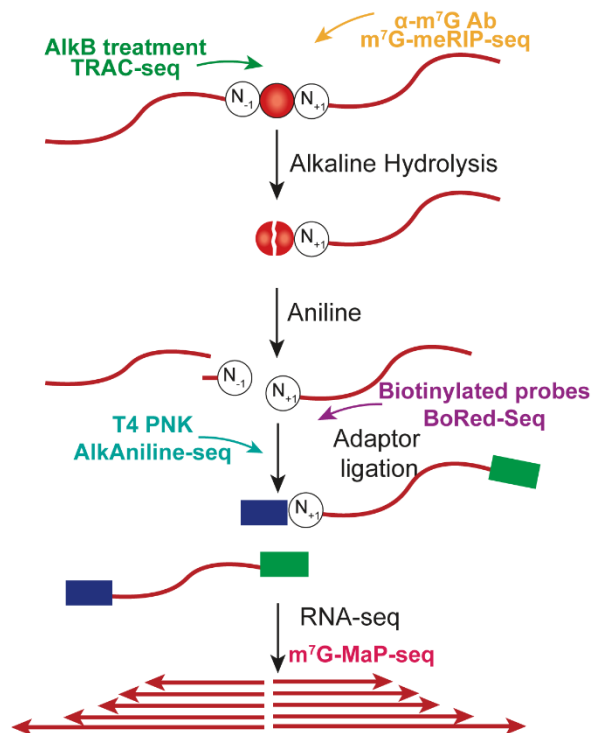


Figure 9. Schematic representation of the workflow followed for all the NaBH₄-based m⁷G detection methods. The distinct variations and the corresponding technique are indicated. Modified from²¹⁸

resolution. However, NaBH₄ treatment is accompanied by a high prevalence of false positives due to random RNA fragmentation consequence of the harsh conditions at which the reaction is produced. This results in elevated variability in the detected positions among studies²¹⁷. In fact, the differences between the mentioned techniques relies in the enrichment approaches used for reducing background signals that can alter the findings. As so, enrichment of the modified RNAs is produced by selection of abasic sites either by covalent bound of biotinylated probes²¹¹ or by adding T4 PNK for obtaining 5'-P- and 3'-OH-ends²¹⁷, as in BoRed-seq and AlkAniline-seq, respectively. TRAC-seq aims to reduce the cross-reactivity of the also NaBH₄ sensitive modifications m³C and D after alkaline treatment by treating the

RNA with AlkB enzyme for m^3C demethylation²¹⁸, while m^7G -MaP-seq is based in the analysis of the mutagenesis rate of the abasic sites to overcome the background cause by random fragmentation²¹³. However, due to the differences in the filters used either in the capture of the cleaved RNAs or the analysis of the sequencing data, variable results are obtained among techniques. As consequence, complementary application of different methods is necessary for accurate results, which enhances the need of development of new technologies for precise and reliable m^7G profiling. Despite the technique limitations, m^7G deposition has been successfully identified in tRNAs and rRNAs, but also in miRNAs and mRNAs^{210,212,217}.

3.6.2. m^7G function in physiological and pathological conditions

Although methylation at 7-guanosine does not alter Watson-Crick base complementarity, it does disrupt non-canonical base pairing, which affects the secondary structure of tRNA¹¹⁹. In fact, m^7G -tRNA modification has been shown to be required for optimal protein translation of specific proteins and regulate tRNA stability^{210,219-221}, as well as to play an essential role in embryonic stem cells self-renewal and differentiation^{210,222}.

At the pathological level, loss of METTL1-cofactor WDR4 in mammals has been associated with primordial dwarfism²²³. *METTL1* overexpression is also linked with tumour aggressiveness in distinct cancer types including sarcoma, lung, liver, colon, gastric, bladder, oesophageal and glioma^{211,219-221,224-228}. Although a common molecular mechanism by impaired translation efficiency (TE) of mRNAs with higher dependency of m^7G tRNA codons has been described²¹⁹, the molecular insights that govern tumourigenesis regulation varies between tumours (Table 2). For example, Orellana *et al.* have recently described that the *METTL1* overexpression observed in several tumours leads to increased abundance of m^7G -modified tRNAs, including Arg-TCT. This results in increased translation of mRNAs enriched in AGA codon, including mRNAs related to cell cycle progression and proliferation. Thus, high levels of *METTL1* drives oncogenic transformation and is associated with poor prognosis²¹⁹. Similarly, *METTL1*-downregulation in the *METTL1*-overexpressing intrahepatic cholangiocarcinoma (ICC) cells reduced translation of mRNAs decoded by m^7G -modified tRNAs. Between this mRNAs, those encoding for cell-cycle proteins such as CCNA2 and CDK6 and endothelial growth factor receptor (EGFR) pathway genes were detected, which lead to decreased phosphorylation of downstream EGFR targets including AKT and mTOR. Thus, *METTL1* downregulation leads to reduced proliferation and cell division in ICC cells²²⁰.

In addition, *METTL1* together with NSUN2 inhibition has been reported to increase HeLa cells sensitivity to 5-fluorouracil (5-FU), a widely used chemotherapeutic agent²²⁹. The potential prognostic value of *METTL1* for evaluating patient survival was corroborated in many tumours by a Pan-cancer analysis. Moreover, the study highlights a connection between *METTL1* overexpression and higher immune infiltration of M2 macrophages²³⁰, suggesting a crucial role of the methyltransferase not only for the tumour progression but also for the tumour microenvironment.

Together, this data suggests that *METTL1* overexpression and aberrant m⁷G modification are critical in cancer development, important prognostic factors, and possible therapeutic targets. However, its role in PCa pathogenesis has not yet been described.

Cancer	<i>METTL1</i> status	Mechanism	Ref.
Lung cancer	Upregulation of <i>METTL1</i> suppress lung cancer	<i>METTL1</i> mediated methylation augments let-7 miRNA formation, which suppresses lung cells migration.	211
Lung cancer	Upregulation of <i>METTL1</i> promotes lung cancer	<i>METTL1</i> or <i>WDR4</i> depletion suppressed cell proliferation, invasion and in vivo tumour progression. Impaired TE of mRNA with higher frequency of m ⁷ G codons in <i>METTL1</i> -deficient cells.	224
ICC	Upregulated	Increased translation efficiency of cell cycle and EGFR pathway related genes with higher content of m ⁷ G-tRNA decoded codons.	220
HCC	Upregulated Poor prognosis	Reduced TE of Cyclin A2, <i>EGFR</i> and <i>VEGFA</i> transcripts through altered codon usage in <i>METTL1</i> -deficient cells.	231
CC	Downregulated in cisplatin resistant (CR) CC cells	<i>METTL1</i> positively regulates miR-149-3p/S100A4/p53 axis in CR-CC cells	232
BC	Upregulated Poor prognosis	Translation regulation of <i>EGFR/EFEMP1</i> transcripts.	228
HNSCC	Upregulated. Poor prognosis	<i>METTL1</i> ablation represses tumour progression and metastasis by specific translation inhibition of genes related with PI3K/AKT/mTOR pathway.	233
NPC	Upregulated. Poor prognosis	<i>METTL1</i> is regulated by ARNT and necessary for EMT and resistance to cisplatin and Docetaxel through direct translation regulation of WNT/ β -catenin pathway.	234
ESCC	Upregulated. Poor prognosis	<i>METTL1</i> -depletion inhibits ESCC initiation and progression through decreased translation of autophagy negative regulators mTOR/ULK.	221
GBM, melanoma and AML	Upregulated, poor prognosis	<i>METTL1</i> -downregulation results in global translation inhibition, cell cycle defects and suppression of tumour growth. MEFs overexpressing <i>METTL1</i> showed increased translation of mRNAs decoded by m ⁷ G-tRNAs, including mRNAs codifying for cell cycle progression and proliferation.	219

Table 2. Tumours associated with aberrant *METTL1* expression levels. ICC: Intrahepatic Cholangiocarcinoma; HCC: Hepatocellular carcinoma; CC: Colon Cancer; BC: Bladder cancer; HNSCC: Head and Neck Squamous Cell Carcinoma; NPC: nasopharyngeal cancer; ESCC: oesophageal carcinoma.

4. Deregulated protein synthesis triggers UPR

Proteins are the fundamental keystones of all cellular structures and biological reactions and, as so, its synthesis is a tightly regulated process with complex quality control mechanisms that protect cells from collapsing when its homeostasis is disrupted. Aberrant deposition of tRNA modifications can impair translational rate and fidelity which triggers stress responses within the cell²³⁵. In addition, intra and extracellular stress can also induce tRNA cleavage which leads to global inhibition of

protein synthesis and induce translation of specific stress-response proteins¹⁵⁶, which shows a mutual connection between tRNAs and protein homeostasis and stress responses. Alterations on protein synthesis or increased protein secretion can lead to an accumulation of misfolded protein aggregates within the endoplasmic reticulum (ER), a condition referred as ER stress²³⁶. Mammalian cells dispose of several mechanism to restore ER homeostasis. The unfolded protein response (UPR) is the first line of action, which can further progress to ER-associated degradation (ERAD), autophagy induction or, in the case of chronic damage, even apoptotic cell death²³⁷.

The UPR aims to restore the proper function of ER and avoid further accumulation of misfolded or damaged proteins by several pro-survival mechanisms, including expansion of the ER membrane, induction of key transcription factors involved in protein folding and quality control, attenuation of the influx of proteins into the ER as well as removal of protein excess by ERAD or lysosomal degradation²³⁸.

UPR is a complex and well-defined mechanism activated by the primary sensor protein BiP, a major chaperone that in normal conditions binds with and inhibits UPR primary receptors. Upon ER stress, BiP is sequestered by the accumulating unfolded proteins and released from the UPR transducers, leading to pathway induction²³⁹. Three different UPR receptors have been described: double-stranded RNA-activated protein kinase (PKR)-like ER kinase (PERK), activating transcription factor 6 (ATF6) and inositol requiring enzyme 1 (IRE1 α) (Figure 10)^{238,240}.

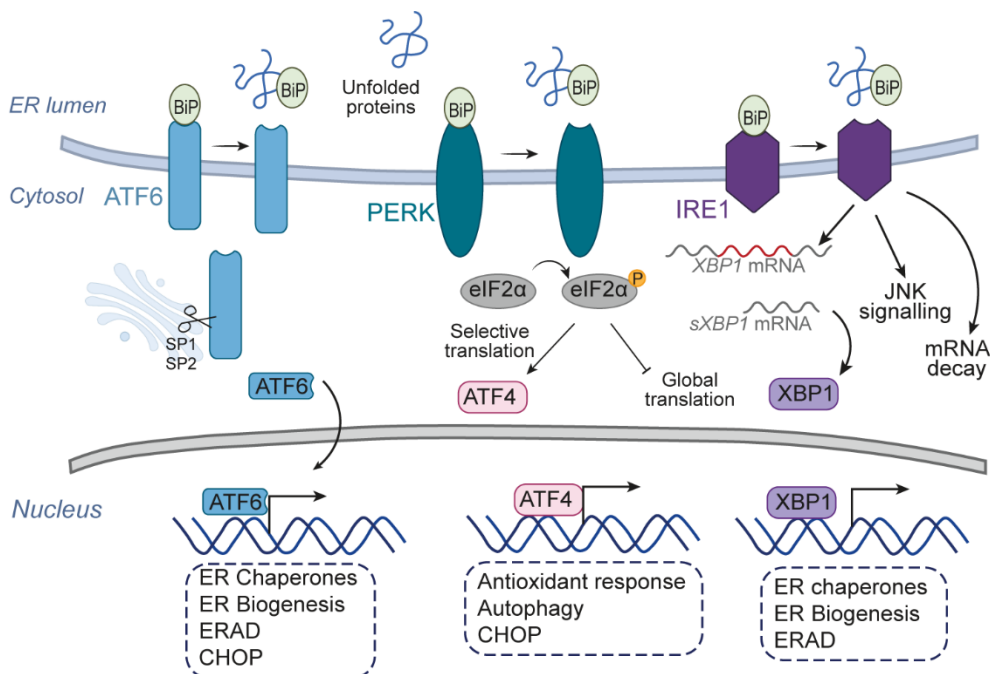


Figure 10. Schematic representation of the three different branches of the UPR pathway. Adapted from²³⁹

PERK is a type I transmembrane protein whose activation inhibit general protein translation by phosphorylating eIF2 α at serine 51. eIF2 α is a key component of the 43S translation pre-initiation complex formed by the binding of 40S ribosomal subunit and the translated to-be mRNA. However,

when phosphorylated, eIF2 α is a cap-dependent translation inhibitor that likewise activates translation of integrated stress response (ISR) specific mRNAs, such as ATF4. ATF4 is a key transducer implicated in the induction of several autophagy-related genes (ATG) and, in maintained stress condition, cell death programs in cooperation with CHOP^{238,241}.

Moreover, IRE1 α exhibit two different domains with independent functions: a protein serine/threonine kinase and an endoribonuclease domain. Once activated, IRE1 α induces spliceosome-independent splicing of the transcription factor XBP-1, leading to its activation. Spliced XBP1 (sXBP1) induces expression of chaperones and ERAD components. Meanwhile its kinase domain activates other stress-induced pathways such as JNK or NF- κ B, the RNase domain promotes mRNA decay regulating protein synthesis^{237,238,242}

Lastly, ATF6 is a type II transmembrane protein constitutively expressed in the ER. Upon activation, ATF6 translocates to the Golgi complex where its N-terminal domain is cleaved by Site-1 and Site-2 proteases (SIP1 and SIP2). The active ATF6 acts as a transcription factor at the nucleus regulating the expression of genes encoding for CHOP, BiP and ERAD components^{238,241}. Besides, ATF6 acts in parallel with XBP1s in regulating the transcription of genes encoding enzymes that promote ER protein translocation, folding, maturation, secretion, and degradation, as well as promote Golgi apparatus biogenesis to increase its secretory capacity^{238,243,244}.

To sum up, UPR encompass a combination of signalling pathways that aim to restore ER proteostasis. Due to its dependence to stress conditions, UPR is often associated with altered environmental conditions, such as nutrient or oxygen deprivation, or intracellular damages as oncogenic mutation. As consequence, UPR is usually linked to autophagy, hypoxia signalling, mitochondrial biogenesis, or reactive oxygen species (ROS) responses. Moreover, UPR dysfunction has been described to be involved in many human diseases including cancer, diabetes, and infectious diseases^{237,245}, making it crucial to understand the mechanism behind the disease promotion in order to develop targeted therapies.

5. Autophagy as a stress response mechanism

One of the principal stress-sensing and regulatory pathways responsible of maintaining cell homeostasis is autophagy. Autophagy is a highly conserved self-degradative mechanism that plays an essential role in source balance during development or nutrient stress, being essential for maintenance of cell integrity by removing aggregated proteins, damaged organelles or intracellular pathogens²⁴⁶. Three different types of autophagy have been described in mammalian cells: microautophagy, macroautophagy and chaperone-mediated autophagy (CMA), culminating all three with the proteolytic degradation of cytoplasmic components within the lysosomes²⁴⁷. During microautophagy, invaginations of the lysosome membrane directly capture cytosolic components. In comparison, macroautophagy is characterised by the formation of an intermediate double membrane

vesicle, the autophagosome, that engulfs the cargo and delivers it to the lysosome. In both mechanisms, large structures such as organelles can be encapsulated in a selective or non-selective basis. CMA differs in the use of chaperones that selectively identify targeted proteins and translocate them through the lysosomal membrane²⁴⁶.

From the three types described, macroautophagy, hereinafter referred as autophagy, is the most widely studied. Constitutively occurring at low levels, autophagy is induced under stress conditions as a source of metabolites that can be reused or as a mechanism to degrade damaged molecules²⁴⁷. Consequently, several human pathologies are linked to autophagy flux alterations, such as neurodegeneration, myopathies, metabolic diseases and cancer²⁴⁸.

5.1. Autophagic process and its molecular regulation

The distinctive characteristic of autophagy is *de novo* formation of an isolation membrane that is thought to be originated from the lipid bilayer from the plasma membrane, ER, Golgi apparatus or the mitochondria²⁴⁹⁻²⁵¹, although no consensus regarding membrane origin has been reached. This membrane named as phagophore expands to engulf cytosolic material such as protein aggregates, organelles or ribosomes, forming a double-membraned vesicle called autophagosome²⁵². In mammals, the autophagosome formation begins at multiple sites within the cytoplasm called phagophore assembly sites (PAS)²⁵³. Once formed and loaded, the autophagosome matures by its fusion with lysosomal membrane and formation of the autolysosome, where the autophagic cargo and the inner membrane are degraded. The degradation products are exported to the cytoplasm through lysosomal permeases for its reutilisation²⁵⁴. Thus, autophagy is a recycle process by which damaged or non-functional components are degraded and use as source for new molecules synthesis. In summary, is a multi-step mechanism constituted by sequential events including induction, nucleation, elongation of the autophagosome, lysosomal fusion and degradation²⁵². Each step of the process is tightly and complex regulated mainly by the autophagy-related proteins (ATG), since both excessive and insufficient autophagy levels can be harmful for the cells²⁵⁵.

The molecular regulation of the process is shown in Figure 11. Briefly, one of the main autophagy induction regulators is the mammalian target of rapamycin (mTOR) kinase, a nutrient-sensing factor that inhibits autophagy in nutrient-rich conditions. When active, mTOR prevents the formation of the ULK1/Atg13/FIP200 complex, responsible at the same time of the activation of the phosphatidylinositol 3-kinase (PI3K) complex. Thus, ULK1 phosphorylation at serine 757 by mTOR inhibits its interaction with the adenosine monophosphate-activated protein kinase (AMPK), which is also a key autophagy inducer by ULK1 activating phosphorylation at serines 317 and 777^{256,257}. Activated ULK1 phosphorylates PI3K complex, inducing nucleation by an enrichment of phosphatidyl inositol triphosphate (PI3P) produced by the PI3K complex protein Vps34. This step is essential for the formation of the initiating phagophore structure and the recruitment of the Atg proteins necessary for autophagosome elongation²⁵⁸.

Autophagosome elongation is dependent on two ubiquitin-like systems: the Atg5-Atg12 conjugation step and the LC3 processing. The first consists in the conjugation of the ubiquitin like protein to Atg12 to Atg5 and their further interaction with Atg16L1 for phagophore curvature induction through asymmetric recruitment of processed LC3B-II. Once the autophagosome is formed, the Atg5-Atg12-Atg16L1 complex is dissociated from the membrane. Upon autophagy induction, the microtubule-associated protein light chain 3 beta (LC3B) is proteolytically cleaved by Atg4 to generate LC3-I, which is then activated and conjugated with phosphatidylethanolamine (PE) to form LC3-II. LC3-II is incorporated in both the inner and outer membranes of the autophagosome and regulates membrane fusion and cargo selection. Synthesis and processing of LC3B is enhanced during autophagy induction, being a common marker employed for autophagy status evaluation²⁵⁹. Another widely used marker of autophagy flux is the sequestosome-1 (SQSTM1/p62) protein, which selectively recognises polyubiquitinated-marked cargo and binds to LC3 protein at the autophagosomes. During autophagy induction, p62 is degraded together with the cargo after autolysosome formation. Autophagy induction, thus, results in p62 decreased levels and its accumulation is mark of autophagy inhibition²⁶⁰.

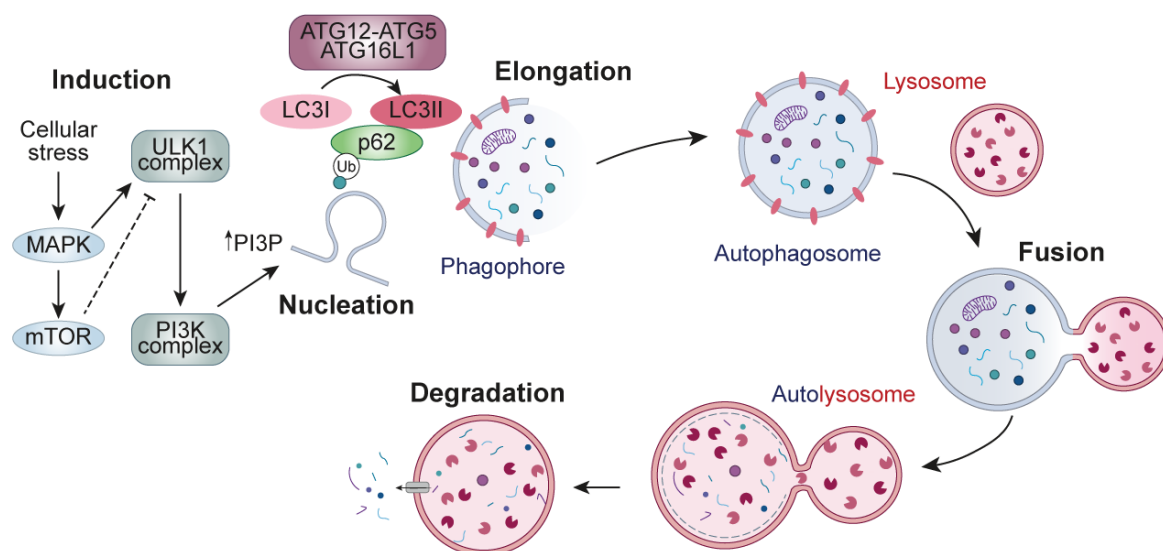


Figure 11. Schematic representation of the autophagic flux and the main regulators of the pathway. Adapted from^{246,261}.

The process continues with the fusion of mature autophagosomes with the lysosomes membranes, which is mediated by Rab GTPases, soluble-N-ethylmaleimide-sensitive factor attachment protein receptor (SNARE) proteins, and membrane anchorage proteins. The autophagolysosome cargo is then degraded by the lysosomal hydrolases and the degradation products are exported to the cytoplasm where can be reused for metabolic processes^{261,262}.

5.2. RNA modifications and autophagy regulation

Recent studies have shown a tight interconnection between RNA modifications and autophagy regulation, specially between m⁶A deposition and autophagy induction or inhibition. Thus, regulation of autophagy by RNA modifications depends on expression modulation of ATG and autophagy-

signaling pathways. For example, METTL3 has been described to reduce the stability of TFEB mRNA, a transcription factor that regulates ATG expression, resulting in its degradation and autophagy inhibition in cardiomyocytes. The opposite effect was also observed by up-regulation of TFEB via ALKBH5²⁶³. Conversely, FTO was identified to induce autophagosome formation by upregulating the positive regulator ULK1 in HeLa cells²⁶⁴ as well as ATG5 and ATG7 in adipocytes²⁶⁵. Parallely, ALKBH5 has been also described as a positive regulator of autophagy by mediating the demethylation of *FIP200* mRNA in Neural Progenitor Cells²⁶⁶. METTL3 has been also described to promote the methylation of the transcription factor FOXO3 and promote its binding to YTHDF1, targeting it for degradation. In consequence, autophagy is blocked via inhibition of FOXO3 translation in liver cancer cells²⁶⁷. In conclusion, m⁶A modification is an important regulator of autophagic pathway, however, its effect is tissue dependent.

METTL1-mediated m⁷G modification has been also shown to be essential for autophagy induction in two independent studies. Thus, downregulation of *METTL1* resulted in increased autophagy activation via dysregulation of the mTOR pathway in lung and ESCCs^{221,268}. In both studies, translation efficiency of negative regulators of autophagy was described, which ultimately leads to the pathway activation^{221,268}. Thus, these results suggests that m⁷G deposition inhibits autophagy activation by regulating the translation of autophagy inhibitors.

5.3. Autophagy dual role in cancer

As previously stated, autophagy is a crucial stress response mechanism whose aim is to restore cell homeostasis under distinct stresses such as metabolic stress. Thus, due to the highly stressful nature of the tumour microenvironment, autophagy and cancer progression are closely related processes. However, this relationship is far from simple. By removing oncogenic proteins, accumulated free radicals as ROS, and preventing genome instability, autophagy acts as a tumorigenesis inhibitory mechanism^{269,270}. Several studies support this idea, since deletion of the gene encoding for the phagophore formation inducing protein Beclin-1, was detected in breast, prostate, and ovarian tumours, resulting in reduced autophagy and increased cellular death^{271,272}. In addition to Beclin-1, other autophagy-related proteins have been described to present a suppressive effect in tumorigenesis. Thus, deficiencies on BIF-1, a Beclin-1 interacting protein, have been detected in lung, colorectal and gastric cancers and its depletion in mice leads to increased tumour formation^{273,274}. Similarly, ATG5 deletion in mice lead to increase liver tumour formation originated from autophagy-deficient hepatocytes²⁷⁵.

However, on the other hand, induction of autophagy promotes cancer cells survival in low-nutrient and hypoxic conditions. In addition, some of the most common altered pathways in cancer, such as mTOR and PI3K, are also tightly related with autophagy regulation^{269,270}. For example, high basal autophagy levels have been identified in pancreatic tumours with RAS-activating mutations. In this

conditions, inhibition of autophagy leads to decrease proliferation and tumour regression^{276,277}. Similarly, autophagy activation has been defined to be essential for the progression of non-small cell lung cancer by maintaining mitochondrial function and lipid homeostasis^{278,279}. This fact further increases the complexity of the relationship between these two processes²⁸⁰. Distinct studies suggest that autophagy may act as a tumour suppressor mechanism in the early stages of malignant transformation, but as the disease progresses, it acquires a more pro-tumorigenic role promoting tumour maintenance and treatments resistance (reviewed in^{269,270}).

Because of the dual role of autophagy in cancer progression, two different therapeutic approaches can be adopted: increase cancer cell susceptibility to therapy through inhibiting autophagy cytoprotective role, or either target apoptosis-resistant cells by inducing autophagic-dependent cell death²⁷⁰. Therapy resistance is one of the major milestones of cancer treatment, so inhibition of autophagy for sensitizing tumour cells to the treatment has been widely studied. Autophagy inhibitors targeting distinct steps of the process have been developed such as repressors of autophagosome or autolysosome formation, as well as Atg proteins inhibition. One example of autophagy inhibitor is the PI3K class II inhibitor 3-methyladenine (3-MA), which has been described to increase treatment sensitivity in oesophageal squamous carcinoma²⁸¹, colon²⁸² and lung cells²⁸³ when added in combination with radiation, 5-FU and cisplatin respectively. Another commonly used autophagy inhibitor is chloroquine (CQ), which blocks the autophagosome and lysosome fusion process. CQ treatment increased therapy response in hepatocarcinoma²⁸⁴, glioblastoma²⁸⁵ and colon cancer²⁸⁶ among others.

However, although targeting autophagy appears a promising strategy for new cancer treatments, the dual role that this pathway plays in the tumour survival makes crucial to precisely understand the underlying molecular mechanism within the disease.

OBJECTIVES



OBJECTIVES

Prostate cancer is the first cancer in number of diagnoses in men worldwide. Due to its high incidence and the limited therapeutic options that efficiently target the most advanced forms of the disease, the search of new biomarkers that allow disease monitoring is essential for the development of effective treatments. In addition, the identification of therapeutic targets that improve the prognosis of those patients that develop resistances to the established treatments is still a pending task. Based on the low mutational burden of prostate tumours and the increasing evidence that supports the essential role of epigenetic modifications in the proliferation and survival capacity of tumoural cells, we hypothesise that epitranscriptomic alterations may play a role in the initiation and progression of PCa as well as in the treatment response. With that aim, here we interrogate the epitranscriptome of PCa with the final aim of identifying epitranscriptomic alterations that may regulate the tumour fate. We specifically focus on unravelling the role of RNA methyltransferases in mCRPC, due to the low survival rates of these patients and the crucial role that these enzymes have been proved to develop in stress and therapy response mechanisms. Thus, the specific objectives of this thesis are:

1. Decipher the epitranscriptome of PCa for the identification of RMPs altered towards disease progression that may act as potential biomarkers and therapeutic targets.
2. Determine the role of METTL1-dependent m⁷G-tRNA methylation in PCa initiation and progression by genetic manipulation of the methyltransferase in distinct *in vitro* and *in vivo* PCa models. Assessment of tumorigenic capacity of *METTL1*-deficient models and unravel of the molecular mechanism underlying.
3. Evaluation of METTL1-dependent tRNA-m⁷G modification therapeutic potential in PCa by combining genetic enzyme inhibition with traditional PCa chemotherapeutic agents and analysing the effect in tumour initiation and progression in distinct murine and human pre-clinical models.

RESULTS



RESULTS

1. Identification and characterization of *METTL1* role in PCa progression

1.1. *METTL1* is upregulated in human and murine PCa and associated with poor prognosis

Several studies highlight the key role that RNA modifications play in development and progression of distinct types of cancer^{105,106}. To unravel the epitranscriptome landscape in PCa and study its contribution to PCa tumorigenesis, we examined gene expression alterations in distinct PCa tumour samples in collaboration with Prof. Arkaitz Carracedo (CICbioGUNE, Bilbao). With this aim, we analysed a total of 132 RMPs codifying genes obtained by using the tool Biomart from Ensemble under the Gene Ontology term “RNA modifying proteins” (RMPs) (GO:0009451) and followed by further literature search and manual curation of the genes. Expression levels of the selected genes were custom analysed by using data downloaded into CANCERTOOL online software²⁸⁷ that uses integrated gene and expression data from several PCa studies^{43,44,46,288,289} and The Cancer Genome Atlas (TCGA)³⁶. Thus, a total of 883 samples, including non-pathological prostate tissues as well as primary and metastatic tumours were compared (Figure 12A). Parallely, in order to identify conserved RNA modifications alterations occurring in murine prostate cancer, we performed high-throughput RNA sequencing (RNA-seq) from prostate tumours from the genetically engineered mouse model of PCa with *Pten* deletion in the prostate epithelium⁷⁹. Three-month old and six-months old mice were used as models of prostatic intraepithelial neoplasia (PIN) and invasive PCa stages, respectively (Figure 13A). As a result, we identified *METTL1* as the most transcriptionally altered gene in PCa in both the examined human datasets and the mice RNA-seq results (Figure 13B). Furthermore, *METTL1* overexpression was found increased during the disease progression, being the levels higher in the more advanced states such as metastatic and invasive prostate carcinoma in human (Figure 13B,C). As an internal control of the analysis accuracy, our data also demonstrated increased expression of *dyskerin* (*DKC1*) in human PCa, a RNA pseudouridine synthase which has been previously reported to be upregulated in PCa²⁹⁰.

The analysis of Disease-Free Survival (DFS) rate from different cohorts using camcAPP²⁹¹ online tool supported this idea. Thus, increased expression of *METTL1* was significantly correlated with worse recurrence prognosis in Cambridge and Stockholm cohorts²⁹² (Figure 13D) and, although not significant, a similar tendency was observed with TCGA data (Figure 13E). Analysis of *METTL1* mRNA expression levels from TCGA data suggested a substantial correlation between increased *METTL1* expression and heightened tumour recurrence.

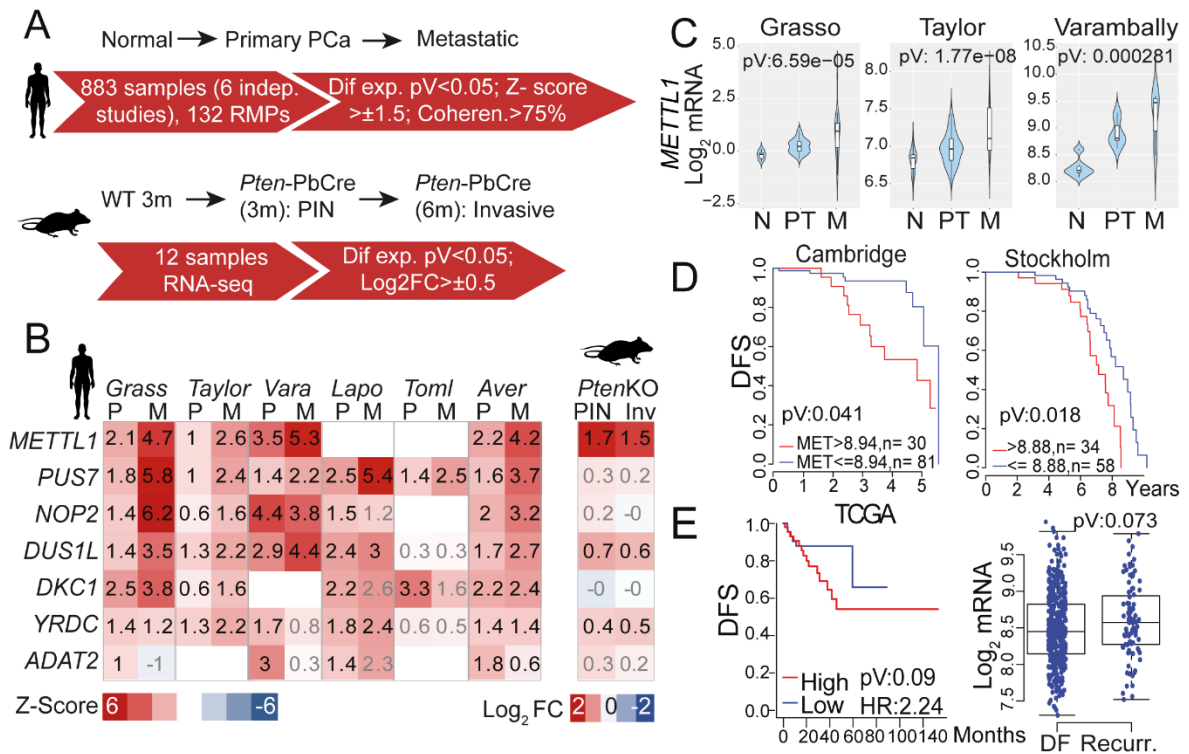


Figure 12. *METTL1* is upregulated in human and mouse Prostate Cancer. **A)** Schematic representation of the workflow employed for the analysis of the RMPs with altered expression in human and mouse PCa. **B)** On the left panel, heatmap of average Z-scores of mRNA expression values in PCa samples compared to healthy tissue. Information from primary tumours (P) and metastatic (M) are shown separately. Data from Grasso (n=N:12, P: 49, M: 27); Taylor (n= N:29, P: 131, M: 19); Varambally (n= N: 6, P: 7, M: 6); Lapointe (n= N: 9, P: 13, M: 4); Tomlins (n= N: 23, P:32, M:20). *Aver* correspond to the Z-score averages for all datasets. Right panel shows Log_2FC of mRNA expression values in *Pten*KO mice versus normal prostate tissue. Prostate intraepithelial neoplasia (PIN) and invasive carcinoma were analysed separately. Non-significant p-values are indicated in grey colour. **C)** Violin plot representation comparing Log_2 of *METTL1* mRNA levels in primary tumour (PT) and metastatic (M) tumours with normal tissue (N) from the Grasso, Taylor and Varambally databases. P-values are indicated. **D)** Kaplan-Meier curves representing the recurrence-free survival probability (DFS) upon the decile expression of *METTL1*. Data from Cambridge and Stockholm cohorts²⁹². **E)** Left panel shows Kaplan-Meier curve representing disease-free survival (DFS) of patients group stratified according *METTL1* expression with data from TCGA³⁶ (n= disease free (DF): 400, recurred (R): 91). Left panel represents log_2 of *METTL1* expression levels in the same database, suggesting that increased expression of *METTL1* correlates with higher recurrence. Mean \pm SD are represented. Statistical tests: ANOVA test (B,C), Logrank Cox test (D,E).

The mRNA levels of the other seven RMPs most altered in PCa were also analysed at distinct disease stages using CANCEERTOOL²⁸⁷, however the differences observed were less consistent within the different databases analysed (Figure 13A). This, together with the higher p-value that all genes exhibited when analysing disease-free survival (DFS) based on expression levels (Figure 13A right panel), resulted that all seven genes had reduced prognostic value compared to *METTL1*. A similar tendency to *METTL1* was observed with its co-factor *WDR4*, whose expression has been shown to be upregulated together with *METTL1* in lung and oesophageal carcinomas^{221,224}. However, despite the expression upregulation in primary and metastatic PCa tumours, the differences in *WDR4* expression did not meet criteria for the analysis of significative altered RMP genes in prostate cancer (Figure 13B).

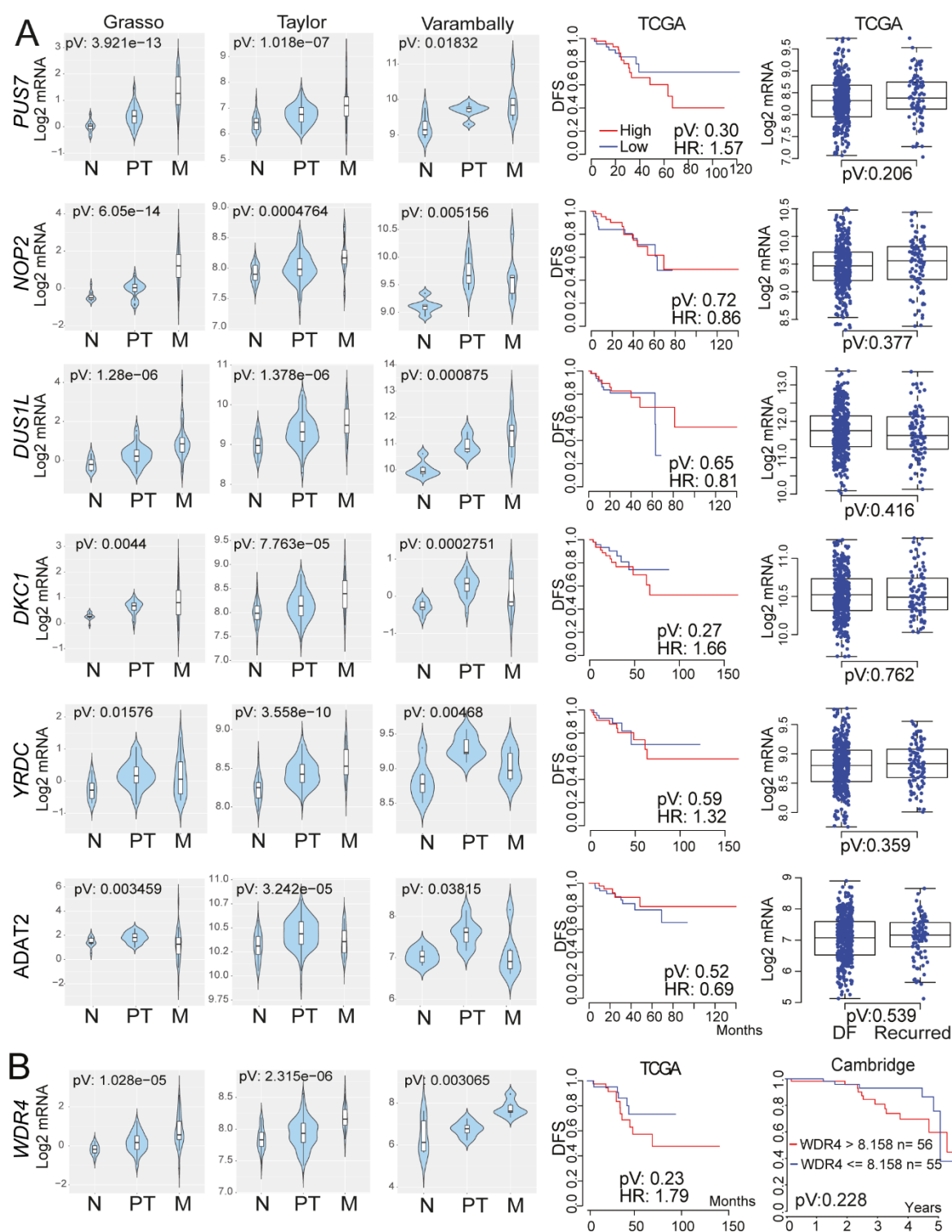


Figure 13. Expression of distinct RMPs in PCa. A,B Left panel show violin plots of Log₂ mRNA expression of the indicated RMPs significantly altered in PCa. Comparison of primary (PT) and metastatic tumours (M) with normal tissue (N) are represented with data from Grasso⁴³, Taylor⁴⁴ and Varambally⁴⁶ data sets. Middle panel show Kaplan-Meier curves of disease-free survival (DFS) according to the decile expression of the indicated genes (**A,B**). Box-plot representing the mRNA expression data from TCGA³⁶ in disease free (DF) and recurred (R) patient samples (**A**) (n= disease free (DF): 400, recurred (R)= 91). **B** Right panel display Kaplan-Meier curve of the probability of biochemical recurrence-free survival (DFS) of patients group categorised upon WDR4 expression with data from Cambridge cohort²⁹². Mean ± SD are represented. Statistical analysis: ANOVA test and Logrank Cox test (**A, B**).

For a further *in vitro* validation of the *in silico* results, *METTL1* mRNA and protein levels were evaluated in both patient samples and commonly used PCa cell lines. Patient samples were obtained

from a small cohort of patients from the Basurto University Hospital in collaboration with Prof. Arkaitz Carracedo (CIC bioGUNE) and Dr. Miguel Unda (Basurto University Hospital). In contrast to patients with benign prostatic hyperplasia, prostate tumour samples showed increased METTL1 protein levels (Figure 14A). Remarkably, *METTL1* expression was found to be positively correlated with S6K phosphorylation (Figure 14A). Phosphorylation of S6K is a readout of PI3K/mTORC1 pathway activation, which is one of the key pathways that regulate essential cellular processes as cell metabolism, growth and proliferation²⁹³. PI3K/mTOR is also known to be one of the main drivers of PCa and frequently associated with a more aggressive disease^{40,49,294}. In addition, the methyltransferase protein and mRNA levels were augmented in PCa-derived cell lines compared with the immortalised benign prostatic cell lines (Figure 14B,C), similar as observed *in silico* and in patients. Thus, this correlation suggests not only that *METTL1* expression could be by some mean regulated by PI3K activation but also enhance its value as a PCa prognostic marker.

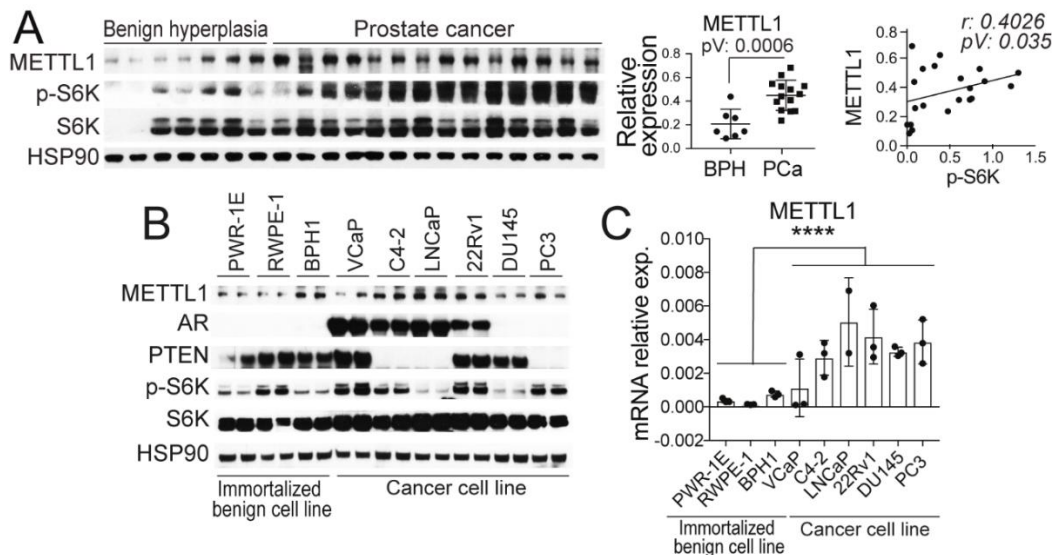


Figure 14. Assaying *METTL1* expression in PCa patient samples and cell lines. **A)** Western blot of METTL1, phosphorylated and total S6K in patients with benign prostatic hyperplasia (BPH) (n=7) and PCa (n=14) samples. Quantification of proteins levels and correlation analysis between METTL1 and phosphor-S6K are also represented. **B,C)** Analysis of protein expression of METTL1, AR, PTEN and S6K on prostate epithelial cell lines (PWR-1E and RWPE-1), benign prostate hyperplasia (BPH1) and prostate cancer cell lines (VCaP, C4-2, LNCaP, 22RV1, DU145 and PC3). **C)** mRNA levels of *METTL1* expression in the distinct prostate cell lines, validating increased expression in tumoural cell lines. Error bars represent minimum and maximum values. Statistical test: one-tailed Student t-test (**A, B, C**) and Spearman correlation test (**A**). ****p<0.0001.

In conclusion, *METTL1* is the most commonly altered epitranscriptomic gene in PCa, specially in metastatic and advanced tumours. High levels of the methyltransferase correlate with worse outcome of the patients, confirming the oncogenic role previously described in other tumours such as lung, oesophageal, glioma or bladder, among others^{221,224,227,228}.

1.2. *METTL1* expression is regulated via PI3K pathway

cBioportal database revealed amplification of *METTL1* genomic sequence in prostate adenocarcinoma, which would justify the increased levels detected. Though, this would not explain

the increased in *METTL1* levels towards disease progression. To understand the role of *METTL1* altered expression in PCa pathogenesis, its connection with some of the most common genetic alterations in PCa was evaluated. It is widely known that PCa progression is strongly dependent upon AR upregulation³⁴, being CRPC state commonly assessed by analysing the expression of androgen-regulated genes such as *KLK2*, *KLK3*, *NKX3.1*, *STEAP2* and *TMPRSS2*²⁹⁵. Thus, to evaluate the link between *METTL1* and AR, an expression correlation analysis of *METTL1* and the AR downstream gene *KLK3*, which encodes for the validated PCa biomarker PSA²⁹⁶, was performed with sequencing data from distinct studies^{36,43,44,46,297} using Cancertool (Figure 15A). As a result, low Pearson correlation values and high variability within studies was obtained. Thus, to draw a conclusion whether *METTL1* expression would depend on AR activation, *METTL1* transcription levels were evaluated in the androgen-sensitive PCa cell line LNCaP upon dihydrotestosterone (DHT) treatment. AR activation by DHT was validated by increased *TRMPSS2* levels (Figure 15B). However, no significant effect on *METTL1* expression after DHT addition was detected by Real Time-quantitative Polymerase Chain Reaction (RT-qPCR) (Figure 15B), suggesting that *METTL1* expression and its role in PCa pathogenesis is AR independent.

Given that patient samples offered a glimpse of a connection between *METTL1* overexpression and PI3K activation, we next analysed whether *METTL1* expression correlated with the PI3K/AKT pathway negative regulator *PTEN*. *PTEN* is deleted in approximately 70% of advanced PCa and a widely used marker for poor prognosis²⁹⁸. *In silico* analysis of *METTL1* and *PTEN* expression levels showed an indirect correlation in four of the five analysed data sets (Figure 15C), suggesting *METTL1* overexpression upon *PTEN* inhibition. Pharmacological inhibition of distinct PI3K/mTOR pathway components was performed to better understand the interconnection between this pathway and *METTL1* regulation (Figure 15D). For analysing *METTL1* dependency on *PTEN*, *PTEN*-expressing and -deficient PCa cell lines were used, DU145 and PC3 respectively. Briefly, BKM120 was employed as a specific inhibitor of PI3K, MK2206 as AKT inhibitor and mTOR was repressed by rapamycin and Torin treatments. The difference between mTOR inhibitors lies in that rapamycin acts mainly as an inhibitor for mTORC1²⁹⁹, meanwhile Torin acts both towards mTORC1 and mTORC2³⁰⁰ (Figure 15D). Downregulation of *METTL1* protein and mRNA levels were observed after mTORC1 and AKT inhibition with rapamycin, MK2206 and Torin treatments in PC3 cells (Figure 15E, F). However, no differences were detected with PI3K inhibitor BKM120. Differences in *METTL1* expression levels but not at protein synthesis were detected upon AKT inhibition, as consequence of the delayed impact of the pathway inhibition at protein levels. Furthermore, similar results were obtained in *PTEN*-expressing line DU145, indicating that *METTL1* expression is regulated downstream of mTOR in a *PTEN*-indirect manner in cell lines (Figure 15G, H).

Once we deciphered the link between *METTL1* expression and PCa pathogenesis, we interrogated whether its altered expression could be used as a prognostic marker for those patients with a reduced

survival rate associated to *PTEN* loss. With that aim, we performed a patient stratification analysis dependent on *PTEN* and *METTL1* expression levels. Patient stratification was performed from recurrent and disease-free tumour samples from TCGA according to Q1 ($Pten^L$) and Q4 ($Pten^H$) quartile expression of *PTEN*, and *METTL1* high (Met^H , \log_2 -normalised expression >8.72) and *METTL1* low (Met^L , \log_2 -normalised expression <8.72). As a result, the combination of low expression of *PTEN* and high *METTL1* expression resulted in a more aggressive disease and worse prognosis (Figure 15I).

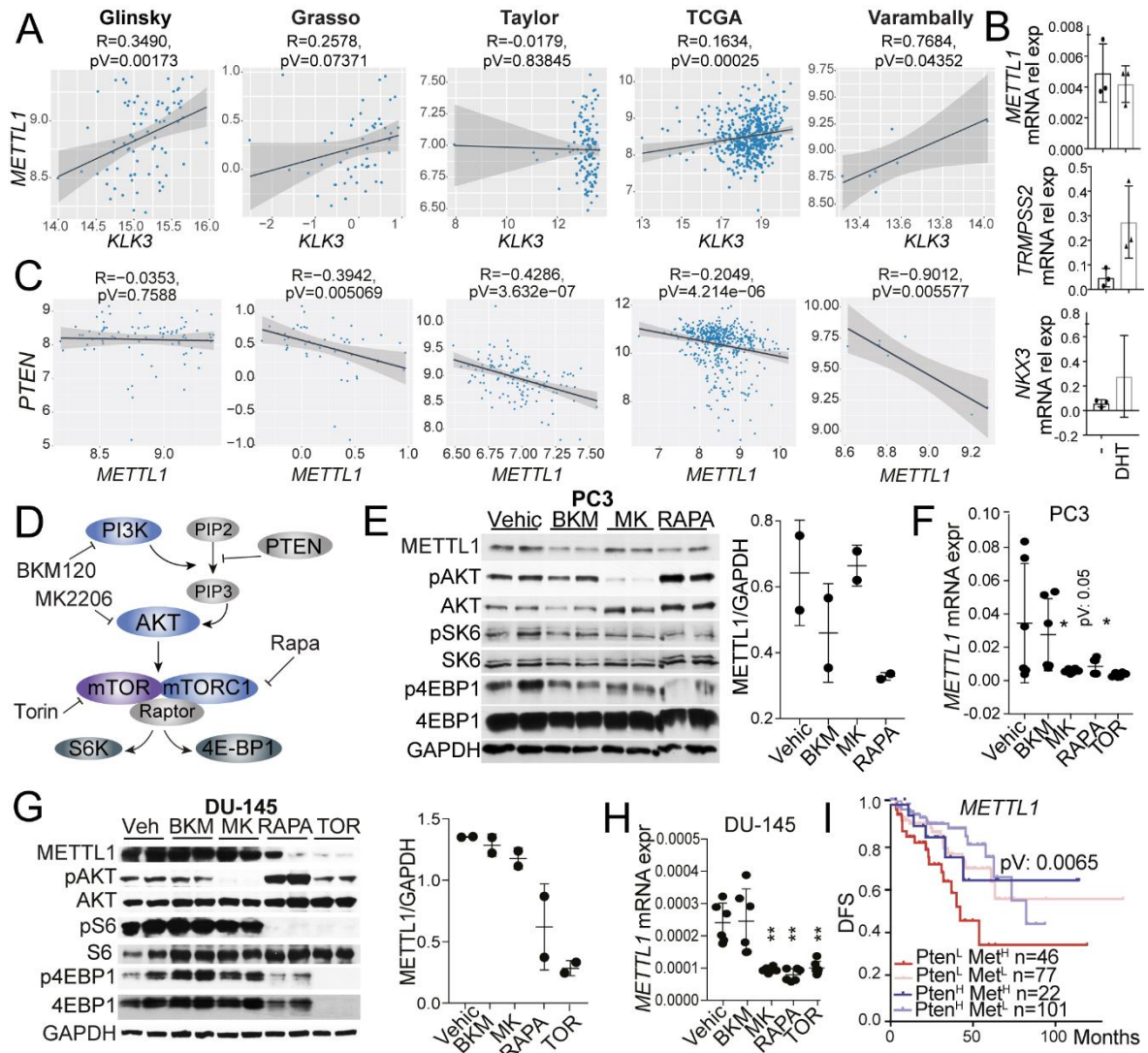


Figure 15. *METTL1* expression regulation is dependent of PI3K pathway but AR independent. **A, C)** Correlation analysis between either *METTL1* and the androgen-dependent gene *KLK3* (**A**) or *METTL1* and *PTEN* (**C**) in five independent human prostate tumours data sets. Each dot represents the \log_2 -normalised gene expression values for each patient and grey areas correspond to the confidence interval limits. Pearson's correlation coefficient (R) and p -value are indicated (Glinsky $n=79$; Grasso $n=88$; Taylor $n=183$; TCGA $n=497$; Varambally $n=19$). **B)** Analysis of *METTL1* expression levels upon DHT treatment in LNCaP cell lines. Mean \pm SD are represented ($n=3$). **D)** Schematic representation of the PI3K pathway with the indicated targets of the distinct inhibitors used. **E-H)** Western blot and RT-qPCR analysis of *METTL1* levels upon the distinct PI3K inhibitors in PC3 (**E-F**) and DU145 cells (**G-H**). For Western blot analysis, cells were treated with the indicated inhibitor for 48 hours and for RT-qPCR for 8 hours. Mean \pm SD are represented ($n=2$ E,G; $n=6$ F, H). **I)** Kaplan-Meier curves representing the disease-free survival (DFS) of patients according to *METTL1* and *PTEN* expression levels. Patient stratification was performed from recurrent and disease-free tumour samples from TCGA according to Q1 ($Pten^L$) and Q4 ($Pten^H$) quartile expression of *PTEN*, and *METTL1* high (Met^H , \log_2 -normalised expression >8.72) and *METTL1* low (Met^L , \log_2 -normalised expression <8.72). Statistical analysis: Pearson's correlation test (A,C); One-tailed student t-test (F,H); Logrank test (I). * $p<0.05$; ** $p<0.01$.

Altogether, we could conclude that the increased levels of *METTL1* during PCa progression are dependent on the higher activation of the PI3K pathway, characteristic of more advanced stages of the disease, being this connection downstream of AKT. In addition, patients with *PTEN* loss and higher levels of *METTL1* exhibit reduced prognosis in comparison with those with lower expression of the methyltransferase, corroborating its potential role as prognosis biomarker.

1.3. *METTL1* is upregulated during PCa progression and highly expressed in luminal cells in PCa murine model

So far, our data suggests that *METTL1* increased expression in PCa is regulated by altered PI3K pathway activation. Since deletions of *Pten* in the mouse prostatic epithelium give rise to invasive carcinoma⁷⁹, we next examined whether *Mettl1* mRNA and protein levels were increased in prostate tissue from a PCa mouse model with a conditional deletion of *Pten* in the prostate epithelium (hereinafter referred as *PtenKO*)⁷⁹. Samples from 3- and 6-months-old *PtenKO* mice with PIN and invasive prostate carcinoma, respectively, and same age *Pten* wild-type (WT) mice were analysed. Thus, increased *Mettl1* levels towards disease progression were detected both at protein (Figure 16A,B) and RNA level (Figure 16C), being especially raised after malignant transformation at six months due to complete *Pten* loss. Remarkably, differences on *Mettl1* levels correlated with increased m⁷G deposition in mice tRNAs. Thus, total RNAs from 3- and 6-month-old *PtenWT* and *PtenKO* mice were extracted, and size selected for tRNA enrichment.

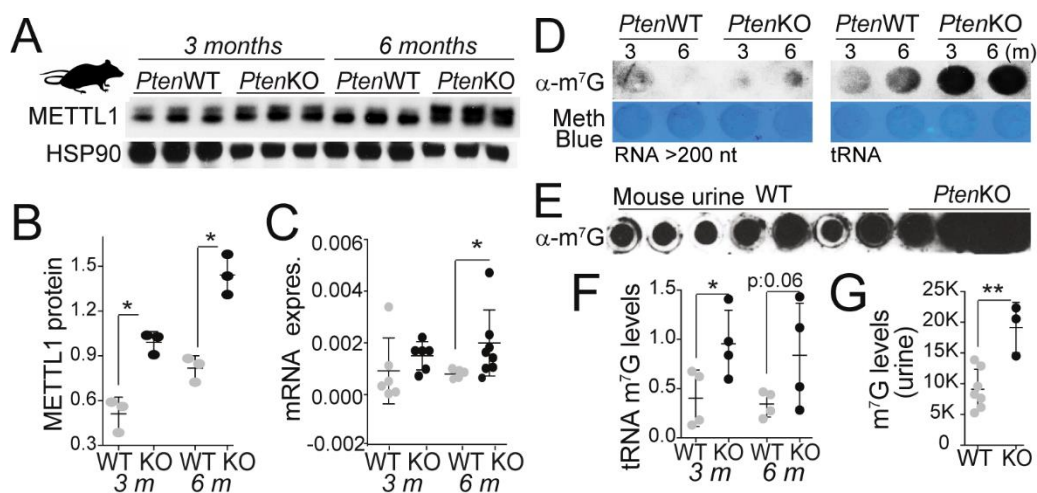


Figure 16. Human and murine prostate cancer progression correlates with higher METTL1 levels. A-C) *Mettl1* protein and mRNA levels in normal and tumoural prostates from *PtenWT* and *PtenKO* mice, respectively. Data from 3- and 6-months-old mice are shown. Mean \pm SD are represented (n=3 for protein, n=5 for mRNA). D-G) Northdot blot of m⁷G levels from large (>200 base pairs (bp)) and small (< 200 bp) tRNAs from 3-months and 6 months-old prostates from *PtenWT* and *PtenKO* mice (D, F) and from urine samples of 6-months-old *PtenWT* and *PtenKO* mice (E, G). Methylene blue was used as RNA loading control. Mean \pm SD are represented (n=4 for RNAs; urine quantification n=7 *PtenWT* mice and n=3 for *PtenKO*). Statistical analysis: one-tailed Student-t Test (B,C,F,G). *p<0.05, **p<0.01.

Analysis by northdot blot with an antibody that specifically recognises internal m⁷G mark, showed increased methylation of *PtenKO*-derived tRNAs when compared to those from healthy mouse (Figure 16 D,F). In addition, the higher m⁷G-tRNA deposition was further enhanced upon tumoural development in 6-month-old mice, concurrently to the raise of *Mettl1* protein.

Moreover, since m^7G is not metabolised and is usually secreted in urine, we performed northdot blot of urine from WT and *Pten*KO mice. Thus, we simultaneously proved that tumour-bearing mice showed increase m^7G -nucleotides secretion and that this rise can be quantitatively detected by this technique with no further treatment of the samples (Figure 16E,G).

Due to the connection between *Mettl1* levels and prostate tumour formation, we then interrogated whether its expression differs within the different cell populations that comprise the prostate. With that aim, immunohistochemistry stainings of *Pten*WT and *Pten*KO prostates were performed. We first observed an increased number of both *Mettl1*⁺ cells and staining intensity in invasive adenocarcinomas compared to the healthy tissue (Figure 17A).

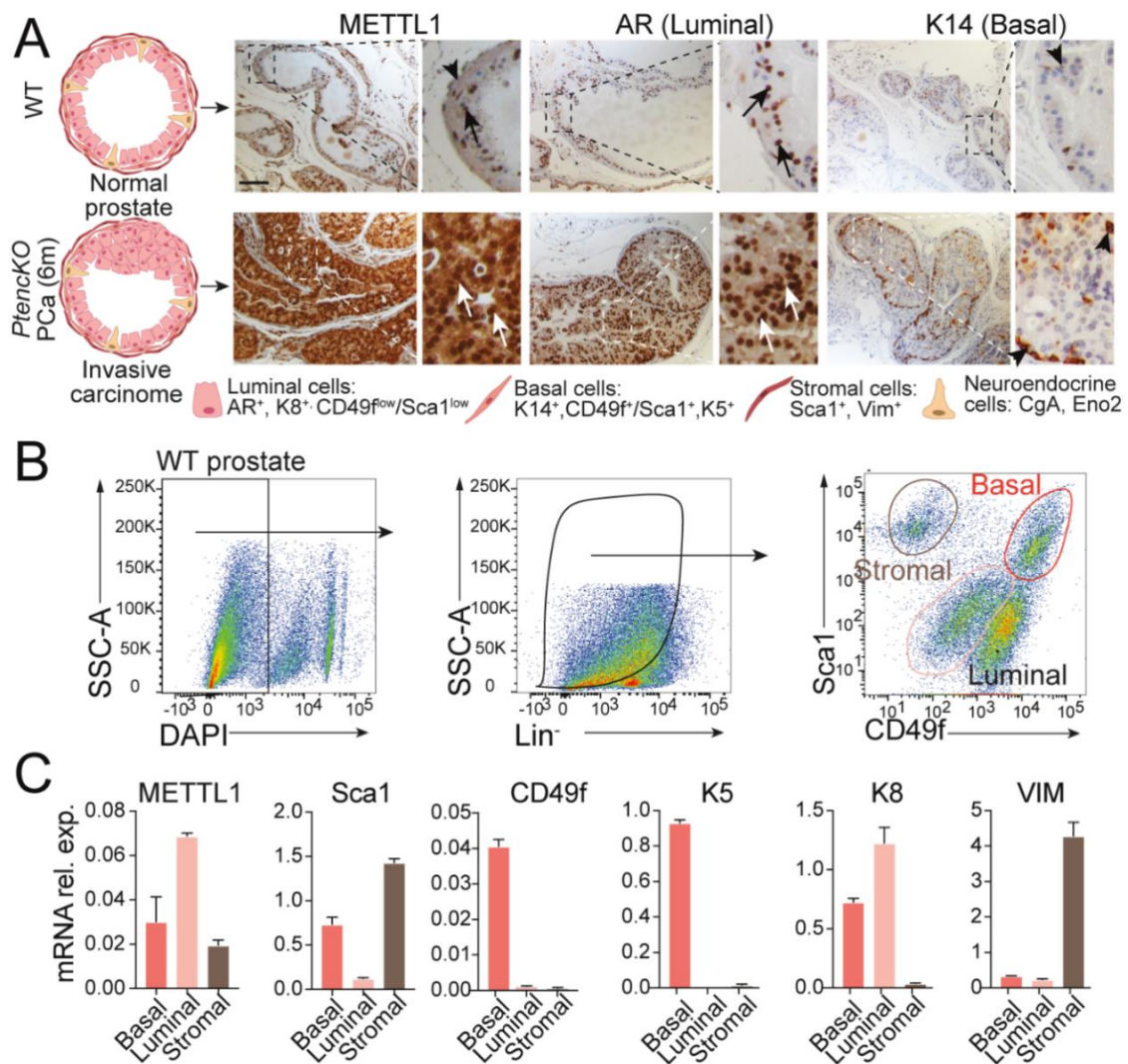


Figure 17. *Mettl1* is overexpressed in prostate invasive carcinoma. **A)** Immunostainings of *Mettl1* expression in luminal (AR⁺) and basal (K14⁺) cells within 6-months-old *Pten*WT and *Pten*KO mice prostates. A schematic representation of the tumour progression to invasive carcinoma in 6-months-old mice is represented. Scale bar corresponds to 50 μ m. Arrows indicate luminal cells and arrowheads label basal cells. **B)** Sorting strategy followed for identification of prostate cell populations. Live (DAPI) and Lin⁻ cells were sorted according to Sca1 and CD49f expression levels for identifying basal, luminal and stromal cells. **C)** RT-qPCR analysis of mRNA expression levels of *Mettl1* and specific surface markers to validate population separation. *K5* was used for basal cells, *K8* for luminal cells and *vimentin* (*VIM*) as marker for stromal cells.

Detailed analysis of the stainings revealed that luminal cells, which expressed AR marker, exhibited the highest *Mettl1* levels. In comparison, staining was less pronounced in the basal compartment

comprised by K14⁺ cells (Figure 17A). The relevance of this result lies in that luminal cells are the most abundant cells within prostate tumour. In addition, although several studies reveal that PCa can have a dual basal or luminal origin, there is a higher tendency for luminal cells to be the preferred cell-of origin^{12,13,17,20,21}. Thus, this would suggest that *Mettl1* is preferentially expressed within the cells of origin of murine prostate tumours.

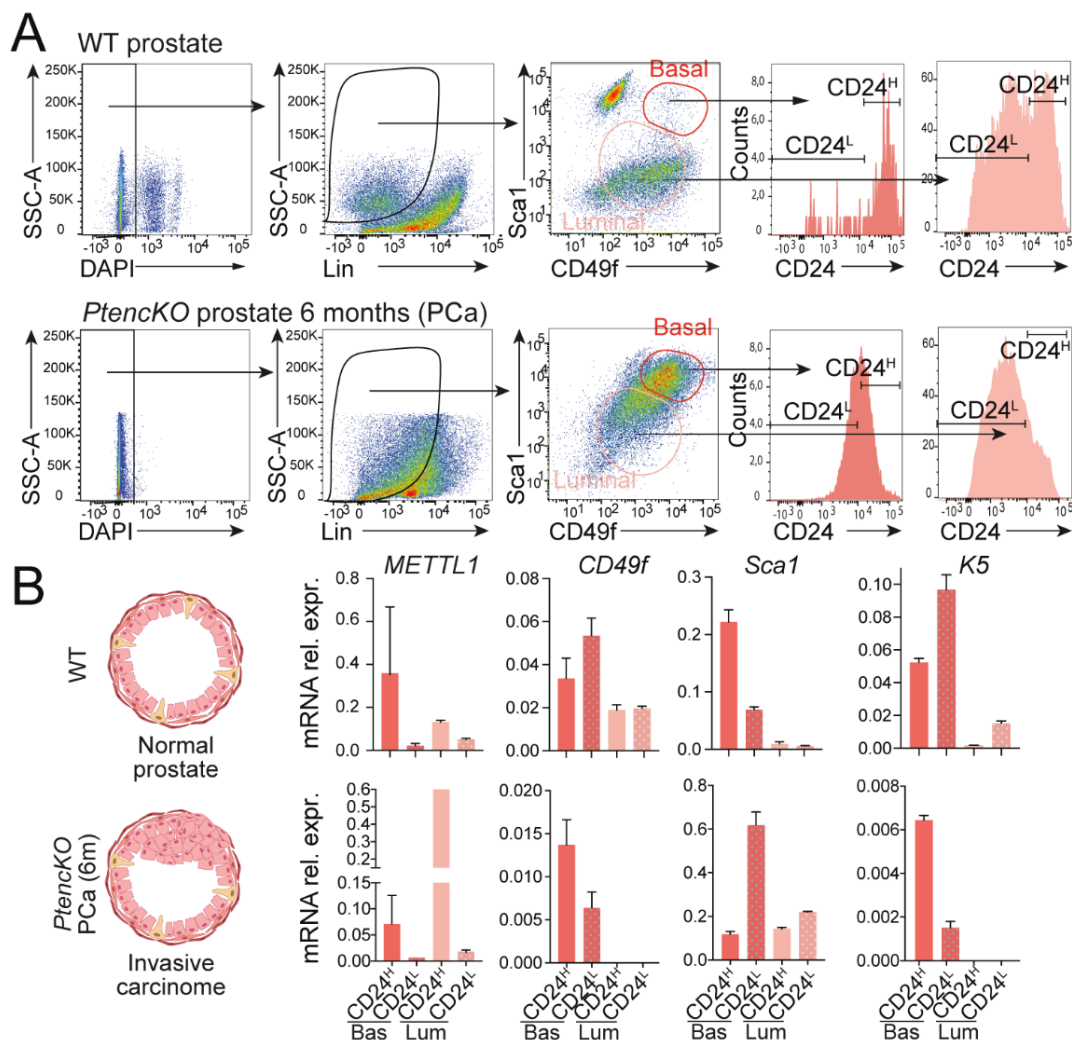


Figure 18. *Mettl1* is highly expressed in luminal cells from murine prostates. **A**) Gating strategy used for sorting of mice prostate cells populations. Following basal (bas), luminal (lum) and stromal sorting, a stratification according to high (CD24^H) or low (CD24^L) CD24 levels was performed. **B**) Expression levels of the *Mettl1* and cell populations surface markers were analysed by RT-qPCR of the subpopulations sorted following strategy described in A. Prostates from 6-months-old *Pten*WT and *Pten*KO were evaluated. Mean \pm SD are represented (n=3).

To further validate *Mettl1* levels in the distinct prostate populations, we established a procedure for specifically isolate the distinct cells populations found within a mouse prostate. With that aim, we performed fluorescence-activated cell sorting (FACS) using specific population-associated markers followed by RT-qPCR. Firstly, live and epithelial and stromal cells from *Pten*WT mice prostates were selected using DAPI⁻ and blood and endothelial Lineage⁻ (CD31⁻CD45⁻Ter119⁻) criteria. Then, three different subpopulations were sorted based in *Sca1* and *CD49f* expression levels: basal cells (Sca1⁺CD49f⁺), luminal cells (Sca1^{low}CD49f^{low}) and stromal cells (Sca1⁺Cd49f^{low}) (Figure 17B). By

RT-qPCR, we validated the higher *Mettl1* expression in the luminal subset from WT prostates observed by immunohistochemistry. The expression of specific population markers was analysed to validate the correct sorting of the distinct cells (Figure 17C).

Once we optimised an appropriate sorting protocol, prostates from 6-months aged *Pten*WT and *Pten*KO mice were extracted and sorted as previously described with the incorporation of the epithelial marker CD24, in order to improve the selection of the epithelial cells³⁰¹ (Figure 18A). Quantification of expression levels demonstrated that *Mettl1* expression was increased in tumoural samples compared to healthy tissue, and that this upregulation was more pronounced in the luminal cells compartment (Figure 18B). Moreover, mRNA levels of the basal population marker K5, as well as the employed sorting markers CD49f and Sca1, were also analysed.

Consequently, our data indicate that *Mettl1* is upregulated during PCa progression in the murine model, and this leads to an increased secretion of m⁷G modified tRNAs that can be detected in the urine. Moreover, its expression is specially increased in luminal cells, often considered as the cell of origin of PCa, suggesting an essential role in the biogenesis of the disease.

2. Identification of METTL1 targets at single-nucleotide resolution

2.1. tRNAs are the main METTL1 targets

Although tRNAs methylation by METTL1 has been known for several years in yeasts, recent studies have revealed that miRNAs and mRNAs might be potential targets of the methyltransferase^{210,302,303}. To validate this, PhotoActivatable-Ribonucleoside-enhanced Cross-Linking ImmunoPrecipitation (PAR-CLIP) data from Bao *et al.* analysis³⁰⁴ was downloaded and evaluated in collaboration with Alejandro Paniagua for identification of METTL1 targets in HEK293 cells. This technique is based in the incorporation of photoreactive ribonucleoside analogues followed by covalent bond of the RNA Binding Protein (RBP) of interest to its target RNA, protein immunoprecipitation and identification of the RNA by high-throughput sequencing (Figure 19A). As expected, tRNAs were identified as the main METTL1 target representing almost half of the analysed RNAs and with a median of over a hundred reads per million (RPMs) per tRNA isoacceptor (Figure 19B,C). The next more common target found were lincRNAs and only a 0.09% of the reads corresponded to miRNAs, meanwhile mRNA represented the 17% of all reads, however, each transcript was represented with a low read coverage (Figure 19B-D).

To further understand METTL1 molecular role, CRISPR-Cas9 technology was employed for generating PC3 cells knock-out (KO) for *METTL1*. With that aim, three different single-guide RNAs (sgRNAs) were designed (sg117, sg119 and sg139) targeting either exon 2 (sg117 and sg139) or 3 (sg119) of *METTL1* genomic sequence and transduced into the cells (Figure 20A). An empty vector expressing Cas9 enzyme but no sgRNA was used as control. Three different control and *METTL1* KO clones were obtained per cell line, two from sg117 (KO1 and KO2 hereinafter) and one from

sg139 (KO3). No efficient KO clones were obtained from the exon 3 targeting-sg119. Analysis of the genomic editing produced after Cas9-mediated cleavage was performed by sequencing of the genomic DNA of all the obtained clones. As a result, insertions and substitutions that lead to changes in the reading frame were detected (Figure 20B). Complete absence of METTL1 protein and mRNA levels was confirmed by Western Blot and RT-qPCR (Figure 20C,D). m^7G modification levels was tested independently by northdot blot and high-performance liquid chromatography (HPLC) analysis on the tRNAs from the PC3 cells, confirming that lack of *METTL1* results in almost a complete depletion of m^7G levels in tRNAs (<200 bp) (Figure 20D,E). No changes on methylation levels of those RNAs with >200 bp in length (including rRNA, lincRNA or mRNA) were detected upon *METTL1* deletion (Figure 10 D).

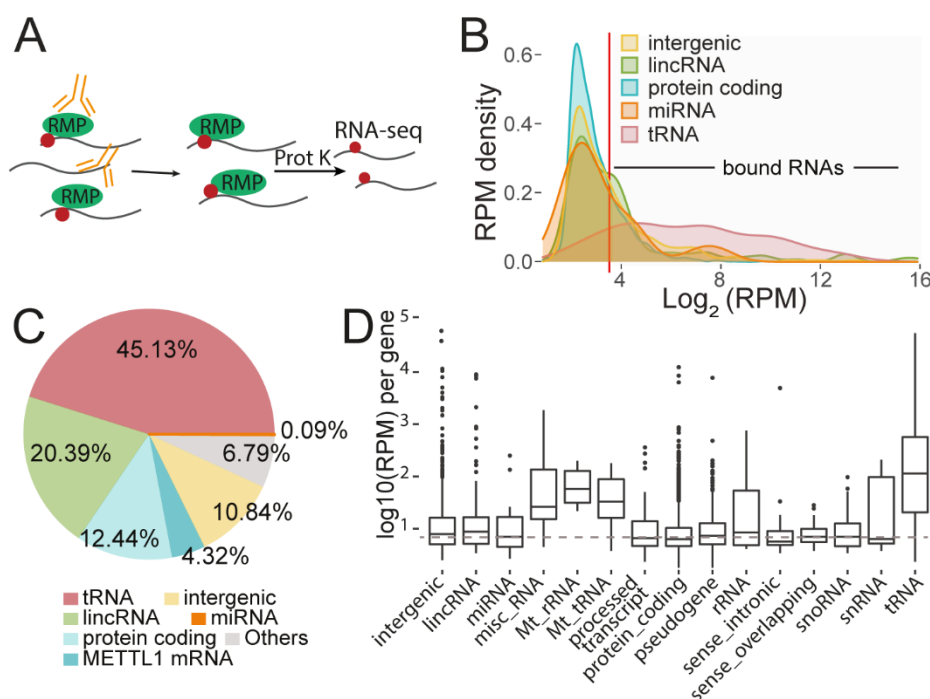
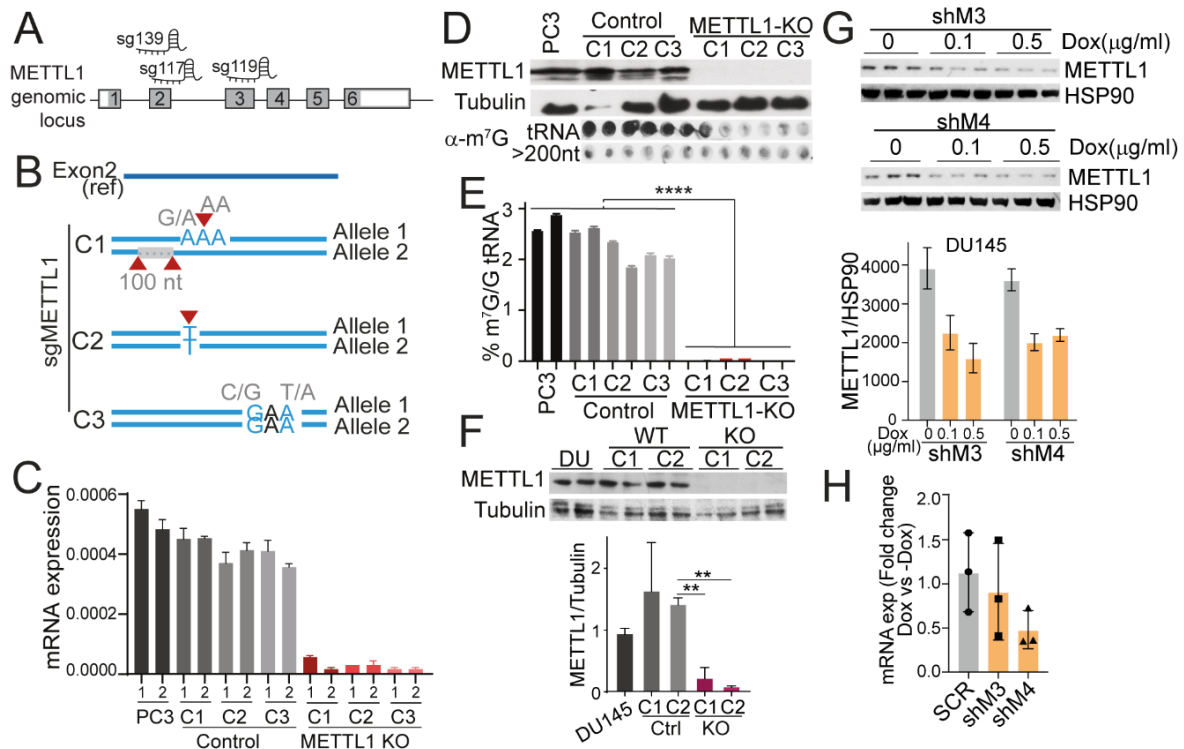


Figure 19. tRNAs are METTL1 preferred targets. **A)** Schematic representation of the molecular basis of PAR-CLIP technique. Red circles represent the epitranscriptomic mark deposited by the RNA Modifying Protein (RMP). **B)** Reads per million (RPM) density distribution identified by PAR-CLIP analysis of the RNAs bound to METTL1 in HEK293T cells. Bam data was retrieved from³⁰⁴, with two different replicates. Red line indicates the third lower quartile of total RPMs. **C)** Percentage of the most abundant PAR-CLIP reads. **D)** Boxplot representing median with interquartile range of reads per million (RPM) per gene of all RNA species found after PAR-CLIP analysis.

A second *METTL1* KO cell line was generated in DU145 cell line, obtaining two distinct KO clones from sg117 and two control clones (Figure 20F). For functional analysis of partial depletion of *METTL1*, silencing of the methyltransferase in DU145 using inducible short-hairping RNA (shRNA) technology was performed, obtaining approximately a 50% silencing of *METTL1* protein and RNA levels upon doxycycline induction (Figure 20G, H).

Thus, we can conclude that tRNAs are the main substate of METTL1 and depletion of the enzyme results in significative decrease of m^7G levels in tRNAs but not in longer RNA species.



2.2. Identification of METTL1 deposition sites at single nucleotide resolution

Once we confirmed tRNAs as the major METTL1 target, we then interrogated whether all tRNA isoacceptors were susceptible of being methylated by METTL1. Besides, we aimed to identify the specific methylation position catalysed by the enzyme at single nucleotide resolution. To address that, we developed a variation of the previously established NaBH₄-based detection techniques^{210-213,217,218} called Borohydride-sequencing (Bo-seq). This technique was developed by former member Silvia D'Ambrosi, but the generation of METTL1-depleted cells during the current study enabled to confirm its specificity. Bo-seq method exploits the increased sensitivity that RNAs modified with N-7-methylguanosines exhibit to NaBH₄ and aniline treatments, which produces RNA cleavage next to the methylation site. Briefly, m⁷G group is reduced in the presence of NaBH₄ which leads to the formation of an abasic site, followed by treatment with aniline that results in the cleavage of the chain by β -elimination³⁰⁵ (Figure 21A). After RNA cleavage, RNA libraries would be prepared for identification by deep sequencing of the RNA cleavage position, which correspond to the m⁷G

deposition sites. Detection of m^7G on tRNAs is hampered by the low abundance of the molecules compared with other RNA species, being necessary a tRNA enrichment within the sample previous to the procedure.

Thereby, total RNAs from PC3 WT and *METTL1* KO cells were extracted and tRNAs enrichment was performed by size selection. Then, tRNAs were deaminoacylated and exposed to $NaBH_4$ and aniline treatment using 7-methylguanosine triphosphate (m^7GTP) as carrier of the reaction, which increased reaction efficiency. This was followed by incubation with T4 polynucleotide kinase (T4 PNK) to ensure phosphorylated 5' ends and 3' hydroxyl ends of the cleaved RNAs to enable adaptor ligation. In addition, randomly formed fragments created due to harsh reactive conditions are non-affected by PNK treatment by their chemical properties, hence this step also ensures an enrichment on modified RNAs. Next, cDNA of tRNAs libraries were prepared and sequenced. Non-treated tRNAs were also analysed as control of random fragmentation (Figure 21B).

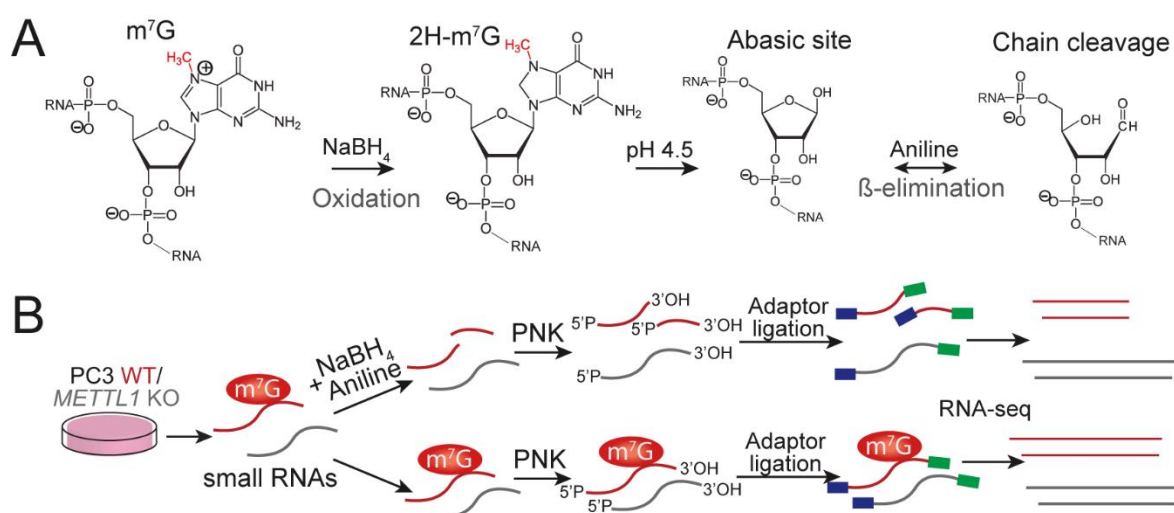


Figure 21. Development of a new variation of $NaBH_4$ -based m^7G detection method: Bo-seq. A) Chemical reaction produced when m^7G group is treated with $NaBH_4$, which results in reduction of the m^7G modification that, in presence of aniline, leads to RNA chain cleavage by β -elimination. B) Schematic representation of the workflow used for generation of treated and non-treated tRNAs libraries for identification of m^7G deposition sites by Bo-seq.

Analysis of sequencing data revealed RNA cleavage in some tRNA isoacceptors including AlaAGC, PheGAA, CysGCA, IleAAT and LysTTT, in samples from WT cells but not in those from *METTL1* KO cells, validating the lack of methylation when *METTL1* is absent (Figure 22A). Besides, other tRNAs such as HisGTG did not exhibited cleavage neither in WT nor KO tRNAs (Figure 22A), implying that those isoacceptors are not *METTL1*-substrates. Alignment of tRNA cleavage sites in WT versus KO RNAs, as well as the binding position of *METTL1* found by PAR-CLIP, revealed that the most common *METTL1*-mediated m^7G location was at the variable loop of tRNAs at position G46 (Figure 22B,C). With these approaches, around 50% of the tRNA isoacceptors were identified as *METTL1* substrates, which supports previously reported analysis (Figure 22D)^{210,211,213}.

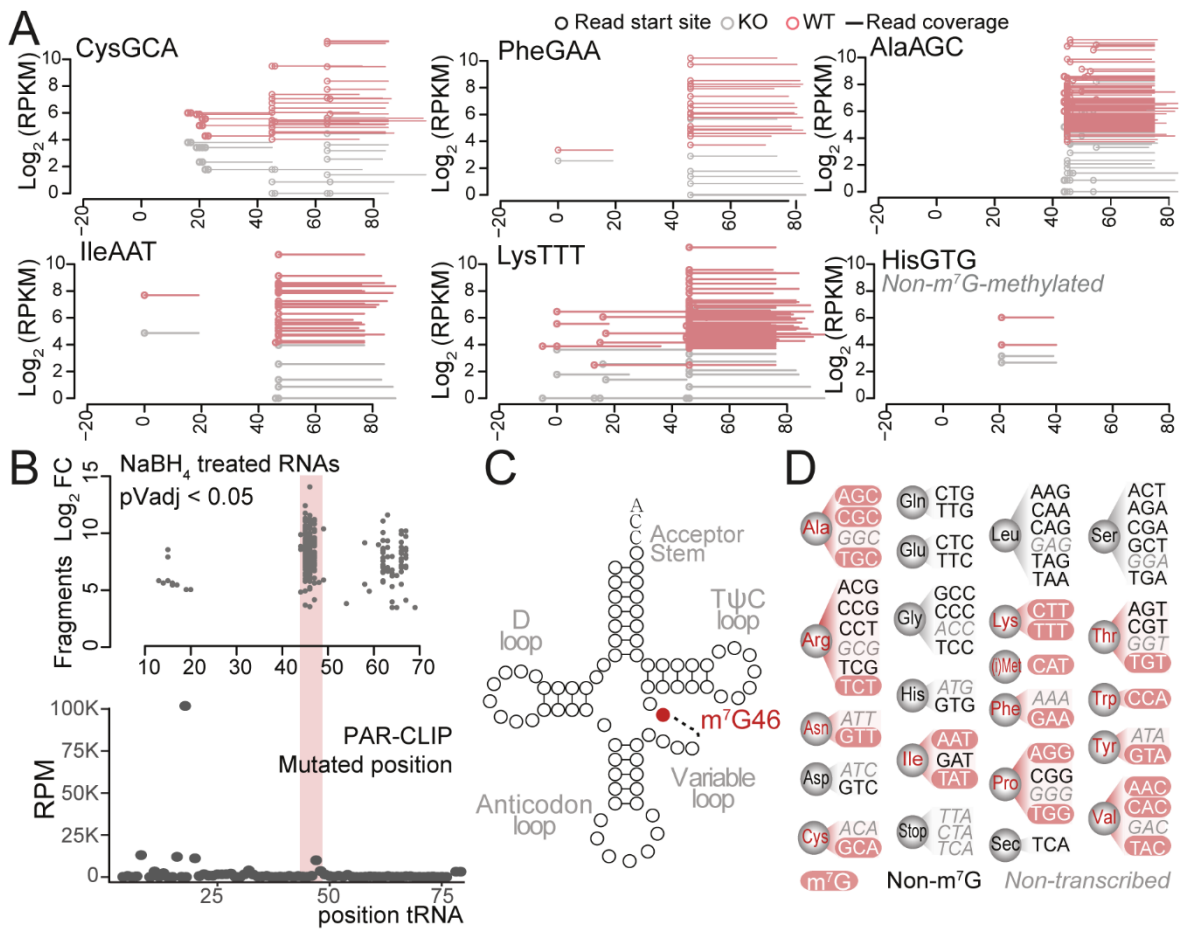


Figure 22. Validation of METTL1-dependent tRNA methylation at position 46. **A**) Normalised cleavage signal of METTL1 methylated (CysGCA, AlaAGC, PheGAA, IleAAT, LysTTT) and non-methylated (HisGTG) tRNAs from PC3 WT (red) and METTL1 KO (grey) cell lines. X-axes correspond to the position within the tRNA molecule and line-length represent reads coverage. **B**) Summary of *m*⁷G deposition sites identified by PAR-CLIP and Bo-seq analysis. Grey dots represent start position of statistically (p-value adjusted <0.05) fragments formed in control vs *METTL1* KO RNAs after NaBH₄ treatment (upper panel) or mutated position identified by PAR-CLIP analysis (lower panel). **C**) Graphical representation of tRNAs secondary structure indicating METTL1-methylated guanines at variable loop (red circle). **D**) Summary of the tRNA isoacceptors identified to be methylated by METTL1 (red) at position 46. Non-methylated isoacceptors are highlighted in grey colour.

2.3. 7-guanine methylation regulates tRNA stability by preventing tRNA-derived fragments biogenesis

Previous studies have reported that loss of METTL1-mediated *m*⁷G methylation results in reduced tRNA stability. In fact, several investigations have established that lack of METTL1 and *m*⁷G tRNA methylation leads to reduced translation efficiency of those mRNAs enriched on codons that are decoded by *m*⁷G-containing-tRNAs^{210,211,219,224,231}. Based on this, we interrogated whether this effect was recapitulated in tRNAs from PCa cell lines. With this aim, both high-throughput sequencing of tRNAs and northern blot analysis were performed to interrogate the abundance of specific mature tRNA isoacceptors, but no differences between WT and *METTL1* KO cell lines were observed (Figure 23A, B).

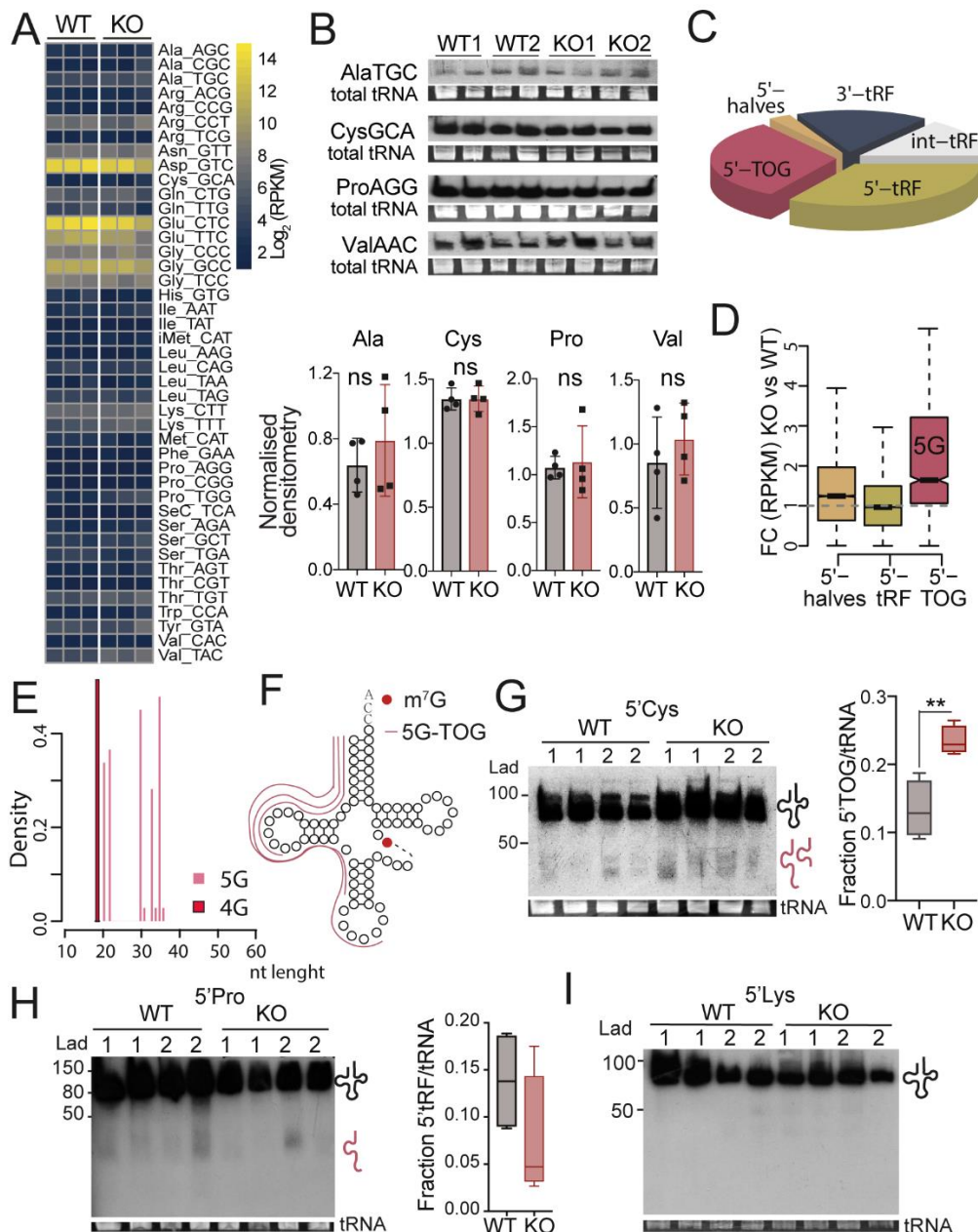


Figure 23. METTL1-mediated m⁷G deposition protects tRNA from endonucleolytic cleavage. **A)** Heatmap representing the log₂ of RPKM (reads per kilobase of transcript per million reads mapped) obtained after tRNA-seq from PC3 WT and METTL1 KO cells. Each row corresponds to a different tRNA isoacceptor and each column represent a different replicate. tRNA expression levels are row-scaled (each row is normalised by their mean expression and standard deviation). **B)** Northern blot (upper panel) and quantification (lower panel) of mature tRNAs of the indicated isoforms normalised to the total RNA. Mean ± SD are represented (n=4). **C)** Pie chart of differentially accumulated tRNA fragments longer than 18 nt in PC3 METTL1 KO cells compared to WT cells. tRNA fragments with Log₂ fold change (FC) >2 and p-value < 0.05 are represented. 3'tRNA-derived fragments (3'tRFs) comprise from -10 to +10 position of tRNA 3'end; int-tRFs correspond to the interior of the mature tRNA sequence; 5' tRNA-derived fragments go from -10 to +10 position to tRNA start site, from which 5' halves are >35 nt long and the remaining are named as 5' tRFs (n=50286) and 5'TOGs when containing 5'terminal oligoguanines (n=1599). **D)** Boxplots representing the average fold change of normalised reads of 5'tRNA-derived fragments in PC3 METTL1 KO vs WT cells. 5'TOGs box represents 5'TOGs derived only from Cys. **E)** Density of the distinct 5'TOGs with five 5'terminal guanines (5G; derived from Cys) and four 5'terminal oligoguanines (4G; derived from Ala) differentially expressed in PC3 METTL1 KO cells compared to WT cells. **F)** Graphical abstract of the fragments formed in absence of METTL1. **G, H, I)** Northern blot of PC3 WT and METTL1 KO cell lines for the indicated probes. Quantification of the detected fragments normalised to full length tRNAs is also shown. Median and min-max values are represented, whiskers represent the interquartile range (n=4). Red safe staining of full length tRNAs was used as loading control. Statistics analysis: one-tailed student-t test. **p<0.01 (**G**).

It is widely established that distinct tRNA modifications regulate the formation of a novel class of small non-coding RNAs derived from tRNA fragmentation (reviewed in¹⁵⁶). Thus, we ascertained for the formation of tRNA fragments in the sequencing data from tRNAs from PC3 WT and *METTL1* KO cells. In the analysis, 5'-derived tRFs (5'tRFs), 3'-derived tRFs (3'tRF), tRNA halves and internal-derived fragments (int-tRFs) were identified (Figure 23C). Firstly, a significant enrichment of 5'tRNA-derived fragments was detected in *METTL1* KO cells compared to those expressing METTL1 (Figure 23D). More interestingly, between all the 5'tRFs identified, *METTL1*-lacking cells showed a significant enrichment of a specific type of fragments named as 5' tRNA terminal oligoguanine-containing tRNA fragments (5'TOGs) (Figure 23E).

A deeper analysis showed that these 5'TOG fragments were characterised for having a size of 20 or 30-35 nt, indicating that they are derived from tRNAs cleavage at the anticodon or D-loop (Figure 23F). Due to their 5' end sequence nature, 5'TOGs are usually derived from Cys (5Gs) and Ala (4Gs) tRNAs. Sequencing data were validated by northern blot with different tRNAs probes in PC3 cells. A considerable increased formation of 5'CysGCA fragments below the RNA marker of 50 nt in *METTL1* KO cells compared to WT was detected (Figure 23G). However, no fragment accumulation in absence of METTL1 was detected in other tRNA substrates of the enzyme such as Lys or Pro (Figure 23H, I), indicating the specificity of the endonucleolytic cleavage of m⁷G-unmethylated Cys tRNAs.

Since several studies have proved that tRNA fragmentation can be induced under stress conditions^{148,165}, we next evaluated fragment formation in response to oxidative stress by NaAsO₂ treatment. Both PC3 WT and *METTL1* KO cell lines showed increased tRNA cleavage after stress, but cells lacking METTL1 exhibited more pronounced fragmentation that manifested at shorter inducing times (Figure 24A,C). This effect was also observed in DU145 cells (Figure 24B). Again, stress-induced endonucleolytic cleavage was specific for Cys (Figure 24C).

Stress-derived 5' halves tRNA fragments are produced by endonucleolytic cleavage at the anti-codon loop by angiogenin^{151,156,162,166}. Due to the high specificity of the fragments formed in the absence of *METTL1*, we then evaluated whether angiogenin would mediate Cys tRNA fragmentation when unmethylated. With this aim, tRNA cleavage was assessed in the presence of the angiogenin inhibitor N65828³⁰⁶ in stress conditions, but no differences were detected (Figure 24D). Whether this tRNA fragmentation is dependent on other kind of ribonuclease requires further investigation.

We next performed an *in vitro* tRNA cleavage assay to validate tRNA fragmentation at G46 in absence of m⁷G mark. With that aim, we synthesised biotinylated oligonucleotides containing the wild type (WT) sequence or mutant version (G46A) of the isoacceptor CysGCA (Figure 24E). Then, synthetic 5'biotinylated-tRNAs were incubated with extracts from PC3 WT and *METTL1* KO cells and pulled down with streptavidin-coated beads to assess oligonucleotides fragmentation (Figure

25E). WT tRNAs would be expected to be cleaved only in KO lysates, being the only condition where methylation would not take place. On its behalf, mutant G46A would be cleaved in both WT and KO cell lysates since the oligonucleotide is not susceptible of being methylated. Captured RNAs were loaded into a polyacrylamide gel and in the Bioanalyzer to analyse 5' end fragment formation. Analysis and quantification of the formed fragments normalised to full length tRNAs revealed an increased formation of fragments from approximately 22 and 30 nt long in the KO extracts of the WT tRNAs. In addition, the mutant G46A was cleaved in fragments of 30 nt in WT lysates, thus confirming that m^7G46 protects from fragmentation at the D and anti-codon loop (Figure 24E).

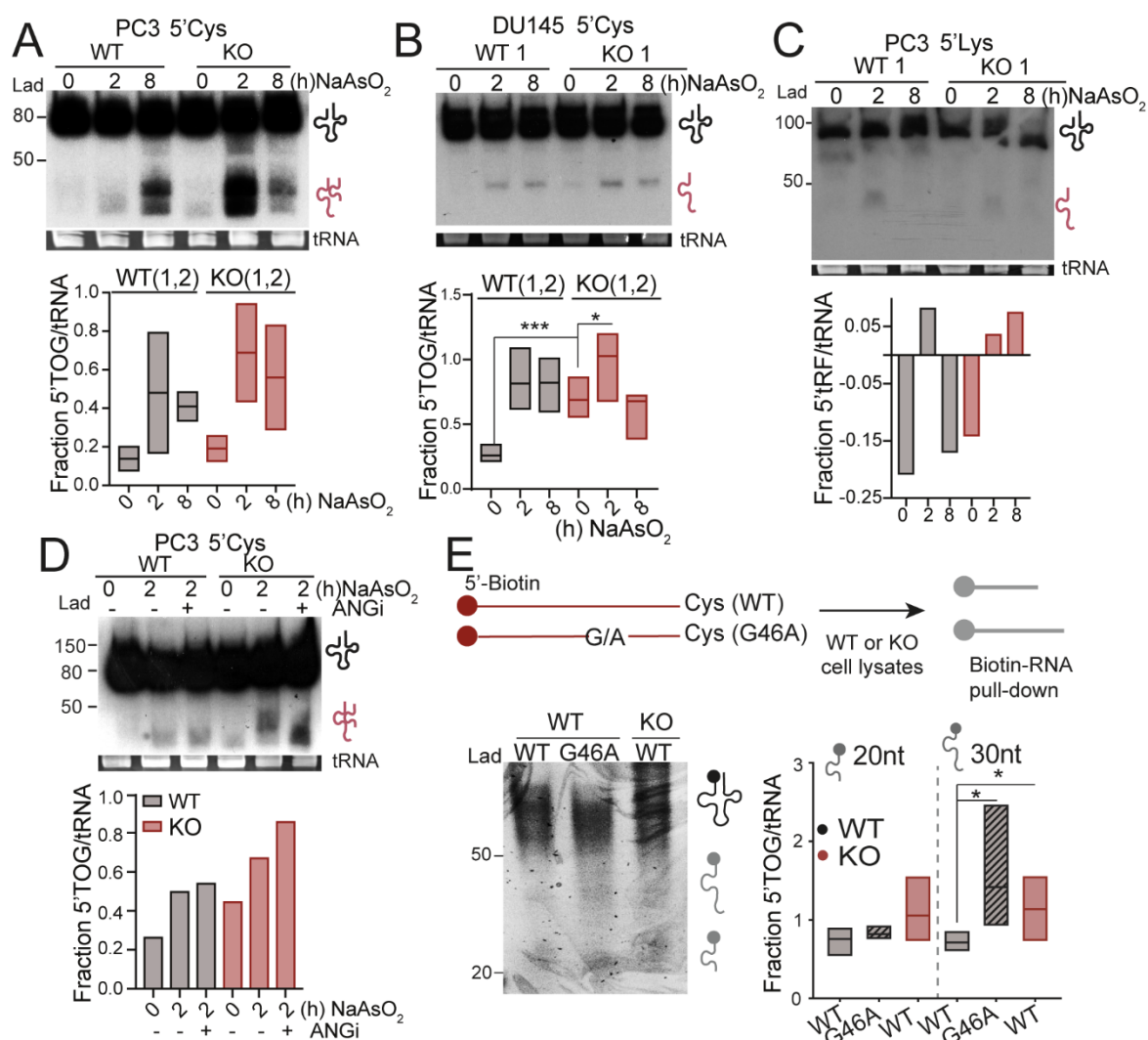


Figure 24. tRNA cleavage in the absence of m^7G46 is enhanced upon stress conditions. **A,B**) Northern blot analysis of Cys-derived tRNA fragments in PC3 (**A**) and DU145 (**B**) WT and *METTL1* KO cells after NaAsO₂ treatment. Collecting times after stress induction are indicated (h). Boxplots represent fragment formation normalised to total tRNAs, indicating median, bars at min-max values (n=4). **C**) Analysis of 5' Lys tRNA derived fragment upon stress. Bars represent normalised fragments with full length tRNAs. **D**) Quantification by northern blot of tRFs derived from Cys in PC3 expressing or *METTL1*-depleted non exposed (0h) or exposed to oxidative stress (2h) and with (+) or without (-) angiogenin inhibitor (ANGi). Normalised fragments formation with full length tRNA are represented (n=2). Red safe staining of all northern blot gels was used as loading control. **E**) Schematic representation of the tRNA *in vitro* cleavage assay and analysis of tRNA fragmentation by TBE polyacrylamide gel. Boxplot represents the fragments identified either with the WT Cys tRNA or the mutated one (G46A) after incubation with extracts from WT or KO cells. Median and min-max values are represented (n=3). One-tailed Student t-test was performed. *p<0.05; ***p<0.001 (**B**, **E**).

Thereby, METTL1-mediated m⁷G deposition at G46 regulates tRNA fragmentation of specific tRNAs that leads to 5'tRFs biogenesis, some of them characterised for presenting multiple guanosines at the 5' end. This fragmentation is enhanced under stress conditions but is not catalysed by angiogenin.

2.4. METTL1-dependent tRNA fragments biogenesis inhibits translation initiation

tRNA cleavage has been described to specifically inhibit global protein translation caused due to the molecular activity of the tRNA derived fragments^{131,151,162,166}. To evaluate whether METTL1-dependent tRNA fragmentation altered protein synthesis, we quantified the rates of protein synthesis in PC3 WT and *METTL1*-depleted cells by using the properties of O-propargyl-puromycin (OP-puro). OP-puro is a puromycin analogue that is incorporated into the nascent peptides and produces a premature termination of protein synthesis. In addition, due to its alkyl motif, OP-puro residues can be covalently bound to an azide-containing molecule such as fluorophores, which will further allow to quantitatively measure translation rates by flow cytometry or microscopy³⁰⁷. Thereby, a significant reduction of protein synthesis rate was observed in PC3 *METTL1* KO cells in comparison with WT cells (Figure 25A), corroborating that tRNA fragmentation observed in the absence of *METTL1* leads to a global repression of protein synthesis. Remarkably, a similar reduction in global protein translation was observed in *METTL1* silenced DU145 cells (sh*METTL1* cell lines) (Figure 25B). This indicates that *METTL1* regulatory role on protein translation is so crucial that even a partial depletion affects to normal proteostasis.

Then, to further understand the molecular mechanism underlying protein inhibition observed in *METTL1* KO cells, we checked whether translation initiation was dysregulated by a decreased expression of the components implicated in the translation initiation complex. However, no differences were observed, which suggest that the translation inhibition observed in *METTL1* KO cells is not caused by an alteration of the synthesis of the translational machinery components (Figure 25C, D). In fact, previous investigations reported that short 5'TOG fragments (named miniTOGs or 5'mTOGs) specifically inhibit protein translation by displacement of the translation initiation complex components from the actively translated or 7-methyl-guanilated (m⁷G-capped) mRNA pool^{131,308}. Thus, to analyse displacement of the translation initiation components eIF4A, eIF4G, eIF4E or the regulatory components YB1 and PABPC1, sepharose beads coated with m⁷G-cap were incubated with lysates from PC3 WT or *METTL1* KO cell lines. Then, beads pulldown and Western blot analysis were performed in order to assess the translation initiation complex components bound in the distinct conditions. As a result, reduced binding of eIF4G, PABPC1, YB1 and eIF4E were detected in PC3 *METTL1* KO cells when compared to controls, but only the latter showed significant differences (Figure 25E). We next interrogated whether this affinity differences were mediated by the biogenesis of 5'TOGs in *METTL1* KO cells.

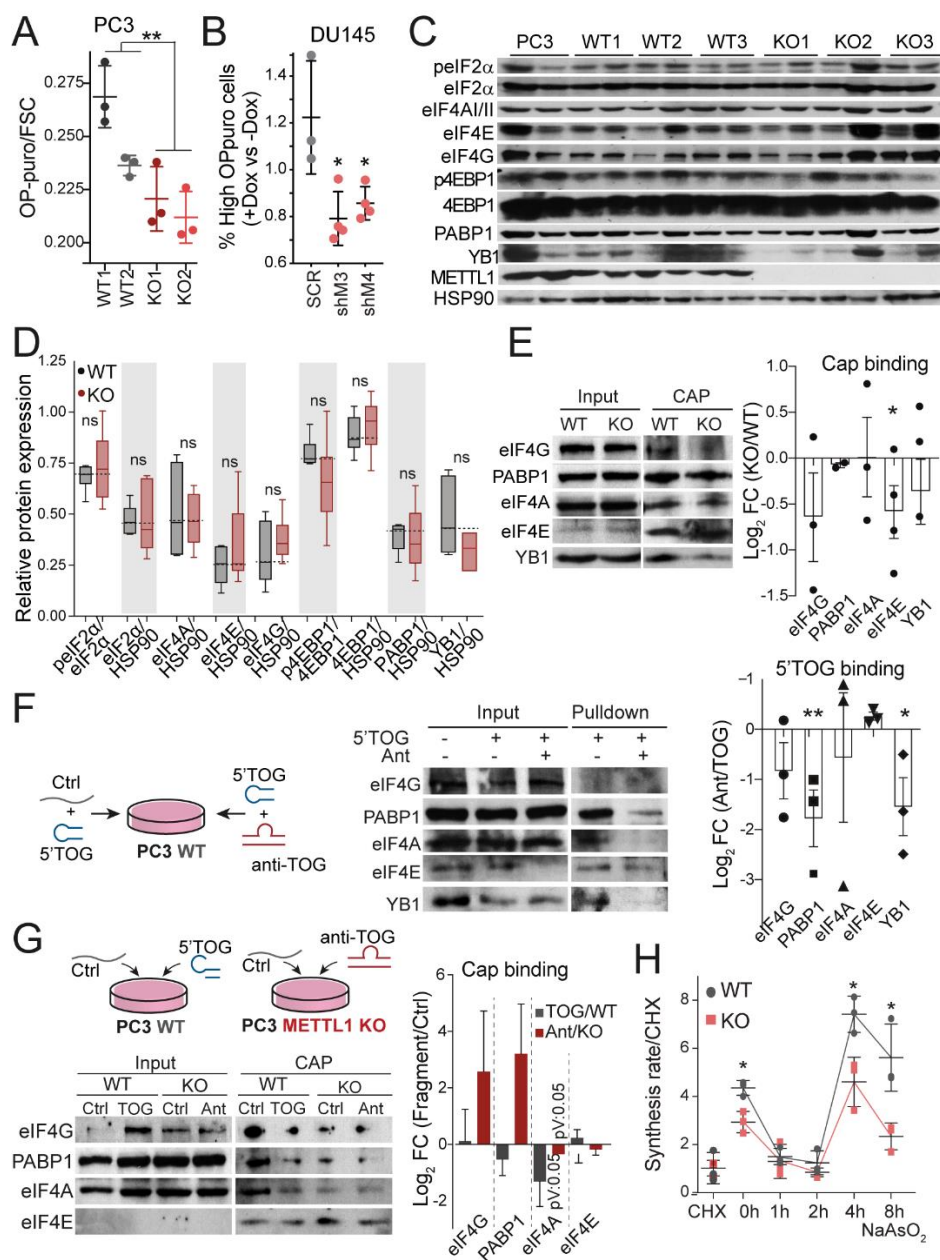


Figure 25. Lack of METTL1 m⁷G-dependent mark results in global protein translation inhibition by displacement of the translation initiation complex through 5'TOG formation. **A)** Quantification of global protein synthesis rate by OP-puromycin-propargyl (OP-puro) incorporation in PC3 WT and *METTL1* KO cells. Fluorescence quantification is normalised to cell size (FSC). Mean \pm SD is shown (n=3). **B,C)** Analysis by Western blot of protein levels of the distinct factors of the translation initiation complex in PC3 control (WT) and *METTL1* depleted cells. PC3 parental cells and two distinct technical replicates per condition are shown. Box plot represent quantification of protein levels. Dotted lines indicate mean protein levels in WT cells for each analysed protein. **D)** Fold change of the percentage of OP-puro positive cells in *METTL1* silenced DU145 cells compared to SCR control. Mean \pm SD are represented (n=3). **E)** Western blot and log₂ fold change (FC) quantification of the translation initiation factors bind to m⁷G-cap separase-coated beads in PC3 WT and *METTL1* KO cells. Images from one representative replicate are shown. Mean \pm SEM are represented (n=3). **F)** Graphical abstract of the approach followed for analysing the translation initiation factors specifically bound to synthetic 5'TOG when transfected in PC3 WT cells in combination with either a scramble or a complementary or anti-TOG oligonucleotide. Western blot of a representative replicate and quantification of the FC of the TOG+Ant normalised to TOG+SCR are represented. Mean \pm SEM are shown (n=3). **G)** Schematic representation of the assay for analysing the TOG-dependency of the displacement of translation initiation factors from the mRNA cap in PC3 cells. PC3 WT cells were transfected either with synthetic biotinylated-5'TOG (5'TOG) or with scramble RNA oligonucleotides. *METTL1* depleted cells were transfected with biotinylated anti-TOG (Ant). Log₂ FC of the densitometry from TOG or Anti-TOG-bound factors normalised to SCR conditions are shown. Mean \pm SEM are represented (n=3). **H)** Measurement of protein translation rate by flow cytometry quantification of OP-puro incorporation in PC3 WT and *METTL1* KO cells upon oxidative stress (NaAsO₂). Data are normalised to cycloheximide (CHX) treated cells. Mean \pm SD is shown (n=3). Statistics analysis: One tailed student-t test (**A-H**) *p<0.05; **p<0.01.

To this end, different *in vitro* experiments were performed. Firstly, PC3 WT cells were transfected with synthetic biotinylated 5'TOGs, that are produced naturally in *METTL1* KO cells, alone or in combination with its reverse-complement oligonucleotides or anti-TOGs, that would specifically bound and inactivate the 5'TOG in an antagomiR similar manner (Figure 25F). Then, biotinylated 5'TOGs fragments were pulldown with streptavidin-coated magnetic beads and bound translation initiation factors were analysed and quantified by Western blot. As a result, some of the factors that comprise the translation initiation complex were detected to pulldown together with synthetic 5'TOGs, specially PABPC1 (Figure 25F). Besides, the co-transfection of anti-TOGs with 5'biotynilated-5'TOGs successfully reduced the affinity of eIF4G/A, PABP1 and YB1 to the 5'TOGs, with significative differences for the affinity to PABP1 and YB1. These results corroborated that *METTL1*-depletion mediated 5'TOG biogenesis inhibit protein synthesis by specifically displacing of the components that conform the translation initiation complex.

We next interrogated whether synthetic 5'TOG could displace the translation initiation complex from capped-mRNAs as in *METTL1* KO cells. Additionally, we analysed whether the displacement of the translation initiation complex could be reverted in *METTL1* KO cells using anti-TOGs that would block 5'TOGs activity. Despite the high variability due to the technical difficulty, synthetic 5'TOGs could remarkably displace both eIF4A and PABP1 in WT cells and we could successfully rescue eIF4G and PABP1 displacement in KO cells transfected with the anti-TOGs sequences (Figure 25G).

Based on this connection between 5'TOG biogenesis and translation inhibition together with the increased fragmentation observed under stress conditions, we next evaluated proteins synthesis alterations over time in response to oxidative stress. Thus, exploring OP-puro capacity to bind to nascent proteins, global translation levels were assayed in PC3 WT and *METTL1* KO cell lines upon NaAsO₂ treatment. As a result, decreased global protein synthesis was observed as expected, but also a diminished recovery capacity of protein synthesis rate in the absence of *METTL1* was detected after stress induction, which suited with the increased accumulation of 5'TOG detected in *METTL1* KO cells under stress conditions (Figure 25H). This suggested that lack of *METTL1* decreases cell ability to respond to stress conditions.

In conclusion, our results validate the displacement of translation initiation complex from actively translate mRNAs in the presence of 5'TOGs fragments originated by an altered epitranscriptome.

3. Phenotypic characterization of *METTL1* depletion

3.1. *METTL1* regulates tumour growth and self-renewal capacity *in vitro* and *in vivo*

Due to the high impact of *METTL1* deletion in the biogenesis of stress-induced tRNA fragments, protein translation inhibition and its high correlation with PCa pathogenesis, we interrogated how the enzyme depletion affected PCa progression. Thus, several *in vitro* approaches were performed with PC3 and DU145 WT and *METTL1* KO cells for evaluating their proliferation potential. We

observed a significant impaired proliferation in adherent conditions in both cell lines in absence of the enzyme (Figure 26A,B).

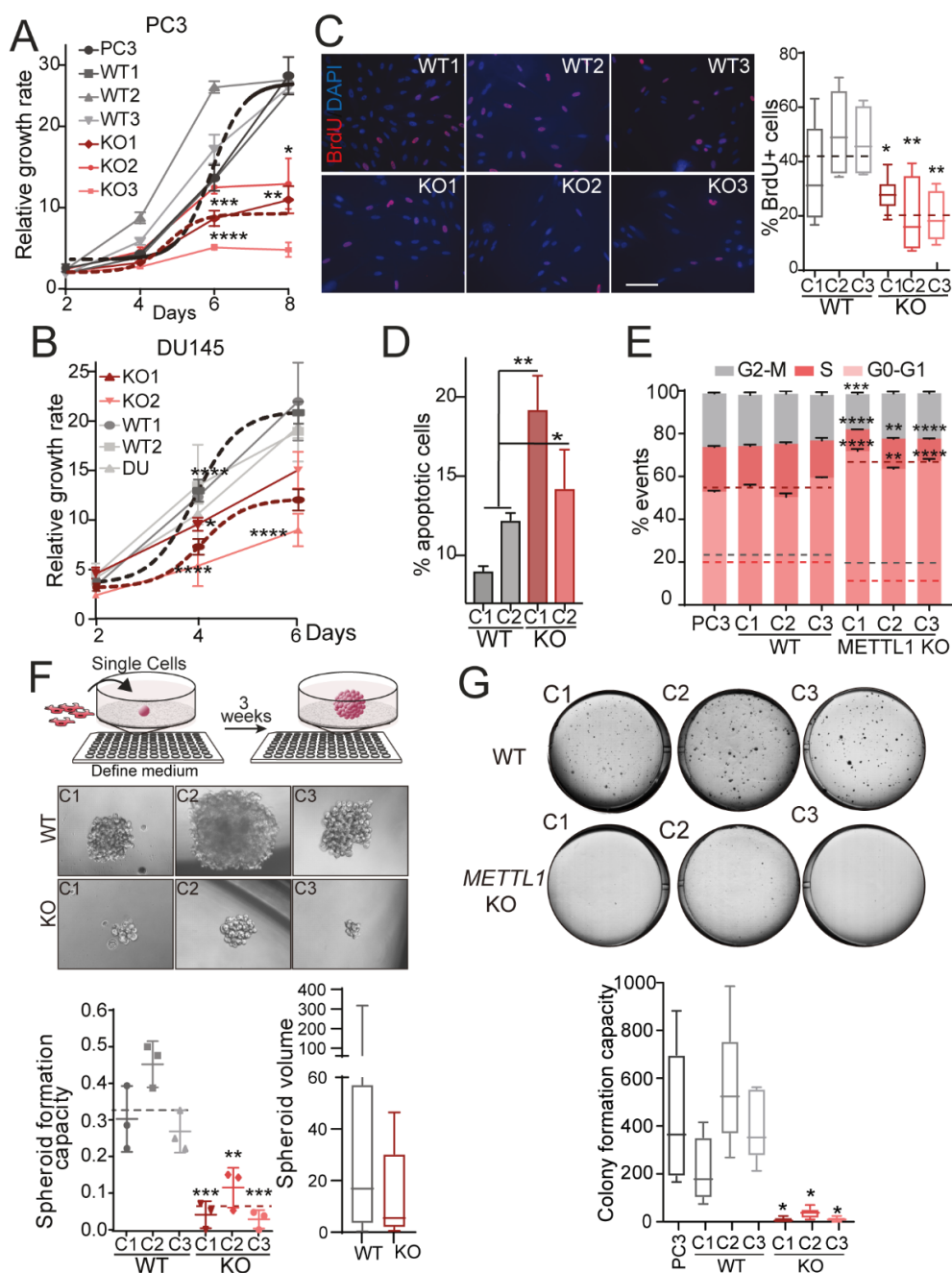


Figure 26. *METTL1* depletion decreases prostate cancer cell proliferation *in vitro*. **A, B**) Growth curves of three clones of PC3 (**A**) and two clones of DU145 (**B**) WT (grey) and *METTL1* KO (red) cell lines. Parental cell line (PC3 or DU145) is also represented. Dotted lines correspond to the average growth of all *METTL1* expressing (parental and WT1, WT2 and WT3) or KO cell lines (KO1, KO2 and KO3). Mean \pm SD is represented (n=6). **C**) Evaluation of cell division by BrdU incorporation in PC3 WT and *METTL1* KO cell lines. Box plots represent mean, interquartile range and min and max values (n=6), and dotted lines correspond to the average values from WT or KO cell lines. **D**) Quantification of percentage of all apoptotic cells in PC3 control and *METTL1*-depleted cells measured by Annexin V and propidium iodide staining by flow cytometry. Mean \pm SD are represented (n=3). **E**) Assessment of self-renewal capacity of PC3 WT (grey) and KO (red) cell lines by single-cell organoid formation capacity in non-adherent conditions. Schematic representation of the approach and representative images are shown. Graph represents the normalised number of spheroids obtained. Mean \pm SD (n=3). Discontinuous lines represent the average from all WT and KO cell lines. Statistics analysis: Two-way ANOVA comparing each KO cell line with average of WT cells (**A, B**); One-way ANOVA comparing each KO cell line with the average data from WT cells (**C, E-G**). One tailed Student's t-test (**D**). *p<0.05; **p<0.01; ***p<0.001; ****p<0.0001.

Impaired proliferation in *METTL1* KO cells was caused by reduced cell division measured by BrdU incorporation, cell cycle arrest in G0-G1 and increased apoptosis rate (Figure 26C). We then evaluated growth capacity in distinct suspension conditions, using single-cell spheroids as a readout of self-renewal capacity of tumourspheres, and colony formation in soft agar as an indicator of cell malignant transformation. In both cases, a combination of reduced number and size of the formed spheroids and colonies in PC3 *METTL1* KO cells was obtained (Figure 26D).

To validate *METTL1* role in tumour formation *in vivo*, xenografts derived from PC3 WT and *METTL1* deficient cells were generated. As a result, a remarkable reduced tumour formation capacity was exhibited upon *METTL1* depletion (Figure 27A). Staining of xenograft sections showed increased staining of the apoptosis marker cleaved-caspase3 and reduced staining of the proliferation marker Ki67 (Figure 27B). Similarly, a decreased tumour growth was observed in xenografts generated from DU145 cell lines stably expressing inducible short-hairping RNAs of *METTL1* (*sh3*, *sh4*) (Figure 27C). These data suggested that inhibition of *METTL1* would be both prevented and therapeutic for PCa.

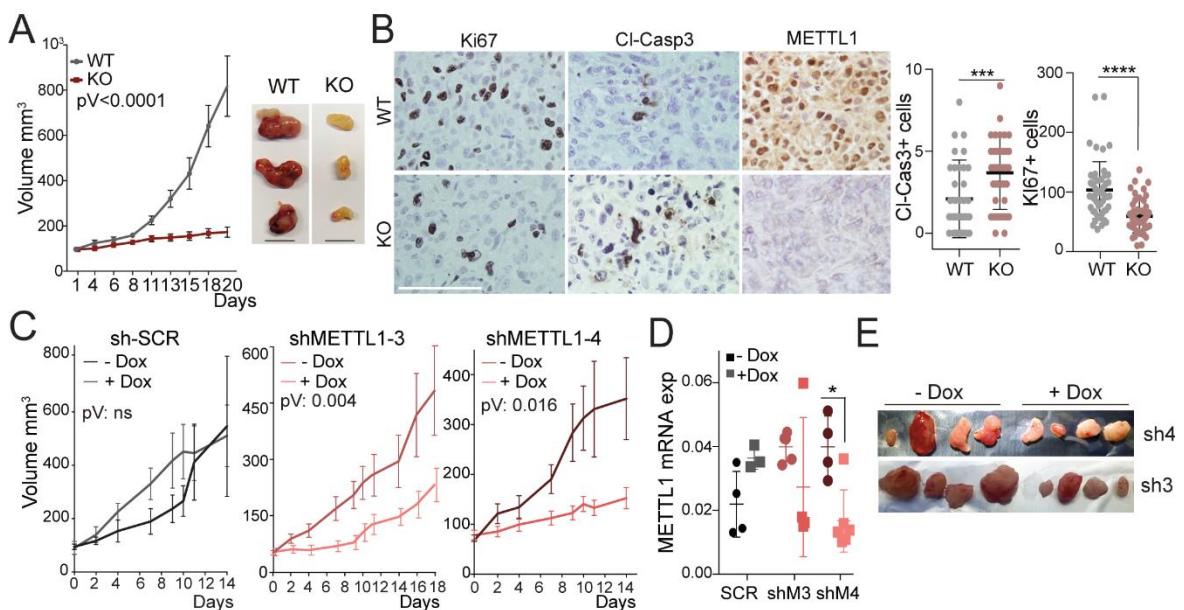


Figure 27. Depletion of *METTL1* impairs tumour growth capacity *in vivo*. **A)** Tumour volume of subcutaneously xenografted PC3 WT (grey) and *METTL1* KO (red) in athymic nude mice. Mean \pm SEM are represented (n=10). Representative images of both types of xenografts- Scale bar represents 1 cm. **B)** Immunohistochemistry staining for assaying *METTL1* depletion as well as proliferative (Ki67⁺) and apoptotic (Cl-Casp3⁺) cells. Quantification represents mean \pm SD, of five mice per genotype with 10 images per tumour. **C)** Tumour volume of xenografted DU145 with inducible silencing of *METTL1*. Control cell line (shSCR) and comparison of sh*METTL1* (+ doxy) with non-induced controls (-dox) are represented. Mean \pm SEM are represented (n=10 for shM3, n=5 for shM4 and shSCR). **D)** RT-qPCR of *METTL1* expression levels of xenografts extracted from control (SCR) or *METTL1*-silenced xenografts. Mean \pm SD are shown. Statistics analysis: One tailed Student's t-test (**B, D**). *p<0.05; ***p<0.01; ****p<0.0001.

To further understand the molecular mechanism underlying the phenotypes observed upon *METTL1* depletion and its dependency on *METTL1* activity, a catalytic dead mutant of the methyltransferase was generated by directed mutagenesis in an inducible lentiviral construct containing a tagged version of the enzyme (HA-*METTL1*) (Figure 28A,B). The mutated aminoacids were selected based on Lin *et al* approach²¹⁰. *METTL1* expression was rescued in *METTL1* KO cells lines by infection

either with a wild type (WT) or a catalytic dead mutant (AFPA) version of the enzyme. The empty plasmid was also transfected as control (eV). Expression of the methyltransferase was validated by Western blot in both WT and AFPA cell lines upon doxycycline induction (Figure 28C,F). In addition, the catalytic ability of the exogenous METTL1 was analysed by Northdot blot assay. Methylation capacity was recovered in both PC3 *METTL1* KO clones generated with re-expression of the WT enzyme, corroborating again its dependency on the methyltransferase (Figure 28C,F). Although the internal m⁷G signal was significantly increased upon doxycycline treatment, non-induced conditions also showed basal methylation levels caused by a leakage induction of the plasmid by the tetracyclines naturally present on the culture medium. Moreover, though re-expression of METTL1 protein was detected in the generated catalytic mutant (AFPA), only a light m⁷G-methylation on the tRNAs was found after doxycycline induction (Figure 28C,F). Based on previous results about the specificity of METTL1 for m⁷G tRNA deposition, no methylation signal would be expected after its catalytic inhibition. Thus, our results indicate that the generated catalytic mutant might conserve a residual methyltransferase activity. Another aspect to considerate is the high variability of the technique and that, even though the samples loaded in the Northdot Blot are enriched with specific RNA species, other types of RNAs besides tRNAs may be present on the smaller fraction interfering with the results. We then investigated how the presence of METTL1 with no methyltransferase activity affected to the previously described phenotypes. Thereby, we analysed proliferation capacity in adherent and suspension conditions in the two distinct *METTL1* KO clones generated with the described constructions. As so, *METTL1* KO cells re-expressing WT METTL1 exhibited increased proliferation and spheroid formation capacity in comparison with eV, but this effect was not observed in those cells expressing a mutant METTL1 (Figure 28D,E,G,H). These results supported that METTL1 promoted cancer cells growth and self-renewal capacity in a catalytic-dependent manner, and the presence of the enzyme did not interfere in this process in a structural manner.

We next questioned whether the 5'TOGs biogenesis upon *METTL1* deprivation played a role in the observed phenotypes. With the aim of recapitulating either *METTL1* KO or WT cells phenotypes in the opposite cell line, PC3 WT cells were transfected with 5'TOG synthetic oligonucleotides and *METTL1* KO cells with anti-TOGs, respectively (Figure 28I). Although the recovery was not always statistically significant, WT cells transfected with 5'TOGs exhibited increased apoptotic and reduced proliferation compared with those transfected with a scramble RNA (Cont) (Figure 28J,K). Remarkably, the opposite effect was observed in KO cells transfected with anti-TOG fragments, corroborating the biological impact of the tRNA fragment biogenesis formed upon the methyltransferase depletion. Altogether, our data suggest that METTL1 catalytic activity promotes cancer cell proliferation and self-renewal of spheroids growing in suspension by preventing 5'TOG formation derived from METTL1-tRNA substrates.

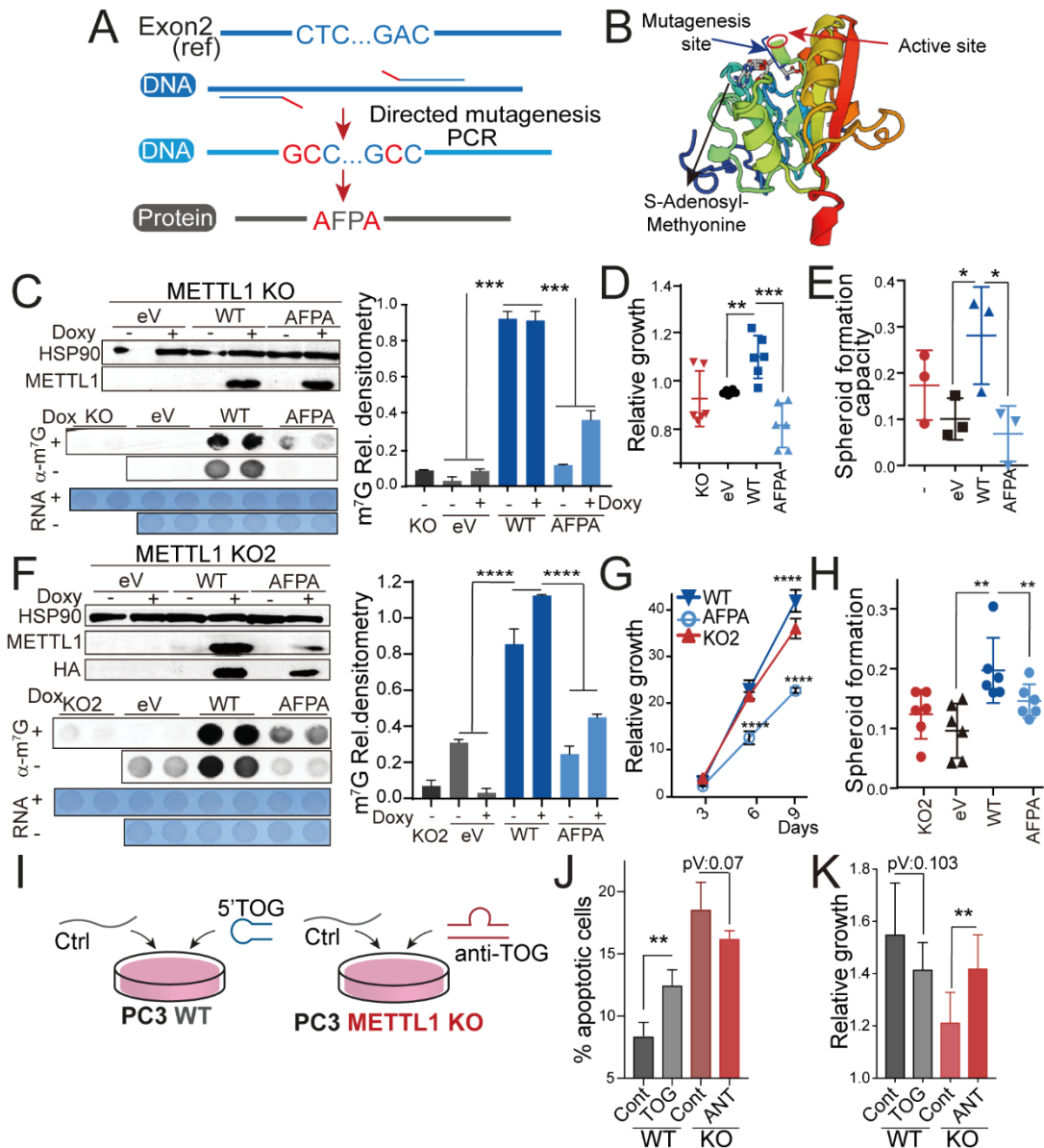


Figure 28. METTL1 methylating activity promotes cell growth. **A)** Schematic representation of the workflow followed for the generation of catalytic dead mutant version of METTL1 by directed mutagenesis. **B)** Representation of METTL1 three-dimensional structure and the mutagenesis targeted site at the catalytic pocket. **C, F)** METTL1 protein expression levels and assessment of m⁷G tRNA levels in two distinct PC3 *METTL1* KO clones with ectopic expression of a doxycycline-inducible HA-tagged wild type (WT) or mutant (AFPA) version of METTL1. Transfection with empty vector (eV) was used as control. Methylene blue is shown as loading control of northdot blot. Mean \pm SD are represented (n=3). **D, E, G, H)** Assessment of proliferation and self-renewal capacity in two distinct clones of PC3 *METTL1* KO cells re-expressing either a wild type METTL1 (WT) or a catalytic dead mutant (AFPA) upon doxycycline induction. Empty vector (eV) and non-transfected cell lines (-, KO) were used as controls. Mean \pm SD are represented (n=6 for proliferation; n=3 for single-cell spheroids). **I)** Schematic representation of *in vitro* transfection in PC3 WT and *METTL1* KO cell lines for assaying the phenotype dependency on 5'TOG formation. **J, K)** Quantification of the percentage of all apoptotic cells (**J**) and proliferation (**K**) in PC3 WT cells transfected either with a control (Cont) or 5'TOG (TOG) synthetic oligonucleotides, and in PC3 *METTL1* KO cells transfected with control or anti-TOG (Ant) synthetic oligonucleotides. Mean \pm SD are represented (n=6). Statistics analysis: Two-way ANOVA (**C, F, G**); one-tailed Student's t test (**D, E, H, J, K**). *p<0.05; **p<0.01; ***p<0.001; ****p<0.0001.

3.2. METTL1 specifically controls translation of stress response-related proteins

Considering the role that METTL1-mediated tRNA methylation exerts in global translational rates in cancer cells, we next investigated whether there were changes in the translatoome of *METTL1* KO cells to unravel the molecular mechanisms responsible of the observed phenotypes.

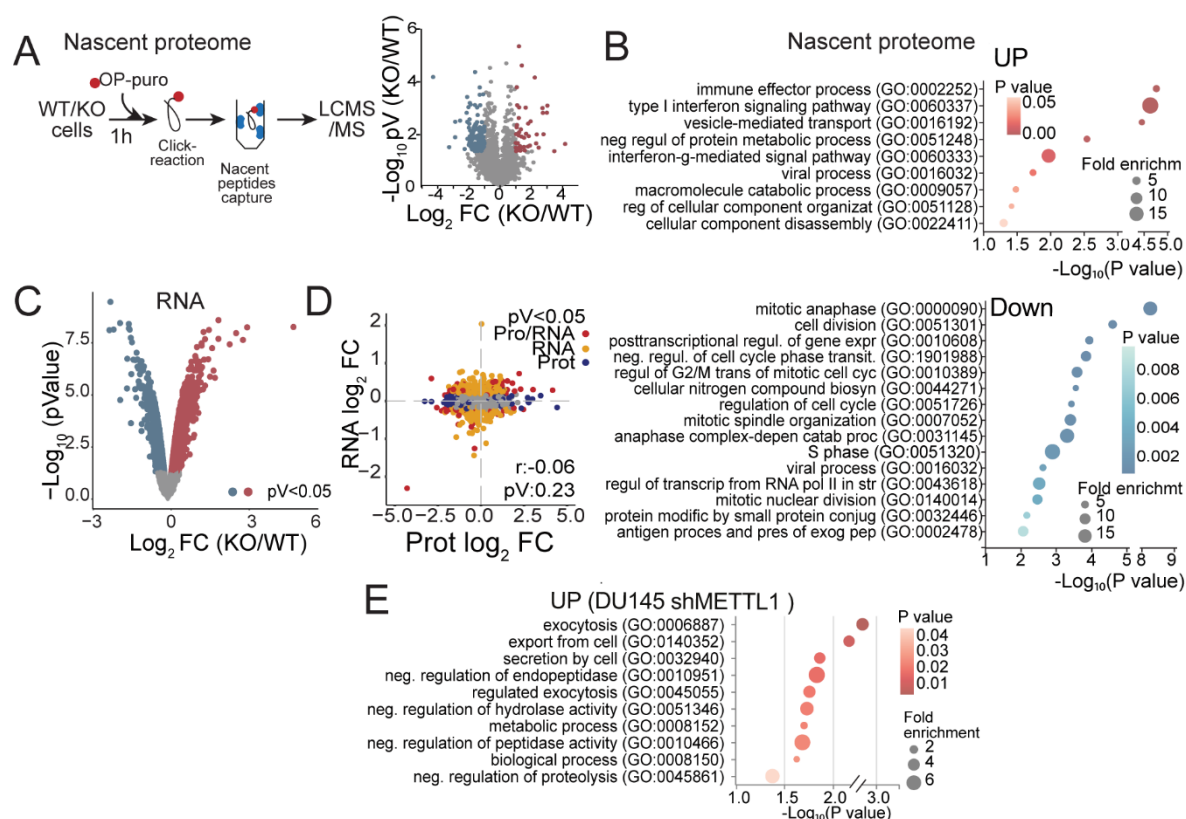


Figure 29. Loss of METTL1-mediated m⁷G deposition alter normal translational programme. **A)** Graphical representation of the workflow used for capturing the nascent proteome of PC3 cells. Lower panel shows volcano plot of the nascent proteins distributed according to their p-value ($-\text{Log}_{10} \text{pV}$) and their abundance between PC3 *METTL1* KO cells compared to WT cells ($\text{Log}_2 \text{FC}$). Coloured dots represent statistically (p -value < 0.05) upregulated (red) and downregulated (blue) proteins in *METTL1* KO cells ($n=4$). **B)** Gene ontology (GO) enrichment analysis of biological processes of the significantly (p -value < 0.05) upregulated (UP, $\text{FC} > 1$) or downregulated (DOWN, $\text{FC} < 1$) nascent proteins in PC3 *METTL1* KO versus WT cells. Categories are ranked based on their statistical p-value ($-\text{Log}_{10} \text{pV}$) and fold enrichment of the genes included in the distinct categories. **C)** Volcano plot of differential mRNA expression (ranked according to their statistical p-value ($-\text{Log}_{10} \text{pV}$) and their relative abundance ($\text{Log}_2 \text{FC}$) between PC3 *METTL1* KO vs WT cells. Coloured dots represent statistically (p -value < 0.05) upregulated (red) and downregulated (blue) mRNA ($n=3$). **D)** Correlation analysis between differentially expressed proteins (Protein $\text{log}_2 \text{FC}$) and mRNA (RNA $\text{log}_2 \text{FC}$) between PC3 *METTL1* KO and control cells. Coloured dots represent significant (p -value < 0.05) altered expressed proteins (blue), mRNAs (yellow) or both (red) for each gene. Pearson correlation (r) factor and p-value (pV) are indicated. **E)** GO category enrichment of biological processes in significantly (p -value < 0.05) differentially expressed proteins identified by label-free quantitative proteomics from DU145 silenced (shRNA +Dox) vs control (shRNA -Dox) cells. Categories are ranked according to their statistical p-value ($-\text{Log}_{10} \text{pV}$).

Thereby, taking advantage of the OP-puro properties, nascent peptides labelled with OP-puro were consecutively captured by an azide-coated resin using a copper catalysed click chemistry that covalently binds azide and alkyne groups³⁰⁹ (Figure 29A). Then, nascent polypeptides were separated by on-bead digestion and analysed by liquid chromatography-tandem mass spectrometry (LC-MS-MS), allowing the identification of nascent molecules enriched in the absence of *METTL1* in PC3 cells. In general terms, and in agreement with the decreased protein synthesis rates in *METTL1* KO cells, volcano plot representation showed a downregulation in protein synthesis in *METTL1* KO cells compared to those expressing the enzyme (Figure 29A). Gene Ontology (GO) term enrichment analysis of the downregulated proteins showed impaired translation of genes involved in cell cycle and mitosis in *METTL1* deficient cells, which would explain the reduced proliferation observed both *in vitro* and *in vivo* (Figure 29B). Strikingly, a more efficient translation of proteins associated with stress responses as type I and type II interferon (IFN) pathway, catabolic processes and vesicle

mediated transport was observed in *METTL1* KO cells (Figure 30B). However, analysis of the transcriptome by an expression microarray did not show a significant downregulation on *METTL1* KO cells (Figure 30C). Thus, the protein translation changes were uncoupled to transcription, since comparison between the protein and the RNA expression levels showed no correlation, indicating that the differences observed in the proteome were caused by alteration in the translational rather than the transcriptional programme (Figure 29D). Similar results were obtained after GO analysis of total proteome from DU145 with inducible silencing for *METTL1* (Figure 29E), which suggested that the phenotype was not cell dependent and consistent even in conditions with no complete deletion of the enzyme.

To corroborate that proteome differences are driven by translational changes, we performed polysome profiling from PC3 WT and *METTL1* KO cell lines³¹⁰. Briefly, the translationally active ribosomes (or polysome) fraction was selectively separated by sucrose gradients and RT-qPCR of the associated mRNAs. We first analysed the obtained profiles and, as expected, a significant reduction of the polysome fraction was found in *METTL1* depleted cells (Figure 30A). Next, the actively translated transcripts were analysed by measuring by RT-qPCR amplification of the RNA present on the polysome fractions (fraction 15-20), since enhanced translation of a gene would lead to an accumulation of its transcripts bound to the translationally active ribosomes.

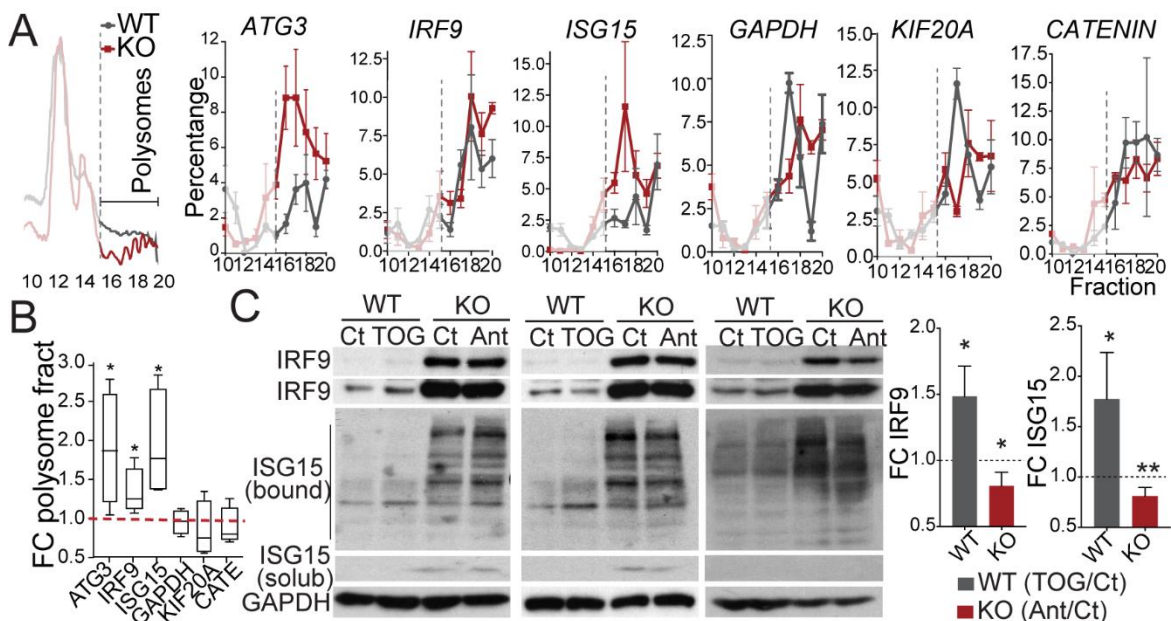


Figure 30. *METTL1*-mediated 5'TOG biogenesis induces translation of specific transcripts. **A)** Representation of polysome profiles in PC3 WT (grey) and *METTL1* KO cells (red) (left panel). Graphs represent the percentage of mRNA abundance of the indicated genes across the fractions obtained by sucrose density gradient ultracentrifugation of extracts from PC3 WT and *METTL1* KO cells. Highlighted fractions represent those which correspond to polysome fraction. Mean \pm SEM are shown (n=4). **B)** Boxplot represent median value (line) and interquartile range fold change (FC) of mRNA abundance in polysome fractions (area under the curve) from *METTL1* KO versus WT cells. Red dotted line corresponds to FC=1. **BC)** Western blot and quantification of the protein levels of the indicated proteins after transfection of PC3 WT cells with scramble control (Ct) or 5'TOG (TOG) RNAs and *METTL1* KO with either control or anti-TOG (Ant) synthetic oligonucleotides. Bar graphs represent the fold change of densitometry quantification of 5'TOG (grey) or anti-TOG (red) vs scramble. Mean \pm SD are represented (n=3). Statistical analysis: Student's t test of fold change(**B**) and comparing the protein expression upon TOG or anti-TOG transfection with SCR control. *p<0.05;**p<0.01.

Thus, we confirmed an enhanced translation of some of the upregulated transcripts identified in the proteome, such as interferon regulatory factor 9 (IRF9), interferon-stimulated gene (ISG15) and the autophagy-related protein ubiquitin-like-conjugating enzyme ATG3, but no differences were observed in some control transcripts as catenin, GAPDH or KIF20A (Figure 30A). The area under the curve of the profiles obtained with the RT-qPCR data was quantified as a quantitative measurement of the differences, which resulted in a significantly increased translational rates of ATG3, IRF9 and ISG15 transcripts (Figure 30B).

Since stress-mediated 5'tRFs take part in the integrated stress response that ultimately inhibit global protein synthesis to specifically favour the translation of specific proteins^{156,176}, we next aimed to elucidate whether the differences observed in IRF9 and ISG15 translation are dependent of 5'TOG biogenesis. Thus, we transfected PC3 WT and *METTL1* KO cell lines with a control (scramble) and either a 5'TOG or anti-TOG oligonucleotides, respectively. We then analysed protein levels of the indicated proteins, which resulted in a significant increased expression of both ISG15 and IRF9 in the WT cells transfected with 5'TOG RNAs. By contrast, transfection of *METTL1* KO cells with the anti-TOG sequences led to a slight but significant reduction in both proteins, which indicates that 5'TOG biogenesis regulates translation of specific transcripts upon *METTL1* removal (Figure 30C).

4. Evaluation of *METTL1* role in stress response pathways

4.1. Loss of *METTL1* alters cell proteostasis without triggering UPR

So far, we have described the essentiality of *METTL1*-mediated m⁷G deposition in maintaining a normal translational programme. Any situation that alters normal proteostasis within the cell causes a stress situation to which the cell needs to respond. Proteostatic stress or alterations in the basal proteomic rates usually leads to formation of misfolded proteins and protein aggregates that results in activation of stress pathways²³⁵. Thus, to evaluate whether *METTL1* deprivation leads to an accumulation of unfolded proteins, a specific staining for protein aggregates was performed in PC3 WT and *METTL1* KO cell lines. A remarkable increase of protein aggregates was detected in cells lacking *METTL1* (Figure 31A) in comparison with control cells, suggesting that *METTL1* plays an essential role in maintaining correct protein homeostasis.

One of the first pathways that are activated in response to misfolded protein accumulation is the ER stress and the unfolded protein response (UPR) pathways³¹¹. As previously described, the UPR pathway aims to restore the correct function of the ER and to reduce the load of misfolded proteins. To decipher the UPR status upon *METTL1* depletion, the three different branches that compose the pathway were evaluated (Figure 10). For a more reliable analysis, two different WT controls and two distinct *METTL1* KO clones were analysed. Thus, mRNA levels of *PERK* and *ATF4* were examined to assay status of the PERK branch. *IRE1α* expression levels and the ratio of spliced XBP1 (XBP1) and unspliced XBP1 (usXBP1) were used as markers of IRE1α section activation. Cleavage-ATF6

protein levels and *CHOP* mRNA were quantified to assess the third branch of the UPR response, which enhances the transcription of ER chaperones. In addition, BiP or GRP78 were used as general indicators of the UPR activation. Even though alteration of some factors such as CHOP, ATF4 and IRE1 α were detected in *METTL1* KO1 cells, no consistency was observed upon the different components of the pathway when comparing different WT and KO clones (Figure 31B,C). Our results suggest that, although a slight dysregulation of some UPR components is detected, no maintained response is triggered by the altered translational program caused by the absence of *METTL1* in PC3 cells, which indicates that other stress response pathways might be altered as consequence.

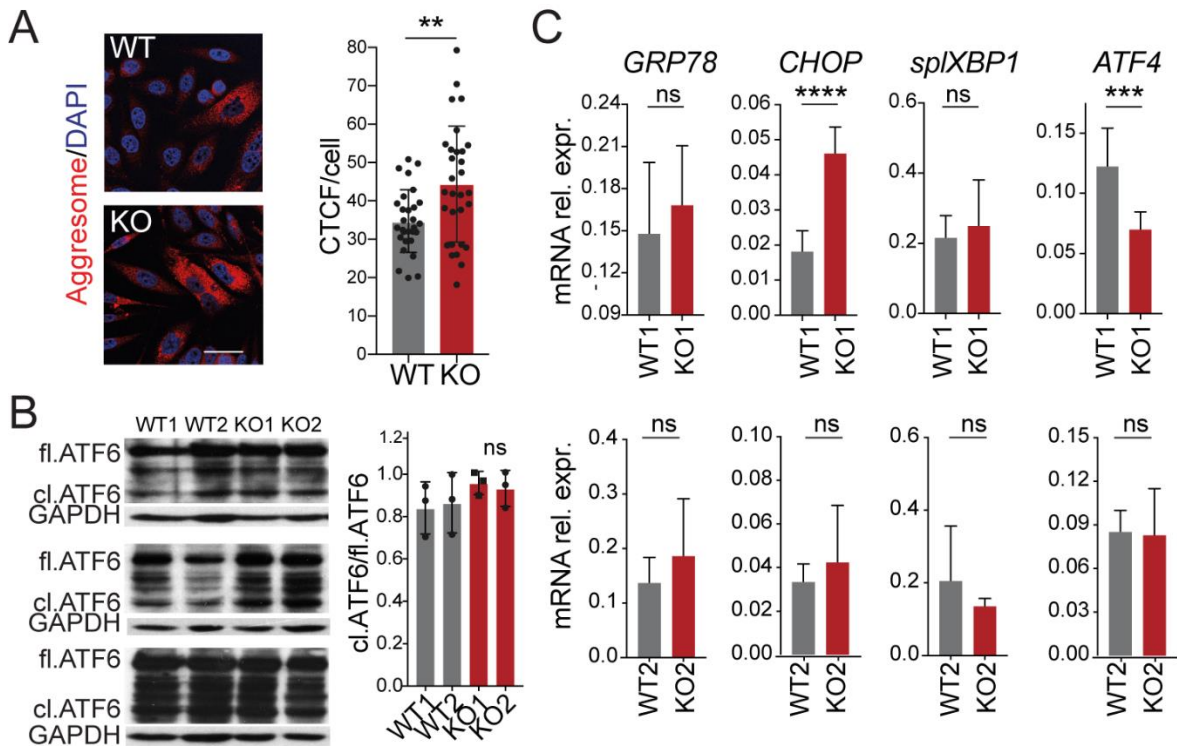


Figure 31. Loss of *METTL1* enhances misfolded protein accumulation but does not activate UPR. **A)** Staining of protein aggregates and quantification by measuring CTCF per cell in PC3 WT and *METTL1* KO cells. Representative images are shown. Scale bar represents 50 μ m. Cell fluorescence of ten pictures per condition was quantified. Mean \pm SD are represented. **B)** Western blot of full length (fl.) of cleaved (cl.) ATF6 in two different clones of PC3 WT and *METTL1*-depleted cells. Three replicates are shown. Graph represents the ratio between cleaved versus full length ATF6 to measure relative activation of the pathway. Mean \pm SD are represented (n=3). **C)** Assessment of UPR activation by quantification of mRNA levels of the indicated components of the three branches in two distinct clones of PC3 control (WT) and *METTL1* KO. Mean \pm SD are shown (n=3). Statistical analysis: One-tailed Student's t-test. Ns: non-significant, *p<0.05; **p<0.01.

4.2. *METTL1* is essential for maintaining a basal autophagic flux

Since no significant activation was detected of the UPR upon *METTL1* deletion, we next focused on the final end of misfolded proteins, the autophagy pathway. In addition, nascent proteome analysis showed a dysregulation of proteins connected with catabolic and secretory processes, and since autophagy is the prime secretory pathway within a cell, we next focus in unravelling whether *METTL1* loss affect the autophagic pathway. With that aim, we assessed the levels of the two broadly used autophagy markers LC3-I/II and p62. LC3-I/II is an autophagosome marker which is enhanced upon autophagy activation because of autophagosome formation (Figure 11). p62, on its behalf, specifically binds ubiquitinated proteins and displace them to the forming autophagosome, resulting

in the degradation of the labelled protein together with p62 during autophagy termination³¹². As a result, in normal conditions, a light but no significant increase of LC3 II or p62 levels was observed in PC3 *METTL1* KO cells compare to WT cells (Figure 33A). To further analyse the autophagic flux, chemical induction or inhibition of the pathway was performed. Chloroquine (CQ) is commonly used to block the autophagosome-lysosome fusion, disrupting the autophagy pathway at the final step. Upon autolysosome inhibition by CQ treatment, a subtle increase of LC3II was detected in WT cells, while *METTL1* KO cells showed a remarkable upregulation of the marker (Figure 32A). Regarding p62, although higher expression was detected in cells lacking *METTL1*, no significant changes were found upon CQ treatment. Normally, CQ treatment would produce accumulation of both LC3II and p62 since their lysosome-dependent degradation is inhibited. Thereby, LC3II/II accumulation and lack of p62 degradation suggest that *METTL1* loss leads to an accumulation of autophagosomes.

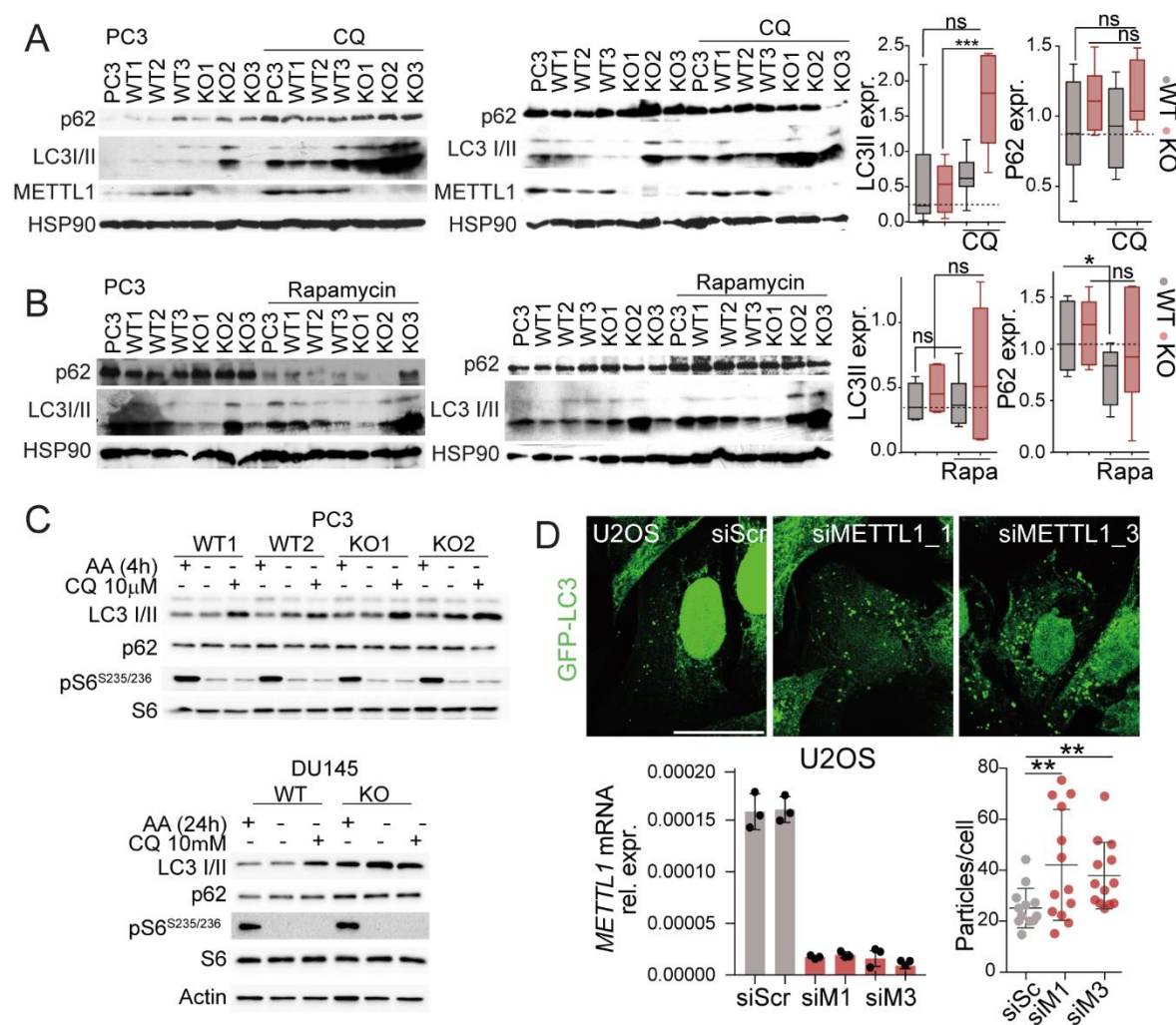


Figure 32. *METTL1* deletion enhances autophagic flux. **A, B** Western blot and quantification of the indicated proteins in three clones of PC3 WT and *METTL1* KO cells growing in normal conditions or with chloroquine (CQ) (A) or rapamycin treatments (B). Mean \pm Max-min values are represented (n=6). **C** Western blot of the indicated autophagy markers in two clones of PC3 WT and *METTL1* KO and one clone of DU145 of each genotype in cells growing in serum-free medium without glucose and with (+) or without (-) essential aminoacids (AA) or with CQ. **D** Representative immunofluorescence images of GFP-LC3 puncta formed in U2OS cells transiently silenced for *METTL1* (siM1, siM3) and control (siSCR). Lower panels show *METTL1* mRNA levels and puncta quantification per cell. Mean \pm SD (n=3 for RT-qPCR). Puncta from every cell from 10 images per condition was quantified. Scale bar represents 25 μ m. Statistical analysis: one-tailed Student's t-test; ns: no-significative; *p<0.05; **p<0.01; ***p<0.001.

To further investigate whether this is due to an increased autophagy activation or to a dysregulation of the autophagy termination, we next evaluated p62 and LC3II levels in rapamycin treated cells. Rapamycin is a mTOR inhibitor and, as so, an inducer of the autophagic pathway. Normally, cells would show enhanced LC3II protein levels and degradation of p62 upon pathway activation. However, when PC3 WT and *METTL1* KO cells were treated with rapamycin, the later did not exhibit a raise in LC3II levels when compared with normal conditions (Figure 32B). Besides, in the absence of *METTL1*, the reduction of p62 was minimal upon rapamycin addition when compared with WT cells, where the changes were significant (Figure 33B). Altogether, these results would suggest an alteration on autophagy termination that avoids the degradation of the autophagosome cargo. More detailed analysis was performed by studying the combined effect of amino acid deprivation or autophagy induction and CQ treatment in PC3 and DU145 WT and *METTL1* KO cells in collaboration with Pr. Raúl Durán (CABIMER, Sevilla). The resulting data corroborated our hypothesis, since increased LC3II levels were detected upon CQ treatment and no changes in p62 were observed (Figure 32C), supporting the obtained results in a second cell line. Altogether, our data indicates that *METTL1* is crucial for a correct autolysosome resolution.

Increased autophagosome formation upon *METTL1* depletion was also evaluated in the sarcoma cell line U2OS stably expressing the LC3 marker coupled to a green fluorescent protein (GFP). *METTL1* was temporary silenced using short-interfering RNAs (siRNAs) and autophagosome formation was evaluated by confocal microscopy and manual quantification of GFP⁺ puncta. Images shown a remarkable accumulation of GFP⁺ puncta in those cells with reduced *METTL1* levels (Figure 32D), validating the increase of autophagosome formation connected with the enzyme loss. This, together with data from^{221,268} indicates that *METTL1* role in regulation of autophagy is not tissue specific.

To decipher whether *METTL1* regulates autophagosome resolution, we analysed the autolysosome formation by specifically labelling lysosomes using lysotracker in PC3 WT and *METTL1* KO cells transiently transfected to express LC3-GFP protein. Briefly, lysotracker fluorescence intensity was analysed by flow cytometry in cells with labelled autophagosomes (GFP⁺) under different conditions (Figure 33A). As expected, higher lysotracker intensity was detected upon *METTL1* depletion suggesting increased lysosome accumulation. More interestingly, enhanced signal was found in WT but not in *METTL1* KO cells upon rapamycin induction, indicating a reduced lysosomal presence in the absence of the methyltransferase (Figure 33A,B). To analyse in detail the autophagosome-lysosome fusion, staining of endogenous LC3II and LAMP1 (lysosomal marker) was performed. Similar to previous experiments, quantification of fluorescence intensity showed increased expression of both markers in PC3 WT cells upon rapamycin treatment, which was not observed in *METTL1* depleted cells. Intriguingly, microscopy pictures showed reduced fluorescence co-localisation upon *METTL1* deletion, suggesting impaired fusion of the vesicles (Figure 33C).

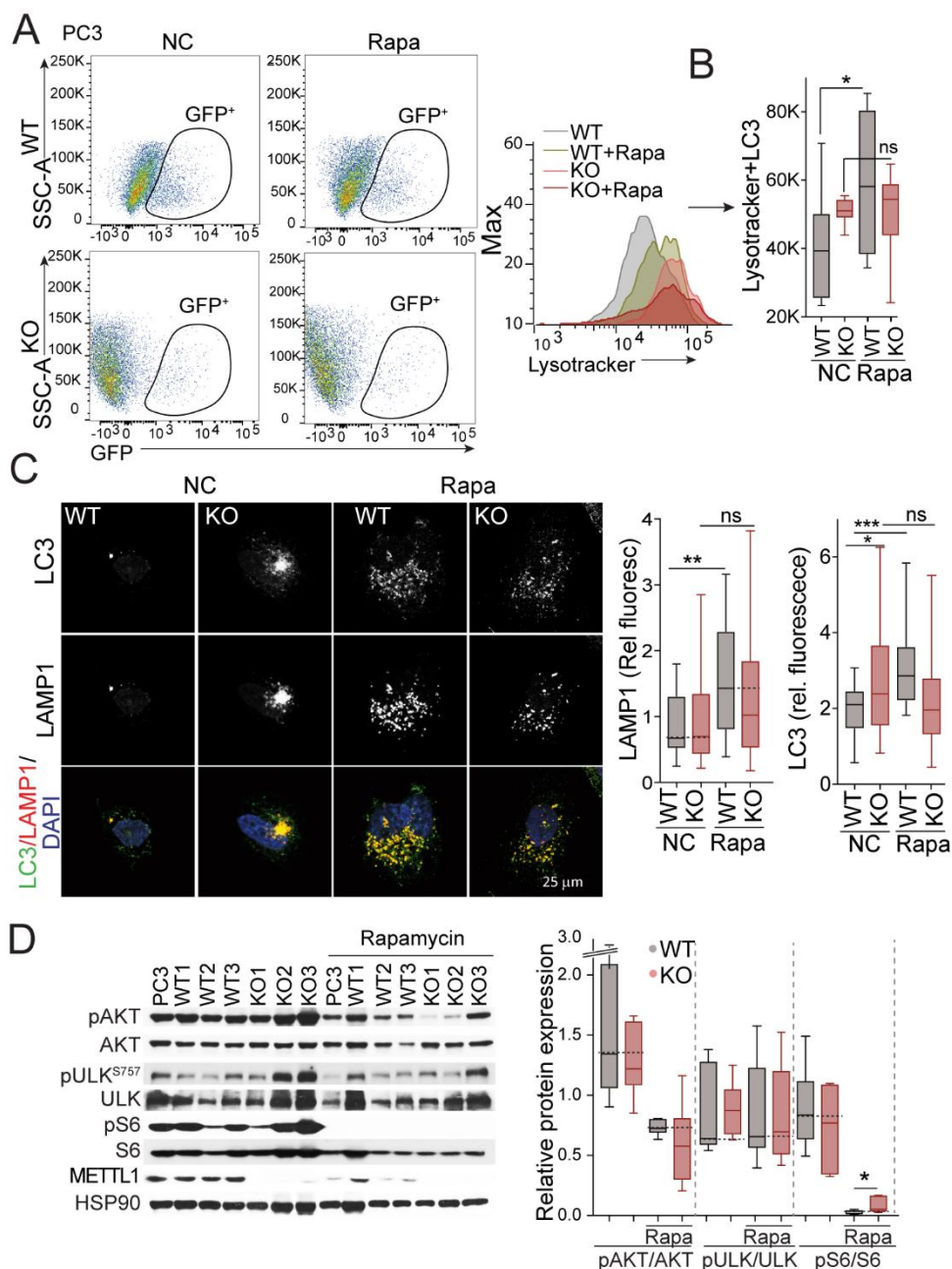


Figure 33. Loss of *METTL1* impairs autophagosome maturation. **A, B**) Analysis by flow cytometry of lysotracker fluorescence intensity in LC3-GFP⁺ PC3 WT and *METTL1* KO cells in normal conditions (NC) or treated with rapamycin (Rapa) (**A**). Boxplot represents intensity quantification. Mean \pm max-min values (n=3) (**B**). **C**) Immunofluorescence and quantification of endogenous LC3 (green) and LAMP1 (red) in PC3 WT and *METTL1* KO cells as markers of autophagosomes and lysosomes, respectively. Normal conditions (NC) and rapamycin (Rapa) treatment are shown. Scale bar represents 25 μ m. Boxplots represent CTCF per cell. Mean \pm max-min values. Intensity of all cells per image from 10 images per condition was quantified. **D**) Western blot from the indicated autophagy-related proteins from PC3 control and *METTL1*-depleted cells in normal conditions and after rapamycin treatment. Quantification is shown in boxplots. Mean \pm max-min values are represented (n=6). Statistical analysis: one tailed Student's t-test; ns: no-significant; *p<0.05; **p<0.01; ***p<0.001.

To further prove whether the role of *METTL1* in autophagy regulation was dependent on translation alteration of autophagy regulators, we next assessed the expression status of downstream effectors of mTORC1 and some key regulators as ULK1. However, no significant differences were detected between PC3 WT and *METTL1* KO cells in none of the components analysed (Figure 33D). Thus,

our data indicates that in PCa cell lines *METTL1*-dependent autophagy disruption is independent of mTORC1 activation.

Moreover, our data is not in concordance with the results observed by Han *et al*²²¹, in which alteration of the autophagic pathway upon *METTL1* downregulation was described to be caused by a decreased translation efficiency of negative regulators of autophagy and mTOR pathway, such as the regulatory-associated protein of mTOR (RPTOR). In consequence, reduced levels of the inactivating phosphorylation at ser758 of ULK1 were detected. However, we did not see this alteration on the inducers or negative regulators of the pathway, indicating that the mechanism that dysregulates autophagy in prostate cancer cell lines differs from oesophageal cell carcinoma.

In summary, *METTL1* deletion leads to an autophagy dysregulation independent of mTOR activation and based in an impaired autophagosome termination that results in accumulation of autophagy vesicles and misfolded proteins in the cytoplasm.

4.3. *METTL1* loss results in ROS accumulation and increased stress sensitivity

Due to autophagy nature as a removal mechanism of protein aggregates, damaged organelles such as mitochondria and oxidized substances, alterations in the mechanism are often associated with increased oxidative damage and reactive oxygen species (ROS) levels³¹³. Thus, we interrogated whether *METTL1* depletion affected the cellular redox balance by measuring ROS levels in PC3 WT and *METTL1* KO cells using 2',7'-Dichlorofluorescein Diacetate (CDFH-DA). Flow cytometry analysis revealed a remarkable increase in ROS production upon *METTL1* depletion (Figure 34A). ROS accumulation is one of the major sources of DNA damage³¹⁴, a status that is commonly quantified by measuring γ H2AX and BRCA1 foci. γ H2AX is a variant of the histone H2AX frequently used as marker of DNA double-strand breaks (DSBs), since rapidly manifests in mammalian nuclei after DNA damage²⁹⁵. BRCA1, on its behalf, is a protein involved in DNA damaged repair that specifically translocates to DNA damage sites³¹⁵. Thus, analysis by immunofluorescence in collaboration with Dr. Pablo Huertas (CABIMER, Sevilla) showed increased formation of γ H2AX⁺ foci in PC3 and DU145 *METTL1* KO cells, a significant induction of BRCA1⁺ foci in PC3 *METTL1* KO cells, and a tendency, although not significant induction of BRCA1⁺ foci in DU145 *METTL1* KO cells (Figure 34B,C).

Previous studies reported that autophagy dysregulation leads to enhanced sensitivity to chemotherapeutic agents³¹⁶. Based on this, together with the increased genotoxic stress observed in absence of *METTL1*, we hypothesised that cells lacking the methyltransferase may have increased sensitivity to distinct stress conditions. Due to the increased accumulation of ROS observed in the absence of *METTL1*, we first evaluated whether deletion of the methyltransferase in PC3 cells increased cell toxicity to oxidative stress. Thus, PC3 *METTL1* KO cells showed impaired proliferation and increased cell death under H₂O₂ and UV treatments, respectively, when compared

with *METTL1*-expressing cells (Figure 34D,E). DU145 overexpressing the enzyme recapitulated this result, showing that higher levels of *METTL1* resulted in increased cell survival (Figure 34F).

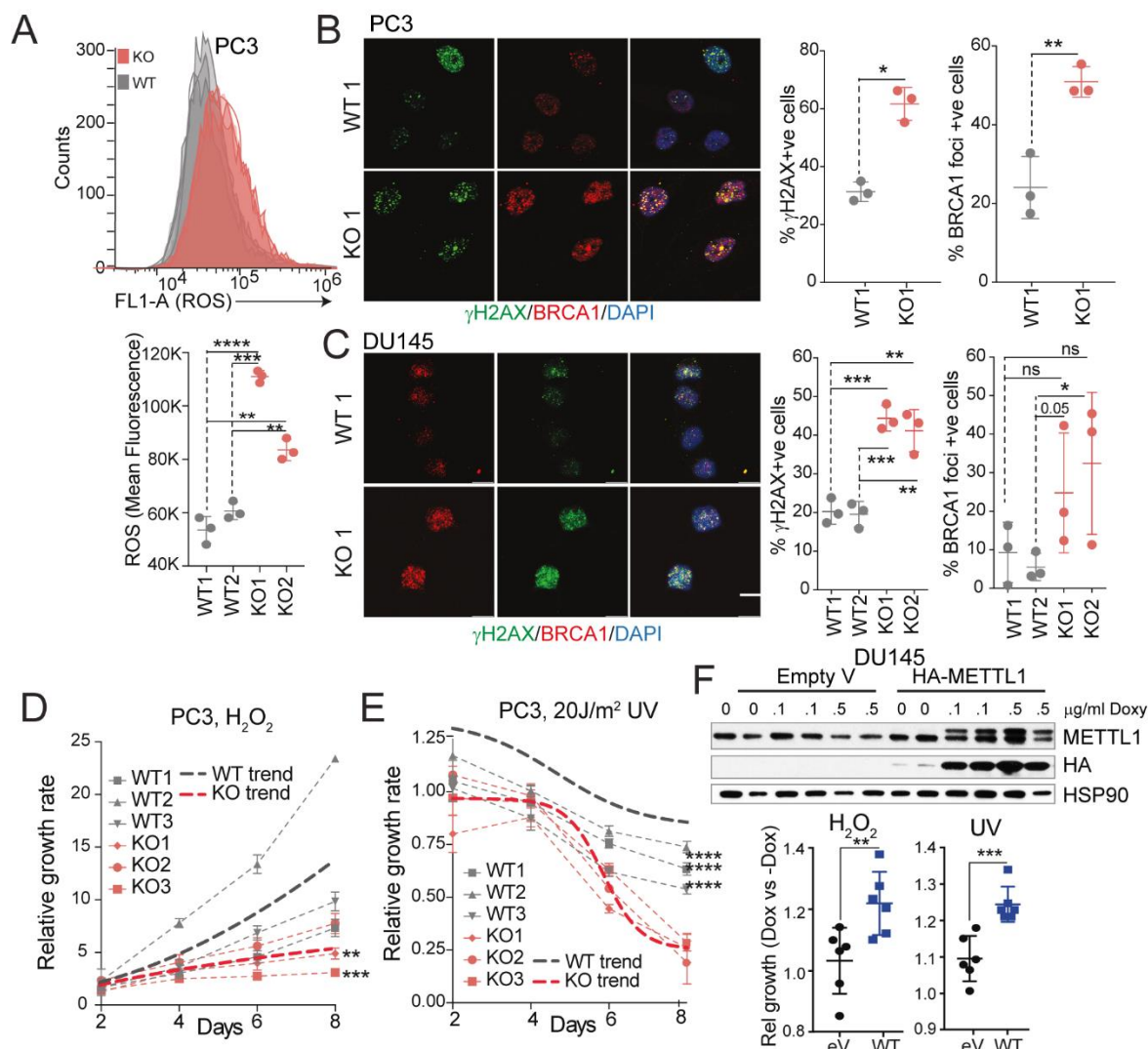


Figure 34. *METTL1* depletion impairs redox balance within the cell increasing oxidative stress sensitivity. **A)** Measurement of Reactive Oxygen Species (ROS) by flow cytometry in two distinct PC3 control and *METTL1* KO cell clones. Flow cytometry histogram and mean fluorescence quantification are shown. Mean \pm SD are represented (n=3). **B,C)** Quantification of DNA damage in PC3 (**B**) and DU145 (**C**) WT and *METTL1*-depleted cells by immunofluorescence of γ H2AX and BRCA1 markers. Representative images and percentage of positive cells for both markers are represented. Mean \pm SD of 3 replicates and 100 cells per replicate were quantified. Scale bar represents 20 μ m. **D, E)** Survival growth curves of three clones of PC3 WT and *METTL1* KO cells exposed to 3725 nM H₂O₂ (**D**) or 20 J/cm² of UV light (**E**). Thick discontinuous lines indicate the average growth of all WT (grey) and KO (red) cell lines. Mean \pm SD is represented (n=6). **F)** Western blot of DU145 overexpressing *METTL1* upon doxycycline treatment (upper panel). Lower panel shows relative growth after 48h of oxidative stress induction with 3725 nM of H₂O₂ or 20 J/cm² of UV light of DU145 control (eV) of *METTL1* (WT) overexpressing cells. Proliferation graphs represent the fold change of doxycycline treated cells versus is non-induced control. Statistical analysis: one tailed Student's t-test (**A-C, F**) and two-way ANOVA comparing each KO cell line with the average of control cells (**D, E**); *p<0.05; **p<0.01; ***p<0.001; ****p<0.0001.

Furthermore, targeting autophagy as a cancer therapeutic approach is gaining interest over the years in a wide variety of cancers including glioblastoma, pancreatic cancer, melanoma and sarcoma³¹⁷. To assess the effect of chemical manipulation of the autophagy pathway upon *METTL1* deletion, we first evaluated cell proliferation after autophagy induction with rapamycin, observing a significant reduction of cell proliferation in PC3 *METTL1* KO cells (Figure 35A). We also evaluate the stress response in PC3 *METTL1* KO cell lines with inducible expression of the WT enzyme and the

catalytic dead mutant AFPA. Re-expression of WT *METTL1* in PC3 KO cells increased proliferation capacity, but the re-expression of a catalytic dead mutant did not show the same effect (Figure 35A right panel). Interestingly, *METTL1* KO cells showed increased cell viability upon autophagosome formation inhibition by class III PI3K inhibitor 3-methyladenine (3-MA) (Figure 35B), which would indicate that part of the reduced viability observed in *METTL1* deficient cells is caused by the accumulation of phagosomes caused by dysregulation of autophagy termination. Similar to rapamycin treatment, re-expression of functional WT *METTL1* resulted in reduced survival upon 3-MA, meanwhile the mutant version recovered part of the cell viability, corroborating the dependency of stress response mechanisms on the methyltransferase activity of the enzyme (Figure 35B right panel).

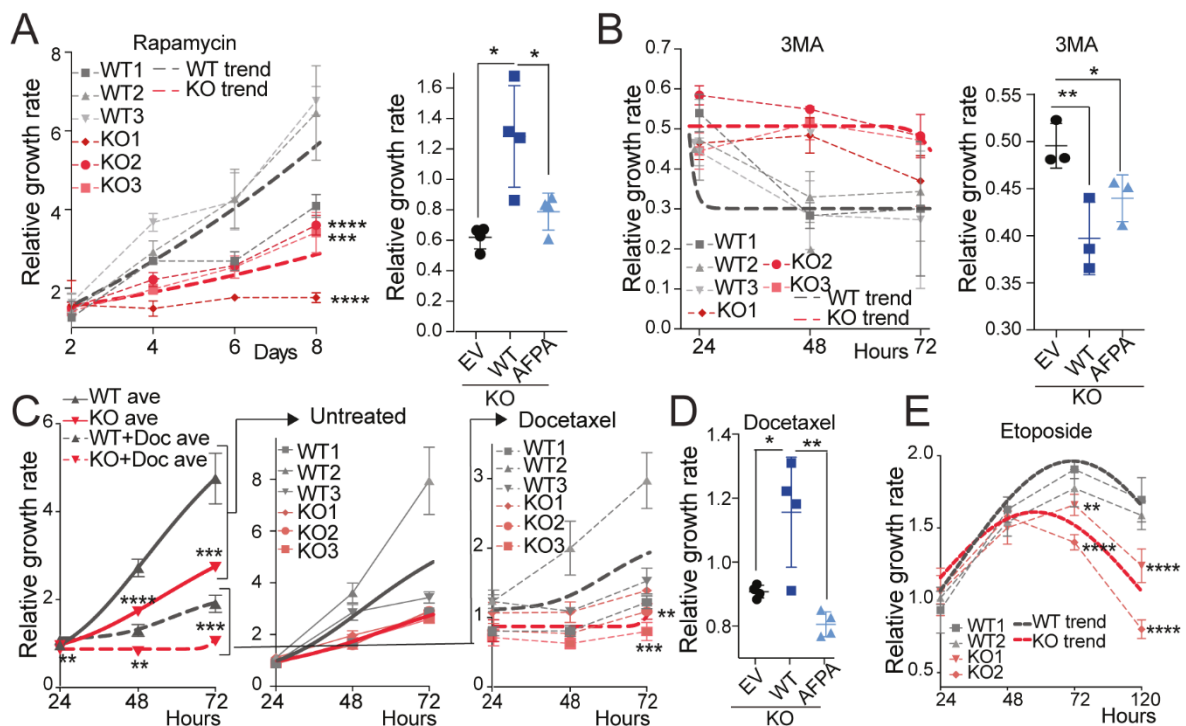


Figure 35. Loss of *METTL1* diminishes cells proliferation upon autophagy induction and PCa chemotherapeutic agents treatment. **A, B**) Growth curves in adherent conditions of three distinct clones of PC3 control (WT) and *METTL1* KO (KO) cells after treatment with 20 nM rapamycin (**A**) or 2 mM 3MA (**B**). Thick discontinuous lines represent the average proliferation rate of all WT (grey) or KO (red) lines. Right panels show the proliferation capacity of PC3 *METTL1* KO cells transduced with distinct doxycycline-inducible constructs: empty vector (eV), HA-*METTL1* (WT) or catalytic dead mutant (AFPA) at 48 h. Growth capacity of induced cells normalised to non-induced cells is represented. Mean \pm SD is shown ($n \geq 3$). **C**) Quantification of proliferation capacity of PC3 WT or *METTL1* KO cells after treatment with 15 nM Docetaxel. Left panel represents the growth trend of three WT (grey) and KO (red) clones with (+Doce) or without Docetaxel. Middle and right panels represent each separated line in normal conditions (middle) and upon Docetaxel treatment (left). Thicker lines indicate the average proliferation of each condition. Mean \pm SD are represented ($n=6$). **D**) Fold change of proliferation capacity of *METTL1* KO cell lines induced compared to non-induced for re-expressing a WT or a catalytic dead mutant version (AFPA) of *METTL1*. Mean \pm SD are shown ($n=4$). **E**) Growth curve of PC3 WT or *METTL1*-depleted cells upon treatment with 7 μ M of Etoposide. Thicker lines represent the average growth for the different genotypes: WT (grey) and KO (red). Mean \pm SEM are shown ($n=6$). Statistical analysis: Two-way ANOVA comparing KO cell lines with the average of all WT lines (**A, B left panels, C, E**); one-tailed Student's t-test (**A, B right panels and D**). * $p < 0.05$; ** $p < 0.01$; *** $p < 0.001$; **** $p < 0.0001$.

Based on *METTL1*-dependent response to stress conditions exhibited by PCa cell lines, we next evaluated whether the methyltransferase loss also affected the sensitivity to commonly used chemotherapy agents. With that aim, we analysed the effect of Docetaxel and Etoposide in PC3 WT

and *METTL1*-depleted cell lines. Docetaxel, a first-line treatment to CRPC that acts as a microtubule assembling inhibitor³¹⁸, resulted in reduced cell viability upon *METTL1* depletion (Figure 35C). Proliferation analysis of the rescued cell lines showed increased sensitivity to the treatment of the *METTL1* KO cells transduced with the mutant enzyme but not with the WT version (Figure 35D), indicating the dependency of the phenotype on METTL1 methyltransferase activity. Conversely, the effect of DNA-damage inducing agents in PCa treatment is still being elucidated, being only approved the combined treatment of Etoposide together with cis-platinum to treat aggressive neuroendocrine PCa³¹⁹⁻³²¹. Thus, we evaluated whether the increased DNA damage caused by loss of *METTL1* affected cell viability upon Etoposide treatment, observing a reduced cell viability at shorter times in PC3 *METTL1* KO cells compared to WT (Figure 35E), demonstrating that METTL1-mediated ROS accumulation increase cell sensitivity to DNA damage-inducing agents.

In summary, METTL1-dependent m⁷G-tRNA translational programme regulates stress sensitivity *in vitro*, resulting in impaired cell survival upon distinct stress stimuli, including chemotherapy agents. This suggests that a combined application of traditional PCa therapy together with METTL1 activity inhibition might be a potential therapeutic target.

5. Characterization of *Mettl1* role *in vivo*

5.1. Generation of a PCa mouse model with *Mettl1* deletion in prostatic epithelium

We have observed that loss of *METTL1* results in impaired proliferation capacity and increased stress sensitivity in cultured cells. To evaluate the therapeutic role of inhibiting the methyltransferase in PCa progression in an *in vivo* model, we generated a *Mettl1* conditional knockout mouse model in the prostate epithelium. Briefly, exon 2 of *Mettl1* genomic sequence was flanked with two LoxP sites using CRISPR-Cas9 technology (Figure 36A), which, when crossed with the previously described *PB-Cre4 x Pten^{flx/flx}* mouse⁷⁷, resulted in deletion of *Mettl1* in epithelial prostatic cells expressing *Probasin*. Thus, we obtained the *PBCre x Pten^{flx/flx}/Mettl1^{flx/flx}* (referred as *PtenKO/Mettl1^{flx}* hereinafter) mouse model, whose *Mettl1* deletion in prostatic tissue was validated by RT-qPCR and immunohistochemistry stainings (Figure 36B,C). We then evaluated m⁷G-tRNAs levels in prostate tissue. Although basal methylation levels were observed, an important decrease was appreciated in *Mettl1*-depleted tissue compared to WT tumours (Figure 36D). Residual m⁷G detected levels could be due to a remaining methyltransferase expression within *Mettl1*-expressing non-epithelial tissue. To corroborate *Mettl1* role as fragment biogenesis regulator, we analysed tRNA fragmentation in *PtenKO* and *PtenKO/Mettl1^{flx}* prostates. Northern blot analysis uncovered that, although tRNA from *Mettl1*-expressing tumours showed increased basal fragmentation compared to cultured cells, tRNA fragmentation was exacerbated in *Mettl1*KO prostates (Figure 36E). Thus, indicating that deletion of *Mettl1* in mouse prostate also regulates tRNA stability and tRNA-derived fragment biogenesis.

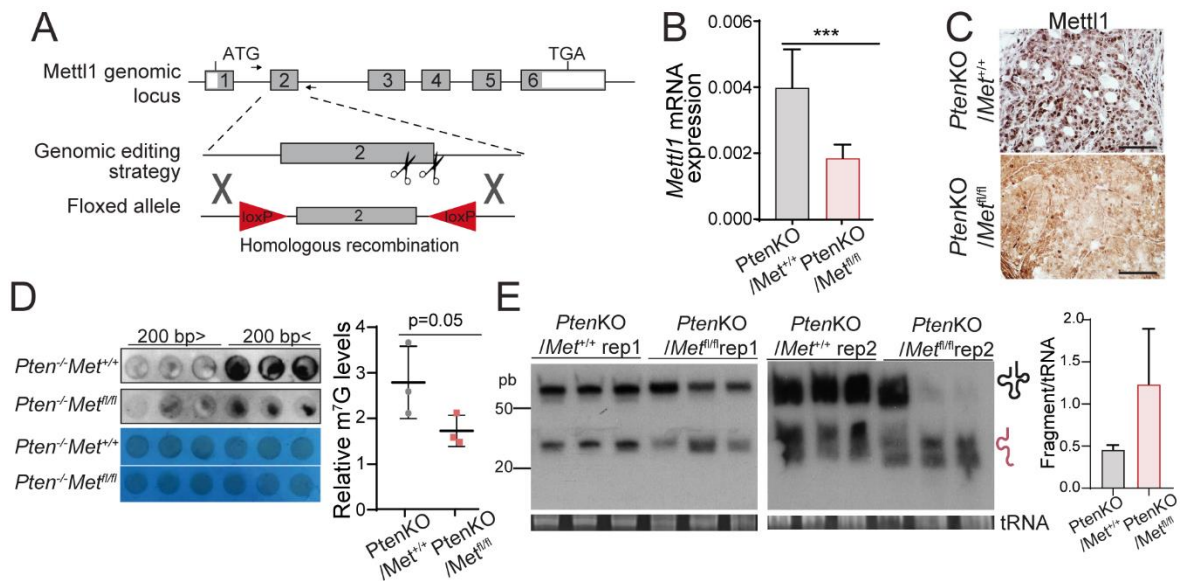
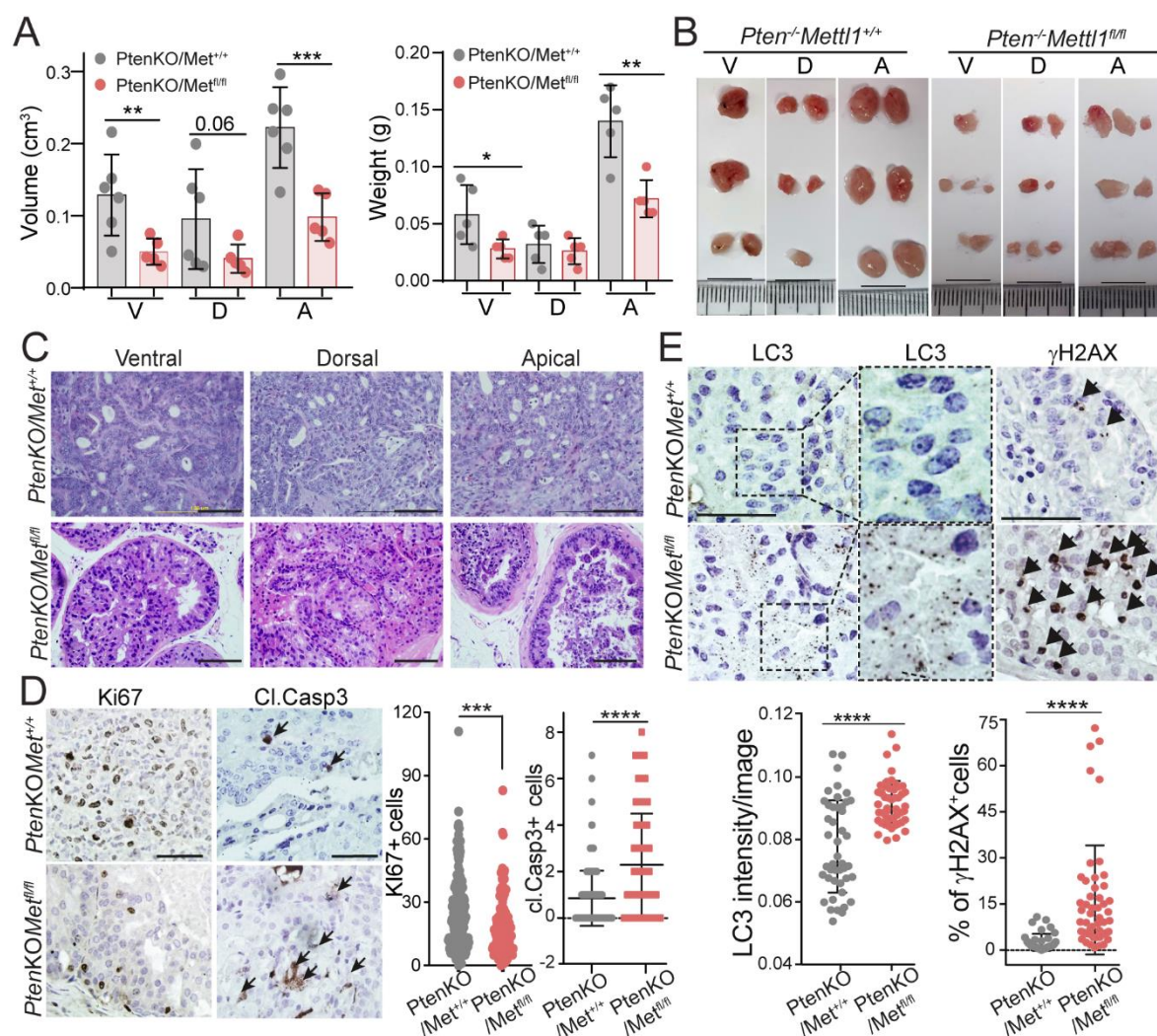


Figure 36. Generation of a prostate cancer mouse model with conditional *Mettl1* deletion. **A)** Schematic representation of the approach used for the generation of the mouse model with deletion of *Mettl1* in the prostatic epithelium. **B)** Quantification of *Mettl1* mRNA levels in 5-month-old *PtenKO/Mettl1*^{+/+} and *PtenKO/Mettl1*^{fl/fl} mice prostates. Mean \pm SD are represented (n=6). **C)** Immunohistochemistry staining of *Mettl1* levels in prostates from PCa mouse model WT and *Mettl1* KO. Scale bar represents 100 μ m. **D)** Analysis of m7G-tRNA levels (200 bp) in *Mettl1*-expressing and -depleted 5-month-old mice prostates. **E)** Northdot blot and densitometry quantification using methylene blue as loading control are represented. Mean \pm SD are shown (n=3) Statistical analysis: One-tailed Student's t-test. ***p<0.001.

5.2. *Mettl1* depletion in murine PCa restores cell composition towards a healthy tissue

Since deletion of *METTL1* in PCa cell lines resulted in impaired cell proliferation, we then interrogated whether *Mettl1* depletion affected prostate tumour formation. Thereby, phenotypic analysis of five-months-old mice revealed that prostate tumours with deletion of *Mettl1* exhibited a remarkable decrease both in tumour mass and volume in all prostate lobes in comparison to those extracted from *PtenKO* mice from the same age (Figure 37A). Histological analysis by Haematoxylin and Eosin (H&E) staining showed a reduced tumorigenic capacity of *Mettl1* deficient tumours, with more differentiated cells and less proliferative epithelium compared to *Mettl1* WT prostates (Figure 37B). Furthermore, proliferative and apoptosis rate of *PtenKO* and *PtenKO/Mettl1*^{fl/fl} tumours were evaluated by immunohistochemistry (IHC) quantification of Ki67 and Cleaved-Casp3 positive cells, respectively, indicating that tumours from *PtenKO/Mettl1*^{fl/fl} mice exhibited reduced proliferative potential and increased apoptosis rate in comparison with *PtenKO* tumours (Figure 37C). Thus, our data indicates that *Mettl1* regulates PCa pathogenesis in mouse via impaired translational programmes originated by the accumulation of tRNA fragments.

We next analysed whether *Mettl1* deletion led to increased autophagic flux and DNA damage at prostate tumours as observed *in vitro*. Immunohistochemistry staining of LC3 showed accumulation of autophagic vesicles in prostates lacking *Mettl1*, confirming the regulatory autophagic role observed *in vitro* (Figure 37D). Quantification of DNA damage rate by γ H2AX staining also resulted in increased formation of DNA damage foci in absence of the enzyme (Figure 37D).



Altogether, our data point out that *Mettl1* not only regulates PCa aggressiveness in the mouse model *Pten*KO but also replicates the increased stress signalling observed *in vitro*, which suggests that inhibition of the methyltransferase activity would have therapeutic potential.

We then interrogated whether *Mettl1* deletion would differentially affect the distinct cell populations that comprise the tumour. Firstly, we evaluated *Mettl1* expression in luminal (K8⁺) and basal (K14⁺) cells within prostates from *Mettl1*^{+/+} and *Mettl1*^{fllox/fllox} *Pten*KO mice. Interestingly, tumours from *Pten*KO/*Mettl1*^{fllox/fllox} mice exhibited a reduced staining in both cell types, but specially the proportion of basal cells was significantly decreased upon *Mettl1* depletion (Figure 38A). To validate

this result that aim, we followed a similar procedure to separate cell populations from five-months-old mice prostates by FACS as previously described.

Briefly, live single prostate epithelial cells were selected by lineage negative markers ($CD31^-$, $CD45^-$, $Ter119^-$) and separated in basal ($Lin^-Sca1^+CD49f^{high+}$), luminal ($Lin^-Sca1^+CD49f^{low}$) and stromal ($Lin^-Sca1^-CD49f^{low}$) cells (Figure 38B). The percentage of cells conforming every population was evaluated in normal prostates ($Pten^{+/+}/Mettl1^{+/+}$), in prostate tumours expressing *Mettl1* ($PtenKO/Mettl1^{+/+}$) and in prostate tumours deficient for the enzyme ($PtenKO/Mettl1^{fl/fl}$). Prostate tumours from $PtenKO/Mettl1^{+/+}$ mice showed a remarkable enrichment of basal cells when compared with normal prostates, which presented more stem-like characteristics. Interestingly, *Mettl1* deletion in tumoural prostates resulted in a cell population shift, characterised by a reduction of basal cells and an increase of luminal, mimicking the distribution observed in non tumoural prostates (Figure 38C). Thus, our data indicated that deletion of *Mettl1* in PCa mouse model has a therapeutic potential since tumoural cell composition of tumours lacking the methyltransferase resemble of non-tumoural tissue, indicating an impaired tumour aggressiveness.

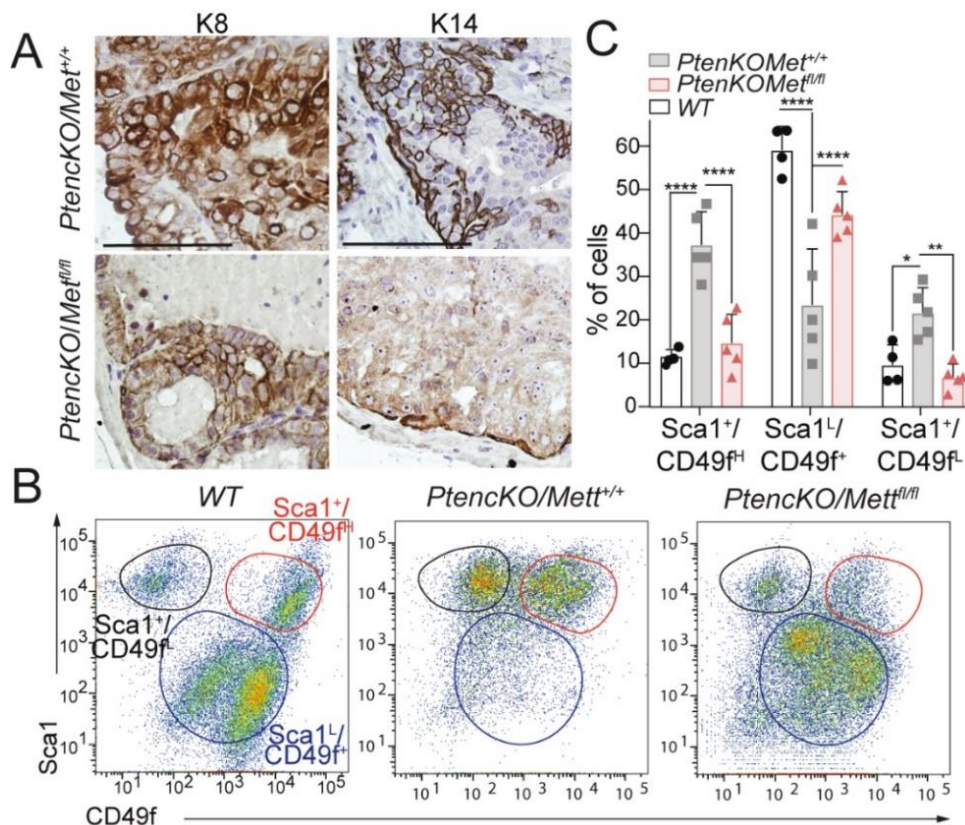


Figure 38. *Mettl1* regulates tumour cell survival in mouse PCa. **A**) Representative images of immunohistochemistry staining of luminal (K8) and basal (K14) markers in $PtenKO/Mettl1^{+/+}$ and $PtenKO/Mettl1^{fl/fl}$ mouse model. Scale bar represents 50 μ m. **B, C**) Separation (**B**) and quantification (**C**) of the distinct cells populations from healthy (WT), and *PtenKO* expressing (*Mettl1^{+/+}*) or *Mettl1*-depleted (*Mettl1^{fl/fl}*) prostates. Cells populations were separating according to distinct surface markers: luminal ($Sca1^L/CD49f^+$), basal ($Sca1^+/CD49f^H$) and stromal ($Sca1^+/CD49f^L$). Graph represents mean \pm SD (n=5). Statistical analysis: Two-way ANOVA (**C**) and Mann-Whitney (**D**). * $p < 0.05$; ** $p < 0.01$; **** $p < 0.0001$.

5.3. METTL1 regulates chemotherapy response *in vivo*

Since deletion of *Mettl1* in mouse prostates resulted in activation of stress pathways and increased genotoxic stress in a similar manner as observed *in vitro*, we next evaluated whether its loss could also affect to chemotherapy response.

Due to shorter generation times compared to mice, xenografts were produced in nude mice by subcutaneous injection of PC3 WT or *METTL1* KO cells followed by chemotherapy treatment once the tumour was formed. Treatment with the microtubule assembly inhibitor Docetaxel impaired proliferation of wild type tumours, meanwhile tumours lacking *METTL1* not only exhibited a decreased proliferation but also significant size reduction, which suggests that cell death is so enhanced that leads to a decrease of tumour size (Figure 39A). Molecular characterisation of the tumours by immunohistochemistry revealed that both WT and *METTL1*-depleted tumours showed a significant reduction of proliferative cells (Ki67⁺) when compared with non-treated conditions (Figure 39B,C). Moreover, this effect was exacerbated in *METTL1* KO xenografts, where the decrease of proliferative cells upon Docetaxel treatment was even higher than in tumours derived from WT cells. Similar effect was observed when analysing apoptotic cells by cleaved-Caspase 3 staining, since increased cell death was detected in both types of tumours after Docetaxel treatment, but the apoptosis in *METTL1* KO tumours treated was remarkably heightened when compared both to WT and non-treated tumours. In addition, accumulation of autophagosomes and increased DNA damaged was also observed (Figure 39B,C), being both markers enhanced upon Docetaxel treatment. Remarkably, an important increase of DNA damage was detected in WT xenografts after treatment, pointing that the mechanism by which Docetaxel impairs tumour growth in PCa is through inducing DNA damage. Depletion of *METTL1* also rose this genotoxic stress induction. Thus, Docetaxel treatment exacerbated the stress activation observed in normal conditions, which lead to an increased sensitivity to the treatment.

We also analysed the effect of Etoposide, a DNA damage inducing agent that showed promising results *in vitro* conditions. Etoposide treatment had little effect in *METTL1* expressing tumours, but considerably reduced *METTL1* KO tumour growth (Figure 39A), which was reflected in quantification of Ki67⁺ cells (Figure 39B,C). However, the effect was more modest when compared to Docetaxel treatment. Curiously, the DNA damaged produced upon Etoposide treatment was remarkably enhanced in *METTL1* expressing tumours but not in the absence of the enzyme when compared to non-treated conditions. This, together with the particularly increased apoptosis induction in *METTL1* KO tumours after treatment, suggests that, due to the increased genotoxic stress observed upon *METTL1* depletion, further induction of DNA damage directly resulted in cell death.

In conclusion, our results indicate that METTL1 play a crucial role in tumour survival, performing a protective role against stress and chemotherapy agents and regulation cancer cell survival. Thus, an

inhibition of the methyltransferase activity of METTL1 combined with traditional chemotherapy arises as a promising therapeutic approach, especially on those patients resistant to traditional therapy and with limited treatment options.

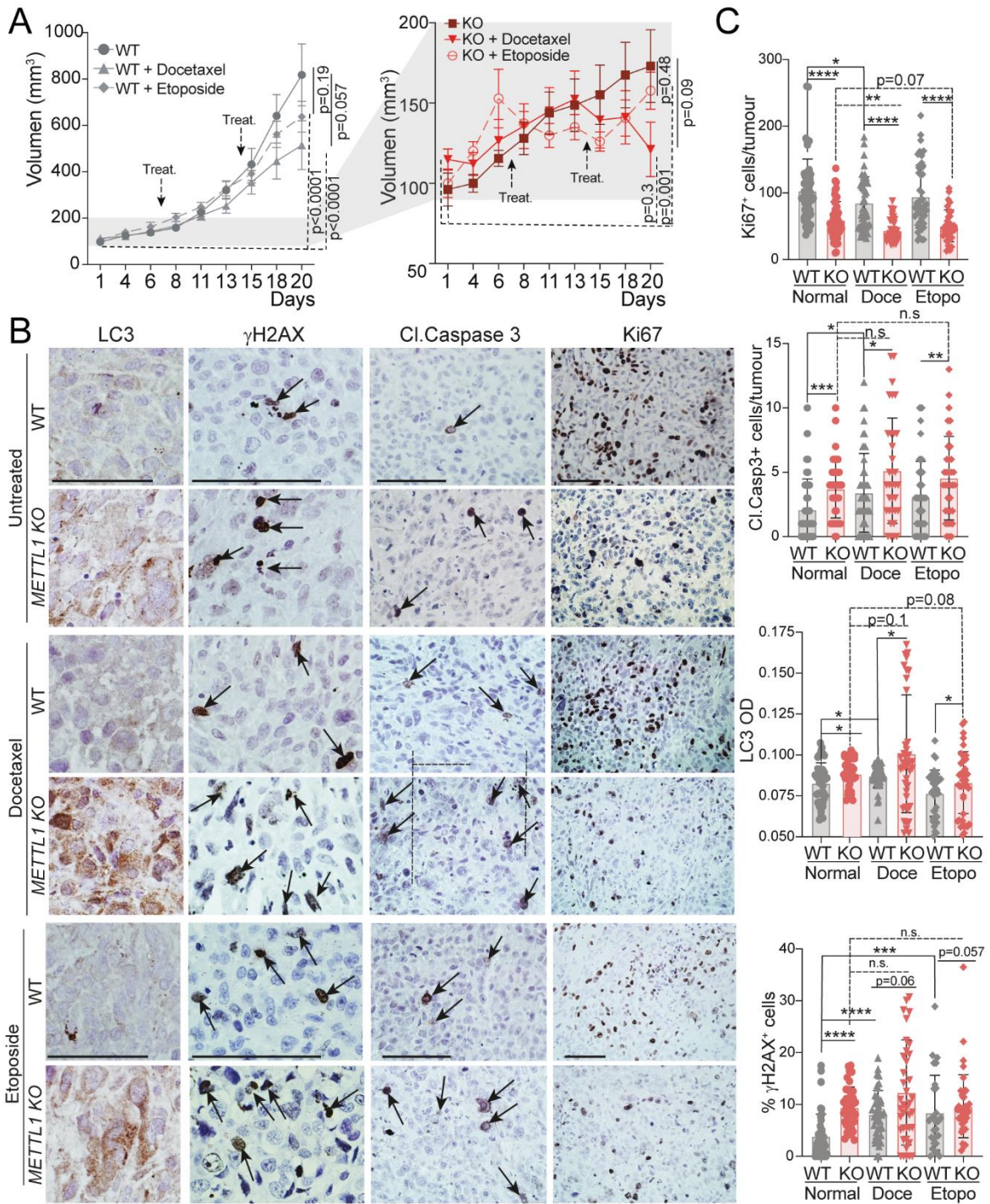


Figure 39. Depletion of METTL1 increases sensitivity to chemotherapeutic agents *in vivo*. **A, B** Tumour volume of xenografts from PC3 WT (**A**) and *METTL1* KO (**B**) subcutaneously injected in nude mice untreated (WT or KO) or treated either with 15 mg/kg (+Docetaxel) or 20 mg/kg Etoposide (+Etoposide) weekly. Arrows indicated days of treatment. Non-treated animals were administered with drugs vehicle. Mean± SEM are represented (n=10). **B**) Representative immunohistochemistry images of autophagy (LC3), DNA damage (γH2AX), apoptosis (cleaved-Caspase 3) and proliferation (Ki67) markers in PC3 WT and *METTL1*-depleted xenografts. Arrows indicate positive cells. **C**) Quantification of positive or % of positive cells (γH2AX) per tumour in immunohistochemistry stainings. Mean± SD are represented (n=5 mice, 10 pictures per mice). Scale bars represents 50 μm. Statistical analysis: 2-way ANOVA (**A**), One-way Mann-Whitney test (**C**), n.s.: non-significant; *p<0.05, **p<0.01, ***p<0.001, ****p<0.0001.

6. Generation of organoids from a Patient-derived xenograft model depleted for *METTL1* expression

Based on the promising results obtained both *in vitro* and *in vivo* regarding reduced tumour progression in absence of *METTL1*, we then interrogated whether the same effect would be recapitulated in a human pre-clinical model. With that aim, *METTL1* silencing in the prostate cancer xenograft LAPC9 model was performed in collaboration with Dr. Marianna Kruihof-de Julio's lab.

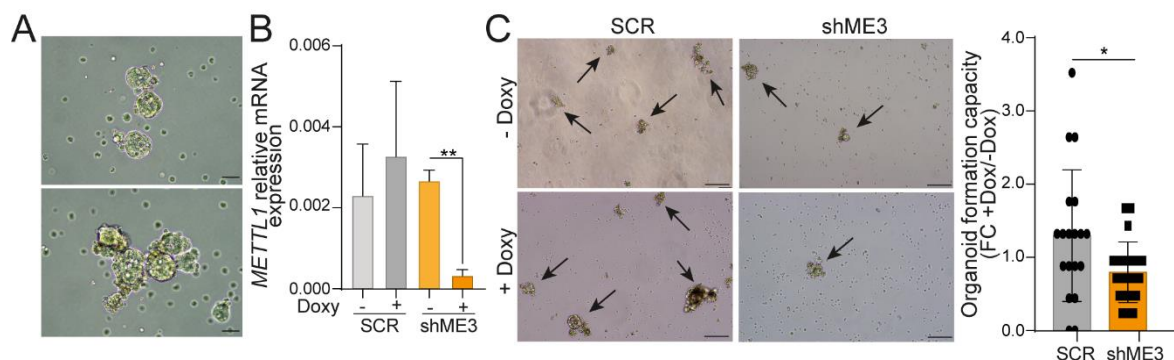


Figure 40. Evaluation of the proliferative effect of *METTL1* silencing in prostate cancer PDX-derived organoid model. **A)** Organoid derivation from the PDXs model LAPC9. Scale bar represents 50 μ m. **B)** Quantification by RT-qPCR of *METTL1*-silencing after 3 days of induction with 0.5 μ g/ml of doxycycline. Mean \pm SD are represented (n=3 technical replicates). **C)** Viability assay of organoids derived from LAPC9 PDXs by measurement of ATP release (luminescence values). Fold change of induced versus non induced conditions are shown. Mean \pm SD is represented (n=4 technical replicates per condition). **D)** Representative images and quantification of organoid formation capacity by manual count of number of organoids obtained by condition after 3 days of doxycycline induction (0.5 μ g/ml). Right panel represents mean \pm SD (n=3 replicates; 8 pictures per condition). Statistics analysis: One-tailed Student's t-test (A-C). *p<0.05;**p<0.01.

LAPC9 is an established AR-independent xenograft model derived from bone metastasis widely used for the generation of three-dimensional and multicellular prostate cancer models^{101,103}. Human organoids were derived from mice-xenografted tissue derived from patients by one week of growth in PCa organoid medium (Figure 40A). We next performed lentivirus infection for stable expression of a doxycycline-inducible plasmid codifying for either a control (SCR) or shRNA targeting *METTL1* (shME3) as previously described in single-cell dissociated organoids. Next, selection for five days was performed. During this time, cells aggregated to form organoids. During organoid formation, cells were induced for three days with 0.5 μ g/ml of doxycycline, after which a significant *METTL1* knockdown expression was observed by RT-qPCR (Figure 40B). To analyse whether the lack of *METTL1* affects organoid formation capacity, manual quantification of the number of organoids bigger than 10 μ m of diameter was performed. Reduced organoid formation capacity was observed upon *METTL1* silencing induction in comparison with the control condition (Figure 40C), which corroborates the essential role of *METTL1* PCa tumourigenesis. Although further investigation is required, *METTL1* arises as an attractive target for prostate cancer therapy. Evaluation of PDX-derived organoid response to chemotherapeutic agents such as Docetaxel or Etoposide, would be crucial to validate the increased sensitivity to these treatments observed both *in vitro* and *in vivo* in a human preclinical model, allowing to faithfully predict patient response to combinatorial treatments. Thus, the generation of a *METTL1*-depleted PDXs model is a powerful

tool that would make possible a detailed and reliable analysis of the expected effect of METTL1 function alteration in the clinic in a more accurate manner than *in vitro* experiments and bypassing the limitations of mouse models.

DISCUSSION



DISCUSSION

Prostate Cancer is the second most diagnosed cancer in men worldwide, which translated in numbers means that approximately 1,3 million new cases are diagnosed every year. Due to the fact that around 10 million men are currently living with a diagnose of prostate cancer^{1,322} and require a treatment or surgical intervention for the condition, PCa entails a major health issue worldwide. During the last years, distinct PSA screening programmes have been established in developed countries improving early detection strategies³²³. This, together with the advancement of treatments for localised disease, as radiotherapy and androgen deprivation therapy, have resulted in a significant reduction of the mortality^{2,324}. However, around 20-40% of the patients will develop recurrence and may progress to more advanced stages of the disease such as mCRPC, characterised by a poor prognosis since the 5-year survival rate does not exceed 30%³²⁵. Thus, metastatic prostate cancer is the cause of over 400.000 annual deaths worldwide, being the limited treatment options the major reason for the low survival rates of the metastatic disease^{323,325}. One of the main challenges to face when dealing with mCRPC is the significant intratumour heterogeneity, which hampers the search of a suitable treatment and reliable prognostic markers that help to stratify the disease. Thus, there is an urgent need to develop new biomarkers of the distinct stages of the pathology as well as identify new potential targets that expand the therapeutic options of these patients, eventually improving their prognosis.

In the last decade, a rising interest is emerging in the study of the role of RNA modifications in distinct diseases, including cancer. A growing body of evidence has uncovered the tight connection between epitranscriptome dysregulation and the initiation and promotion of tumourigenesis in several types of tumours¹⁰⁴⁻¹⁰⁶. In consequence, a great effort is being made in deciphering the molecular insights that turn RNA modifications into cancer regulators. In the present study we interrogate the epitranscriptome of PCa with the aim of identifying new targetable biomarkers that broaden the therapeutic options for mCRPC patients. By analysing distinct PCa expression databases, we identify the tRNA methyltransferase *METTL1* as the most commonly altered RMP in PCa. Due to their function in protein synthesis regulation, tRNA modifications are emerging as key players in cancer development and progression, yet the underlying molecular mechanisms are still poorly understood¹⁰⁴. In the last years, several studies have associated overexpression of *METTL1* with the development and progression of a wide variety of tumours such as sarcoma, lung, liver colon, gastric, bladder cancer, and glioma^{211,219-221,224-228,268,326}. However, although *METTL1* oncogenic role has been reported in distinct cancer types, its connection with PCa pathogenesis has not yet been described. This study identifies *METTL1* as a potential prognostic marker for PCa evolution, since its expression increases with disease progression, being highest in advanced metastatic tumours. In addition, a significant correlation between increased *METTL1* levels and

reduced DFS is observed, which boosts its prognostic value and poses it as a potential therapeutical target.

The availability of reliable mouse models that mimic patient conditions is often one of the main limitations of translating clinical conditions to basic research. However, our data prove that the widely used *Pten*KO PCa mouse model recapitulates the increased methyltransferase and m⁷G-tRNA associated levels upon disease progression. This demonstrates its validity for studying the role of the methyltransferase in the pathology evolution. Moreover, it has been known for years that m⁷G modification is not metabolised and increased modified nucleosides can be detected in blood or urine of tumour-bearing rodents and cancer patients^{327,328}. By Northern blot of non-treated nor processed urine samples from *Pten*WT and KO mice, we successfully detect excreted m⁷G-modified nucleosides in both mice genotypes, with significant enhanced methylation in urine from tumour bearing-mice as consequence of *METTL1* overexpression. Thus, we not only demonstrate that increase *METTL1* levels results in increase excretion of modified nucleosides, but we also propose a potential non-invasive diagnostic method that would allow identification of advanced PCa using liquid biopsies in a rapid and economic manner that would result in an increase of patients' welfare. The importance of this kind of discoveries relies in that, for years, the principal biomarker used for PCa diagnosis as well and monitorisation of treatment response is the quantification of prostate specific antigen (PSA) on blood. However, it has been widely proved that PSA present several limitations. The appearance of false positives or negatives are not rare, and higher PSA levels can be detected in both PCa and the initial states of benign prostatic hyperplasia, which may lead to unnecessary treatment or overdiagnosis with the associated side effects³²³. For all these reasons, the discovery of novel biomarkers that expand the data collected by established biomarkers as PSA is essential. Therefore, detection of methylation levels in addition to PSA standardised classification would help to rapidly detect more aggressive forms of PCa.

In line with previous findings in distinct cancer types, we identify *METTL1* as an overexpressed gene on PCa, however the mechanism underlying this higher expression remains unknown. In consequence, we interrogate the correlation between *METTL1* expression and some of the most common alterations in PCa such as AR and PTEN-PI3K pathways. Although no consistent correlation is detected between AR-transcriptional substrate *KLK3* and *METTL1* in all data sets analysed, we find that *METTL1* expression is regulated by PI3K pathway effectors, probably downstream AKT. Thus, here we provide evidence of the regulation of tRNA methylation downstream of PI3K pathway through the control of *METTL1*. In addition, our data uncovers a new downstream effector of one of the most commonly altered pathways in advanced prostate cancer. In fact, we demonstrate that increased *METTL1* levels together with *PTEN* loss is associated with worse prognosis, which facilitates patient stratification essential for the design of specialised and target therapies to improve patient prognosis. Previous studies in embryonic stem cells have reported that

METTL1 expression is dependent of AKT and ribosomal S6 kinase³²⁹, in agreement with our data. *METTL1* pro-tumorigenic capacity has been also associated with *PTEN* suppression in hepatocellular carcinoma and an AKT-mTOR signalling pathway activation through *METTL1* positive feedback loop was observed in lung adenocarcinoma cell lines²⁶⁸. Altogether, these data indicate a complex regulatory scenario of *METTL1* expression dependent of one of the most studied pathways in health and disease, integrating the regulation of essential biological processes as proliferation with epitranscriptomic programmes, which highlights once more the importance of the epitranscriptome in cell homeostasis.

One of the main limitations of studying RNA modifications is the lack of sensitive and reproducible detection methods. The gold standard for quantitative detection of distinct modifications is chromatography with tandem mass spectrometry (LC-MS/MS), but its requirement of high quality and amount of starting material, complex sample processing steps, advanced and expensive equipment and trained personal limit the technique application³³⁰. Here, we use Northdot blot as a fast, accurate and low-cost method for quantitative detection of m⁷G-modification in both cell and tissue tRNA samples. This method stands out for the possibility of directly use low amounts of biological samples, with no need of further treatment nor use of expensive and complex equipment, which could be translated into rapid and easy development of diagnostic kits. In addition, we propose Bo-seq for identification of m⁷G deposition at single nucleotide resolution, by which around of 50% of the tRNAs isoacceptors are identified to exhibit *METTL1*-mediated m⁷G modification at position 46 at the variable loop, corroborating recent reports^{210,212,219,220,224}. The high proportion of false positives is the major limitation of all single-nucleotide resolution detection techniques, since the harsh environment in which NaBH₄ reaction is produced results in significant background signal due to RNA degradation. Distinct approaches have been developed to overcome this issue. MeRIP-seq is based in the use of antibodies that specifically recognise the internal methylation for modified RNA enrichment, meanwhile TRAC-seq exploits de demethylase activity of AlkB enzyme to remove the also NaBH₄-reactive m³C modification²¹⁸. Meanwhile m⁷G-MaP-seq analyses the mutational rates instead of the reverse transcription termination in order to overcome the background produced by random RNA fragmentation²¹³. However, the addition of the extra steps necessary for each of the techniques translates in the need of higher amount of starting material and the development of high-cost and time-consuming techniques. Thereby, here we propose a simpler technique that, similar to AlkAniline-seq²¹⁷, is based in the use of T4 PNK treatment for m⁷G-modified RNAs enrichment. Though, the previous tRNA enrichment together with a single-end sequencing with a threshold of 15 million reads per sample emerges as a variation of AlkAniline-seq that allows reliable and precise identification of m⁷G deposition sites at single nucleotide resolution.

By immunohistochemistry staining and evaluation of gene expression within the distinct prostatic cell populations, this study demonstrates that *Mettl1* is mainly expressed in the luminal compartment

in both healthy and tumour-bearing mice, being overexpressed upon oncogenic transformation. Growing body of evidence designate luminal cells as the preferred cell-of-origin of PCa^{11-13,18,21}, which indicates that *Mettl1* is predominantly expressed in PCa tumour-initiating cells. This suggests that *Mettl1* may play an important role in regulating PCa tumourigenesis. In fact, we find that deletion of *METTL1* significantly suppresses cancer cell growth, cell division and spheroid formation capacity *in vitro*. Moreover, by generation of xenografts with cells with complete or partial depletion of *METTL1* expression, we prove that the methyltransferase is essential both for tumour initiation and proliferation. Besides, we demonstrate that proliferation and spheroid formation capacity are rescued after overexpressing a catalytic active version of *METTL1*, indicating that *METTL1*-mediated RNA methylation has tumourigenic potential. Thus, in line with previous studies^{219,220,224,225,228,268}, our data supports *METTL1* oncogenic role via its function as tRNA methyltransferase.

Interestingly, this phenotype is recapitulated in the PCa mouse model with specific deletion of *Mettl1* in the prostatic epithelium generated in this study by crossing homozygous *Mettl1*-floxed mice with the previously established *Pten*KO PCa mouse model⁷⁹. Since *Mettl1* has been previously reported to be essential for correct mESCs differentiation²¹⁰, the viability of the model resides in that deletion of both *Pten* and *Mettl1* occurs after mice puberty (7 weeks), by inducing Cre expression under *Probasin* gene promoter. Remarkably, we prove that the obtained model faithfully recapitulates the *in vitro* characteristics by exhibiting significant reduction of *Mettl1* and m⁷G-associated levels. Thereby, we establish a pre-clinical *in vivo* model able to reproduce the molecular features of *METTL1* deletion in human cell lines, corroborating its suitability for unravelling the role of the methyltransferase on a complex system. In addition, our data unveils that deletion of *Mettl1* in prostatic tumours result in a significant reduction of tumour volume and weight of all three prostatic lobes with less aggressive characteristics as immunohistochemistry analysis reflects. Reduced proliferation and increased apoptosis are also observed in *Mettl1*-deficient tumours, corroborating the pro-tumoural role of the methyltransferase. In fact, our data demonstrate that *Mettl1* depletion in prostate tumours results in a switch of the cell populations that comprise the tumour to a composition that resemble healthy prostates, indicating such an essential role in tumourigenesis that its loss leads to a total tumour remodelling.

Mechanistically, our data demonstrate that lack of m⁷G-tRNA due to *METTL1* deletion does not alter the pull of mature tRNAs in PCa cells as in other tumour/tissue contexts^{219,221,224,231}. Our study unveils that *METTL1*-mediated m⁷G deposition protects tRNAs from endonucleolytic cleavage, resulting in accumulation of tRNA-derived fragments when absent. More interestingly, we discover that the most abundant tRNA-fragments identified in *METTL1*-deficient cells are those derived from Cys tRNA, characterised by presenting an oligoguanine sequence at their 5' end by which are called 5'TOGs. Moreover, here we unveil increased fragmentation under stress conditions. tRNA fragmentation can

be produced as a response to distinct stimuli including stress, and RNA modifications have been widely proved to play an essential role in their biogenesis¹⁵⁶. For example, the m⁵C tRNA methyltransferase NSUN2 has been described to regulate 5'tRNA fragments formation that repress protein translation and trigger stress signals and proteostatic stress^{162,189}. Due to its stressful nature, cancer is strongly associated with tRNA fragmentation³³¹ and a high diversity of tRFs have been described in PCa^{332,333}. For years, it was thought that tRFs were mere products from tRNA decay, however growing evidence is highlighting their biological relevance in regulating several essential processes¹⁵⁶. As so, 5'TOG have been described to repress cap-dependent translation by displacing translation initiation factors from mRNA and produce a global repression of protein synthesis as well as favour cap-independent translation^{131,166,308}. The functional implications of tRNAs fragments in cellular processes regulation and cancer development are now beginning to be elucidated¹⁵⁶. Thus, our data reveals that in PCa *METTL1*-deficient cells, 5'TOGs repress global translation rates by displacing the translation initiation factors from the mature mRNA. Interestingly, our data shows that partial *METTL1* silencing also produces a significant protein synthesis inhibition, indicating that its effect is so evident that is observable even with residual expression of the enzyme. Moreover, we demonstrated that 5'TOG accumulation specifically represses the translation of genes involved in tumourigenesis and tumour progression as well as induces the synthesis of proteins involved in stress responses. In addition, we find no differences in neither eIF2 α phosphorylation nor UPR activation, which indicates that differential translation is not mediated by any of these mechanisms. Although translation initiation defects independent of eIF2 α through *METTL1* inhibition has been described in liver cancer cells²²⁰, *METTL1*-mediated tRNA fragmentation has not been previously described^{219,221,222,224,231,233}. In contrast, the molecular insights of *METTL1* oncogenic roles have been associated to a reduced translation efficiency of those transcripts with higher dependency on m⁷G tRNA codons. Thereby, here we demonstrate a novel translational regulation through 5'TOGs tRNA fragments biogenesis mediated by *METTL1*-m⁷G tRNA methylation, that specifically regulates the translation of pro-survival and proliferation genes. Moreover, the common target region and action mechanism of *METTL1* and NSUN2 suggests that the variable loop may be essential for regulating tRNA-fragment biogenesis that coordinate stress responses^{162,334}. More interestingly, accumulation of tRNA-derived fragments is also observed in our *Pten*KO/*Mettl1*^{fllox} mouse model, which not only corroborates the reliability of the murine model but supports the molecular mechanism underlying the decreased tumourigenesis observed both *in vitro* and *in vivo*.

Due to its fundamental biological base, protein synthesis rate and translational programmes are highly regulated processes, and homeostasis alteration is often associated with triggering of stress responses. Here we show that *METTL1* depletion results in accumulation of protein aggregates in the cytoplasm of the cells due to an alteration in the autophagy pathway. Autophagy is the main catabolic mechanism by which the cell degrades and recycle damaged organelles and molecules, and

its dysregulation is associated with stressful states²⁵⁴. Thus, here we prove that the accumulation of autophagosomes observed in *METTL1*-depleted cells is caused by dysregulation of autophagosome-lysosome fusion and, in consequence, of the autophagy termination. To support this, we find that induction of autophagy by the mTOR inhibitor Rapamycin significantly reduce proliferation of cells depleted for *METTL1*. Moreover, our data elucidates that inhibition of autophagy induction actually increases survival capacity of *METTL1* KO cells, indicating that the accumulation of autophagosomes is a stressful event that impairs cell proliferation and survival. Although previous studies identified autophagy induction upon *METTL1* downregulation, the reduced translation efficiency of negative regulators of autophagy²²¹ or a METTL1-mediated AKT/mTORC1 pathway activation²⁶⁸ were described as the underlying cause. However, no protein changes nor phosphorylation differences of autophagy inhibitors are detected in our study, which suggest that the mechanism that drives autophagy dysregulation is different in prostate cancer compared to oesophageal cell carcinoma and lung cancer cells. In contrast, we find an increased translation efficiency of ATG3. ATG3 is one of the components of the second ubiquitin-like system that regulates the autophagosome formation by participating in the conjugation of LC3B-I to PE for complete maturation of LC3B-II, which then is integrated in the growing autophagosome²⁴⁶. Increased levels of ATG3 have been described to produce increased autophagic flux³³⁵, which may imply that part of the autophagosome accumulation produced by the dysregulation of the autolysosome formation could be cause by this increase in ATG3. However, no experimental validation has been performed

In addition, our study reveals that this blockade of autophagy termination results in a dysregulation of redox homeostasis within cells lacking *METTL1*, which is also associated with increased genotoxic stress. In consequence, cells exhibit increased sensitivity to cytotoxic stress conditions and chemotherapeutic agents such as Docetaxel or Etoposide *in vitro*, in a methyltransferase-dependent manner, which indicates the relevance of the methylation in response to distinct stress. Remarkably, the reduced response capacity to environmental stress that cells exhibit in the absence of METTL1 opens the door to a new possibility of combining traditional chemotherapeutic agents with inhibition of METTL1 activity, which would increase the sensitivity of the tumours to the treatment. These results are in line with previous reports, where *METTL1* inhibition has been associated with increased chemosensitivity^{219-221,224-226,228,229,231,233,268}, however no molecular explanation of this effect is reported.

The same effect is observed in *Mettl1*-depleted prostates from tumour-bearing mice, which exhibit increased DNA damage and alteration of autophagic flux upon *Mettl1* deletion, suggesting an enhanced sensitivity to stress responses as observed *in vitro*. By generating xenografts of edited PCa cell lines, we demonstrate that tumours depleted for *METTL1* exhibited reduced proliferation capacity but, especially, an exacerbated cell death upon Docetaxel and Etoposide treatment that

resulted in even a decreased in tumour size. Thus, our data highlights that *METTL1* depletion sensitises PCa tumours to external stress signals such as chemotherapy agents.

Lastly, here we present a human pre-clinical model by generation of Patient Derived Xenografts organoids, which are widely used for evaluation of therapeutic potential of distinct drugs due to their ability to resemble tumour structure with distinct cell populations. In this study we successfully generate *METTL1*-downregulated organoids that exhibit impaired viability and organoid formation capacity than its *METTL1*-expressing counterparts. These results recapitulate *METTL1*-tumourigenic regulative potential, which turn the organoids in a potent tool for drug screening evaluation combined with *METTL1*-silencing. Their multi-cellular composition together with the human origin and reduced generation time compared to mouse model, make them a reliable model that could predict the clinical outcome of distinct treatments.

In summary, our study provides strong evidence supporting the oncogenic function of *METTL1* and m^7G tRNA modification in PCa. In addition, we uncover a novel layer of gene expression regulation and selective translation control mediated by m^7G -dependent tRNA fragments in PCa cells. In consequence, *METTL1*-deficient cells are more sensitive to stress stimuli and exhibit disturbed redox balance and increased DNA damage. *METTL1* inhibition results in impaired tumour progression and increased sensitivity to chemotherapeutic agents. Our discoveries may open new directions for creating treatment techniques, since transfection of exogenous 5'TOG into *METTL1*-expressing cells successfully recapitulates *METTL1*-depletion phenotypes. Thus, the 5'TOG dependency of the cytotoxic effect on prostate rise its potential as therapeutic agents. The delivery of short synthetic oligonucleotides into *METTL1*-overexpressing tumours arise as an attractive strategy to increase tumour sensitivity to traditional therapy and, in consequence, impair disease progression, appearance of recurrences and resistances and broaden the therapeutic options of patients with mCRPC. Besides, the short lifespan of RNA oligonucleotides would reduce the possible side effects that often accompany cancer treatments, significantly improving patients's welfare.

Another interesting approach would be to specifically inhibit *METTL1* methyltransferase activity, since we have broadly proved that it is the underlying cause of the phenotypes observed both *in vitro* and *in vivo*. Although no inhibitor of *METTL1* activity has been yet established, a specific inhibitor of the m^6A -mRNA methyltransferase *METTL3* has been recently developed³³⁶. This molecule has been demonstrated to effectively reduce Acute Myeloid Leukaemia (AML) growth and increase differentiation and apoptosis, arising as a potential therapeutic strategy against AML. Due to the high homology between proteins from *METTL* family, the development of *METTL1* inhibitor represents a viable and promising opportunity for anticancer therapy by targeting the epitranscriptome.

CONCLUSIONS



CONCLUSIONS

Taken together, our findings highlight the dependence of prostate tumours progression and survival on abnormal tRNA methylation. This work contributes to understand the mechanism underlying tRNA processing in tumoural cells as well as their connection with stress response mechanisms and arises tRNA methyltransferases as potential therapeutic targets.

Thus, the data obtained during this PhD thesis research leads to the following conclusions:

- I. The tRNA-methyltransferase *METTL1* is overexpressed in PCa, specially in metastatic tumours, and its upregulation is correlated with poor patient prognosis.
- II. *METTL1* upregulation in PCa is dependent on *PTEN* overexpression, being its transcription regulated by the PI3K pathway downstream AKT.
- III. *METTL1* preferentially methylates tRNAs at 7-guanosine located at position 46, targeting the variable loop of approximately 50% of the tRNAs isoacceptors.
- IV. Loss of *METTL1*-dependent m⁷G mark does not affect mature tRNAs pool but enhances tRNA-derived fragment formation, particularly biogenesis of 18-35 nt long-5'TOG fragments.
- V. Accumulation of 5'TOG fragments simultaneously alters normal translational programme and inhibits global protein synthesis by displacement of translation initiation complex factors from the actively translated mRNAs.
- VI. *METTL1*-depletion results in impaired proliferation and self-renewal capacity of PCa cells *in vitro* and *in vivo* in a methyltransferase-dependent manner.
- VII. Exogenous incorporation of 5'TOG recapitulates the phenotype observed upon *METTL1* deletion.
- VIII. *METTL1* is mainly expressed in prostatic luminal cells and its depletion results in a reduced tumour proliferation and in a remodelling of tumour cell populations into a non-tumoural-like composition.
- IX. *METTL1*-dependent m⁷G tRNA modification is essential for correct autophagy termination and its loss results in accumulation of protein aggregates, ROS and DNA damage that ultimately leads to increase sensitivity to stress conditions and traditional PCa treatments both *in vitro* and *in vivo*.

GRAPHICAL SUMMARY

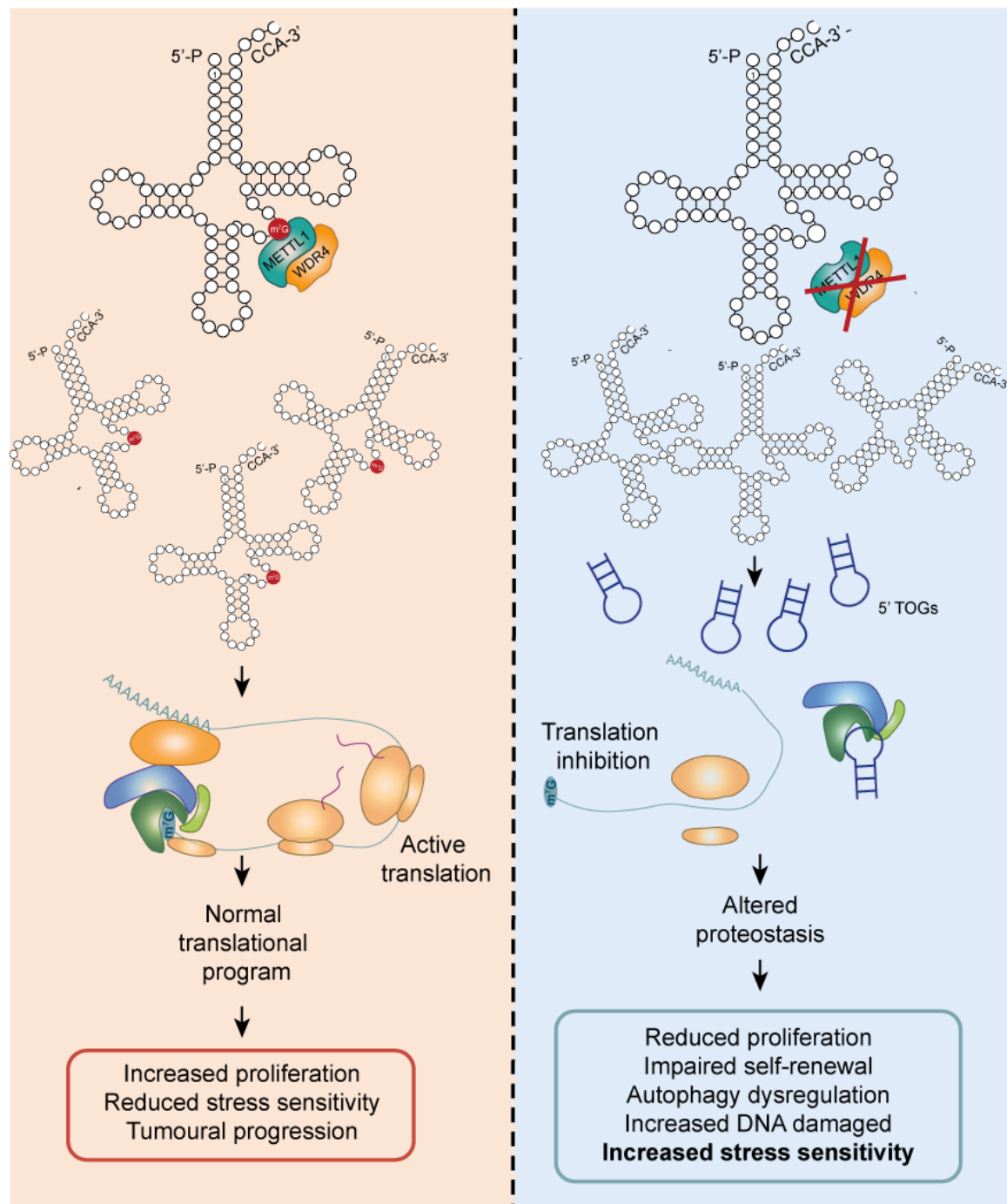


Figure 41. Schematic representation of the molecular mechanism identified in PCa cell lines after *METTL1* depletion- In normal conditions, prostate tumours present overexpression of *METTL1* which results in high methylation of those tRNAs substrate of the enzyme. In this situation, tumours are characterised by elevated proliferation and high capacity to respond to stress situations such as chemotherapy agents, which leads to increase tumour survival and development of therapy resistance. Conversely, depletion or inhibition of *METTL1* results in loss of m⁷G mark on tRNAs, which results in tRNA fragmentation. In consequence, accumulated 30-40 nt 5' TOGs bind to translation initiation complex factors and produce their displacement from actively translated mRNAs, which leads to global translation inhibition and alteration of the translational programme. As a result, cells exhibit reduced translation of cell cycle and proliferation-related proteins and enhanced translation of those involved in stress-response pathways. This, together with a dysregulation of the autophagic pathway, results in an accumulation of protein aggregates and ROS, which in turns leads to increase DNA damage, which hypersensitise PCa cells to any stress condition such as chemotherapeutic agents.

MATERIAL AND METHODS



MATERIALS AND METHODS

1. Common laboratory solutions

For the preparation of all buffers, water purified with Milli-Q reagent Grade Water Ultrafiltration System (Millipore) was used. Composition of the buffers comes as follows:

1x PBS (PBS)	2.68 mM KCl, 1.47 mM KH ₂ PO ₄ , 137 mM NaCl, 7.98 mM Na ₂ HPO ₄
1x PBS-T	1x PBS + 0.05% (v/v) Tween-20 (Panreac Applichem, A4974,0500)
20x TBS	0.5 M Tris, 1 M NaCl, 0.05 M KCl, pH =8.0
1x TBS-T	1x TBS + 0.1% (v/v) Tween-20 (Panreac Applichem, A4974,0500)
50x TAE	2M Tris, 0.05 M EDTA, pH=8.0
10x TBE	0.9 M Tris, 0.9 M H ₃ BO ₃ , 0.02 N EDTA, pH=8.3
LB	0.5% Yeast extract, 1% tryptone, 1% NaCl
Agar LB	LB + 2% agar
ECL	0.1 M Tris-HCl pH8.5, 0.2 mM coumaric acid, 1.25 mM Luminol
10x SDS-PAGE	0.25M Tris, 2M glycine, 0.5% SDS
10x Transfer buffer	0.25M Tris, 1.92M glycine
20x SSC	0.3M sodium citrate, 3M NaCl, pH 7
Lower Tris	1.5M Tris-HCl pH8.8, 14mM SDS
Upper Tris	0.5M Tris-HCl pH 6.8, 14mM SDS
Stacking gel	5% polyacrylamide, 0.06 M Tris-HCl pH 6.8, 0.1% SDS, 0.1% Ammonium persulfate (APS), 0.01% TEMED
Resolving gel	8-12% polyacrylamide, 375 mM Tris-HCl pH 8.8, 0.1% SDS, 0.12% APS, 0.012% TEMED

2. Cloning and site directed mutagenesis

For the generation of CRISPR/Cas9 cell lines, three different single-guide RNAs (sgRNAs) targeting exon 2 and 3 of human *METTL1* were designed using crispor software (<http://crispor.tefor.net/>): sg117-5'-TATGTCTGCAAACCTCCACTTGGG-3'; sg119-5' TACGGAGACAGGCGATGTTCTGG-3' and sg139-5'- CAAGTGGAGTTTGCAGACATAGG-3'. All three sgRNAs were separately cloned in the lentiviral expressing vector lentiCRISPR-v2 (Addgene, 83480).

For generation of cells stably expressing inducible shRNA for human *METTL1*, shRNA sequences obtained from Sigma Human Mission shRNA library were cloned into the doxycycline-inducible

pLKO.1-TetON-blasti vector (shMETTL1-3 (cat number: NM_005371, clone ID: TRCN0000331664) and sh METTL1-4 (cat number: NM_005371, clone ID: TRCN0000035958). METTL1 HA-tagged protein was generated by cloning into the retroviral doxycycline-inducible pTRIPZ vector (Dharmacon)³³⁷ with the open reading frame (ORF) obtained from Source BioScience (clone: X96698; IMAGE clone: 36006). All the cloning and sequencing primers are indicated on Table 3.

METTL1 catalytic dead mutant was designed based on^{210,329} data. Briefly, the human complementary sequence to the mouse LFPD motif previously identified as the catalytic pocket was found by BLAST analysis. METTL1 mutagenesis was generated in the doxycycline-inducible pTRIPZ-HA-METTL1 plasmid. Sequence mutagenesis was performed using Q5 Site-Directed Mutagenesis Kit (NEB, E0554S) and the substitutions L160A (CTC/GCC) and D163A (GAC/GCC) using the primers specified at Table 3. After bacteria transformation and DNA purification, the plasmid was sequenced before further use with specific primers for METTL1 or the TRIPZ vector (Table 3).

Primer name	Purpose	Sequence (5'-3')
CRISPR_Fw	Sequencing primers for lentiCRISPRv2	CAGTTTTAAAATTATGTTTTAAAATGGAC
HA-METTL1-Fw	Cloning HA-METTL1 into pTRIPZ	CAGAGCTCGTTTAGTGAACCGTCAGATC GCACCGGTACCATGGCTTATCCTTACGAC GTGCCTGACTACGCCGGAAGCGGAATGG CAGCCGAGACTCGGAA
HA-METTL1-Rv	Cloning HA-METTL1 into pTRIPZ	AGGTCCAGGATTCTCCTCGACGTCACCG CATGTTAGCAGACTTCTCTGCCCCTC TCCGCTTCCGTGACCAGGCAGGCTG
hMETTL1-Fw	Sequencing primer for human METTL1	GCCATGAAGCACCTTCCTAAC
METTL1 gDNAseq_Fw	Genomic human METTL1 PCR amplification and sequencing	GTTCTTCGCTCCACTCACTC
METTL1 gDNAseq_Rv	Genomic human METTL1 PCR amplification and sequencing	CAAAAAGAGGGCCTGAGTGTT
METTL1_gDNA_Fw	CRISPR targeted region amplification	GTTCTTCGCTCCACTCACTC
METTL1_gDNA_Rv	CRISPR targeted region amplification	CAAAAAGAGGGCCTGAGTGTT
Mutage_METTL1_Rv	Mutagenesis METTL1	GAAGGCGAAGAACATCTTTGTCAGC
pLKO_seq_Fw	pLKO.1tetON sequencing	GGCAGGGATATTCACCATTATCGTTTCAG A

Primer name	Purpose	Sequence (5'-3')
pLKO_seq_Fw	pLKO.1tetON sequencing	GGCAGGGATATTCACCATTATCGTTT CAGA
pLKO_seq_Rv	pLKO.1tetON sequencing	CAAAGTGGATCTCTGCTGTCC
Sg117r_METTL1_Fw	sgRNA cloning into lentiCRISPRv2	CACCGTATGTCTGCAAACCTCCACTT
Sg117r_METTL1_Rv	sgRNA cloning into lentiCRISPRv2	AAACAAGTGGAGTTTGCAGACATAC
Sg119r_METTL1_Fw	sgRNA cloning into lentiCRISPRv2	CACCGTACGGAGACAGGCGATGTTC
Sg119r_METTL1_Rv	sgRNA cloning into lentiCRISPRv2	AAACGAACATCGCCTGTCTCCGTAC
Sg139f_METTL1_Fw	sgRNA cloning into lentiCRISPRv2	CACCGCAAGTGGAGTTTGCAGACAT
Sg139f_METTL1_Rv	sgRNA cloning into lentiCRISPRv2	AAACATGTCTGCAAACCTCCACTTGC
shMETTL1-1-Fw	shMETTL1 cloning in pLKO.teton	CCGGCCACATTTCAAGCGGACAAA CTCGAGTTTGTCCGCTTGAAATGTGG GTTTTG
shMETTL1-1-Rv	shMETTL1 cloning in pLKO.teton	AATTA AAAACCCACATTTCAAGCGG ACAACTCGAGTTTGTCCGCTTGAAA TGTGGG
shMETTL1-2-Fw	shMETTL1 cloning in pLKO.teton	CCGGGATGACCCAAAGGATAAGAAA CTCGAGTTTCTTATCCTTTGGGTCAT CTTTTTG
shMETTL1-2-Rv	shMETTL1 cloning in pLKO.teton	AATTA AAAAGATGACCCAAAGGATA AGAACTCGAGTTTCTTATCCTTTGG GTCATC
TOPO_M13_Fw	pTOPO vector screening	GTAAAACGACGGCCAG
TOPO_M13_Rv	pTOPO vector screening	CAGGAAACAGCTATGAC
TRIPZ-Fw	pTRIPZ sequencing	ACGTATGTCGAGGTAGGCGTGTAC
TRIPZ-Rv	pTRIPZ sequencing	ACGTATGTCGAGGTAGGCGTGTAC

Table 3. Primers used for the cloning and sequencing of the indicated human and plasmid sequences.

3. Cell culture procedures

3.1. Cell lines and culture conditions

Human prostate cancer cell lines PC3, VCap and DU145, human sarcoma cell line U2OS and the lentivirus productive line HEK293FT were cultured in Dulbecco's Modified Eagle Medium (DMEM) containing L-Glutamine and pyruvate (Gibco, 41966-029) supplemented with 10% Fetal bovine serum (FBS, 10270-196, Gibco) and 1% Penicillin/streptomycin (Gibco, 15140-122), herein after referred as DMEM medium. 22Rv1 and LNCaP were cultured in Roswell Park Memorial Institute (RPMI) with L-Glutamine and pyruvate (Gibco, 21875091) supplemented with 10% FBS

and 1% Penicillin/streptomycin. BPH1 cells were culture in Roswell Park Memorial Institute (RPMI) with 20% FBS, 20 ng/ml DHT (Sigma, D-073), 5 µg/ml transferrin (Sigma, T8158), 5 ng/ml sodium selenite (Sigma, 214485) and 5 µg/ml insulin (Sigma, 10516). PWR-1E and RWPE-1 were grown in Keratinocyte Serum Free Medium (K-SFM) (Gibco, 17005042) supplemented with 0.05 mg/ml Bovine Pituitary Extract (BPE) and 5 ng/ml Endothelial Growth Factor (EGF) (Supplements for K-SFM, Gibco, 37000-015). Cell passages were performed using 0.25% Trypsin-EDTA (Gibco, 25200-056) and PBS. LAPC9 cells were cultured in Advanced DMEM/F12 (ThermoFisher Scientific, 12634010) containing 10 mM Hepes (Thermo Fisher Scientific, 15630080), 2 mM GlutaMAX supplement (Thermo Fisher Scientific, 35050061), and 100 µg/ml Primocin (InVivoGen, ant-pm-1), referred from hereinafter as basis medium, supplemented with the following factors for organoid culture (PCa organoid medium): 10 µM Y-27632-HCl (Selleckchem, S1049), 5% fetal calf serum (Gibco #10270-106), 1× B-27 supplement (Thermo Fisher Scientific, 17504044), 10 mM Nicotinamide (Sigma, N0636), 500 ng/ml R-spondin1 (Peprotech, 120-38), 1.25 mM N-acetylcysteine (Sigma, A9165), 10 µM SB-202190 (Selleckchem, S1077), 100 ng/ml Noggin (Peprotech, 250-38), 500 nM A83-01 (Tocris, 2939), 10 nM DHT (Sigma, D-073-1ml), 10 ng/ml Wnt3a (Peprotech, 315-20), 50 ng/ml Hepatocyte growth factor (HGF, Peprotech, 100-39), 50 ng/ml EGF (Peprotech, AF-100-15), 10 ng/ml Fibroblast growth factor 10 (FGF10, Peprotech, 100-26), 1 ng/ml FGF2 (Peprotech, 100-18B), 1 µM prostaglandin E2 (PGE2, Tocris, 2296).

All cells were maintained at 37°C in a humidified atmosphere with 5% CO₂ and were monthly tested for mycoplasma by PCR and maintained mycoplasma-free. PC3, 22Rv, DU145 VCap, C4-2, 22Rv1, LNCap, BPH1, RWPE-1, PWR-1E and HEK293FT were kindly provided by Pr. A Carracedo (CIC-bioGUNE, Spain). U2OS-GFP-LC3 cell line was kindly provided by Dr. Raúl Durán (CABIMER, Spain). LAPC9 were kindly provided by Prof. Marianna Kruithof-de Julio (DBMR, University of Bern, Switzerland).

3.2. Lentivirus production and generation of stable cell lines

For lentiviral particle production, two 10 cm plates with 4x10⁶ productive HEK293FT cells were plated per every 10 cm plate of target cells. 6-8h after seeding, cells were transfected either with calcium phosphate or JetPEI (PolyPlus,101-40N) and with a mixture of 5 µg of the plasmid of interest, 1.6 µg of envelope vector (pVSV-G), 1.6 µg of packaging plasmid and 1.6 µg of Rev-expressing vector. For 2nd generation plasmids, pTAT and psPAX2 were used as packaging and Rev-expressing vectors respectively, meanwhile pRRE and pREV were transfected for 3rd generation plasmids (Table 4).

For transfection with calcium phosphate, DNA solution was prepared in 500 µL of 250 mM CaCl₂ and mixed while bubbling with an equal volume of 2x HEPES-buffer Saline (280 mM NaCl, 10 mM KCl, 1.5 mM Na₂HPO₄·2H₂O, 12 mM dextrose and 50 mM HEPES, pH 7.05). After incubating for

30 min at room temperature, the mixture was added dropwise to the cells. The following day, cell medium was changed to minimise cell death.

When transfecting with JetPEI, DNA mixture and 25 μ L of jetPEI were separately resuspended in 250 μ l of 150 mM NaCl. The jetPEI solution was then added to the DNA solution, mixed by vortexing and incubated for 30 minutes at room temperature. The mixture was added to the cells with 7 ml of fresh DMEM medium and homogenised by gently swirling the plates.

Vector	Selection	Description
lentiCRISPR empty	Blasticidin	Lentiviral plasmid expressing Cas9 protein
lentiCRISPR s139	Blasticidin	Lentiviral plasmid expressing Cas9 protein and sgRNA117 targeting <i>METTL1</i>
lentiCRISPR sg117	Blasticidin	Lentiviral plasmid expressing Cas9 protein and sgRNA117 targeting <i>METTL1</i>
lentiCRISPR sg119	Blasticidin	Lentiviral plasmid expressing Cas9 protein and sgRNA117 targeting <i>METTL1</i>
pEGFP-LC3	G418	Constitutive plasmid expressing LC3 GFP-labelled protein
pLKO_SCR	Blasticidin	Doxycycline-inducible lentiviral pLKO plasmid expressing human a scramble sequence
pLKO_shMET_1	Blasticidin	Doxycycline-inducible lentiviral pLKO plasmid expressing human shMETTL1-1
pLKO_shMET_2	Blasticidin	Doxycycline-inducible lentiviral pLKO plasmid expressing human shMETTL1-2
pREV		3 rd generation lentiviral-Rev expressing plasmid
pRRE		3 rd generation lentiviral packaging plasmid
psPAX2		2 nd generation lentiviral-Rev expressing plasmid
pTAT		2 nd generation lentiviral packaging plasmid
pVSV-G		2 nd and 3 rd generation lentiviral envelop plasmid
TRIPZ EV	Puromycin	Doxycycline-inducible lentiviral TRIPZ plasmid expressing stuffer sequence
TRIPZ-HA-METTL1	Puromycin	Doxycycline-inducible lentiviral TRIPZ plasmid expressing tagged human METTL1
Tripz-HA-METTL1-AFPA	Puromycin	Doxycycline-inducible lentiviral TRIPZ plasmid expressing a catalytic dead mutant of METTL1 tagged with HA

Table 4. Description of the plasmids used for the generation of both stable and transient cell lines

For cell infection, viral supernatants from 48 and 72 h after transfection were collected, filtrated through at 0.45 μ m filter and concentrated using Lenti-X concentrator (Takara, 631232) according to manufacturer's instructions. Lentivirus were resuspended in 200 μ L of DMEM medium and added to the target cells in medium supplemented with 8 μ g/ml of Protamine sulfate (Sigma, 1578612). Transduced cells were selected using 2 μ g/ml puromycin (Santa Cruz Biotechnology, sc-108071A)

or 10 µg/ml blasticidin (Santa Cruz Biotechnology, sc-495389) for 3 or 5 days respectively, depending on the selection cassette.

3.2.1. Generation of *METTL1* knock-out cell lines by CRISPR-Cas9 technology

For genomic editing of *METTL1*, lentiCRISPRv2 plasmid containing the three sgRNAs previously described were separately infected into PC3 and DU145 cells. As control, an empty vector expressing Cas9 protein was also transduced. For ensuring a homogenous editing of the gene, single-cell clones were generated by low density seeding in p96 plates and selection by microscope visualization. The knock-out (KO) efficiency was tested by RT-qPCR and Western Blot.

3.2.2. gDNA extraction and CRISPR-Cas9 editing validation

Extraction of genomic DNA (gDNA) from PC3 CRISPR WT and KO cells in culture was performed following proteinase K protocol. Briefly, cells were collected with a solution containing 30 mM Tris-HCl pH 8.0, 10 mM EDTA, 0.4% SDS and 100 µg of proteinase K (Roche, 03115828001). After incubation at 56°C overnight, phenol/Chloroform/Isoamyl (25:24:1, Panreac, A0889,025) was added to the extracts followed by centrifugation. Supernatant was collected, incubated with 500 µl of chloroform (Fisher Chemical, C/4920/15) and aqueous phase was separated by centrifugation. After supernatant collection, 1:10 of the collected volume of 3M AcNa and 2x volumes of 100% EtOH (Emsure, 1.00983.2511) were added and incubated for 3h at -80°C. gDNA was precipitated by centrifugation for 30 min at 4°C and 15000 rpm. The pellet was then washed with 70% EtOH and resuspended in nuclease free water (Ambion, W4502). Then, the DNA was quantified by NanoDrop ND-1000 (Isogen Lifescience) and the genomic region targeted by the designed sgRNAs-Cas9 complexes was amplified by standard PCR conditions with NZYTaQ II 2x Green Master Mix (Nzytech, MB358) and specific primers (Table 3). Half of the amplification volume was used for PCR validation and the other half was cloned into pCR™2.1-TOPO® vector using TOPO® TA Cloning® Kit (ThermoFisher, 450641) according to the manufacturer's instructions. Competent DH5α bacteria transformation was performed using standard conditions and GeneJET Plasmid Miniprep kit (ThermoFisher, K0503) was used for plasmid isolation. Sequencing of three different colonies was performed with TOPO vector specific primers and the analysis of the sequences were performed with ClustalW.

3.2.3. Generation of *METTL1* knock-down cell lines

DU145 cell lines were silenced for *METTL1* by infection with the lentiviral doxycycline-inducible pLKO.1-TetON-puro vector (Addgene, 21915) modified for blasticidin resistance. The non-specific scramble plasmid modified from Tet-pLKO.1-puro-scrambled (Addgene, #47541) was transduced into the cells as control. Two shRNAs sequences against *METTL1* mRNA were used (shMETTL1-3 and shMETTL1-4). Silencing efficiency was tested both by RT-qPCR and Western blot after an induction for 3 days with 0.1 µg/ml and 0.5 µg/ml of doxycycline (Sigma, D9891). For experimental

procedures, shRNAs expression was pre-induced for 3 days with 0.1 µg/ml of doxycycline and then induced for the experiment length at 0.25 µg/ml or directly induced with 0.5 µg/ml for 3-5 days.

3.2.4. Generation of catalytic dead mutant cell lines

METTL1 KO clones were transduced with the lentiviral constructs expressing either the wild type (WT or HA-METTL1-WT) or the catalytically dead mutant (HA-METTL1-AFPA) version of the enzyme. Infection with the empty vector (pTRIPZ-EV) was used as a control. Re-expression of the enzyme was confirmed by Western Blot and methylation activity was evaluated by Northdot Blot analysis. Enzyme expression was induced with 0.5 µg/ml doxycycline for 5 days for Western Blot and Northdot Blot analysis and with 0.1 µg/ml doxycycline for growth curves assays.

3.3. Transitory *METTL1* silencing in U2OS-GFP cell lines

Transient silencing of *METTL1* was performed in U2OS cells stably expressing GFP-LC3 protein with short-interfering RNAs (siRNAs). 150.000 cells were seeded in 6-well plates (Falcon) the day before transfection. For each well, 25 nM of the siRNAs indicated at Table 5 were prepared in 200 µl of serum-free DMEM medium. Then, 12 µl of INTERFERin reagent (Polyplus, 409.10) were added to the mix and incubated for 10 min at room temperature to allow complexes formation. Cell medium was removed and 2 ml of fresh DMEM medium was added. Transfection mix was added dropwise to the cells and homogenised by gently swirling the plate.

Name	Target gene	Ref.	Supplier	Sequence (5'-3')
5'TOG	CysGCA	N/A	IDT customised	GGGGGUAUAGCUCAGGGG UGAGCAUUUGACUG
AllStars Negative control	No target	1027280	Qiagen	N/A
AntiTOG	CysGCA 5'TOG complementary	N/A	IDT customised	CAGUCAAAUGCUCUACCC CUGAGCUAUACCC
Biotin antiTOG	Biotinylated CysGCA 5'TOG complementary	N/A	IDT customised	Biotin- CAGUCAAAUGCUCUACCC CUGAGCUAUACCC
Biotin-5'TOG	Biotinylated CysGCA	N/A	IDT customised	Biotin- GGGGGUAUAGCUCAGGGG UGAGCAUUUGACUG
Hs_METTL1_1	METTL1	SI00076 118	Qiagen	N/A
Hs_METTL1_3	METTL1	SI00076 132	Qiagen	N/A

Table 5. Sequences or references of the siRNAs and synthetic oligonucleotides transiently transfected in cell lines.

Gene silencing was tested 48 h after transfection by RT-qPCR and at 72 h by Western Blot. LC3 puncta of individual cells were manually counted using Image J software and normalised to the number of cells per image. 10 different images were quantified per condition.

3.4. Transfection of synthetic 5'TOG and anti-TOG oligonucleotides

150.000 or 2×10^6 PC3 cells were seeded in 6-well or 10 cm plates respectively and transfected the following day with INTERFERin reagent (Polyplus, 409.10) as previously described. Following manufacturer's instructions, cells were transfected with 25 nM of either a scramble control, 5'TOG or an anti-TOG oligonucleotides (see Table 5) prepared in either 200 or 500 μ l of serum-free DMEM medium, for 6-well or 10 cm plates respectively. Cells were collected 48 hours after transfection unless otherwise stated, according to the conditions suitable for the following experiment.

3.5. Transitory transfection of GFP-LC3 plasmid

PC3 cells lines WT and KO for *METTL1* were transitory transfected with pEGFP-LC3 (Addgene, #21073, Table 4) with JetPEI, for transient expression of the GFP-tagged version of LC3 protein for autophagosome visualization. Similar as described for lentivirus production, 10 μ g of pEGFP-LC3 plasmid was diluted in 150 mM NaCl and then combined with JetPEI-containing solution. Transfected cells were selected with 50 μ g/ml of G418 (Santa Cruz Biotechnology, sc-29065) for three days and all experiments were performed within a week after selection for ensuring an optimal plasmid expression.

3.6. Cell proliferation assay

Evaluation of cell proliferation in adherent conditions was performed by seeding from 3.000 to 15.000 cells per well in 12-well plates. Three to six technical replicates were seeded per condition and time point. Cell growth was evaluated for up to 8 days and cells were collected every one or two days, depending on curve length. In the case of the catalytic dead mutant proliferation rescue, 0.1 μ g/ml of doxycycline was added to the cells in the curve seeding. For TOG-transfected cells, curve seeding was performed 24 hours after transfection.

For plate collection, cells were washed twice with PBS and fixed at 4°C with 4% paraformaldehyde (Panreac, 252931.1214) for at least 30 min. Wells were stained with 500 μ l of a solution composed of 0.1% of crystal violet (Sigma, C6158) and 10% methanol (Honeywell, 32213) for 1 hour in agitation. Then, plates were thoroughly washed with dH₂O and dried overnight at room temperature. Once the plates were dry, crystal violet was dissolved in 500 μ l of 10% acetic acid (Millipore, 1.00063.1011) for 40 min on a rocker. Cell density was quantified by measuring optical absorbance at 595 nm using Plate Infinite Reader 200 Pro (TECAN). 10% acetic acid was used as blank. All quantifications were normalised to day 0 measurements to reduce the differences due to cell seeding.

3.7. Cell survival assay

Survival evaluation of PC3 WT or *METTL1* KO cells was analysed under different conditions: 15 nM Docetaxel (Sigma, 01885), 3725 nM of freshly prepared H₂O₂ (Santa Cruz Biotechnology, sc-203336A, 20 nM Rapamycin (LClabs, 53123-88-9), 20 J/cm² UV pulse (Stratalinker 2400 (Stratagene)), 7 μM Etoposide (Sigma, E1383-100mg), being all drugs prepared in DMEM medium. Evaluation of 3-methyl adenine (3MA, Sigma, 189490) effect was performed in Earle's Balance Salts Solution medium (EBSS, Sigma, E2888) supplemented with 4.5g/L of glucose and 2mM of 3MA. All the treatments were added 8 hours after seeding, simultaneously to day 0 seeding control collection. In the case of the *METTL1* WT or catalytic dead mutant re-expressing cell lines, a pre-induction of 3 days with 0.1 μg/ml of doxycycline was used and an induction of 0.25μg/ml was maintained during the experiment. Medium was refreshed every two days and cell proliferation was evaluated by crystal violet staining. Cell proliferation was measured as previously indicated.

3.8. Soft agar colony formation assay

The anchorage-independent growth capacity of the cells was assayed by soft-agar. Briefly, 1.5 ml of DMEM medium containing 0.6% of low melting agarose (Sigma, 2070) was poured into 6-well plates. Agar was cooled for 1h at 4°C for solidifying the bottom layer. A second layer with 0.3% low melting agarose and 2.500 cells in 1.5 ml of DMEM medium was spread over the bottom layer. Then, plates were maintained for 15 min at 4°C to enable agar solidification and then moved to a CO₂ incubator. Six technical replicates were seeded per condition. Cell colonies were grown for 14-21 days and 0.5 ml of DMEM medium was carefully added weekly to ensure agar moisture and avoid colony disaggregation. For colony visualization, soft-agar plates were stained with 0.005% crystal violet in 1% methanol and scanned (Canon scanner), and the number of colonies was quantified using the “analyse particles” plugin of ImageJ. As a seeding control, 20.000 cells were seeded in 12-wells plate, collected the following day, and stained with crystal violet as previously described. The number of colonies was normalised to the seeding control absorbance measurement at 595 nm.

3.9. Single-cell spheroids generation

To prevent cell adhesion, p96-well plates were previously treated with 12 g/L of poly-2-hydroxyethyl methacrylate (polyHEMA, Santa Cruz Biotechnology, sc-253284) resuspended in ethanol (Supelco, 1.00983.2511) and dried overnight at 65°C. Once the liquid was evaporated, between 1-1.5 cell per well was seeded by performing serial dilutions. Single-cell wells were selected by microscopic observation. Spheroids were growth for 18-21 days in DMEM/F12 (Gibco, 10565018) medium supplemented with 1x B27 (Gibco, 17504-044), 0.02 μg/ml of EGF (Gibco, PH60315), 0.004 μg/ml bFGF (ThermoFisher, 68-8785-63), 8% BSA (Nzytech, MB04602) and 1% penicillin/streptomycin. Two weeks after seeding, 100 μl of spheroid medium were carefully added to avoid medium evaporation. The number of obtained spheroids was normalised with the number of single-cell wells

identified at the beginning of the experiment. Pictures were taken using Nikon Eclipse Ti-S microscope and JenOPTIK ProgRes C3 camera. Spheroids volume was estimated using ImageJ and the formula $\text{volume} = \text{length} \times \text{width}^2 \times 0.526$.

3.10. Organoid culture and proliferation assay

3.10.1. Organoid derivation

Tumour tissue xenografted on NSG (NOD/scid/gamma) mice was collected in basis medium and mechanically disrupted for reducing its size. After washing with basis medium, tissue was centrifuged for 5 min at 300 g and incubated for 90 min at 37°C with collagenase type I (Thermo Fisher Scientific, 17100017), 15 µg/ml of DNaseI (Roche, 10104159001) and 10 µM Y-27632-HCl Rock inhibitor (Selleckchem, S1049). Ten times the tissue volume was added of the enzyme mix to ensure complete dissociation and the solution was mixed every 20 minutes. Once completed larger pieces digestion, tissue was washed with basis medium and centrifuged for 5 min at 300 g. Then, pellet was resuspended in 2 ml of TrypLE select (Gibco, 12563011) and incubated for 10 min at 37°C. TrypLe was diluted with basis medium and cell suspension was passed through a 40 µm cell strainer (Thermo Fisher Scientific, 352235) and centrifuged. Dissociated cells were resuspended in 2 ml of PCa organoid medium and manually counted. 400.000 cells per well were seeded in 6-well ultra-low attachment plates (ULA, Corning, Costar, #3474) or in poly-HEMA pre-treated normal 6-well plates. Medium top up or refreshment was performed every two days and the media was not prepared for longer than 7 days and maintained at 4°C.

3.10.2. Organoid lentiviral infection

Lentiviral particles were generated and concentrated as previously described and titrated on HEK293FT cells to ensure correct infection. Formed organoids were dissociated with tryple, counted, and 160.000 cells were seeded per well in ULA 24-well plates in PCa organoid medium supplemented with 4µg/ml of polybrene (Sigma, TR-1003). Then, 10 µl of viral particles containing either pTRIPZ scramble (SCR) or codifying for shMETTL1-3 sequence were added. Non-infected cells were used as selection control. The day after, PCa organoid medium was refreshed and blasticidin selection was added 48 h after infection. *METTL1* silencing was assessed by RT-qPCR after 3 days of 0.5 µg/ml doxycycline induction, with no induced cells as control per each condition. RNA extraction was performed with Trizol like detailed hereunder.

3.10.3. Expansion of xenografted LAPC9 in NSG mice

Since LAPC9 cells do not proliferate *in vitro*, cell expansion was performed by subcutaneous injection in two flanks of NSG mice. After organoid dissociation, 1.000.000 cells per flank were resuspended in 50 µl of cold Matrigel (Corning, 356234), injected subcutaneously using 25G needles and expanded for three weeks. Once expanded, tumours were extracted and frozen in basis medium supplemented in 10% dimethyl sulfoxide (DMSO, Sigma, D-8418).

3.10.4. Organoid formation capacity quantification

100.000 cells per well in 24-well ULA plates of LAPC9 SCR and sh*METTL1*-3 cells were seeded in PCa organoid medium and induced for four days with 0.5 µg/ml doxycycline. Non-induced condition was used as control. Once formed, the number of organoids with a diameter bigger to 10 µm were manually quantified and induced conditions were normalised with non-induced. At least 20 pictures per conditions were acquired using white field microscope.

3.11. **PI3K pathway inhibition and DHT treatment**

To evaluate the dependence of *METTL1* expression on PI3K pathway, PC3 and DU145 parental cell lines were grown in DMEM medium and treated with inhibitors of different components of PI3K pathway: 20 nM Rapamycin, 125-250 nM Torin-1 (Tocris, 4247), 5µM MK2206 (Selleckchem, S1078) and 100 nM BKM120 (Selleckchem, S2247) were added for the indicated times. All chemicals were resuspended in DMSO in concentrations at least 1000x higher than the working dilution. Two technical replicates were done per experiment and each experiment was repeated three times. Treatment of 22Rv1 cells with DHT (Sigma, D-073-1ml) was performed for 6 hours at 10 nM.

4. **Molecular and cell biology techniques**

4.1. **Assaying autophagy dysregulation**

4.1.1. Evaluating autophagy flux under normal and autophagy-inducing or blocking conditions

The autophagy pathway was evaluated in PC3 cells in normal conditions and after treatment for 24 hours with 20 nM of Rapamycin, or for 6 h with 10 µM chloroquine (CQ, Sigma-Aldrich, C6628-25G), for induction or blockade of the pathway respectively. The conditions were maintained in Western Blot, flow cytometry and immunofluorescence experiments unless otherwise specified.

Further evaluation of the lysosome-autophagosome fusion was performed with the pH sensitive probe LysoTracker DeepRed (ThermoFisher, L12492), which was added to the cells for 30 min at 50 nM. Cells were treated with Rapamycin and CQ as stated before and were then collected following the immunofluorescence or flow cytometry protocols. Three biological replicates were acquired per condition. Immunofluorescence images were taken using Leica SP5 confocal microscope at 60x magnification and optical zoom 2x. Fluorescence intensity of individual cells was quantified in ten images by measuring the Corrected Total Cell Fluorescence (CTCF) using the formula: $CTCF = \text{Integrated Density} - (\text{Area of selected cells} \times \text{Mean background fluorescence})$. For flow cytometry analysis of the PC3 WT or *METTL1* KO cells transiently transfected with GFP-LC3 and treated with lysotracker, lysotracker mean intensity (APC channel) was calculated in previously selected GFP+

cells. Three technical replicates per condition and cell line were analysed, using three different control and three different KO clones.

4.2. Flow cytometry analysis

4.2.1. A6poptosis quantification

70.000 cells were seeded in 12-well plates and collected 48 h later by trypsinization. Medium supernatant, PBS washes and trypsinised cells were collected and centrifuged at 1200 rpm for 4 min. After PBS washes, cells were pelleted and resuspended in 100 μ l of Annexin V Binding Buffer (10nM HEPES/NaOH (pH 7,4), 140mM NaCl 2,5mM CaCl₂) containing 1 mg/ml Propidium Iodide (PI, Sigma, P4170) and 10 mg/ml RNase A (Roche, 10109142001). Then, 3 μ l of Annexin V (AnnV, Immunostep, ANXVF-200T) was added to each sample. Cells were then incubated for 15 min at room temperature and in the dark. Once incubated, 50 μ l of Annexin binding buffer was added and cells were analysed by BD Accuri C6 flow cytometer (BD Biosciences). All events excluding cell debris were evaluated and the percentage of dying cells was analysed using FlowJo software. All necrotic (PI⁺AnnV⁻), early apoptotic (PI⁻AnnV⁺) and late apoptotic (PI⁺AnnV⁺) cells were considered as dying cells. Three technical replicates were used for each condition.

4.2.2. Measurement of global protein synthesis by O-propargyl-puromycin incorporation

Protein synthesis rate was quantified in PC3 cells WT and *METTL1* KO. Briefly, 6-well plates were incubated in DMEM medium supplemented with 20 μ M of the puromycin analogue O-propargyl-puromycin (OP-puro, Medchem Source LLP, HY-15680) for 1h at 37°C, as described in³⁰⁷. Protein synthesis under stress conditions was tested as showed in Figure 42. Thus, 200 μ M of NaAsO₂ (Supelco, 1062771000) was added to the cells for 2 h, and cells were collected, 1, 2, 4 or 8 h after treatment addition. Cells were trypsinised, centrifuged and fixed with 1% PFA in PBS for 15 min on ice. One PBS wash was performed, cells were permeabilized with PBS supplemented with 3% FBS and 0.1% saponin (Santa Cruz Biotechnology, sc-280079) for 5 min at room temperature. Then, the conjugation of the incorporated OP-puro to a fluorophore was performed by an azide-alkyne cycloaddition using the Click-iT Cell Reaction Buffer Kit (Jena Bioscience, CLK-073) and 5 μ M of Alexa Cy5.5 conjugated to azide (Jena Bioscience, CLK-1059). The reaction was initiated by vortexing and incubated for 30 min. Then, cells were washed twice in PBS with permeabilisation buffer and then resuspended in PBS. Controls with OP-puro but not cycloaddition reaction, without OP-puro but with cycloaddition reaction and either of the conditions were used as basal intensity controls. Non-synthesis control was used by incubating cells with 0.1 mg/ml of cycloheximide (CHX, Santa Cruz Biotechnology, sc-3508). Fluorescence intensity was measured by flow cytometry (Accuri C6). In normal conditions fluorescence intensity was normalised to the average cell size by quantification of mean forward scatter (FSC) due to the size difference between cell lines. For protein

synthesis measurement under stress conditions, fold change of fluorescence intensity in the experimental condition divided by the values of the same cell line treated with CHX is represented.

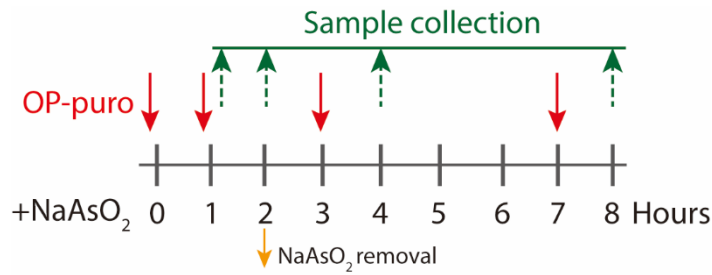


Figure 42. Schematic workflow used for protein synthesis evaluation under stress conditions. Point 0 indicates NaAsO₂ addition and its removal 2 hour later is also indicated. The specified hours represent time after NaAsO₂ addition. Red arrows represent OP-puro incorporation points, one hour before sample collection (green arrows).

4.2.3. Cell cycle analysis

For cell cycle analysis, cells in culture were collected with trypsin and washed twice with PBS. Cell pellet was resuspended in 100 μ l of PBS and fixed with 1ml of cold 70% ethanol for 10 min on ice. Cells were pelleted by centrifugation for 5 min at 1200 rpm and then resuspended in 500 μ l of Staining Buffer containing 1 μ g/ml Propidium Iodide (Sigma, 81845) and 50 μ g/ml of RNase A (Roche, 10109142001) in PBS. Samples were then incubated for 30 min at room temperature in the dark analysis was performed with Accuri C6 flow cytometer (BD Biosciences). DNA content was quantified using FlowJo software (BD Biosciences). Cell debris and aggregates were eliminated by gating the cells forward versus side scatter and FSC-H versus FSC-A respectively. Three technical replicates were used for cell type.

4.2.4. ROS measurement

For quantification of intracellular ROS, PC3 WT and *METTL1* KO cells were seeded in 6-well plates. 80% confluent cells were trypsinised and resuspended in DMEM medium supplemented with 20 μ M of 2',7'-Dichlorofluorescein Diacetate (DCHF-DA, Calbiochem, 287810) in the dark. Cells were incubated for 30 min at 37°C in the dark and then washed twice with PBS. Then, cells were resuspended in homemade Hank's buffered salt solution (HBSS) supplemented with 5% FBS and measured with BD Accuri C6 (BD biosystems). All measurements were performed within 30 minutes after DCHF-DA incubation for avoiding diffusion of the tracker. Mean fluorescence intensity was quantified with FlowJo software and three replicates were analysed per cell line.

4.3. Cell Immunofluorescence

Cells were seeded on cover glasses (Menzel-Glaser, 630-1846) and grown in DMEM medium until 80% of confluence. For cell collection, two PBS washes were performed followed by fixation for 10 min with 4% PFA (Panreac Applichem, 252931) and permeabilization with 0.2% Triton X-100 (Panreac Applichem, 20801423141611) in PBS for 10 min. Fixation was performed with 4% PFA for all antibodies excepting METTL1 (*), for which the fixation was performed with 100% ice-cold methanol. Samples were blocked for 1 h at room temperature with 5% goat serum (Gibco) in PBS. Incubation with the primary antibodies diluted in blocking solution was performed overnight at 4°C,

using antibodies listed in Table 6. Next day, cells were washed three times with 0.05% Tween-20 in PBS and incubated in the dark for 1 hour with fluorophore-conjugated secondary antibodies diluted 1:800 in blocking solution. Nuclei were stained with 0.5 µg/ml of DAPI (Sigma, D9542) for 10 min and cover glasses were mounted with Mowiol (Sigma, 81381). Fluorescence pictures were acquired with Leica SP5 confocal microscope or Thunder Imager (Leica DM6B). For BrdU incorporation during S phase, a similar protocol was followed. Cells were treated with 10 µM BrdU (Sigma, 19-160) for 1 hour previous to collection. For the staining, coverslips were treated with 2N HCl for 30 min at room temperature, then washed thoroughly and incubated with the specific antibody.

Antibody	Host	Application	Dilution	Company	Reference
Anti-BrdU	Rat	IF	1:1000	Abcam	Ab6326
Anti-LAMP2	Mouse	WB	1:100	Santa Cruz Biotech	Sc-18822
Anti-LC3A/B	Rabbit	IF	1:100	Cell signaling	12741
Anti-METTL1*	Rabbit	IF	1:1000	Abcam	Ab157997
Anti-pSTAT1	Mouse	WB	1:1000	Santa Cruz Biotech	Sc-8394
Anti-pyH2AX	Rabbit	IF	1:200	Cell signaling	9718s

Table 6. List of antibodies with the working dilutions used for cell immunofluorescence.

4.3.1. Quantification of protein aggregates

Aggresomes formation was assayed in PC3 cell lines using PROTEOSTAT Aggresome detection kit (Enzo LifeSciences, ENZ-51035). Briefly, actively growing cells were seeded in cover glasses and fixed with 4% PFA for 30 min at room temperature. After PBS washes, permeabilization solution (1x assay buffer, 0.5% Triton X-100, 30 mM EDTA pH 8) was added to the cells for 30 min on ice, followed by incubation with Dual Detection Reagent for 30 min at room temperature and in the dark according to manufacturer's instructions. Glasses were then mounted and visualized with Lecia SP5 confocal microscope. Fluorescence intensity of individual cells was quantified in ten images per condition by measuring the CTCF.

4.4. Immunohistochemistry

After collection, tissues were fixed overnight with 4% PFA and maintained overnight in 70% EtOH. Tissue dehydration, paraffin embedding and sectioning was performed by the Molecular Pathology Unit at CIC. For immunohistochemistry staining, samples were dewaxed and rehydrated with a battery composed by xylene (Panreac, 251769) and decreasing graded ethanol to water (100%-50%). Antigen retrieval was performed for 20 minutes at low power microwave either in citrate buffer (10 mM Sodium Citrate, 2M HCl, 0.1% Tween-20, pH 6) or Tris-EDTA (10 mM Citric Acid, 2 mM EDTA, 0.05% Tween-20, pH 9) depending on the antibody used (Table 7). Slides were cooled down at room temperature and incubated with 3% H₂O₂ (Santa Cruz Biotechnology, sc-203336A) for

blocking endogenous peroxidase. Then, samples were washed with PBS and permeabilised with 0.2% Triton X-10 for 10 minutes. Blocking was performed for 30 min when using the serum included in IMPRESS kit (Vector Laboratories) or for 1 hour with homemade 2.5% goat serum (Gibco, 16210064). Incubation with the primary antibodies indicated in Table 7 was performed at 4°C overnight. After PBS washes, specie specific-ImmPress HRP Kit (Vector Laboratories, MP7451) was used for secondary antibody incubation. Peroxidase reaction was developed with Impact DABSubstrate kit (Vector Laboratories, SK4105) and cells were counterstained with Haematoxylin (Sigma, 1051750500). Finally, slides were dehydrated and mounted with Dibutylphthalate polystyrene xylene (DPX, Sigma-Aldrich, 06522). White field images were acquired using an Olympus BX-51 Microscope and ImageJ software was used for image quantifications.

For LC3 staining quantification, 3,3'-diaminobenzidine (DAB) and haematoxylin channels were separated using the H-DAB option from Colour Deconvolution plugin of ImageJ software. DAB intensity was measured and optical density (OD) were calculated using the following formula: $OD = \log(\text{max intensity} / \text{Mean intensity})$; where max intensity is 255 for 8-bit images. For measuring DNA damage, the percentage of γ H2AX positive cells was calculated by dividing the number of cells with γ H2AX foci between the total number of nuclei in every picture.

Antibody	Dilution	Host	Antigen retrieval	DAB	Company	Reference
Anti-AR	1:100	Rabbit	Citrate	10 min	Cell signaling	5153
Anti-CIcasp3	1:100	Rabbit	Citrate	10 min	Cell signaling	9661S
Anti-K14	1:100	Rabbit	Tris-EDTA	5 min	Covance	PRB-155P-100
Anti-K8		Rabbit	Citrate	5 min	Abcam	ab59400
Anti-Ki67	1:100	Rabbit	Citrate	10 min	Vector Labs	VP-K451
Anti-LC3A/B	1:100	Rabbit	Citrate	10 min	Cell signaling	12741
Anti-METTL1	1:100	Rabbit	Tris-EDTA	7 min	Invitrogen	54280
Anti-pSTAT1	1:100	Mouse	Citrate	10 min	Santa Cruz Biotechnology	sc-8394
Anti-p γ H2AX	1:200	Rabbit	Citrate	10 min	Cell signaling	9718s

Table 7. Antibodies used for IHC staining of paraffin embedded tissue. Antigen retrieval conditions and dilutions are indicated for each antibody.

4.5. Western Blot

For protein extraction from cells in culture, pre-confluent cells were washed twice with PBS and scratched with RIPA lysis buffer (150mM NaCl, 40mM Tris pH 7,6; 1% Triton X-100, 1mM EDTA, 1mM MgCl₂) supplemented with cOmplete EDTA-free proteases inhibitor cocktail (Roche, 11873580001) and phosphatases inhibitors (1mM Sodium Fluoride, 1mM Sodium Orthovanadate and 1mM β -glycerophosphate, all from SIGMA). To extract proteins from mouse and human tissue,

samples were snap-frozen in liquid nitrogen and transferred to lysis buffer without detergents into homogenization tubes with ceramic beads. Tissue was disrupted using FastPrep-24™ 5G Instrument (MP Biomedicals™) and two cycles of 30'' at 6m/sec. Then, detergents were added, and protein extracts were cleared by centrifugation for 10 min at 13,000rpm and 4°C. Total protein quantification was performed using Pierce BCA Protein Assay Kit (Thermo Scientific, 23225) and a BSA standard curve. Absorbance at 562 nm was read in Plate Infinite Reader 200 Pro (TECAN). Equal amounts of protein were prepared in 5X Laemmli buffer (10% SDS, 50 mM Tris pH 6.8, 10% glycerol (VWR, 24388295), 1% β-mercaptoethanol (Sigma, M3148), 0.01 M dithiothreitol (DTT, Merck, 10197777001) and 0.2 mg/ml bromophenol blue (Sigma, B0126) and denaturalised for 5 min at 95°C. Samples were loaded onto 8-12% polyacrylamide (PAA) (Serva, 10687.01) resolving and 5% stacking gels, and run for 2 hours at 120 V. Proteins were then transferred for 90-120 min at 100V to 0.2 μm pore size nitrocellulose membranes (Amersham, GE-10600001) with Biorad Wet blotting system. Protein transference was confirmed by Ponceau staining (0.1% of Ponceau (Sigma, P3504) in 5% of acetic acid.

Antibody	Host	Application	Dilution	Company	Reference
Anti-4EBP1	Rabbit	WB	1:1000	Cell signaling	9644S
Anti-AKT	Rabbit	WB	1:1000	Cell signaling	9272S
Anti-AR	Rabbit	WB	1:1000	Cell signaling	5153
Anti-ATG3	Rabbit	WB	1:1000	Cell signaling	3415
Anti-BrdU	Rat	IF	1:1000	Abcam	Ab6326
Anti-eIF2α	Rabbit	WB	1:1000	Cell signaling	5324
Anti-eIF4A1/II	Mouse	WB	1:1000	Santa Cruz Biotechnology	Sc-377315
Anti-eIF4E	Mouse	WB	1:1000	Santa Cruz Biotechnology	Sc-9976
Anti-eIF4G	Mouse	WB	1:1000	Santa Cruz Biotechnology	Sc-133155
Anti-ERK	Rabbit	WB	1:1000	Cell signaling	5324
Anti-GAPDH	Rabbit	WB	1:1000	Cell signaling	2118
Anti-HA	Rabbit	WB	1:1000	Biolegend	901514
Anti-HSP90	Mouse	WB	1:1000	Santa Cruz Biotechnology	Sc-515081
Anti-IRF9	Mouse	WB	1:1000	Santa Cruz Biotechnology	Sc-365893
Anti-ISG15	Mouse	WB	1:1000	Santa Cruz Biotechnology	Sc-69701

Antibody	Host	Application	Dilution	Company	Reference
Anti-LC3A/B	Rabbit	WB	1:1000	Cell signaling	12741
Anti-METTL1	Rabbit	WB/IF	1:1000/1:1000	Abcam	Ab157997
Anti-mTOR	Mouse	WB	1:1000	Genetex	GTX630198
Anti-p4EBP1	Rabbit	WB	1:1000	Cell signaling	2855L
Anti-p62	Mouse	WB	1:1000	BD bioscience	610832
Anti-PABP1	Rabbit	WB	1:1000	Cell signaling	4992
Anti-pAKT	Rabbit	WB	1:1000	Cell Signaling	4060
Anti-peIF2α	Rabbit	WB	1:2000	Cell signaling	3597
Anti-pERK	Rabbit	WB	1:1000	Cell signaling	4376
Anti-pmTOR	Rabbit	WB	1:1000	Biosource	44-1125G
Anti-pS6	Rabbit	WB	1:1000	Cell signaling	4858
Anti-pS6K	Rabbit	WB	1:1000	Cell signaling	9205S
Anti-pSTAT1	Mouse	WB	1:1000	Santa Cruz Biotechnology	Sc-8394
Anti-PTEN	Rabbit	WB	1:1000	Cell signaling	9559
Anti-pULK1^{ser757}	Rabbit	WB	1:1000	Cell signaling	6888
Anti-S6	Mouse	WB	1:1000	Santa Cruz Biotechnology	Sc-74459
Anti-S6K	Rabbit	WB	1:1000	Cell signaling	9202
Anti-STAT1	Mouse	WB	1:1000	Santa Cruz Biotechnology	Sc-417
Anti-tubulin	Rabbit	WB	1:1000	Abcam	Ab15246
Anti-ubiquitin	Mouse	WB	1:1000	Invitrogen	13-1600
Anti-ULK1	Rabbit	WB	1:1000	Cell signaling	8054
Anti-YB1	Mouse	WB	1:1000	Santa Cruz Biotechnology	Sc-101198

Table 8. List of antibodies used for Western blot protein visualization. Host species and working dilution are specified.

Membranes were blocked with TBS-T 5% skimmed milk (Nestlé) and primary antibodies (listed on Table 8) were prepared in blocking solution supplemented with 0.01% azide. After incubation overnight at 4°C, membranes were washed three times with TBS-T and incubated at room temperature for 1 h in rotation with horseradish Peroxidase-conjugated secondary antibodies anti-mouse (Cytiva, NXA931V) or anti-Rabbit (Cytiva, NA934V) prepared at 1:5000 dilution in TBS-T. Signal was detected using homemade Enhanced Electrochemiluminescence Reagent or ECL (0.1 M

Tris-HCl pH8.5, 0.2 mM coumaric acid, 1.25 mM Luminol), Fujifilm super RX (Fujifilm, 4741019289) films and Hypercassette (Amersham, RPN 11643). Band intensities were quantified with ImageJ software and protein expression was normalised to housekeeping protein levels such as HSP90, tubulin or GAPDH.

5. Analysis of global and specific protein synthesis

5.1. Total proteome analysis

For total proteome analysis, one pre-confluent p100 plate of PC3 WT1 and *METTL1* KO1 cells were collected per replicate and three replicates were analysed per cell line. Cells were collected by trypsinisation and washed three times with PBS. Pellets were snap frozen in liquid nitrogen. Protein digestion and mass spectrometry analysis was performed by the Proteomics Unit of CIC bioGUNE (Bilbao). Briefly, cells were lysed in buffer containing 2M thiourea (Sigma, T8656), 7M Urea (ThermoFisher Scientific, 10578260), 4% CHAPS (ThermoFisher Scientific, 28300) and 200 mM DTT (Sigma, 10197777001) and incubated for 30 min at room temperature and in agitation. Samples were digested following FASP protocol described in³³⁸. Trypsin incubation was performed overnight at 37°C in conditions of 1 volume of trypsin per 10 volumes of protein and extracts were then cleared by centrifugation.

5.2. Capture of nascent polypeptides

24x10⁶ of PC3 WT and *METTL1* KO cells in culture were treated with DMEM medium supplemented with 20 µM OP-puro for 1h at 37°C. For collection, cells were detached by trypsinization, washed twice with PBS and cells pellets were snap-frozen in liquid nitrogen. Cells were incubated for 10 min on ice with lysis buffer provided with the kit supplemented with proteases inhibitors previously described and sonicated twice with pulses of 3 seconds. 5 mg of OP-puro tagged proteins were captured in a pre-washed azide-tagged resin by a Cu(I)-catalysed azide-alkyne cycloaddition reaction that was performed with Click Chemistry Capture Kit (Jena Bioscience, CLK-1065). Click reaction was performed for 16 hours in rotation and protein reduction and alkylation was performed for 30 min according to manufacturer's conditions. For removal of non-covalently bound peptides, resins were then washed with high stringency buffer, and protease digestion by overnight incubation with trypsin was performed on-beads.

For on-beads digestion proteins were denatured in 8M urea, reduced with 5mM DTT and alkylated with 25 mM iodoacetamide (Sigma, I1149). Sample was diluted in ammonium bicarbonate to 1.5 M urea and Trypsin was added in same ration described above and incubated overnight at 37°C as described elsewhere³³⁸.

5.3. Mass spectrometry analysis of global and nascent proteome

The obtained polypeptides from both previously described strategies were analysed by liquid chromatography followed by mass spectrometry (HPLC-MS/MS) by the Proteomics Unit of CIC bioGUNE (Bilbao). Briefly, previous to sample acquisition, digested proteins were concentrated in a speed-vac, and desalted using C18 stage tips (Millipore, ZTC18M096). Then, samples were analysed in a hybrid trapped ion mobility spectrometry – quadrupole time of flight mass spectrometer (timsTOF Pro with PASEF, Bruker Daltonics) coupled online either to a nano Elute (Bruker) or EvoSep ONE liquid chromatograph (EvoSep). Protein identification and quantification was carried out using MaxQuant software³³⁹ using default settings except for an LFQ min. ratio count of 1. Searches were carried out using Uniprot/Swissprot databases, with precursor and fragment tolerances of 20ppm and 0.05 Da respectively. Only those proteins identified with at least two peptides at FDR<1% were considered for further analysis. Data (LFQ intensities) was loaded onto Perseus platform³⁴⁰ and further processed (log₂ transformation, imputation).

For functional annotation of the differentially expressed gene sets, the Gene Ontology online tool (<http://geneontology.org/>) was used. Thus, we identified gene subsets with common functional annotations in Biological Process categories with high statistical significance. Fisher's Exact test was applied with Bonferroni correction.

5.4. Polysome profiling

Six 150 cm plates were seeded per replicate, three replicates were used for PC3 WT1 and *METTL1* KO1 cell lines. At 80% of confluence, cells were treated for 5 min at 37°C with 0.1 mg/ml of CHX to stop protein synthesis. After two washes of PBS supplemented with 0.1 mg/ml CHX, cells were collected by scrapping and cell pellet was resuspended in lysis buffer (20 mM Tris-HCl, 100 mM KCl, 5mM MgCl₂, 0.3% Igepal, 0.1 mg/ml CHX, protease inhibitors). RNA-protein content was measured using Smart-Spect Plus spectrophotometer (Biorad) and equal amounts of extracts were loaded into the gradients. Previous to cell collection, 7-50% sucrose (Sigma, S0389) gradients (20mM Tris-HCl pH7.5, 100 mM KCl, 5 mM MgCl₂, 1% CHX) were prepared in tubes (Beckman Coulter, 331374) by snap freezing layers of 50%, 33.56%, 21.33% and 7% of sucrose followed by overnight thawing at 4°C. Then, extracts were loaded in balanced gradients and separated by ultracentrifugation for 2:45 h at 4°C and 39000 rpm with no break. 500 µl fractions were collected using Density Gradient Fractionation system (Brandel). Half of the volume of every fraction was used for RNA extraction with warm phenol and proteins were precipitated with trichloroacetic acid (TCA, Fisher Chemical, T/3000/50) from the remaining volume. For RNA extraction, fractions were mixed with an equal volume of 60°C-heated Phenol-Chloroform and a solution containing 10 mM Tris, 350 mM NaCl, 10 mM EDTA, 1% SDS and 42% Urea, followed by RNA precipitation with isopropanol. cDNA and RT-qPCR were performed with the sixteen different fractions from every

replicate and the primers used are listed on Table 9. Quantification of the percentage of transcripts within each fraction was calculated as follows: $\% = ((2^{-(Ct1-Ctx)} / \text{Summatory Cts in all fractions}) \times 100$, where Ctx is the Ct value of any fraction.

For protein extraction, 1/3 of fresh prepared 50% TCA was added to 1 volume of each fraction and the mix was incubated overnight at -20°C. Then, samples were centrifuged at 13,000 rpm for 15 min at 4°C and washed twice with cold acetone (Emsure, 1.00014.1011). Protein pellet was dried using SpeedVac for 10 min and resuspended in 30 µl of 1x Laemmli buffer. 15 µl of 2M Tris pH 8 and incubated at -20°C overnight. Before loading onto polyacrylamide gels, proteins were boiled at 95°C for 5 min.

5.5. Biotinylated 5'TOG oligonucleotides pulldown

Two 10 cm culture plates per condition of PC3-WT cells were transfected using INTERFERin (Polyplus) reagent with 40 nM of a mix 1:1 of either scramble control together with biotinylated-5'TOG oligonucleotides, or a mix of biotinylated-5'TOG with 5'Anti-TOG nucleotides. 12 hours after transfection, plates were washed twice with cold PBS. Then, 3 ml of PBS were added, and cells were UV crosslinked twice at 254 nm with 150 mJ/cm² with Stratalinker 2400 and harvested with the PBS by scrapping. Cells were pelleted, resuspended in Lysis buffer (50 mM Tris-HCl pH 7.4, 100 mM NaCl, 0.5% Triton X-100, 0.5% sodium deoxycholate (Sigma, 30970), 0.1% SDS, 5 mM EDTA, supplemented with 0.1 U/µL RNAsin (Promega, N2611) and protease inhibitors) and sonicated three times for 10 s at 10 W on ice. Protein extracts were cleared by centrifugation at 12000 rpm for 12 min and 4°C. Per sample, 45 µl of streptavidin-C1 MyOne Dynabeads (ThermoFisher, 65001) were washed following manufacturer's instructions and using the magnetic rack DynaMag-2 (ThermoFisher, 12321D). 600 µg of extracts were incubated with pre-washed beads for 2 h in rotation at 4°C. After incubation, beads were washed twice with lysis buffer, twice with High-salt buffer (50mM Tris/HCl, 1000 mM NaCl, 0.5% Triton X-100, 0.25 % sodium deoxycholate, 1M Urea, 5 mM EDTA, 1mM DTT) and once with PNK/Tween buffer (50 mM tris, 10 mM MgCl₂, 0.2% Tween-20). Then, beads were pelleted by centrifugation and resuspended in 30 µl of 1.5x Laemmli buffer supplemented with 100 mM DTT. Elution was performed by boiling the samples at 75°C for 10 min in shaking at 1100 rpm. Eluted proteins were loaded in a 10% SDS-PAGE gel and subjected to Western Blotting.

5.6. Cap Binding assay

Pulldown of proteins bound to m⁷G-caps was performed as previously described in ^{341,342}. Briefly, pre-confluent PC3 WT and *METTL1* KO cells were scrapped with lysis buffer (10 mM Tris-HCl, 140 mM KCl, 4 mM MgCl₂, 1mM DTT, 1mM EDTA, 1% NP-40, protease inhibitors and homemade phosphatase inhibitors) and incubated on ice for 30 min. Lysates were cleared by centrifugation at 12000 rpm for 30 min at room temperature and quantified using Pierce™ BCA Protein Assay Kit.

Per sample, 30 µl of 7-methyl-GTP-Sepharose beads (Jena Bioscience, AC-155S) were washed following to manufacturer's instructions. 200 µg of protein extracts diluted in lysis buffer to 1 mg/ml were incubated with the pre-washed beads overnight in rotation at 4°C. Then, beads were centrifuged for 5 min at 4°C and 5000 rpm and washed twice with lysis buffer supplemented with 0.5% NP-40 and twice with PBS. Before Western blotting, samples were mixed with Laemmli buffer, then boiled at 95°C for 5 min, and loaded in 10% polyacrilamide gels. Translation initiation factors were checked by antibody incubation and developed with ECL.

6. RNA methods

6.1. RNA extraction and quantitative real-time PCR (RT-qPCR)

For assaying mRNA levels by RT-qPCR, RNA was extracted from cells using either Nucleospin RNA kit (Macherey-Nagel, 740955.250) or NZY Total RNA isolation kit (NzyTech, MB13402) following the manufacturer's instructions. For mouse tissue, samples were snap-frozen in liquid nitrogen and transferred to lysis buffer into homogenization tubes with ceramic beads. Tissue was homogenized using FastPrep-24™ 5G Instrument (MP Biomedicals™) by two cycles of 30'' at 6m/sec. Then, manufacturer's protocol was followed. Concentration was measured using NanoDrop ND-1000 (Thermo Scientific).

Primer name	Purpose	Sequence (5'-3')
ATF4_Fw	SYBR RT-qPCR amplification	TCGATGCTCTGTTTCGAATG
ATF4_Rv	SYBR RT-qPCR amplification	CTGCTCCTTCTCCTTCATGC
ATG3_Fw	SYBR RT-qPCR amplification	CAATGGGCTACAGGGGAAGA
ATG3_Rv	SYBR RT-qPCR amplification	TGTTTGCACCGCTTATAGCA
Bcatenine_Fw	SYBR RT-qPCR amplification	CTTGTGCGTACTGTCCTTCG
Bcatenine_Rv	SYBR RT-qPCR amplification	TGTTTGCACCGCTTATAGCA
CHOP-Fw	SYBR RT-qPCR amplification	CAGAACCAGCAGAGGTCACA
CHOP-Rv	SYBR RT-qPCR amplification	AGCTGTGCCACTTTCCTTTC
GAPDH_Fw	SYBR and UPL RT-qPCR amplification	GAGTCCACTGGCGTCTTCAC
GAPDH_Rv	SYBR and UPL RT-qPCR amplification	GTTACACCCATGACGAACA
GRP78_Fw	SYBR RT-qPCR amplification	TGTTCAACCAATTATCAGCAAATC
GRP78_Rv	SYBR RT-qPCR amplification	TTCTGCTGTATCCTCTTCACCAGT
IRE1_Fw	SYBR RT-qPCR amplification	ACGCCCACTCTGTATGTTGG
IRE1_Rv	SYBR RT-qPCR amplification	ATCCCCCATGGAACGACCTG
IRF9_Fw	SYBR RT-qPCR amplification	TGTTGCTGAGCCCTACAAGG

Primer name	Purpose	Sequence (5'-3')
IRF9_Rv	SYBR RT-qPCR amplification	AGTGGGATGGTGGGTGTAAG
ISG15_Fw	SYBR RT-qPCR amplification	TCTTTGCCAGTACAGGAGCT
ISG15_Rv	SYBR RT-qPCR amplification	GGGACACCTGGAATTCGTTG
KIF20A_Fw	SYBR RT-qPCR amplification	ACTGCTCTGTCTCTCTACCT
KIF20A_Rv	SYBR RT-qPCR amplification	GGTAACAAGGGCCTAACCT
PERK_Fw	SYBR RT-qPCR amplification	ATCCCCCATGGAACGACCTG
PERK_Rv	SYBR RT-qPCR amplification	ACCCGCCAGGGACAAAAATG
STAT1_Fw	SYBR RT-qPCR amplification	ATGGCAGTCTGGCGGCTGAATT
STAT1_Rv	SYBR RT-qPCR amplification	CCAAACCAGGCTGGCACAATTG
sXBP1_Fw	SYBR RT-qPCR amplification	TGCTGAGTCCGCAGCAGGTG
sXBP1_Rv	SYBR RT-qPCR amplification	GCTGGCAGGCTCTGGGGAAG
usXBP1_Fw	SYBR RT-qPCR amplification	TAAGACAGCGCTTGGGGATG
usXBP1_Rv	SYBR RT-qPCR amplification	GCACGTAGTCTGAGTCGTGC

Table 9. Oligonucleotides designed for RT-qPCR amplification of the specified human genes by SYBR green.

From 500 ng to 1 µg of RNA were used for cDNA synthesis with NZY First-Strand cDNA Synthesis Kit (NzyTech, MB125). RT-qPCR reactions were carried out in in QuantiStudio 3 and QuantiStudio 5 (ThermoFisher Scientific) Real-Time PCR Systems. Amplification detection was performed using either 2x Taqman Fast Universal PCR Master Mix (Applied biosystems, 4366) or 2x NZY qPCR Green Master Mix (Nzytech, MB125) with specific designed primers. DNA primers used for qPCR are listed in Table 9 and 10, meanwhile the Taqman and UPL probes are displayed at Table 11. Each sample was loaded in triplicates and a negative control without cDNA was included for each gene tested. The comparative threshold cycle method (Ct) was used for calculating the ddCt values, which were normalised against GAPDH values or otherwise stated.

Primer name	Purpose	Sequence (5'-3')
ActinB_Fw	SYBR RT-qPCR amplification	ggctgtattcccctccatcg
ActinB_Rv	SYBR RT-qPCR amplification	ccagttggtaacaatgccatgt
CD49f_Fw	UPL RT-qPCR amplification	gcggtactttcactaaggact
CD49f_Rv	UPL RT-qPCR amplification	ttctttgttctacacggacga
Krt5_Fw	UPL RT-qPCR amplification	cagagctgaggaacatgcag
Krt5_Rv	UPL RT-qPCR amplification	cattctcagccgtggtacg
Krt8_Fw	UPL RT-qPCR amplification	agttcgctccttcattgac
Krt8_Rv	UPL RT-qPCR amplification	gctgcaacaggctccact

Primer name	Purpose	Sequence (5'-3')
METTL1_Fw	UPL RT-qPCR amplification	gctatgggtggcttgtagtgg
METTL1_Rv	UPL RT-qPCR amplification	cttcacccgaatctccagac
Mettl1_genot_Fw	Genotyping Mettl1flox mice	atctgcagccatagcctcat
Mettl1_genot_Rv	Genotyping Mettl1flox mice	tctaacctgctgagatggca
Ms_CD24_Fw	SYBR RT-qPCR amplification	aacatctagagagtcgcgcc
Ms_CD24_Rv	SYBR RT-qPCR amplification	ggaaacgggtgcaacagatgt
Sca1_Fw	UPL RT-qPCR amplification	cccctaccctgatggagtct
Sca1_Rv	UPL RT-qPCR amplification	tgttctttactttcctgtttgagaa
Vimentin_Fw	UPL RT-qPCR amplification	ccaaccttttctccctgaac
Vimentin_Rv	UPL RT-qPCR amplification	ttgagtgggtgtcaaccaga

Table 10. Sequences of oligonucleotides used for RT-qPCR quantification of mouse samples.

Gene	Probe	Specie	Reference	Supplier
CD34	Taqman	Mouse	Mm00519283_m1	ThermoFisher
CD49f	UPL	Mouse	#45	Roche
CD49F	Taqman	Mouse	Mm01333831_m1	ThermoFisher
GAPDH	Taqman	Human	Hs0.758991_g1	ThermoFisher
GAPDH	UPL	Human	#45	Roche
GAPDH	Taqman	Mouse	Mm99999915_g1	ThermoFisher
Krt5	UPL	Mouse	#22	Roche
Krt8	UPL	Mouse	#67	Roche
METTL1	Taqman	Human	Hs01096146_m1	ThermoFisher
Sca1	UPL	Mouse	#16	Roche
Vimentin	UPL	Mouse	#109	Roche

Table 11. List of Taqman and UPL probes used for RT-qPCR of human and mouse samples. UPL complementary primers are listed on table 9 or 10.

6.2. Total RNA extraction

Total RNA was extracted from cells in culture of mouse prostate using Qiazol (Qiagen, 79306). Briefly, samples were collected in 1ml of Qiazol and incubated for 10 min at room temperature for ensure cell lysis. Snap frozen tissue was mechanically disrupted as previously described. Then, 200 μ l of chloroform (Fisher Chemical, C/4920/15) was added and samples were homogenised by vortexing and centrifuged for 30 min at 4°C and 11.000 rpm. The aqueous phase was collected, transferred to a new tube and mixed with an equal volume of isopropanol (Honeywell, 33539) and

1:10 of 3M sodium acetate. Mixture was incubated for at least 2 h at -80°C and RNA was precipitated by centrifugation for 30 min at 4°C and 11.000 rpm. RNA pellets were washed, dried, and resuspended in 40 µl of Nuclease free water (Ambion, AM9932). After quantification, 1 µl of DNase I Turbo (Invitrogen, AM2238) was added per every 10 µg of RNA and incubated for 30 min at 37°C for DNA removal. Then, RNA purification was performed by collection of the aqueous phase after acid phenol:chloroform (Ambion, AM9722) addition. Then, 3x collected volume of 100% Ethanol (Emsure 1.00983.251), 1:10 of 3 M of sodium acetate and 0.75 µl of Glycoblue (Invitrogen, AM9515) were mixed with the aqueous phase and precipitated for 2 h at -80°C or overnight at -20°C. RNA was centrifuged and pellet was washed with 70% Ethanol. RNA integrity was confirmed by TBE-agarose gel electrophoresis and quantified with NanoDrop ND-1000.

6.3. tRNA extraction

Total RNA extraction was performed as previously described. After DNase treatment, RNA was precipitated and at least 10 µg of total RNA was size selected using mirVana miRNA isolation kit (Invitrogen, AM1561). Following manufacturer's instruction, fractions enriched in either small (<200 bp) or large (>200 bp) RNAs were eluted in 30 µl of nuclease-free water (Ambion, AM9932) using non-sticky 1.5 ml tubes (Invitrogen, AM12450).

6.4. tRNA-seq m⁷G identification at single nucleotide resolution by high-throughput sequencing or Bo-seq

tRNAs libraries were prepared from size-selected tRNAs from PC3 WT1 and *METTL1* KO1 cells. Four independent biological replicates per condition were used. m⁷G modification was detected by NaBH₄-Aniline treatment, using non-treated samples as control conditions. Briefly, tRNAs were de-aminoacylated by incubation for 30 min at 37°C with a solution containing 1 mM EDTA and 0.1 M Tris-HCl pH 9. According to ³⁴³, at least 5 µg of tRNAs were treated with a solution of 0.2 M Tris-HCl pH, 0.01 M MgCl₂ and 0.2 M KCl supplemented with 10 µg of m⁷GTP (NEB) per 10 µg of tRNAs and incubated for 5 min at 85°C. Freshly prepared 1 M NaBH₄ was added to a final concentration of 0.5 M and samples were then incubated for 30 min on ice. Treated tRNAs were desalted with Micro Bio-Spin 6 columns (Biorad, 7326221EDU) and ethanol precipitated. To induce complete β-elimination and cleavage of RNAs at methylated guanines, reduced RNAs were treated with aniline/acetate/water solution (1:3:7) (Sigma). To ensure phosphorylated 5' ends and 3' OH ends of tRNAs, incubation with T4 PNK (NEB, B0210S) was performed followed by heat inactivation and ethanol precipitation. tRNA libraries were generated using NEXTFLEX Small RNA-Seq Kit v3 (Bioo Scientific Corp.) for Illumina Platforms, by the Genomic Unit at CIC bioGUNE. Briefly, 3'adenylated and 5'phosphorylated adapters suitable for Illumina RNA sequencing were ligated to the small RNA fraction. RNA was reverse-transcribed at 50°C for 1 h (SuperScript III cDNA synthesis kit, Invitrogen), followed by PCR amplification with Phusion DNA

polymerase (Thermo scientific) and size-selected before sequencing. All samples were multiplexed and sequenced in HiSeq2500 platform.

6.1. tRNA-seq and m⁷G-methylation analysis

tRNA sequencing and methylation bioinformatic analysis was performed by collaborator Dr. Sabine Diettmann (Washington University School of Medicine in St. Louis) as follows. Raw sequencing FASTQ files were trimmed with *'cutadapt'* of the 'TGGAATTCTCGGGTGCCAAGG' adapter retaining reads with a minimum length of 23 nt. Reads were subsequently trimmed by 4 nt on both ends following platform recommendations. Reads were aligned to the GRCh38 (hg38) reference genome using *bowtie* (bowtie-bio.sourceforge.net) with parameters '-m 500 -v 2', allowing a maximum of 500 multiple mappings and two mismatches. tRNA genomic coordinates on hg38 were obtained from the *'GtRNadb'* database (gtrnadb.ucsc.edu). Reads on tRNA coordinates were processed using *'htseq-count'* from the Python package *'HTSeq'* (htseq.readthedocs.io) with the *'-samout'* option and counts for individual reads representing tRNA fragments and their multiple sequence alignments on tRNAs were extracted from the resulting sam files using custom PERL scripts. Fragments with less than 10 counts over all samples were removed and a pseudo-count of 1 was added. Count data of tRNA fragments, which were shorter than 0.7 of the full tRNA length, was normalised, and differential abundance of tRNA fragments was evaluated for 3 replicates per condition or treatment using the R package *'DESeq2'* (<https://bioconductor.org/packages/release/bioc/html/DESeq2.html>). To determine fragments that were specifically up regulated in WT cells that are not treated with NaBH₄/Aniline, which are expected to be cleaved at the m⁷G methylation position, we applied the statistical model in *'DESeq2'* with *'design ~ (condition + treated + condition:treated'*, where condition represented KO and WT. To evaluate methylation in miRNA, pri-miRNA coordinates were obtained from *miRBase* (www.mirbase.org), reads on pri-miRNA coordinates were extracted using *'htseq-count'*, and the same statistical model in *DESeq2* was applied.

6.2. Quantification of m⁷G levels by Northdot blot

Total RNA was extracted and size selected as previously described. 10 ng of small (<200 nt) and large RNAs (>200 nt) were prepared in a final volume of 100 µl with 1:200 dilution of RedSafe (Intron Biotechnology, 21141). Samples were directly blotted onto 0.2 µm nitrocellulose membranes (Amersham, GE-10600001) using Milliblot D (Millipore) connected to the vacuum system. Once dried, membrane was crosslinked twice with 120 mJ/cm² in UV Stratalinker 2400 (Stratagene), then blocked with 5% BSA in RNA-free PBS-Tween for 1 hour. Primary anti-m⁷G antibody (MBL, RN017M) was prepared in blocking solution and incubated overnight at 4°C followed by 1 h-room temperature incubation with anti-mouse HRP-conjugated secondary antibodies. Signal was detected using homemade ECL.

As loading control, membranes were stained with 0.04% Methylene blue (Sigma) in 0.3 M Sodium acetate pH 5.2 for 10 min. ECL signal and membrane staining was quantified by densitometry and ImageJ software. Methylene blue staining intensity was used to normalize X-ray films. For measuring m⁷G levels in mouse urine, fresh urine was collected and directly loaded into nitrocellulose membranes and protocol was performed as previously described. Biological replicates are indicated for each experiment.

6.3. LC/MS-MS quantification of m⁷G tRNA levels

Total RNA from PC3 parental, two empty vector controls and two KO clones was extracted and size selected for tRNA enrichment as previously described. Two technical replicates per cell line were used. LC/MS-MS analysis was performed in collaboration with Dr. Mark Helm (Institute of Pharmaceutical and Biomedical Sciences, Germany) similar as described in²¹⁵.

6.4. tRNA *in vitro* cleavage assay

For assaying tRNA cleavage *in vitro*, synthetic 5' Biotinylated-Cys oligonucleotides (IDT) (Table 12) were incubated with extracts from PC3 WT and *METTL1* KO cells. Briefly, 0.5 mg of pre-washed Dynabeads-MyOne-Streptavidin were incubated with 4 µg of 5' biotinylated synthetic tRNAs for 30 min at room temperature for ensuring oligonucleotide binding. In parallel, cells were collected with lysis buffer (1% NP-40, 25 mM Tris pH 7.4, 30 mM NaCl, 10 mM MgCl₂ and protease inhibitors), incubated for 30 min at 4°C and cleared by centrifugation. tRNA-bound-beads were washed twice and incubated with cell extracts for 1h at 4°C in a rotating wheel, followed by two washes with washing buffer (10 mM Tris-HCl pH 7.5, 1 mM EDTA, 2 M NaCl). Then, cleaved 5' tRNA fragments were eluted from the beads in TE buffer pH 9.5 for 30 min at room temperature in rotation. tRNA fragmentation was observed using 1.0 mm 15% polyacrylamide 8M urea-TBE gels and 2100 Bioanalyzer RNA Nanochip (Agilent). For quantification of tRNA fragmentation, the area below the peaks in the RNA Nanochip profile was calculated and normalise to the tRNA corresponding peak.

Oligonucleotide	Coding	Sequence (5'-3')
Cys-WT	WT cysteine tRNA	GGGGGUAUAGCUCAGGGGUAGAGCAUUU GACUGCAGAUCAAGAGGUCCUGGUUCA AAUCCAGGUGCCCCC
Cys-G46A	Mutated cysteine tRNA at position 46	GGGGGUAUAGCUCAGGGGUAGAGCAUUU GACUGCAGAUCAAGAGA UCCUGGUUCA AAUGGUGCCCCC

Table 12. Sequences of the synthetic oligonucleotides used for *in vitro* assessment of Cys-CGA fragmentation.

6.5. Transcriptomic analysis in PC3 cell lines

RNA was extracted from PC3 WT and *METTL1* KO cells using NZY Total RNA Isolation according to the manufacturer's instructions. The RNA integrity was assessed using Agilent 2100 Bioanalyzer

(Agilent, Palo Alto, CA). Microarray analysis was performed by Genomic Unit at CIC. Briefly, chip microarray hybridisations and data were generated with Affymetrix Clariom S Assay Human (Affymetrix) (>20,000 well-annotated genes), performing labelling and hybridizations according to Affymetrix. 100 ng of total RNA were amplified and labelled using GeneChip WT Plus reagent kit (Affymetrix, 902280) and then hybridised to Clariom S human Array (Affymetrix, 902927). Washing and scanning were performed using GeneChip System of Affymetrix (GeneChip Hybridization Oven 645, GeneChip Fluidics Station 450 and GeneChip Scanner 7G). For the analysis, raw data were normalised by robust multiarray analysis (RMA) via the oligo package³⁴⁴ and subsequently analysed to detect genes differentially expressed between *METTL1*-KO and WT cells was performed by Alejandro Paniagua (Universidad de Valencia) using the limma package³⁴⁵. Differentially expressed genes in *METTL1*-KO vs WT with Benjamini–Hochberg corrected *P* values < 0.05 were considered significant.

6.6. Northern blotting

Total RNA was extracted from PC3 and DU145 WT and *METTL1* KO as previously described. 1.0 mm 15% polyacrylamide 8M urea-TBE gels were homemade and pre-run for minimum for 1 h at 180 V in 1xTBE for ion stabilization. 6 to 10 µg of total RNA were loaded into pre-run gels, run for 1 h at 180 V in 1xTBE, and transferred to a Nylon Hybond-NX membrane (Amersham, RPN203T) for 1 h at 45 V by wet electrophoresis (Biorad) in 0.5xTBE. Membranes were dried and crosslinked twice with 120 mJ in UV Stratalinker 2400.

Probe name	Purpose	Sequence (5'-3')
5'Cys-CGA	Northern blot probe	TACCCCTGAGCTATACCC
5'Pro	Northern blot probe	ATACCCCTAGACCAACGAGCC
5'Lys	Northern blot probe	CCGACTGAGCTAGCCGGGC
5'Ser	Northern blot probe	ACCGCTCGGCCAGACTAC

Table 13. List of probes used for tRNA fragmentation analysis by Northern blot.

For probe hybridisation, membranes were pre-hybridised at 52°C for 1 h in ULTRAhyb™ Ultrasensitive Hybridization Buffer (Invitrogen, AM8670) or homemade Church & Gilbert hybridization buffer (7% SDS, 500 mM Na-phosphate buffer, 1% BSA, 1 mM EDTA). 20 pmol of the single stranded DNA probes listed on Table 13 were radiolabelled at the 5' end by incubating with 70 µCi of ³²P-ATP (Perkin Elmer, BLU002Z250UC) with T4 PNK (NEB, M0201) for 1 h at 37°C. Non-bound radioisotope was removed using Oligo Clean and Concentrator (Zymo Research, D4061) columns. After denaturalisation for 5 min at 95°C, probes were added to hybridisation buffer and membranes were incubated overnight in rotation at 55°C. The following day, membranes were washed once with high stringency buffer (2x SSC, 0.5% SDS) for 30 min at 37°C and once with low stringency buffer (0.5xSSC and 0.05% SDS) for 20 min at 37°C. Membranes were dried and exposed

overnight at -80°C with X-ray films. For assaying tRNA fragmentation under stress responses, cells were treated with $200\mu\text{M}$ of NaAsO_2 for two hours, collecting the cells 2 or 8 h after stress induction. For unravelling the role on angiogenin in tRNA fragmentation, $96\mu\text{M}$ of angiogenin inhibitor N65828 was added 8h before collection. Total tRNAs loading was measured by incubation of urea gels with RedSafe and used as loading control. Densitometry quantification was performed using ImageJ software.

7. Mouse lines and *in vivo* assays

7.1. Ethical statements

All mice were housed at the Animal Research Core Facility at CIC-bioGUNE and at the University of Salamanca, maintained in ventilated filter cages under specific pathogen free (SPF) conditions with food and water available *ad libitum*. All mouse experiments were carried out following the ethical guidelines established by the Biosafety and Bioethics Committee at CIC bioGUNE (under protocol P-CBG-CBBA-0715) and at the University of Salamanca (under protocols #269, #506, #595) and by the Competent Authority of the Basque Country and Castilla y León.

7.2. Xenograft generation in immunodeficient mice

Tumour initiating and growth capacity were evaluated by subcutaneous injection of PC3 WT and *METTL1* KO cell lines and DU145 SCR and sh*METTL1*, respectively. 1×10^6 DU145 cells and 1.5×10^6 PC3 cells per condition mixed in a 1:1 proportion with Matrigel were injected in both flanks of seven-week-old BALB/c Nu/Nu male mice. Doxycycline for shRNA induction in DU145 xenografts was administered *in vivo* in the food pellets once the tumour started to grow (Research diets, D1200402). Tumours were measured three times a week and tumour volume was estimated using the formula $\text{volume} = \text{length} \times \text{width}^2 \times 0.526$. Mice were weighted once a week for monitoring animal wellbeing. For chemotherapeutic treatments of PC3-xenografts, 15 mg/kg of Docetaxel and 20 mg/kg of Etoposide were intraperitoneally injected weekly for three weeks in randomly selected animals. The treatment was first administrated when the tumours started to grow exponentially. After termination, tumours were dissected, weighted and snap frozen in liquid nitrogen for RNA and protein extraction and fixated with 4% PFA for immunohistochemistry staining.

7.3. Prostate Cancer mouse model deficient for *Mettl1* in prostate epithelium

Based on *in silico* analysis that proved removal of exon 2 of *Mettl1* results in an early truncated METTL1 protein with no catalytic activity, a conditional mouse model by introducing loxP sites flanking exon 2 of *Mettl1* was generated (Figure 37A). Briefly, two complementary RNA oligonucleotides containing the target-specific sequence for guiding Cas9 to exon 2 and the adjacent intron were designed using the Spanish National Biotechnology Center (CNB)-CSIC web tool (<http://bioinfogp.cnb.csic.es/tools/breakingcas/>). These oligos correspond to crRNAs (CRISPR RNAs) and are listed on Table 14. In addition, the 872 nt single-stranded oligodeoxynucleotides

(ssODN) containing two LoxP sequences in the same orientation, which flank exon 2, and two single mutations disrupting the protospacer adjacent motif or PAM sequences, were designed as a template for homologous recombination. All three oligos together with the tracrRNA (trans-activating CRISPR RNA) were produced by chemical synthesis by Integrated DNA technologies (IDT). The crRNA and tracrRNA sequences were annealed to obtain the mature sgRNA. A mixture formed by 30 ng/μl recombinant Cas9 protein (IDT), 20 ng/μl of annealed sgRNA, and 10 ng/μl of ssODN was microinjected into C57BL/6J zygotes by the transgenic facility of University of Salamanca (NUCLEUS platform). For identification of edited founders, a PCR amplification that produced an amplicon of 957 bp for edited alleles was performed. PCR products from founders were subcloned into pBlueScript (Stratagene) and confirmed by Sanger sequencing. The founders were crossed with WT C57BL/6 J (produced at NUCLEUS) to eliminate possible unwanted off-targets.

Heterozygous mice were re-sequenced and crossed to give rise to edited heterozygous, and homozygous and genotyping across generations was performed (primers listed on table_). The insertion of LoxP sites resulted in an increased of the PCR product of 10 bp. Floxed mice were then crossed with the previously described model *Pten*^{lox/x} *PbCre*⁷⁷ provided by Pr. Piere Pandolfi, characterized by a PTEN deletion specific at the prostate epithelium. Decreased *Mettl1* expression was evaluated in the prostate of *Pb-Cre x Pten*^{lox/lox} *x Mettl1*^{lox/lox} mice by RT-qPCR.

Name	Sequence (5'-3')
crRNA guide1	rU rA rA rG rA rG rC rC rA rU rG rA rU rG rA rUr C rC rA rA rG rU rU rU rU rA rG rA rG rC rU rA rU rG rC rU
crRNA guide2	rU rG rG rC rU rU rG rU rU rA rG rG rU rA rA rU rA rA rG rC rG rU rU rU rU rA rG rA rG rC rU rA rU rG rC rU
ssODN	CGGGTAAATAAAAATTTTAAAATATACATAAAACAAAGTAGTGCTCCAGT GCCTTAGGCAGTCAGTCTCTGGGAAAACCTTACACACATCAGTACCCAGA AGAACTTGGCAGATCTGCAGCCATAGCCTCATGATGGGACTGATTCACAC CCTAGAAGCCAATAACTTCGTATAATGTATGCTATACGAAGTTATGGGGA CTTCCCATTACACCTTCTACATACCACATGGTCCCTGCATGCAGAGTTTTT TTCTAAGCCTACCACCCACCCCAACTCTTACACAAAATGTCTGCACTG GTATGTACAACAGTCTCATGTGCTCATGTCTTCTTTCTAATAGCCCTGTG AAGCCAGAGGAAATGGACTGGTCTGAGCTTTACCCAGAGTTCTTTGCTCC GCTTATTCAAATAAGAGCCATGATGATCCAAAAGATGAGAAAGAAAAG CACTCTGGGGCCCAAGTGGAGTTTGCAGACATAGGCTGTGGCTATGGTGG CTTGTTAGGTAATAAGCTCGCCCTTTTCTTGGGACAGGGAGAGGCCTGGG TTCTGCCATCTCAGCAGGTTAGAGGCAGGATTAGTTGACCTTTCCTCCTG GGACCAGACAGCAGTGACATCAGTGTGGAGAGCCTCCACCTTCCTTCTAC TCTGGGTCATAACTTCGTATAATGTATGCTATACGAAGTTATTGTGGCCTT TGCCCTGGAGGAGGGAGGGGCTGCCTCAGATGTATCTGAGAACCCCGG TTGTTCTGTCTAGCTCCAGTGGCTCCAGTCCCTCCGTGAGCCATTCCACTG CCTTGTGCTGGGTCAGTGAGCCGGGTCAGCACAAGCGTCAGAGATCAGCT CCAGTGGCCACTGATCCTGAA

Table 14. Sequences of the oligonucleotides synthesized for the generation of edited *Mettl1*^{lox/lox} mice.

7.4. Prostate dissociation for analysis of prostate cell populations

For characterization of cell populations present in the prostate of $Pten^{flox/flox} \times PbCre \times Mettl1^{+/+}$ and $Pten^{flox/flox} \times PbCre \times Mettl1^{fl/fl}$ mice, the ventral (V), dorsal (D) and apical (AP) prostate lobes of 5-month-old mice were dissected. Then, prostate tissue or tumours were dissociated for 1 hour at 37°C in rotation with DMEM-F12 medium containing 5% FBS and 1x collagenase Type I (ThermoFisher, 17100017) and 1x hyaluronidase (Stem Cell, #07461). After centrifugation, the pellet was incubated or 1 hour at 37°C with 0.25% trypsin, followed by treatment with 5 mg/ml dispase II (Sigma, D4693) and 1 U/μl DNase (Sigma, DN25) for 30 min at 37°C. Dissociated cells were then filtered through a 0.45 μm cell strainer and stained for different prostate populations with specific fluorochrome or biotin-labelled antibodies (Table 15) for 15-30 min in the dark. For visualised biotin-labelled antibodies, a second incubation of 20 min in the dark was performed with a secondary streptavidine-eFluor710 labelled antibody. Then, samples were washed, analysed and/or sorted using BD FACS Aria II (BD Biosciences). DAPI gating was used to separate viable from dead cells and Lineage⁻ (CD31, Cd45 and Ter119) to separate epithelial and stromal cells from blood and endothelial cells. CD49f and Sca1 were used to separate prostate populations: stromal ($Sca1^{High}CD49f^{low}$), basal ($Sca1^{High}CD49f^{High}$) and luminal ($Sca1^{Low}CD49f$). Additionally, each of the previous populations were sorted with the epithelial marker CD24, and RNA extraction was performed using Total RNA Purification Plus Kit (NorGen Biotek Corp, 48300) and RT-qPCR was performed as previously described. FACS analysis was performed using FlowJo software.

1 ^{ary} Antibody	Host	Marker	Dilution	Company	Reference
CD24-PE-Cy7	Rat	CD24	1:100	eBioscience	25-0242-80
CD31-Biotin	Rat	Lineage	1:250	eBioscience	13-0311-82
CD45-Biotin	Rat	Lineage	1:500	BD Biosciences	15886978
CD49f-PE	Rat	ITGA6	1:500	eBioscience	12-0495-83
Sca1-APC	Rat	LY6A/E	1:100	eBioscience	17-59581-82
Streptavidine-eFluor710		Biotin	1:100	eBioscience	49-4317-82
Ter119-Biotin	Rat	Lineage	1:100	eBioscience	13-5921-82

Table 15. Primary and secondary antibodies used for flow cytometry sorting of mouse prostate populations. The host specie, dilution and reference of the product are indicated.

7.5. mRNA expression in PCa mouse model

The transcriptomic analysis in mouse prostate samples was performed in collaboration with Professor A. Carracedo (CIC bioGUNE) and Dr Tomas DiDomenico (CNIO). Briefly, RNA from four biological replicates per genotype was extracted from tissues as previously described. Tissues from $Pten^{flox/flox} \times PbCre$ and WT mice at 3 and 6 months of age were collected. RNA concentration and integrity were evaluated using Qubit RNA HS Assay Kit (Thermo Fisher Scientific, Q32855) and

Agilent RNA 6000 Nano Chips (Agilent Technologies, 5067-1511), respectively. Sequencing libraries, which were performed at the Genomics Unit at CIC bioGUNE, were prepared using TruSeq Stranded Total RNA Human/Mouse/Rat kit (Illumina Inc., RS-122-2201), following TruSeq Stranded Total RNA Sample Prep-guide (Part # 15031048 Rev. E). 500 ng of total RNA were treated for rRNA depletion followed by RNA purification and fragmentation. cDNA first strand was synthesised with SuperScript-II Reverse Transcriptase (Thermo Fisher Scientific, 18064-014). cDNA second strand was synthesised with Illumina reagents at 16°C for 1 hour. Then, A-tailing and adaptor ligation were performed. Finally, enrichment of libraries was achieved by PCR. All samples were multiplexed and sequenced in HiSeq4000 platform (Illumina).

Sequenced reads were analysed using the nextpresso pipeline³⁴⁶ as follows. Sequencing quality was checked with FastQC v0.11.7 (<http://www.bioinformatics.babraham.ac.uk/projects/fastqc/>). Reads were aligned to the mouse reference genome GRCm38 with TopHat-2.0.10 using Bowtie 1.0.0 and SAMtools0.1.19, allowing two mismatches and twenty multihits. Read counts were obtained with HTSeq-count v0.6.1, using the mouse GRCm38 gene annotation. Differential expression was performed with DESeq2(6), using a 0.05 FDR. GSEAPreranked³⁴⁷ was used to perform gene set enrichment analysis for several gene signatures on a pre-ranked gene list, setting 1000 gene set permutations. Only those gene sets with significant enrichment levels (FDR q-value < 0.25) were considered.

8. PCa patient samples

RNA and protein samples from prostate patients were obtained from a collaboration with Dr. Miguel Unda at Hospital Universitario Basurto (Bilbao). RNA and protein samples from prostate patients with hyperplasia or developed prostate cancer were obtained upon informed consent and with evaluation and approval from the corresponding ethics committee (CEIC code OHEUN11-12 and OHEUN14-14) and described elsewhere³⁴⁸. Paraffin-embedded prostate samples and data from patients included in this study were provided by the Biobank Hospital Universitario Puerta de Hierro Majadahonda (HUPHM)/Instituto de Investigación Sanitaria Puerta de Hierro-Segovia de Arana (IDIPHISA) (PT17/0015/0020 in the Spanish National Biobanks Network), they were processed following standard operating procedures with the appropriate approval of the Ethics and Scientific Committees.

9. *In silico* analysis of gene expression and mutation load data from human prostate tumour data sets

For analysis of expression levels in different diseases status or recurrence in human prostate tumours, CANCEERTOOL²⁸⁷ was combined with complementary analysis on various data sets^{36,43,44,46,289,297}. The obtained data were pre-processed, background corrected, and log₂ transformation and quantile normalization according to²⁸⁷. Differential expression was computed by means of Z-scores as the

number of standard deviations of expression of cancerous samples relative to mean of expression in a reference population (Primary Tumour vs Normal and Metastasis versus Normal). For evaluation of statistical differences between the diverse groups, ANOVA test was performed. Finally, coherence was calculated as the percentage of data sets in which the gene is significant out of the number of data sets in which the gene appears (ANOVA P-value significant value < 0.05). Only genes with consistent differential expression in at least 3 data sets and 75% of coherence were considered as significant. Correlation analyses (Pearson's correlations), data^{36,43,46,297} were retrieved from CANCEERTOOL²⁸⁷.

For disease-free survival, TCGA³⁶ expression data were organised into deciles. Cox proportional-hazards model was performed to evaluate the association between survival time of patients and expression levels of primary tumours. For the analysis of biochemical recurrence free survival of patient groups from Cambridge and Stockholm cohorts, data were retrieved from camcAPP²⁹¹.

Genomic alteration analysis was performed from data from prostate cancer patients from^{36,44,45,49}. The sequence of coding regions of indicated genes of all tumours was compared with genome reference GRCh38.p11. Percentage of insertions, deletions and mutations of primary tumours and metastatic patients was computed.

REFERENCES



REFERENCES

- 1 Sung, H. *et al.* Global Cancer Statistics 2020: GLOBOCAN Estimates of Incidence and Mortality Worldwide for 36 Cancers in 185 Countries. *CA Cancer J Clin* **71**, 209-249 (2021). <https://doi.org:10.3322/caac.21660>
- 2 Rawla, P. Epidemiology of Prostate Cancer. *World J Oncol* **10**, 63-89 (2019). <https://doi.org:10.14740/wjon1191>
- 3 McNeal, J. E. Normal histology of the prostate. *Am J Surg Pathol* **12**, 619-633 (1988). <https://doi.org:10.1097/00000478-198808000-00003>
- 4 Oliveira, D. S. M. *et al.* The mouse prostate: a basic anatomical and histological guideline. <https://www.bjbms.org/ojs/index.php/bjbms> (2020). <https://doi.org:https://www.bjbms.org/ojs/index.php/bjbms/article/view/917>
- 5 van Leenders, G. J. & Schalken, J. A. Epithelial cell differentiation in the human prostate epithelium: implications for the pathogenesis and therapy of prostate cancer. *Crit Rev Oncol Hematol* **46 Suppl**, S3-10 (2003). [https://doi.org:10.1016/s1040-8428\(03\)00059-3](https://doi.org:10.1016/s1040-8428(03)00059-3)
- 6 Xin, L. Cells of Origin for Prostate Cancer. *Adv Exp Med Biol* **1210**, 67-86 (2019). https://doi.org:10.1007/978-3-030-32656-2_4
- 7 Brawer, M. K. Prostatic intraepithelial neoplasia: an overview. *Rev Urol* **7 Suppl 3**, S11-18 (2005).
- 8 Wu, X., Gong, S., Roy-Burman, P., Lee, P. & Culig, Z. Current mouse and cell models in prostate cancer research. *Endocr Relat Cancer* **20**, R155-170 (2013). <https://doi.org:10.1530/ERC-12-0285>
- 9 Shen, M. M. & Abate-Shen, C. Molecular genetics of prostate cancer: new prospects for old challenges. *Genes Dev* **24**, 1967-2000 (2010). <https://doi.org:10.1101/gad.1965810>
- 10 Zhang, D. *et al.* Developing a Novel Two-Dimensional Culture System to Enrich Human Prostate Luminal Progenitors that Can Function as a Cell of Origin for Prostate Cancer. *Stem Cells Transl Med* **6**, 748-760 (2017). <https://doi.org:10.5966/sctm.2016-0243>
- 11 Chua, C. W. *et al.* Single luminal epithelial progenitors can generate prostate organoids in culture. *Nat Cell Biol* **16**, 951-961, 951-954 (2014). <https://doi.org:10.1038/ncb3047>
- 12 Karthaus, W. R. *et al.* Identification of multipotent luminal progenitor cells in human prostate organoid cultures. *Cell* **159**, 163-175 (2014). <https://doi.org:10.1016/j.cell.2014.08.017>
- 13 Wang, X. *et al.* A luminal epithelial stem cell that is a cell of origin for prostate cancer. *Nature* **461**, 495-500 (2009). <https://doi.org:10.1038/nature08361>
- 14 Yoo, Y. A. *et al.* Bmi1 marks distinct castration-resistant luminal progenitor cells competent for prostate regeneration and tumour initiation. *Nat Commun* **7**, 12943 (2016). <https://doi.org:10.1038/ncomms12943>
- 15 Lawson, D. A. *et al.* Basal epithelial stem cells are efficient targets for prostate cancer initiation. *Proc Natl Acad Sci U S A* **107**, 2610-2615 (2010). <https://doi.org:10.1073/pnas.0913873107>
- 16 Goldstein, A. S., Huang, J., Guo, C., Garraway, I. P. & Witte, O. N. Identification of a cell of origin for human prostate cancer. *Science* **329**, 568-571 (2010). <https://doi.org:10.1126/science.1189992>
- 17 Choi, N., Zhang, B., Zhang, L., Ittmann, M. & Xin, L. Adult murine prostate basal and luminal cells are self-sustained lineages that can both serve as targets for prostate cancer initiation. *Cancer Cell* **21**, 253-265 (2012). <https://doi.org:10.1016/j.ccr.2012.01.005>
- 18 Zhang, D., Zhao, S., Li, X., Kirk, J. S. & Tang, D. G. Prostate Luminal Progenitor Cells in Development and Cancer. *Trends Cancer* **4**, 769-783 (2018). <https://doi.org:10.1016/j.trecan.2018.09.003>
- 19 Lu, T. L. *et al.* Conditionally ablated Pten in prostate basal cells promotes basal-to-luminal differentiation and causes invasive prostate cancer in mice. *Am J Pathol* **182**, 975-991 (2013). <https://doi.org:10.1016/j.ajpath.2012.11.025>

- 20 Wang, Z. A. *et al.* Lineage analysis of basal epithelial cells reveals their unexpected plasticity and supports a cell-of-origin model for prostate cancer heterogeneity. *Nat Cell Biol* **15**, 274-283 (2013). <https://doi.org:10.1038/ncb2697>
- 21 Wang, Z., Toivanen, R., Bergren, S. K., Chambon, P. & Shen, M. M. Luminal cells are favored as the cell of origin for prostate cancer. *Cell Rep* **8**, 1339-1346 (2014). <https://doi.org:10.1016/j.celrep.2014.08.002>
- 22 Barron, D. A. & Rowley, D. R. The reactive stroma microenvironment and prostate cancer progression. *Endocr Relat Cancer* **19**, R187-204 (2012). <https://doi.org:10.1530/ERC-12-0085>
- 23 Trewartha, D. & Carter, K. Advances in prostate cancer treatment. *Nat Rev Drug Discov* **12**, 823-824 (2013). <https://doi.org:10.1038/nrd4068>
- 24 Sekhoacha, M. *et al.* Prostate Cancer Review: Genetics, Diagnosis, Treatment Options, and Alternative Approaches. *Molecules* **27** (2022). <https://doi.org:10.3390/molecules27175730>
- 25 Francini, E. & Taplin, M. E. Prostate cancer: Developing novel approaches to castration-sensitive disease. *Cancer* **123**, 29-42 (2017). <https://doi.org:10.1002/cncr.30329>
- 26 Mansinho, A., Macedo, D., Fernandes, I. & Costa, L. Castration-Resistant Prostate Cancer: Mechanisms, Targets and Treatment. *Adv Exp Med Biol* **1096**, 117-133 (2018). https://doi.org:10.1007/978-3-319-99286-0_7
- 27 Ryan, C. J. *et al.* Abiraterone in metastatic prostate cancer without previous chemotherapy. *N Engl J Med* **368**, 138-148 (2013). <https://doi.org:10.1056/NEJMoa1209096>
- 28 Attard, G. *et al.* Selective inhibition of CYP17 with abiraterone acetate is highly active in the treatment of castration-resistant prostate cancer. *J Clin Oncol* **27**, 3742-3748 (2009). <https://doi.org:10.1200/JCO.2008.20.0642>
- 29 Beer, T. M. *et al.* Enzalutamide in metastatic prostate cancer before chemotherapy. *N Engl J Med* **371**, 424-433 (2014). <https://doi.org:10.1056/NEJMoa1405095>
- 30 de Bono, J. S. *et al.* Prednisone plus cabazitaxel or mitoxantrone for metastatic castration-resistant prostate cancer progressing after docetaxel treatment: a randomised open-label trial. *Lancet* **376**, 1147-1154 (2010). [https://doi.org:10.1016/S0140-6736\(10\)61389-X](https://doi.org:10.1016/S0140-6736(10)61389-X)
- 31 Kantoff, P. W. *et al.* Sipuleucel-T immunotherapy for castration-resistant prostate cancer. *N Engl J Med* **363**, 411-422 (2010). <https://doi.org:10.1056/NEJMoa1001294>
- 32 Mateo, J. *et al.* DNA-Repair Defects and Olaparib in Metastatic Prostate Cancer. *N Engl J Med* **373**, 1697-1708 (2015). <https://doi.org:10.1056/NEJMoa1506859>
- 33 Le, D. T. *et al.* Mismatch repair deficiency predicts response of solid tumors to PD-1 blockade. *Science* **357**, 409-413 (2017). <https://doi.org:10.1126/science.aan6733>
- 34 Huggins, C. & Hodges, C. V. Studies on prostatic cancer: I. The effect of castration, of estrogen and of androgen injection on serum phosphatases in metastatic carcinoma of the prostate. 1941. *J Urol* **168**, 9-12 (2002). [https://doi.org:10.1016/s0022-5347\(05\)64820-3](https://doi.org:10.1016/s0022-5347(05)64820-3)
- 35 Ruggero, K., Farran-Matas, S., Martinez-Tebar, A. & Aytes, A. Epigenetic Regulation in Prostate Cancer Progression. *Curr Mol Biol Rep* **4**, 101-115 (2018). <https://doi.org:10.1007/s40610-018-0095-9>
- 36 Cancer Genome Atlas Research, N. The Molecular Taxonomy of Primary Prostate Cancer. *Cell* **163**, 1011-1025 (2015). <https://doi.org:10.1016/j.cell.2015.10.025>
- 37 Taavitsainen, S. *et al.* Single-cell ATAC and RNA sequencing reveal pre-existing and persistent cells associated with prostate cancer relapse. *Nat Commun* **12**, 5307 (2021). <https://doi.org:10.1038/s41467-021-25624-1>
- 38 Sztupinszki, Z. *et al.* Detection of Molecular Signatures of Homologous Recombination Deficiency in Prostate Cancer with or without BRCA1/2 Mutations. *Clin Cancer Res* **26**, 2673-2680 (2020). <https://doi.org:10.1158/1078-0432.CCR-19-2135>
- 39 Quigley, D. A. *et al.* Genomic Hallmarks and Structural Variation in Metastatic Prostate Cancer. *Cell* **174**, 758-769 e759 (2018). <https://doi.org:10.1016/j.cell.2018.06.039>
- 40 Armenia, J. *et al.* The long tail of oncogenic drivers in prostate cancer. *Nat Genet* **50**, 645-651 (2018). <https://doi.org:10.1038/s41588-018-0078-z>
- 41 Pritchard, C. C. *et al.* Inherited DNA-Repair Gene Mutations in Men with Metastatic Prostate Cancer. *N Engl J Med* **375**, 443-453 (2016). <https://doi.org:10.1056/NEJMoa1603144>

- 42 Consortium, E. P. *et al.* Expanded encyclopaedias of DNA elements in the human and mouse
genomes. *Nature* **583**, 699-710 (2020). <https://doi.org:10.1038/s41586-020-2493-4>
- 43 Grasso, C. S. *et al.* The mutational landscape of lethal castration-resistant prostate cancer.
Nature **487**, 239-243 (2012). <https://doi.org:10.1038/nature11125>
- 44 Taylor, B. S. *et al.* Integrative genomic profiling of human prostate cancer. *Cancer Cell* **18**,
11-22 (2010). <https://doi.org:10.1016/j.ccr.2010.05.026>
- 45 Fraser, M. *et al.* Genomic hallmarks of localized, non-indolent prostate cancer. *Nature* **541**,
359-364 (2017). <https://doi.org:10.1038/nature20788>
- 46 Varambally, S. *et al.* Integrative genomic and proteomic analysis of prostate cancer reveals
signatures of metastatic progression. *Cancer Cell* **8**, 393-406 (2005).
<https://doi.org:10.1016/j.ccr.2005.10.001>
- 47 Barbieri, C. E. *et al.* Exome sequencing identifies recurrent SPOP, FOXA1 and MED12
mutations in prostate cancer. *Nat Genet* **44**, 685-689 (2012). <https://doi.org:10.1038/ng.2279>
- 48 Beltran, H. *et al.* Divergent clonal evolution of castration-resistant neuroendocrine prostate
cancer. *Nat Med* **22**, 298-305 (2016). <https://doi.org:10.1038/nm.4045>
- 49 Robinson, D. *et al.* Integrative clinical genomics of advanced prostate cancer. *Cell* **161**,
1215-1228 (2015). <https://doi.org:10.1016/j.cell.2015.05.001>
- 50 Jenkins, R. B., Qian, J., Lieber, M. M. & Bostwick, D. G. Detection of c-myc oncogene
amplification and chromosomal anomalies in metastatic prostatic carcinoma by fluorescence
in situ hybridization. *Cancer Res* **57**, 524-531 (1997).
- 51 Visakorpi, T. *et al.* In vivo amplification of the androgen receptor gene and progression of
human prostate cancer. *Nat Genet* **9**, 401-406 (1995). <https://doi.org:10.1038/ng0495-401>
- 52 Pourmand, G. *et al.* Role of PTEN gene in progression of prostate cancer. *Urol J* **4**, 95-100
(2007).
- 53 Yoshimoto, M. *et al.* Interphase FISH analysis of PTEN in histologic sections shows
genomic deletions in 68% of primary prostate cancer and 23% of high-grade prostatic intra-
epithelial neoplasias. *Cancer Genet Cytogenet* **169**, 128-137 (2006).
<https://doi.org:10.1016/j.cancergencyto.2006.04.003>
- 54 Holcomb, I. N. *et al.* Comparative analyses of chromosome alterations in soft-tissue
metastases within and across patients with castration-resistant prostate cancer. *Cancer Res*
69, 7793-7802 (2009). <https://doi.org:10.1158/0008-5472.CAN-08-3810>
- 55 Barbieri, C. E., Chinnaiyan, A. M., Lerner, S. P., Swanton, C. & Rubin, M. A. The
Emergence of Precision Urologic Oncology: A Collaborative Review on Biomarker-driven
Therapeutics. *Eur Urol* **71**, 237-246 (2017). <https://doi.org:10.1016/j.eururo.2016.08.024>
- 56 Wang, G., Zhao, D., Spring, D. J. & DePinho, R. A. Genetics and biology of prostate cancer.
Genes Dev **32**, 1105-1140 (2018). <https://doi.org:10.1101/gad.315739.118>
- 57 Kinney, S. R. *et al.* Opposing roles of Dnmt1 in early- and late-stage murine prostate cancer.
Mol Cell Biol **30**, 4159-4174 (2010). <https://doi.org:10.1128/MCB.00235-10>
- 58 Varambally, S. *et al.* The polycomb group protein EZH2 is involved in progression of
prostate cancer. *Nature* **419**, 624-629 (2002). <https://doi.org:10.1038/nature01075>
- 59 Xu, K. *et al.* EZH2 oncogenic activity in castration-resistant prostate cancer cells is
Polycomb-independent. *Science* **338**, 1465-1469 (2012).
<https://doi.org:10.1126/science.1227604>
- 60 Lin, P. C. *et al.* Epigenomic alterations in localized and advanced prostate cancer. *Neoplasia*
15, 373-383 (2013). <https://doi.org:10.1593/neo.122146>
- 61 Martignano, F. *et al.* GSTP1 Methylation and Protein Expression in Prostate Cancer:
Diagnostic Implications. *Dis Markers* **2016**, 4358292 (2016).
<https://doi.org:10.1155/2016/4358292>
- 62 Mahon, K. L. *et al.* Methylated Glutathione S-transferase 1 (mGSTP1) is a potential plasma
free DNA epigenetic marker of prognosis and response to chemotherapy in castrate-resistant
prostate cancer. *Br J Cancer* **111**, 1802-1809 (2014). <https://doi.org:10.1038/bjc.2014.463>
- 63 Suzuki, H., Ueda, T., Ichikawa, T. & Ito, H. Androgen receptor involvement in the
progression of prostate cancer. *Endocr Relat Cancer* **10**, 209-216 (2003).
<https://doi.org:10.1677/erc.0.0100209>

- 64 Jarrard, D. F. *et al.* Deletional, mutational, and methylation analyses of CDKN2 (p16/MTS1) in primary and metastatic prostate cancer. *Genes Chromosomes Cancer* **19**, 90-96 (1997).
- 65 Pakneshan, P., Xing, R. H. & Rabbani, S. A. Methylation status of uPA promoter as a molecular mechanism regulating prostate cancer invasion and growth in vitro and in vivo. *FASEB J* **17**, 1081-1088 (2003). <https://doi.org:10.1096/fj.02-0973com>
- 66 Ashour, N. *et al.* A DNA hypermethylation profile reveals new potential biomarkers for prostate cancer diagnosis and prognosis. *Prostate* **74**, 1171-1182 (2014). <https://doi.org:10.1002/pros.22833>
- 67 Wu, X. *et al.* Generation of a prostate epithelial cell-specific Cre transgenic mouse model for tissue-specific gene ablation. *Mech Dev* **101**, 61-69 (2001). [https://doi.org:10.1016/s0925-4773\(00\)00551-7](https://doi.org:10.1016/s0925-4773(00)00551-7)
- 68 Hubbard, G. K. *et al.* Combined MYC Activation and Pten Loss Are Sufficient to Create Genomic Instability and Lethal Metastatic Prostate Cancer. *Cancer Res* **76**, 283-292 (2016). <https://doi.org:10.1158/0008-5472.CAN-14-3280>
- 69 Gingrich, J. R. *et al.* Metastatic prostate cancer in a transgenic mouse. *Cancer Res* **56**, 4096-4102 (1996).
- 70 Ahuja, D., Saenz-Robles, M. T. & Pipas, J. M. SV40 large T antigen targets multiple cellular pathways to elicit cellular transformation. *Oncogene* **24**, 7729-7745 (2005). <https://doi.org:10.1038/sj.onc.1209046>
- 71 Irshad, S. & Abate-Shen, C. Modeling prostate cancer in mice: something old, something new, something premalignant, something metastatic. *Cancer Metastasis Rev* **32**, 109-122 (2013). <https://doi.org:10.1007/s10555-012-9409-1>
- 72 Ahmad, I., Sansom, O. J. & Leung, H. Y. The role of murine models of prostate cancer in drug target discovery and validation. *Expert Opin Drug Discov* **4**, 879-888 (2009). <https://doi.org:10.1517/17460440903049308>
- 73 Grabowska, M. M. *et al.* Mouse models of prostate cancer: picking the best model for the question. *Cancer Metastasis Rev* **33**, 377-397 (2014). <https://doi.org:10.1007/s10555-013-9487-8>
- 74 Song, M. S., Salmena, L. & Pandolfi, P. P. The functions and regulation of the PTEN tumour suppressor. *Nat Rev Mol Cell Biol* **13**, 283-296 (2012). <https://doi.org:10.1038/nrm3330>
- 75 Podsypanina, K. *et al.* Mutation of Pten/Mmac1 in mice causes neoplasia in multiple organ systems. *Proc Natl Acad Sci U S A* **96**, 1563-1568 (1999). <https://doi.org:10.1073/pnas.96.4.1563>
- 76 Di Cristofano, A., Pesce, B., Cordon-Cardo, C. & Pandolfi, P. P. Pten is essential for embryonic development and tumour suppression. *Nat Genet* **19**, 348-355 (1998). <https://doi.org:10.1038/1235>
- 77 Trotman, L. C. *et al.* Pten dose dictates cancer progression in the prostate. *PLoS Biol* **1**, E59 (2003). <https://doi.org:10.1371/journal.pbio.0000059>
- 78 Maddison, L. A., Nahm, H., DeMayo, F. & Greenberg, N. M. Prostate specific expression of Cre recombinase in transgenic mice. *Genesis* **26**, 154-156 (2000). [https://doi.org:10.1002/\(sici\)1526-968x\(200002\)26:2<154::aid-gene18>3.0.co;2-2](https://doi.org:10.1002/(sici)1526-968x(200002)26:2<154::aid-gene18>3.0.co;2-2)
- 79 Chen, Z. *et al.* Crucial role of p53-dependent cellular senescence in suppression of Pten-deficient tumorigenesis. *Nature* **436**, 725-730 (2005). <https://doi.org:10.1038/nature03918>
- 80 Floc'h, N. *et al.* Dual targeting of the Akt/mTOR signaling pathway inhibits castration-resistant prostate cancer in a genetically engineered mouse model. *Cancer Res* **72**, 4483-4493 (2012). <https://doi.org:10.1158/0008-5472.CAN-12-0283>
- 81 Aytes, A. *et al.* ETV4 promotes metastasis in response to activation of PI3-kinase and Ras signaling in a mouse model of advanced prostate cancer. *Proc Natl Acad Sci U S A* **110**, E3506-3515 (2013). <https://doi.org:10.1073/pnas.1303558110>
- 82 Ellwood-Yen, K. *et al.* Myc-driven murine prostate cancer shares molecular features with human prostate tumors. *Cancer Cell* **4**, 223-238 (2003). [https://doi.org:10.1016/s1535-6108\(03\)00197-1](https://doi.org:10.1016/s1535-6108(03)00197-1)
- 83 Bleijs, M., van de Wetering, M., Clevers, H. & Drost, J. Xenograft and organoid model systems in cancer research. *EMBO J* **38**, e101654 (2019). <https://doi.org:10.15252/embj.2019101654>

- 84 DiMasi, J. A., Reichert, J. M., Feldman, L. & Malins, A. Clinical approval success rates for investigational cancer drugs. *Clin Pharmacol Ther* **94**, 329-335 (2013). <https://doi.org:10.1038/clpt.2013.117>
- 85 Byrne, A. T. *et al.* Interrogating open issues in cancer precision medicine with patient-derived xenografts. *Nat Rev Cancer* **17**, 254-268 (2017). <https://doi.org:10.1038/nrc.2016.140>
- 86 Shultz, L. D. *et al.* Human lymphoid and myeloid cell development in NOD/LtSz-scid IL2R gamma null mice engrafted with mobilized human hemopoietic stem cells. *J Immunol* **174**, 6477-6489 (2005). <https://doi.org:10.4049/jimmunol.174.10.6477>
- 87 Fichtner, I. *et al.* Anticancer drug response and expression of molecular markers in early-passage xenotransplanted colon carcinomas. *Eur J Cancer* **40**, 298-307 (2004). <https://doi.org:10.1016/j.ejca.2003.10.011>
- 88 Kim, M. P. *et al.* Generation of orthotopic and heterotopic human pancreatic cancer xenografts in immunodeficient mice. *Nat Protoc* **4**, 1670-1680 (2009). <https://doi.org:10.1038/nprot.2009.171>
- 89 Beckhove, P. *et al.* Efficient engraftment of human primary breast cancer transplants in nonconditioned NOD/Scid mice. *Int J Cancer* **105**, 444-453 (2003). <https://doi.org:10.1002/ijc.11125>
- 90 Cutz, J. C. *et al.* Establishment in severe combined immunodeficiency mice of subrenal capsule xenografts and transplantable tumor lines from a variety of primary human lung cancers: potential models for studying tumor progression-related changes. *Clin Cancer Res* **12**, 4043-4054 (2006). <https://doi.org:10.1158/1078-0432.CCR-06-0252>
- 91 Taetle, R. *et al.* Use of nude mouse xenografts as preclinical screens. Characterization of xenograft-derived melanoma cell lines. *Cancer* **60**, 1836-1841 (1987). [https://doi.org:10.1002/1097-0142\(19871015\)60:8<1836::aid-cnrc2820600827>3.0.co;2-o](https://doi.org:10.1002/1097-0142(19871015)60:8<1836::aid-cnrc2820600827>3.0.co;2-o)
- 92 Hennessey, P. T. *et al.* Promoter methylation in head and neck squamous cell carcinoma cell lines is significantly different than methylation in primary tumors and xenografts. *PLoS One* **6**, e20584 (2011). <https://doi.org:10.1371/journal.pone.0020584>
- 93 Wang, Y. *et al.* Development and characterization of efficient xenograft models for benign and malignant human prostate tissue. *Prostate* **64**, 149-159 (2005). <https://doi.org:10.1002/pros.20225>
- 94 George, E. *et al.* A patient-derived-xenograft platform to study BRCA-deficient ovarian cancers. *JCI Insight* **2**, e89760 (2017). <https://doi.org:10.1172/jci.insight.89760>
- 95 Dai, L., Lu, C., Yu, X. I., Dai, L. J. & Zhou, J. X. Construction of orthotopic xenograft mouse models for human pancreatic cancer. *Exp Ther Med* **10**, 1033-1038 (2015). <https://doi.org:10.3892/etm.2015.2642>
- 96 Shi, J., Li, Y., Jia, R. & Fan, X. The fidelity of cancer cells in PDX models: Characteristics, mechanism and clinical significance. *Int J Cancer* **146**, 2078-2088 (2020). <https://doi.org:10.1002/ijc.32662>
- 97 Ben-David, U. *et al.* Patient-derived xenografts undergo mouse-specific tumor evolution. *Nat Genet* **49**, 1567-1575 (2017). <https://doi.org:10.1038/ng.3967>
- 98 Julien, S. *et al.* Characterization of a large panel of patient-derived tumor xenografts representing the clinical heterogeneity of human colorectal cancer. *Clin Cancer Res* **18**, 5314-5328 (2012). <https://doi.org:10.1158/1078-0432.CCR-12-0372>
- 99 Kondo, J. & Inoue, M. Application of Cancer Organoid Model for Drug Screening and Personalized Therapy. *Cells* **8** (2019). <https://doi.org:10.3390/cells8050470>
- 100 Granat, L. M. *et al.* The promises and challenges of patient-derived tumor organoids in drug development and precision oncology. *Animal Model Exp Med* **2**, 150-161 (2019). <https://doi.org:10.1002/ame2.12077>
- 101 Karkampouna, S. *et al.* Patient-derived xenografts and organoids model therapy response in prostate cancer. *Nat Commun* **12**, 1117 (2021). <https://doi.org:10.1038/s41467-021-21300-6>
- 102 McCulloch, D. R., Opeskin, K., Thompson, E. W. & Williams, E. D. BM18: A novel androgen-dependent human prostate cancer xenograft model derived from a bone metastasis. *Prostate* **65**, 35-43 (2005). <https://doi.org:10.1002/pros.20255>

- 103 Craft, N. *et al.* Evidence for clonal outgrowth of androgen-independent prostate cancer cells from androgen-dependent tumors through a two-step process. *Cancer Res* **59**, 5030-5036 (1999).
- 104 Delaunay, S. & Frye, M. RNA modifications regulating cell fate in cancer. *Nat Cell Biol* **21**, 552-559 (2019). <https://doi.org/10.1038/s41556-019-0319-0>
- 105 Nombela, P., Miguel-Lopez, B. & Blanco, S. The role of m(6)A, m(5)C and Psi RNA modifications in cancer: Novel therapeutic opportunities. *Mol Cancer* **20**, 18 (2021). <https://doi.org/10.1186/s12943-020-01263-w>
- 106 Barbieri, I. & Kouzarides, T. Role of RNA modifications in cancer. *Nat Rev Cancer* **20**, 303-322 (2020). <https://doi.org/10.1038/s41568-020-0253-2>
- 107 Haruehanroengra, P., Zheng, Y. Y., Zhou, Y., Huang, Y. & Sheng, J. RNA modifications and cancer. *RNA Biol* **17**, 1560-1575 (2020). <https://doi.org/10.1080/15476286.2020.1722449>
- 108 Boccaletto, P. *et al.* MODOMICS: a database of RNA modification pathways. 2021 update. *Nucleic Acids Res* **50**, D231-D235 (2022). <https://doi.org/10.1093/nar/gkab1083>
- 109 Jonkhout, N. *et al.* The RNA modification landscape in human disease. *RNA* **23**, 1754-1769 (2017). <https://doi.org/10.1261/rna.063503.117>
- 110 Frye, M. & Blanco, S. Post-transcriptional modifications in development and stem cells. *Development* **143**, 3871-3881 (2016). <https://doi.org/10.1242/dev.136556>
- 111 Frye, M., Harada, B. T., Behm, M. & He, C. RNA modifications modulate gene expression during development. *Science* **361**, 1346-1349 (2018). <https://doi.org/10.1126/science.aau1646>
- 112 Basanta-Sanchez, M., Temple, S., Ansari, S. A., D'Amico, A. & Agris, P. F. Attomole quantification and global profile of RNA modifications: Epitranscriptome of human neural stem cells. *Nucleic Acids Res* **44**, e26 (2016). <https://doi.org/10.1093/nar/gkv971>
- 113 Jia, G. *et al.* Oxidative demethylation of 3-methylthymine and 3-methyluracil in single-stranded DNA and RNA by mouse and human FTO. *FEBS Lett* **582**, 3313-3319 (2008). <https://doi.org/10.1016/j.febslet.2008.08.019>
- 114 Ontiveros, R. J., Stoute, J. & Liu, K. F. The chemical diversity of RNA modifications. *Biochem J* **476**, 1227-1245 (2019). <https://doi.org/10.1042/BCJ20180445>
- 115 Esteve-Puig, R., Bueno-Costa, A. & Esteller, M. Writers, readers and erasers of RNA modifications in cancer. *Cancer Lett* **474**, 127-137 (2020). <https://doi.org/10.1016/j.canlet.2020.01.021>
- 116 Jia, G. *et al.* N6-methyladenosine in nuclear RNA is a major substrate of the obesity-associated FTO. *Nat Chem Biol* **7**, 885-887 (2011). <https://doi.org/10.1038/nchembio.687>
- 117 Zheng, G. *et al.* ALKBH5 is a mammalian RNA demethylase that impacts RNA metabolism and mouse fertility. *Mol Cell* **49**, 18-29 (2013). <https://doi.org/10.1016/j.molcel.2012.10.015>
- 118 Liao, S., Sun, H. & Xu, C. YTH Domain: A Family of N(6)-methyladenosine (m(6)A) Readers. *Genomics Proteomics Bioinformatics* **16**, 99-107 (2018). <https://doi.org/10.1016/j.gpb.2018.04.002>
- 119 Yang, X. *et al.* 5-methylcytosine promotes mRNA export - NSUN2 as the methyltransferase and ALYREF as an m(5)C reader. *Cell Res* **27**, 606-625 (2017). <https://doi.org/10.1038/cr.2017.55>
- 120 Phizicky, E. M. & Hopper, A. K. tRNA biology charges to the front. *Genes Dev* **24**, 1832-1860 (2010). <https://doi.org/10.1101/gad.1956510>
- 121 Lyons, S. M., Fay, M. M. & Ivanov, P. The role of RNA modifications in the regulation of tRNA cleavage. *FEBS Lett* **592**, 2828-2844 (2018). <https://doi.org/10.1002/1873-3468.13205>
- 122 Berg, M. D. & Brandl, C. J. Transfer RNAs: diversity in form and function. *RNA Biol* **18**, 316-339 (2021). <https://doi.org/10.1080/15476286.2020.1809197>
- 123 Pan, T. Modifications and functional genomics of human transfer RNA. *Cell Res* **28**, 395-404 (2018). <https://doi.org/10.1038/s41422-018-0013-y>
- 124 Asano, K. *et al.* Metabolic and chemical regulation of tRNA modification associated with taurine deficiency and human disease. *Nucleic Acids Res* **46**, 1565-1583 (2018). <https://doi.org/10.1093/nar/gky068>

- 125 Schaffrath, R. & Leidel, S. A. Wobble uridine modifications—a reason to live, a reason to
die?! *RNA Biol* **14**, 1209-1222 (2017). <https://doi.org/10.1080/15476286.2017.1295204>
- 126 Chan, C. T. *et al.* Reprogramming of tRNA modifications controls the oxidative stress
response by codon-biased translation of proteins. *Nat Commun* **3**, 937 (2012).
<https://doi.org/10.1038/ncomms1938>
- 127 Ranjan, N. & Rodnina, M. V. tRNA wobble modifications and protein homeostasis.
Translation (Austin) **4**, e1143076 (2016). <https://doi.org/10.1080/21690731.2016.1143076>
- 128 Lorenz, C., Lunse, C. E. & Morl, M. tRNA Modifications: Impact on Structure and Thermal
Adaptation. *Biomolecules* **7** (2017). <https://doi.org/10.3390/biom7020035>
- 129 Kadaba, S. *et al.* Nuclear surveillance and degradation of hypomodified initiator tRNAMet
in *S. cerevisiae*. *Genes Dev* **18**, 1227-1240 (2004). <https://doi.org/10.1101/gad.1183804>
- 130 Schaefer, M. *et al.* RNA methylation by Dnmt2 protects transfer RNAs against stress-
induced cleavage. *Genes Dev* **24**, 1590-1595 (2010). <https://doi.org/10.1101/gad.586710>
- 131 Guzzi, N. *et al.* Pseudouridylation of tRNA-Derived Fragments Steers Translational Control
in Stem Cells. *Cell* **173**, 1204-1216 e1226 (2018). <https://doi.org/10.1016/j.cell.2018.03.008>
- 132 Novoa, E. M., Pavon-Eternod, M., Pan, T. & Ribas de Pouplana, L. A role for tRNA
modifications in genome structure and codon usage. *Cell* **149**, 202-213 (2012).
<https://doi.org/10.1016/j.cell.2012.01.050>
- 133 Gerber, A. P. & Keller, W. An adenosine deaminase that generates inosine at the wobble
position of tRNAs. *Science* **286**, 1146-1149 (1999).
<https://doi.org/10.1126/science.286.5442.1146>
- 134 Gerber, A. P. & Keller, W. RNA editing by base deamination: more enzymes, more targets,
new mysteries. *Trends Biochem Sci* **26**, 376-384 (2001). [https://doi.org/10.1016/s0968-0004\(01\)01827-8](https://doi.org/10.1016/s0968-0004(01)01827-8)
- 135 Alazami, A. M. *et al.* Mutation in ADAT3, encoding adenosine deaminase acting on transfer
RNA, causes intellectual disability and strabismus. *J Med Genet* **50**, 425-430 (2013).
<https://doi.org/10.1136/jmedgenet-2012-101378>
- 136 Guy, M. P. *et al.* Defects in tRNA Anticodon Loop 2'-O-Methylation Are Implicated in
Nonsyndromic X-Linked Intellectual Disability due to Mutations in FTSJ1. *Hum Mutat* **36**,
1176-1187 (2015). <https://doi.org/10.1002/humu.22897>
- 137 Freude, K. *et al.* Mutations in the FTSJ1 gene coding for a novel S-adenosylmethionine-
binding protein cause nonsyndromic X-linked mental retardation. *Am J Hum Genet* **75**, 305-
309 (2004). <https://doi.org/10.1086/422507>
- 138 Rezgui, V. A. *et al.* tRNA tKUUU, tQUUG, and tEUUC wobble position modifications fine-
tune protein translation by promoting ribosome A-site binding. *Proc Natl Acad Sci U S A*
110, 12289-12294 (2013). <https://doi.org/10.1073/pnas.1300781110>
- 139 Zinshteyn, B. & Gilbert, W. V. Loss of a conserved tRNA anticodon modification perturbs
cellular signaling. *PLoS Genet* **9**, e1003675 (2013).
<https://doi.org/10.1371/journal.pgen.1003675>
- 140 Tuorto, F. *et al.* Queuosine-modified tRNAs confer nutritional control of protein translation.
EMBO J **37** (2018). <https://doi.org/10.15252/emboj.201899777>
- 141 Thiaville, P. C. *et al.* Global translational impacts of the loss of the tRNA modification t(6)A
in yeast. *Microb Cell* **3**, 29-45 (2016). <https://doi.org/10.15698/mic2016.01.473>
- 142 Torres, A. G., Batlle, E. & Ribas de Pouplana, L. Role of tRNA modifications in human
diseases. *Trends Mol Med* **20**, 306-314 (2014).
<https://doi.org/10.1016/j.molmed.2014.01.008>
- 143 Tuorto, F. *et al.* The tRNA methyltransferase Dnmt2 is required for accurate polypeptide
synthesis during haematopoiesis. *EMBO J* **34**, 2350-2362 (2015).
<https://doi.org/10.15252/emboj.201591382>
- 144 Mattick, J. S. & Makunin, I. V. Non-coding RNA. *Hum Mol Genet* **15 Spec No 1**, R17-29
(2006). <https://doi.org/10.1093/hmg/ddl046>
- 145 Iorio, M. V. & Croce, C. M. MicroRNA dysregulation in cancer: diagnostics, monitoring
and therapeutics. A comprehensive review. *EMBO Mol Med* **4**, 143-159 (2012).
<https://doi.org/10.1002/emmm.201100209>

- 146 Mendell, J. T. & Olson, E. N. MicroRNAs in stress signaling and human disease. *Cell* **148**,
1172-1187 (2012). <https://doi.org/10.1016/j.cell.2012.02.005>
- 147 Gebetsberger, J. & Polacek, N. Slicing tRNAs to boost functional ncRNA diversity. *RNA Biol* **10**, 1798-1806 (2013). <https://doi.org/10.4161/rna.27177>
- 148 Sobala, A. & Hutvagner, G. Transfer RNA-derived fragments: origins, processing, and
functions. *Wiley Interdiscip Rev RNA* **2**, 853-862 (2011). <https://doi.org/10.1002/wrna.96>
- 149 Wang, Q. *et al.* Identification and functional characterization of tRNA-derived RNA
fragments (tRFs) in respiratory syncytial virus infection. *Mol Ther* **21**, 368-379 (2013).
<https://doi.org/10.1038/mt.2012.237>
- 150 Saikia, M. *et al.* Genome-wide identification and quantitative analysis of cleaved tRNA
fragments induced by cellular stress. *J Biol Chem* **287**, 42708-42725 (2012).
<https://doi.org/10.1074/jbc.M112.371799>
- 151 Yamasaki, S., Ivanov, P., Hu, G. F. & Anderson, P. Angiogenin cleaves tRNA and promotes
stress-induced translational repression. *J Cell Biol* **185**, 35-42 (2009).
<https://doi.org/10.1083/jcb.200811106>
- 152 Emara, M. M. *et al.* Angiogenin-induced tRNA-derived stress-induced RNAs promote
stress-induced stress granule assembly. *J Biol Chem* **285**, 10959-10968 (2010).
<https://doi.org/10.1074/jbc.M109.077560>
- 153 Lee, Y. S., Shibata, Y., Malhotra, A. & Dutta, A. A novel class of small RNAs: tRNA-
derived RNA fragments (tRFs). *Genes Dev* **23**, 2639-2649 (2009).
<https://doi.org/10.1101/gad.1837609>
- 154 Kumar, P., Anaya, J., Mudunuri, S. B. & Dutta, A. Meta-analysis of tRNA derived RNA
fragments reveals that they are evolutionarily conserved and associate with AGO proteins to
recognize specific RNA targets. *BMC Biol* **12**, 78 (2014). <https://doi.org/10.1186/s12915-014-0078-0>
- 155 Anderson, P. & Ivanov, P. tRNA fragments in human health and disease. *FEBS Lett* **588**,
4297-4304 (2014). <https://doi.org/10.1016/j.febslet.2014.09.001>
- 156 Rosace, D., Lopez, J. & Blanco, S. Emerging roles of novel small non-coding regulatory
RNAs in immunity and cancer. *RNA Biol* **17**, 1196-1213 (2020).
<https://doi.org/10.1080/15476286.2020.1737442>
- 157 Haussecker, D. *et al.* Human tRNA-derived small RNAs in the global regulation of RNA
silencing. *RNA* **16**, 673-695 (2010). <https://doi.org/10.1261/rna.2000810>
- 158 Cole, C. *et al.* Filtering of deep sequencing data reveals the existence of abundant Dicer-
dependent small RNAs derived from tRNAs. *RNA* **15**, 2147-2160 (2009).
<https://doi.org/10.1261/rna.1738409>
- 159 Vitali, P. & Kiss, T. Cooperative 2'-O-methylation of the wobble cytidine of human
elongator tRNA(Met)(CAT) by a nucleolar and a Cajal body-specific box C/D RNP. *Genes Dev* **33**, 741-746 (2019). <https://doi.org/10.1101/gad.326363.119>
- 160 Cosentino, C. *et al.* Pancreatic beta-cell tRNA hypomethylation and fragmentation link
TRMT10A deficiency with diabetes. *Nucleic Acids Res* **46**, 10302-10318 (2018).
<https://doi.org/10.1093/nar/gky839>
- 161 Wang, X. *et al.* Queuosine modification protects cognate tRNAs against ribonuclease
cleavage. *RNA* **24**, 1305-1313 (2018). <https://doi.org/10.1261/rna.067033.118>
- 162 Blanco, S. *et al.* Aberrant methylation of tRNAs links cellular stress to neuro-developmental
disorders. *EMBO J* **33**, 2020-2039 (2014). <https://doi.org/10.15252/emboj.201489282>
- 163 Huang, B. *et al.* tRF/miR-1280 Suppresses Stem Cell-like Cells and Metastasis in Colorectal
Cancer. *Cancer Res* **77**, 3194-3206 (2017). <https://doi.org/10.1158/0008-5472.CAN-16-3146>
- 164 Yu, M. *et al.* tRNA-derived RNA fragments in cancer: current status and future perspectives.
J Hematol Oncol **13**, 121 (2020). <https://doi.org/10.1186/s13045-020-00955-6>
- 165 Thompson, D. M., Lu, C., Green, P. J. & Parker, R. tRNA cleavage is a conserved response
to oxidative stress in eukaryotes. *RNA* **14**, 2095-2103 (2008).
<https://doi.org/10.1261/rna.1232808>

- 166 Ivanov, P., Emara, M. M., Villen, J., Gygi, S. P. & Anderson, P. Angiogenin-induced tRNA fragments inhibit translation initiation. *Mol Cell* **43**, 613-623 (2011). <https://doi.org:10.1016/j.molcel.2011.06.022>
- 167 Ivanov, P. *et al.* G-quadruplex structures contribute to the neuroprotective effects of angiogenin-induced tRNA fragments. *Proc Natl Acad Sci U S A* **111**, 18201-18206 (2014). <https://doi.org:10.1073/pnas.1407361111>
- 168 H, G. *et al.* Endogenous tRNA-Derived Fragments Suppress Breast Cancer Progression via YBX1 Displacement. *Cell* **161** (2015). <https://doi.org:10.1016/j.cell.2015.02.053>
- 169 Kim, H. K. *et al.* A transfer-RNA-derived small RNA regulates ribosome biogenesis. *Nature* **552**, 57-62 (2017). <https://doi.org:10.1038/nature25005>
- 170 Kim, H. K. *et al.* A tRNA-Derived Small RNA Regulates Ribosomal Protein S28 Protein Levels after Translation Initiation in Humans and Mice. *Cell Rep* **29**, 3816-3824 e3814 (2019). <https://doi.org:10.1016/j.celrep.2019.11.062>
- 171 Fu, H. *et al.* Stress induces tRNA cleavage by angiogenin in mammalian cells. *FEBS Lett* **583**, 437-442 (2009). <https://doi.org:10.1016/j.febslet.2008.12.043>
- 172 Li, Q. *et al.* NSUN2-Mediated m5C Methylation and METTL3/METTL14-Mediated m6A Methylation Cooperatively Enhance p21 Translation. *J Cell Biochem* **118**, 2587-2598 (2017). <https://doi.org:10.1002/jcb.25957>
- 173 Thompson, D. M. & Parker, R. Stressing out over tRNA cleavage. *Cell* **138**, 215-219 (2009). <https://doi.org:10.1016/j.cell.2009.07.001>
- 174 Holcik, M. & Sonenberg, N. Translational control in stress and apoptosis. *Nat Rev Mol Cell Biol* **6**, 318-327 (2005). <https://doi.org:10.1038/nrm1618>
- 175 Clemens, M. J. Targets and mechanisms for the regulation of translation in malignant transformation. *Oncogene* **23**, 3180-3188 (2004). <https://doi.org:10.1038/sj.onc.1207544>
- 176 Harding, H. P. *et al.* Regulated translation initiation controls stress-induced gene expression in mammalian cells. *Mol Cell* **6**, 1099-1108 (2000). [https://doi.org:10.1016/s1097-2765\(00\)00108-8](https://doi.org:10.1016/s1097-2765(00)00108-8)
- 177 Gebauer, F. & Hentze, M. W. Molecular mechanisms of translational control. *Nat Rev Mol Cell Biol* **5**, 827-835 (2004). <https://doi.org:10.1038/nrm1488>
- 178 Martinez-Salas, E., Ramos, R., Lafuente, E. & Lopez de Quinto, S. Functional interactions in internal translation initiation directed by viral and cellular IRES elements. *J Gen Virol* **82**, 973-984 (2001). <https://doi.org:10.1099/0022-1317-82-5-973>
- 179 Chen, Z. *et al.* Transfer RNA demethylase ALKBH3 promotes cancer progression via induction of tRNA-derived small RNAs. *Nucleic Acids Res* **47**, 2533-2545 (2019). <https://doi.org:10.1093/nar/gky1250>
- 180 Woo, H. H. & Chambers, S. K. Human ALKBH3-induced m(1)A demethylation increases the CSF-1 mRNA stability in breast and ovarian cancer cells. *Biochim Biophys Acta Gene Regul Mech* **1862**, 35-46 (2019). <https://doi.org:10.1016/j.bbagr.2018.10.008>
- 181 Shimada, K. *et al.* A novel human AlkB homologue, ALKBH8, contributes to human bladder cancer progression. *Cancer Res* **69**, 3157-3164 (2009). <https://doi.org:10.1158/0008-5472.CAN-08-3530>
- 182 Rapino, F. *et al.* Codon-specific translation reprogramming promotes resistance to targeted therapy. *Nature* **558**, 605-609 (2018). <https://doi.org:10.1038/s41586-018-0243-7>
- 183 Delaunay, S. *et al.* Elp3 links tRNA modification to IRES-dependent translation of LEF1 to sustain metastasis in breast cancer. *J Exp Med* **213**, 2503-2523 (2016). <https://doi.org:10.1084/jem.20160397>
- 184 Cheng, J. X. *et al.* RNA cytosine methylation and methyltransferases mediate chromatin organization and 5-azacytidine response and resistance in leukaemia. *Nat Commun* **9**, 1163 (2018). <https://doi.org:10.1038/s41467-018-03513-4>
- 185 Bloniarz, D., Adamczyk-Grochala, J., Lewinska, A. & Wnuk, M. The lack of functional DNMT2/TRDMT1 gene modulates cancer cell responses during drug-induced senescence. *Aging (Albany NY)* **13**, 15833-15874 (2021). <https://doi.org:10.18632/aging.203203>
- 186 Schaefer, M., Hagemann, S., Hanna, K. & Lyko, F. Azacytidine inhibits RNA methylation at DNMT2 target sites in human cancer cell lines. *Cancer Res* **69**, 8127-8132 (2009). <https://doi.org:10.1158/0008-5472.CAN-09-0458>

- 187 Ladang, A. *et al.* Elp3 drives Wnt-dependent tumor initiation and regeneration in the
intestine. *J Exp Med* **212**, 2057-2075 (2015). <https://doi.org/10.1084/jem.20142288>
- 188 Zhang, H. *et al.* GSK-3beta-regulated N-acetyltransferase 10 is involved in colorectal cancer
invasion. *Clin Cancer Res* **20**, 4717-4729 (2014). <https://doi.org/10.1158/1078-0432.CCR-13-3477>
- 189 Blanco, S. *et al.* Stem cell function and stress response are controlled by protein synthesis.
Nature **534**, 335-340 (2016). <https://doi.org/10.1038/nature18282>
- 190 Lu, L., Zhu, G., Zeng, H., Xu, Q. & Holzmann, K. High tRNA Transferase NSUN2 Gene
Expression is Associated with Poor Prognosis in Head and Neck Squamous Carcinoma.
Cancer Invest **36**, 246-253 (2018). <https://doi.org/10.1080/07357907.2018.1466896>
- 191 Chen, X. *et al.* 5-methylcytosine promotes pathogenesis of bladder cancer through
stabilizing mRNAs. *Nat Cell Biol* **21**, 978-990 (2019). <https://doi.org/10.1038/s41556-019-0361-y>
- 192 Frye, M. & Watt, F. M. The RNA methyltransferase Misu (NSun2) mediates Myc-induced
proliferation and is upregulated in tumors. *Curr Biol* **16**, 971-981 (2006).
<https://doi.org/10.1016/j.cub.2006.04.027>
- 193 Mei, L. *et al.* RNA methyltransferase NSUN2 promotes gastric cancer cell proliferation by
repressing p57(Kip2) by an m(5)C-dependent manner. *Cell Death Dis* **11**, 270 (2020).
<https://doi.org/10.1038/s41419-020-2487-z>
- 194 Gao, Y. *et al.* NOP2/Sun RNA methyltransferase 2 promotes tumor progression via its
interacting partner RPL6 in gallbladder carcinoma. *Cancer Sci* **110**, 3510-3519 (2019).
<https://doi.org/10.1111/cas.14190>
- 195 Li, Y. *et al.* Novel long noncoding RNA NMR promotes tumor progression via NSUN2 and
BPTF in esophageal squamous cell carcinoma. *Cancer Lett* **430**, 57-66 (2018).
<https://doi.org/10.1016/j.canlet.2018.05.013>
- 196 Delaunay, S. *et al.* Mitochondrial RNA modifications shape metabolic plasticity in
metastasis. *Nature* **607**, 593-603 (2022). <https://doi.org/10.1038/s41586-022-04898-5>
- 197 Li, X. & Meng, Y. Expression and prognostic characteristics of m(5) C regulators in low-
grade glioma. *J Cell Mol Med* **25**, 1383-1393 (2021). <https://doi.org/10.1111/jcmm.16221>
- 198 Pan, J., Huang, Z. & Xu, Y. m5C RNA Methylation Regulators Predict Prognosis and
Regulate the Immune Microenvironment in Lung Squamous Cell Carcinoma. *Front Oncol*
11, 657466 (2021). <https://doi.org/10.3389/fonc.2021.657466>
- 199 Yang, R. *et al.* The RNA methyltransferase NSUN6 suppresses pancreatic cancer
development by regulating cell proliferation. *EBioMedicine* **63**, 103195 (2021).
<https://doi.org/10.1016/j.ebiom.2020.103195>
- 200 Awah, C. U., Winter, J., Mazdoom, C. M. & Ogunwobi, O. O. NSUN6, an RNA
methyltransferase of 5-mC controls glioblastoma response to temozolomide (TMZ) via
NELFB and RPS6KB2 interaction. *Cancer Biol Ther* **22**, 587-597 (2021).
<https://doi.org/10.1080/15384047.2021.1990631>
- 201 Hicks, D. G. *et al.* The expression of TRMT2A, a novel cell cycle regulated protein,
identifies a subset of breast cancer patients with HER2 over-expression that are at an
increased risk of recurrence. *BMC Cancer* **10**, 108 (2010). <https://doi.org/10.1186/1471-2407-10-108>
- 202 Rossello-Tortella, M. *et al.* Epigenetic loss of the transfer RNA-modifying enzyme TYW2
induces ribosome frameshifts in colon cancer. *Proc Natl Acad Sci U S A* **117**, 20785-20793
(2020). <https://doi.org/10.1073/pnas.2003358117>
- 203 Rodriguez, V. *et al.* Chromosome 8 BAC array comparative genomic hybridization and
expression analysis identify amplification and overexpression of TRMT12 in breast cancer.
Genes Chromosomes Cancer **46**, 694-707 (2007). <https://doi.org/10.1002/gcc.20454>
- 204 Jana, S., Hsieh, A. C. & Gupta, R. Reciprocal amplification of caspase-3 activity by nuclear
export of a putative human RNA-modifying protein, PUS10 during TRAIL-induced
apoptosis. *Cell Death Dis* **8**, e3093 (2017). <https://doi.org/10.1038/cddis.2017.476>
- 205 Ji, P. *et al.* Systematic analyses of genetic variants in chromatin interaction regions identified
four novel lung cancer susceptibility loci. *J Cancer* **11**, 1075-1081 (2020).
<https://doi.org/10.7150/jca.35127>

- 206 Tomikawa, C. 7-Methylguanosine Modifications in Transfer RNA (tRNA). *Int J Mol Sci* **19**
(2018). <https://doi.org:10.3390/ijms19124080>
- 207 Alexandrov, A., Martzen, M. R. & Phizicky, E. M. Two proteins that form a complex are
required for 7-methylguanosine modification of yeast tRNA. *RNA* **8**, 1253-1266 (2002).
<https://doi.org:10.1017/s1355838202024019>
- 208 Alexandrov, A., Grayhack, E. J. & Phizicky, E. M. tRNA m7G methyltransferase
Trm8p/Trm82p: evidence linking activity to a growth phenotype and implicating Trm82p in
maintaining levels of active Trm8p. *RNA* **11**, 821-830 (2005).
<https://doi.org:10.1261/rna.2030705>
- 209 Phizicky, E. M. & Alfonzo, J. D. Do all modifications benefit all tRNAs? *FEBS Lett* **584**,
265-271 (2010). <https://doi.org:10.1016/j.febslet.2009.11.049>
- 210 Lin, S. *et al.* Mettl1/Wdr4-Mediated m(7)G tRNA Methylome Is Required for Normal
mRNA Translation and Embryonic Stem Cell Self-Renewal and Differentiation. *Mol Cell*
71, 244-255 e245 (2018). <https://doi.org:10.1016/j.molcel.2018.06.001>
- 211 Pandolfini, L. *et al.* METTL1 Promotes let-7 MicroRNA Processing via m7G Methylation.
Mol Cell **74**, 1278-1290 e1279 (2019). <https://doi.org:10.1016/j.molcel.2019.03.040>
- 212 Zhang, L. S. *et al.* Transcriptome-wide Mapping of Internal N(7)-Methylguanosine
Methylome in Mammalian mRNA. *Mol Cell* **74**, 1304-1316 e1308 (2019).
<https://doi.org:10.1016/j.molcel.2019.03.036>
- 213 Enroth, C. *et al.* Detection of internal N7-methylguanosine (m7G) RNA modifications by
mutational profiling sequencing. *Nucleic Acids Res* **47**, e126 (2019).
<https://doi.org:10.1093/nar/gkz736>
- 214 Letoquart, J. *et al.* Structural and functional studies of Bud23-Trm112 reveal 18S rRNA N7-
G1575 methylation occurs on late 40S precursor ribosomes. *Proc Natl Acad Sci U S A* **111**,
E5518-5526 (2014). <https://doi.org:10.1073/pnas.1413089111>
- 215 Thuring, K., Schmid, K., Keller, P. & Helm, M. LC-MS Analysis of Methylated RNA.
Methods Mol Biol **1562**, 3-18 (2017). https://doi.org:10.1007/978-1-4939-6807-7_1
- 216 Wintermeyer, W. & Zachau, H. G. Tertiary structure interactions of 7-methylguanosine in
yeast tRNA Phe as studied by borohydride reduction. *FEBS Lett* **58**, 306-309 (1975).
[https://doi.org:10.1016/0014-5793\(75\)80285-7](https://doi.org:10.1016/0014-5793(75)80285-7)
- 217 Marchand, V. *et al.* AlkAniline-Seq: Profiling of m(7) G and m(3) C RNA Modifications at
Single Nucleotide Resolution. *Angew Chem Int Ed Engl* **57**, 16785-16790 (2018).
<https://doi.org:10.1002/anie.201810946>
- 218 Lin, S., Liu, Q., Jiang, Y. Z. & Gregory, R. I. Nucleotide resolution profiling of m(7)G tRNA
modification by TRAC-Seq. *Nat Protoc* **14**, 3220-3242 (2019).
<https://doi.org:10.1038/s41596-019-0226-7>
- 219 Orellana, E. A. *et al.* METTL1-mediated m(7)G modification of Arg-TCT tRNA drives
oncogenic transformation. *Mol Cell* **81**, 3323-3338 e3314 (2021).
<https://doi.org:10.1016/j.molcel.2021.06.031>
- 220 Dai, Z. *et al.* N(7)-Methylguanosine tRNA modification enhances oncogenic mRNA
translation and promotes intrahepatic cholangiocarcinoma progression. *Mol Cell* **81**, 3339-
3355 e3338 (2021). <https://doi.org:10.1016/j.molcel.2021.07.003>
- 221 Han, H. *et al.* N(7)-methylguanosine tRNA modification promotes esophageal squamous
cell carcinoma tumorigenesis via the RPTOR/ULK1/autophagy axis. *Nat Commun* **13**, 1478
(2022). <https://doi.org:10.1038/s41467-022-29125-7>
- 222 Deng, Y., Zhou, Z., Ji, W., Lin, S. & Wang, M. METTL1-mediated m(7)G methylation
maintains pluripotency in human stem cells and limits mesoderm differentiation and vascular
development. *Stem Cell Res Ther* **11**, 306 (2020). <https://doi.org:10.1186/s13287-020-01814-4>
- 223 Shaheen, R. *et al.* Mutation in WDR4 impairs tRNA m(7)G46 methylation and causes a
distinct form of microcephalic primordial dwarfism. *Genome Biol* **16**, 210 (2015).
<https://doi.org:10.1186/s13059-015-0779-x>
- 224 Ma, J. *et al.* METTL1/WDR4-mediated m(7)G tRNA modifications and m(7)G codon usage
promote mRNA translation and lung cancer progression. *Mol Ther* (2021).
<https://doi.org:10.1016/j.ymthe.2021.08.005>

- 225 Tian, Q. H. *et al.* METTL1 overexpression is correlated with poor prognosis and promotes hepatocellular carcinoma via PTEN. *J Mol Med (Berl)* **97**, 1535-1545 (2019). <https://doi.org/10.1007/s00109-019-01830-9>
- 226 Zhou, W. *et al.* Derivation and Validation of a Prognostic Model for Cancer Dependency Genes Based on CRISPR-Cas9 in Gastric Adenocarcinoma. *Front Oncol* **11**, 617289 (2021). <https://doi.org/10.3389/fonc.2021.617289>
- 227 Li, L. *et al.* Prognostic role of METTL1 in glioma. *Cancer Cell Int* **21**, 633 (2021). <https://doi.org/10.1186/s12935-021-02346-4>
- 228 Ying, X. *et al.* METTL1-m(7) G-EGFR/EFEMP1 axis promotes the bladder cancer development. *Clin Transl Med* **11**, e675 (2021). <https://doi.org/10.1002/ctm2.675>
- 229 Okamoto, M. *et al.* tRNA modifying enzymes, NSUN2 and METTL1, determine sensitivity to 5-fluorouracil in HeLa cells. *PLoS Genet* **10**, e1004639 (2014). <https://doi.org/10.1371/journal.pgen.1004639>
- 230 Gao, Z. *et al.* A Comprehensive Analysis of METTL1 to Immunity and Stemness in Pan-Cancer. *Front Immunol* **13**, 795240 (2022). <https://doi.org/10.3389/fimmu.2022.795240>
- 231 Chen, Z. *et al.* METTL1 promotes hepatocarcinogenesis via m(7) G tRNA modification-dependent translation control. *Clin Transl Med* **11**, e661 (2021). <https://doi.org/10.1002/ctm2.661>
- 232 Liu, Y. *et al.* Overexpressed methyltransferase-like 1 (METTL1) increased chemosensitivity of colon cancer cells to cisplatin by regulating miR-149-3p/S100A4/p53 axis. *Aging (Albany NY)* **11**, 12328-12344 (2019). <https://doi.org/10.18632/aging.102575>
- 233 Chen, J. *et al.* Aberrant translation regulated by METTL1/WDR4-mediated tRNA N7-methylguanosine modification drives head and neck squamous cell carcinoma progression. *Cancer Commun (Lond)* **42**, 223-244 (2022). <https://doi.org/10.1002/cac2.12273>
- 234 Chen, B. *et al.* N(7)-methylguanosine tRNA modification promotes tumorigenesis and chemoresistance through WNT/beta-catenin pathway in nasopharyngeal carcinoma. *Oncogene* **41**, 2239-2253 (2022). <https://doi.org/10.1038/s41388-022-02250-9>
- 235 Suzuki, T. The expanding world of tRNA modifications and their disease relevance. *Nat Rev Mol Cell Biol* **22**, 375-392 (2021). <https://doi.org/10.1038/s41580-021-00342-0>
- 236 Walter, P. & Ron, D. The unfolded protein response: from stress pathway to homeostatic regulation. *Science* **334**, 1081-1086 (2011). <https://doi.org/10.1126/science.1209038>
- 237 Senft, D. & Ronai, Z. A. UPR, autophagy, and mitochondria crosstalk underlies the ER stress response. *Trends Biochem Sci* **40**, 141-148 (2015). <https://doi.org/10.1016/j.tibs.2015.01.002>
- 238 Hetz, C. The unfolded protein response: controlling cell fate decisions under ER stress and beyond. *Nat Rev Mol Cell Biol* **13**, 89-102 (2012). <https://doi.org/10.1038/nrm3270>
- 239 Zhang, Z. *et al.* Redox signaling and unfolded protein response coordinate cell fate decisions under ER stress. *Redox Biol* **25**, 101047 (2019). <https://doi.org/10.1016/j.redox.2018.11.005>
- 240 Cao, S. S. & Kaufman, R. J. Unfolded protein response. *Curr Biol* **22**, R622-626 (2012). <https://doi.org/10.1016/j.cub.2012.07.004>
- 241 Rutkowski, D. T. & Hegde, R. S. Regulation of basal cellular physiology by the homeostatic unfolded protein response. *J Cell Biol* **189**, 783-794 (2010). <https://doi.org/10.1083/jcb.201003138>
- 242 Maurel, M., Chevet, E., Tavernier, J. & Gerlo, S. Getting RIDD of RNA: IRE1 in cell fate regulation. *Trends Biochem Sci* **39**, 245-254 (2014). <https://doi.org/10.1016/j.tibs.2014.02.008>
- 243 Acosta-Alvear, D. *et al.* The unfolded protein response and endoplasmic reticulum protein targeting machineries converge on the stress sensor IRE1. *Elife* **7** (2018). <https://doi.org/10.7554/eLife.43036>
- 244 Bommasamy, H. *et al.* ATF6alpha induces XBP1-independent expansion of the endoplasmic reticulum. *J Cell Sci* **122**, 1626-1636 (2009). <https://doi.org/10.1242/jcs.045625>
- 245 Zhao, L. & Ackerman, S. L. Endoplasmic reticulum stress in health and disease. *Curr Opin Cell Biol* **18**, 444-452 (2006). <https://doi.org/10.1016/j.ceb.2006.06.005>

- 246 Glick, D., Barth, S. & Macleod, K. F. Autophagy: cellular and molecular mechanisms. *J Pathol* **221**, 3-12 (2010). <https://doi.org/10.1002/path.2697>
- 247 Yang, Z. & Klionsky, D. J. Mammalian autophagy: core molecular machinery and signaling regulation. *Curr Opin Cell Biol* **22**, 124-131 (2010). <https://doi.org/10.1016/j.ceb.2009.11.014>
- 248 Wirawan, E., Vanden Berghe, T., Lippens, S., Agostinis, P. & Vandenabeele, P. Autophagy: for better or for worse. *Cell Res* **22**, 43-61 (2012). <https://doi.org/10.1038/cr.2011.152>
- 249 Axe, E. L. *et al.* Autophagosome formation from membrane compartments enriched in phosphatidylinositol 3-phosphate and dynamically connected to the endoplasmic reticulum. *J Cell Biol* **182**, 685-701 (2008). <https://doi.org/10.1083/jcb.200803137>
- 250 Simonsen, A. & Tooze, S. A. Coordination of membrane events during autophagy by multiple class III PI3-kinase complexes. *J Cell Biol* **186**, 773-782 (2009). <https://doi.org/10.1083/jcb.200907014>
- 251 Weidberg, H., Shvets, E. & Elazar, Z. Biogenesis and cargo selectivity of autophagosomes. *Annu Rev Biochem* **80**, 125-156 (2011). <https://doi.org/10.1146/annurev-biochem-052709-094552>
- 252 Mizushima, N. Autophagy: process and function. *Genes Dev* **21**, 2861-2873 (2007). <https://doi.org/10.1101/gad.1599207>
- 253 Chen, Y. & Klionsky, D. J. The regulation of autophagy - unanswered questions. *J Cell Sci* **124**, 161-170 (2011). <https://doi.org/10.1242/jcs.064576>
- 254 Yang, Z. & Klionsky, D. J. An overview of the molecular mechanism of autophagy. *Curr Top Microbiol Immunol* **335**, 1-32 (2009). https://doi.org/10.1007/978-3-642-00302-8_1
- 255 Komatsu, M. *et al.* Constitutive autophagy: vital role in clearance of unfavorable proteins in neurons. *Cell Death Differ* **14**, 887-894 (2007). <https://doi.org/10.1038/sj.cdd.4402120>
- 256 Kim, J., Kundu, M., Viollet, B. & Guan, K. L. AMPK and mTOR regulate autophagy through direct phosphorylation of Ulk1. *Nat Cell Biol* **13**, 132-141 (2011). <https://doi.org/10.1038/ncb2152>
- 257 Jung, C. H. *et al.* ULK-Atg13-FIP200 complexes mediate mTOR signaling to the autophagy machinery. *Mol Biol Cell* **20**, 1992-2003 (2009). <https://doi.org/10.1091/mbc.E08-12-1249>
- 258 Xie, Z. & Klionsky, D. J. Autophagosome formation: core machinery and adaptations. *Nat Cell Biol* **9**, 1102-1109 (2007). <https://doi.org/10.1038/ncb1007-1102>
- 259 Kabeya, Y. *et al.* LC3, a mammalian homologue of yeast Apg8p, is localized in autophagosome membranes after processing. *EMBO J* **19**, 5720-5728 (2000). <https://doi.org/10.1093/emboj/19.21.5720>
- 260 Bjorkoy, G. *et al.* Monitoring autophagic degradation of p62/SQSTM1. *Methods Enzymol* **452**, 181-197 (2009). [https://doi.org/10.1016/S0076-6879\(08\)03612-4](https://doi.org/10.1016/S0076-6879(08)03612-4)
- 261 Chang, N. C. Autophagy and Stem Cells: Self-Eating for Self-Renewal. *Front Cell Dev Biol* **8**, 138 (2020). <https://doi.org/10.3389/fcell.2020.00138>
- 262 Nakamura, S. & Yoshimori, T. New insights into autophagosome-lysosome fusion. *J Cell Sci* **130**, 1209-1216 (2017). <https://doi.org/10.1242/jcs.196352>
- 263 Song, H. *et al.* METTL3 and ALKBH5 oppositely regulate m(6)A modification of TFEB mRNA, which dictates the fate of hypoxia/reoxygenation-treated cardiomyocytes. *Autophagy* **15**, 1419-1437 (2019). <https://doi.org/10.1080/15548627.2019.1586246>
- 264 Jin, S. *et al.* m(6)A RNA modification controls autophagy through upregulating ULK1 protein abundance. *Cell Res* **28**, 955-957 (2018). <https://doi.org/10.1038/s41422-018-0069-8>
- 265 Wang, X. *et al.* m(6)A mRNA methylation controls autophagy and adipogenesis by targeting Atg5 and Atg7. *Autophagy* **16**, 1221-1235 (2020). <https://doi.org/10.1080/15548627.2019.1659617>
- 266 Li, G. *et al.* Bone-derived mesenchymal stem cells alleviate compression-induced apoptosis of nucleus pulposus cells by N6 methyladenosine of autophagy. *Cell Death Dis* **11**, 103 (2020). <https://doi.org/10.1038/s41419-020-2284-8>
- 267 Lin, Z. *et al.* RNA m(6) A methylation regulates sorafenib resistance in liver cancer through FOXO3-mediated autophagy. *EMBO J* **39**, e103181 (2020). <https://doi.org/10.15252/emboj.2019103181>

- 268 Wang, C. *et al.* Methyltransferase-like 1 regulates lung adenocarcinoma A549 cell proliferation and autophagy via the AKT/mTORC1 signaling pathway. *Oncol Lett* **21**, 330 (2021). <https://doi.org:10.3892/ol.2021.12591>
- 269 Wilde, L., Tanson, K., Curry, J. & Martinez-Outschoorn, U. Autophagy in cancer: a complex relationship. *Biochem J* **475**, 1939-1954 (2018). <https://doi.org:10.1042/BCJ20170847>
- 270 Kocaturk, N. M. *et al.* Autophagy as a molecular target for cancer treatment. *Eur J Pharm Sci* **134**, 116-137 (2019). <https://doi.org:10.1016/j.ejps.2019.04.011>
- 271 Qu, X. *et al.* Promotion of tumorigenesis by heterozygous disruption of the beclin 1 autophagy gene. *J Clin Invest* **112**, 1809-1820 (2003). <https://doi.org:10.1172/JCI20039>
- 272 Yue, Z., Jin, S., Yang, C., Levine, A. J. & Heintz, N. Beclin 1, an autophagy gene essential for early embryonic development, is a haploinsufficient tumor suppressor. *Proc Natl Acad Sci U S A* **100**, 15077-15082 (2003). <https://doi.org:10.1073/pnas.2436255100>
- 273 Takahashi, Y. *et al.* Bif-1 interacts with Beclin 1 through UVRAG and regulates autophagy and tumorigenesis. *Nat Cell Biol* **9**, 1142-1151 (2007). <https://doi.org:10.1038/ncb1634>
- 274 Coppola, D. *et al.* Down-regulation of Bax-interacting factor-1 in colorectal adenocarcinoma. *Cancer* **113**, 2665-2670 (2008). <https://doi.org:10.1002/cncr.23892>
- 275 Takamura, A. *et al.* Autophagy-deficient mice develop multiple liver tumors. *Genes Dev* **25**, 795-800 (2011). <https://doi.org:10.1101/gad.2016211>
- 276 Yang, A. *et al.* Autophagy is critical for pancreatic tumor growth and progression in tumors with p53 alterations. *Cancer Discov* **4**, 905-913 (2014). <https://doi.org:10.1158/2159-8290.CD-14-0362>
- 277 Perera, R. M. *et al.* Transcriptional control of autophagy-lysosome function drives pancreatic cancer metabolism. *Nature* **524**, 361-365 (2015). <https://doi.org:10.1038/nature14587>
- 278 Guo, J. Y. & White, E. Autophagy is required for mitochondrial function, lipid metabolism, growth, and fate of KRAS(G12D)-driven lung tumors. *Autophagy* **9**, 1636-1638 (2013). <https://doi.org:10.4161/auto.26123>
- 279 Strohecker, A. M. *et al.* Autophagy sustains mitochondrial glutamine metabolism and growth of BrafV600E-driven lung tumors. *Cancer Discov* **3**, 1272-1285 (2013). <https://doi.org:10.1158/2159-8290.CD-13-0397>
- 280 Kimmelman, A. C. & White, E. Autophagy and Tumor Metabolism. *Cell Metab* **25**, 1037-1043 (2017). <https://doi.org:10.1016/j.cmet.2017.04.004>
- 281 Chen, Y. S. *et al.* Autophagy inhibition contributes to radiation sensitization of esophageal squamous carcinoma cells. *Dis Esophagus* **24**, 437-443 (2011). <https://doi.org:10.1111/j.1442-2050.2010.01156.x>
- 282 Li, J. *et al.* Inhibition of autophagy by 3-MA enhances the effect of 5-FU-induced apoptosis in colon cancer cells. *Ann Surg Oncol* **16**, 761-771 (2009). <https://doi.org:10.1245/s10434-008-0260-0>
- 283 Liu, F., Liu, D., Yang, Y. & Zhao, S. Effect of autophagy inhibition on chemotherapy-induced apoptosis in A549 lung cancer cells. *Oncol Lett* **5**, 1261-1265 (2013). <https://doi.org:10.3892/ol.2013.1154>
- 284 Guo, X. L. *et al.* Inhibition of autophagy enhances anticancer effects of bevacizumab in hepatocarcinoma. *J Mol Med (Berl)* **91**, 473-483 (2013). <https://doi.org:10.1007/s00109-012-0966-0>
- 285 Sotelo, J., Briceno, E. & Lopez-Gonzalez, M. A. Adding chloroquine to conventional treatment for glioblastoma multiforme: a randomized, double-blind, placebo-controlled trial. *Ann Intern Med* **144**, 337-343 (2006). <https://doi.org:10.7326/0003-4819-144-5-200603070-00008>
- 286 Sasaki, K. *et al.* Chloroquine potentiates the anti-cancer effect of 5-fluorouracil on colon cancer cells. *BMC Cancer* **10**, 370 (2010). <https://doi.org:10.1186/1471-2407-10-370>
- 287 Cortazar, A. R. *et al.* CANCEERTOOL: A Visualization and Representation Interface to Exploit Cancer Datasets. *Cancer Res* **78**, 6320-6328 (2018). <https://doi.org:10.1158/0008-5472.CAN-18-1669>
- 288 Tomlins, S. A. *et al.* Integrative molecular concept modeling of prostate cancer progression. *Nat Genet* **39**, 41-51 (2007). <https://doi.org:10.1038/ng1935>

- 289 Lapointe, J. *et al.* Gene expression profiling identifies clinically relevant subtypes of prostate cancer. *Proc Natl Acad Sci U S A* **101**, 811-816 (2004). <https://doi.org:10.1073/pnas.0304146101>
- 290 Sieron, P. *et al.* DKC1 overexpression associated with prostate cancer progression. *Br J Cancer* **101**, 1410-1416 (2009). <https://doi.org:10.1038/sj.bjc.6605299>
- 291 Dunning, M. J. *et al.* Mining Human Prostate Cancer Datasets: The "camcAPP" Shiny App. *EBioMedicine* **17**, 5-6 (2017). <https://doi.org:10.1016/j.ebiom.2017.02.022>
- 292 Ross-Adams, H. *et al.* Integration of copy number and transcriptomics provides risk stratification in prostate cancer: A discovery and validation cohort study. *EBioMedicine* **2**, 1133-1144 (2015). <https://doi.org:10.1016/j.ebiom.2015.07.017>
- 293 Hemmings, B. A. & Restuccia, D. F. PI3K-PKB/Akt pathway. *Cold Spring Harb Perspect Biol* **4**, a011189 (2012). <https://doi.org:10.1101/cshperspect.a011189>
- 294 Engelman, J. A., Luo, J. & Cantley, L. C. The evolution of phosphatidylinositol 3-kinases as regulators of growth and metabolism. *Nat Rev Genet* **7**, 606-619 (2006). <https://doi.org:10.1038/nrg1879>
- 295 Bennett, B. T., Bewersdorf, J. & Knight, K. L. Immunofluorescence imaging of DNA damage response proteins: optimizing protocols for super-resolution microscopy. *Methods* **48**, 63-71 (2009). <https://doi.org:10.1016/j.ymeth.2009.02.009>
- 296 Attard, G. *et al.* Prostate cancer. *Lancet* **387**, 70-82 (2016). [https://doi.org:10.1016/S0140-6736\(14\)61947-4](https://doi.org:10.1016/S0140-6736(14)61947-4)
- 297 Glinsky, G. V., Glinskii, A. B., Stephenson, A. J., Hoffman, R. M. & Gerald, W. L. Gene expression profiling predicts clinical outcome of prostate cancer. *J Clin Invest* **113**, 913-923 (2004). <https://doi.org:10.1172/JCI20032>
- 298 Jamaspishvili, T. *et al.* Clinical implications of PTEN loss in prostate cancer. *Nat Rev Urol* **15**, 222-234 (2018). <https://doi.org:10.1038/nrurol.2018.9>
- 299 Laplante, M. & Sabatini, D. M. mTOR signaling in growth control and disease. *Cell* **149**, 274-293 (2012). <https://doi.org:10.1016/j.cell.2012.03.017>
- 300 Thoreen, C. C. *et al.* An ATP-competitive mammalian target of rapamycin inhibitor reveals rapamycin-resistant functions of mTORC1. *J Biol Chem* **284**, 8023-8032 (2009). <https://doi.org:10.1074/jbc.M900301200>
- 301 DA, L., L, X., RU, L., D, C. & ON, W. Isolation and functional characterization of murine prostate stem cells. *Proceedings of the National Academy of Sciences of the United States of America* **104** (2007). <https://doi.org:10.1073/pnas.0609684104>
- 302 L, P. *et al.* METTL1 Promotes let-7 MicroRNA Processing via m7G Methylation. *Molecular cell* **74** (2019). <https://doi.org:10.1016/j.molcel.2019.03.040>
- 303 LS, Z. *et al.* Transcriptome-wide Mapping of Internal N 7-Methylguanosine Methylome in Mammalian mRNA. *Molecular cell* **74** (2019). <https://doi.org:10.1016/j.molcel.2019.03.036>
- 304 Bao, X. *et al.* Capturing the interactome of newly transcribed RNA. *Nat Methods* **15**, 213-220 (2018). <https://doi.org:10.1038/nmeth.4595>
- 305 Chetsanga, C. J. & Makaroff, C. Alkaline opening of imidazole ring of 7-methylguanosine. 2. Further studies on reaction mechanisms and products. *Chem Biol Interact* **41**, 235-249 (1982). [https://doi.org:10.1016/0009-2797\(82\)90092-8](https://doi.org:10.1016/0009-2797(82)90092-8)
- 306 Kao, R. Y. *et al.* A small-molecule inhibitor of the ribonucleolytic activity of human angiogenin that possesses antitumor activity. *Proc Natl Acad Sci U S A* **99**, 10066-10071 (2002). <https://doi.org:10.1073/pnas.152342999>
- 307 Liu, J., Xu, Y., Stoleru, D. & Salic, A. Imaging protein synthesis in cells and tissues with an alkyne analog of puromycin. *Proc Natl Acad Sci U S A* **109**, 413-418 (2012). <https://doi.org:10.1073/pnas.1111561108>
- 308 Lyons, S. M., Gudanis, D., Coyne, S. M., Gdaniec, Z. & Ivanov, P. Identification of functional tetramolecular RNA G-quadruplexes derived from transfer RNAs. *Nat Commun* **8**, 1127 (2017). <https://doi.org:10.1038/s41467-017-01278-w>
- 309 Forester, C. M. *et al.* Revealing nascent proteomics in signaling pathways and cell differentiation. *Proc Natl Acad Sci U S A* **115**, 2353-2358 (2018). <https://doi.org:10.1073/pnas.1707514115>

- 310 Sagliocco, F. A., Moore, P. A. & Brown, A. J. Polysome analysis. *Methods Mol Biol* **53**, 297-311 (1996). <https://doi.org/10.1385/0-89603-319-8:297>
- 311 Bhattarai, K. R., Riaz, T. A., Kim, H. R. & Chae, H. J. The aftermath of the interplay between the endoplasmic reticulum stress response and redox signaling. *Exp Mol Med* **53**, 151-167 (2021). <https://doi.org/10.1038/s12276-021-00560-8>
- 312 Klionsky, D. J. *et al.* Guidelines for the use and interpretation of assays for monitoring autophagy (4th edition)(1). *Autophagy* **17**, 1-382 (2021). <https://doi.org/10.1080/15548627.2020.1797280>
- 313 Ureshino, R. P., Rocha, K. K., Lopes, G. S., Bincoletto, C. & Smaili, S. S. Calcium signaling alterations, oxidative stress, and autophagy in aging. *Antioxid Redox Signal* **21**, 123-137 (2014). <https://doi.org/10.1089/ars.2013.5777>
- 314 Li, L., Tan, J., Miao, Y., Lei, P. & Zhang, Q. ROS and Autophagy: Interactions and Molecular Regulatory Mechanisms. *Cell Mol Neurobiol* **35**, 615-621 (2015). <https://doi.org/10.1007/s10571-015-0166-x>
- 315 Wu, J., Lu, L. Y. & Yu, X. The role of BRCA1 in DNA damage response. *Protein Cell* **1**, 117-123 (2010). <https://doi.org/10.1007/s13238-010-0010-5>
- 316 Hasan, A. *et al.* Crosstalk Between ROS and Autophagy in Tumorigenesis: Understanding the Multifaceted Paradox. *Front Oncol* **12**, 852424 (2022). <https://doi.org/10.3389/fonc.2022.852424>
- 317 Levy, J. M. M., Towers, C. G. & Thorburn, A. Targeting autophagy in cancer. *Nat Rev Cancer* **17**, 528-542 (2017). <https://doi.org/10.1038/nrc.2017.53>
- 318 Petrylak, D. P. *et al.* Docetaxel and estramustine compared with mitoxantrone and prednisone for advanced refractory prostate cancer. *N Engl J Med* **351**, 1513-1520 (2004). <https://doi.org/10.1056/NEJMoa041318>
- 319 Cattrini, C., Capaia, M., Boccardo, F. & Barboro, P. Etoposide and topoisomerase II inhibition for aggressive prostate cancer: Data from a translational study. *Cancer Treat Res Commun* **25**, 100221 (2020). <https://doi.org/10.1016/j.ctarc.2020.100221>
- 320 Onbasli, K. *et al.* The improved killing of both androgen-dependent and independent prostate cancer cells by etoposide loaded SPIONs coupled with NIR irradiation. *Biomater Sci* **10**, 3951-3962 (2022). <https://doi.org/10.1039/d2bm00107a>
- 321 Koguchi, D. *et al.* Effect of cisplatin on metastatic castration-resistant prostate cancer with BRCA2 mutation: A case report. *Urol Case Rep* **38**, 101712 (2021). <https://doi.org/10.1016/j.eucr.2021.101712>
- 322 Disease, G. B. D., Injury, I. & Prevalence, C. Global, regional, and national incidence, prevalence, and years lived with disability for 354 diseases and injuries for 195 countries and territories, 1990-2017: a systematic analysis for the Global Burden of Disease Study 2017. *Lancet* **392**, 1789-1858 (2018). [https://doi.org/10.1016/S0140-6736\(18\)32279-7](https://doi.org/10.1016/S0140-6736(18)32279-7)
- 323 Sandhu, S. *et al.* Prostate cancer. *Lancet* **398**, 1075-1090 (2021). [https://doi.org/10.1016/S0140-6736\(21\)00950-8](https://doi.org/10.1016/S0140-6736(21)00950-8)
- 324 Pernar, C. H., Ebot, E. M., Wilson, K. M. & Mucci, L. A. The Epidemiology of Prostate Cancer. *Cold Spring Harb Perspect Med* **8** (2018). <https://doi.org/10.1101/cshperspect.a030361>
- 325 Roviello, G. *et al.* Castration-resistant prostate cancer with bone metastases: toward the best therapeutic choice. *Med Oncol* **39**, 145 (2022). <https://doi.org/10.1007/s12032-022-01739-3>
- 326 Campeanu, I. J. *et al.* Multi-omics integration of methyltransferase-like protein family reveals clinical outcomes and functional signatures in human cancer. *Sci Rep* **11**, 14784 (2021). <https://doi.org/10.1038/s41598-021-94019-5>
- 327 Lin, W., Mackenzie, J. W. & Clark, I. Effect of transplanted osteogenic sarcoma on urinary RNA catabolites. *Cancer Lett* **35**, 47-57 (1987). [https://doi.org/10.1016/0304-3835\(87\)90055-3](https://doi.org/10.1016/0304-3835(87)90055-3)
- 328 Stillwell, W. G. *et al.* Urinary excretion of nitrate, N-nitrosoproline, 3-methyladenine, and 7-methylguanine in a Colombian population at high risk for stomach cancer. *Cancer Res* **51**, 190-194 (1991).

- 329 Cartlidge, R. A. *et al.* The tRNA methylase METTL1 is phosphorylated and inactivated by PKB and RSK in vitro and in cells. *EMBO J* **24**, 1696-1705 (2005). <https://doi.org:10.1038/sj.emboj.7600648>
- 330 Helm, M. & Motorin, Y. Detecting RNA modifications in the epitranscriptome: predict and validate. *Nat Rev Genet* **18**, 275-291 (2017). <https://doi.org:10.1038/nrg.2016.169>
- 331 Pliatsika, V. *et al.* MINTbase v2.0: a comprehensive database for tRNA-derived fragments that includes nuclear and mitochondrial fragments from all The Cancer Genome Atlas projects. *Nucleic Acids Res* **46**, D152-D159 (2018). <https://doi.org:10.1093/nar/gkx1075>
- 332 Honda, S. *et al.* Sex hormone-dependent tRNA halves enhance cell proliferation in breast and prostate cancers. *Proc Natl Acad Sci U S A* **112**, E3816-3825 (2015). <https://doi.org:10.1073/pnas.1510077112>
- 333 Olvedy, M. *et al.* A comprehensive repertoire of tRNA-derived fragments in prostate cancer. *Oncotarget* **7**, 24766-24777 (2016). <https://doi.org:10.18632/oncotarget.8293>
- 334 Hussain, S. *et al.* NSun2-mediated cytosine-5 methylation of vault noncoding RNA determines its processing into regulatory small RNAs. *Cell Rep* **4**, 255-261 (2013). <https://doi.org:10.1016/j.celrep.2013.06.029>
- 335 Zhuang, L. *et al.* Atg3 Overexpression Enhances Bortezomib-Induced Cell Death in SKM-1 Cell. *PLoS One* **11**, e0158761 (2016). <https://doi.org:10.1371/journal.pone.0158761>
- 336 Yankova, E. *et al.* Small-molecule inhibition of METTL3 as a strategy against myeloid leukaemia. *Nature* **593**, 597-601 (2021). <https://doi.org:10.1038/s41586-021-03536-w>
- 337 Torrano, V. *et al.* The metabolic co-regulator PGC1alpha suppresses prostate cancer metastasis. *Nat Cell Biol* **18**, 645-656 (2016). <https://doi.org:10.1038/ncb3357>
- 338 Wisniewski, J. R., Zougman, A., Nagaraj, N. & Mann, M. Universal sample preparation method for proteome analysis. *Nat Methods* **6**, 359-362 (2009). <https://doi.org:10.1038/nmeth.1322>
- 339 Cox, J. & Mann, M. MaxQuant enables high peptide identification rates, individualized p.p.b.-range mass accuracies and proteome-wide protein quantification. *Nat Biotechnol* **26**, 1367-1372 (2008). <https://doi.org:10.1038/nbt.1511>
- 340 Tyanova, S. *et al.* The Perseus computational platform for comprehensive analysis of (prote)omics data. *Nat Methods* **13**, 731-740 (2016). <https://doi.org:10.1038/nmeth.3901>
- 341 AC, H. *et al.* Genetic dissection of the oncogenic mTOR pathway reveals druggable addiction to translational control via 4EBP-eIF4E. *Cancer cell* **17** (2010). <https://doi.org:10.1016/j.ccr.2010.01.021>
- 342 N, G. *et al.* Pseudouridylation of tRNA-Derived Fragments Steers Translational Control in Stem Cells. *Cell* **173** (2018). <https://doi.org:10.1016/j.cell.2018.03.008>
- 343 C, Z. *et al.* The human 18S rRNA base methyltransferases DIMT1L and WBSCR22-TRMT112 but not rRNA modification are required for ribosome biogenesis. *Molecular biology of the cell* **26** (2015). <https://doi.org:10.1091/mbc.E15-02-0073>
- 344 Carvalho, B. S. & Irizarry, R. A. A framework for oligonucleotide microarray preprocessing. *Bioinformatics* **26**, 2363-2367 (2010). <https://doi.org:10.1093/bioinformatics/btq431>
- 345 Ritchie, M. E. *et al.* limma powers differential expression analyses for RNA-sequencing and microarray studies. *Nucleic Acids Res* **43**, e47 (2015). <https://doi.org:10.1093/nar/gkv007>
- 346 Graña, O. R.-C., M. ; Riverola-Fernández, F. ; Pisano, D.G. ; González-Peña, D. . Nextpresso: Next Generation Sequencing Expression Analysis Pipeline. *Current Bioinformatics* **13**, 583-591 (2018). <https://doi.org:10.2174/1574893612666170810153850>
- 347 Subramanian, A. *et al.* Gene set enrichment analysis: a knowledge-based approach for interpreting genome-wide expression profiles. *Proc Natl Acad Sci U S A* **102**, 15545-15550 (2005). <https://doi.org:10.1073/pnas.0506580102>
- 348 Zabala-Letona, A. *et al.* mTORC1-dependent AMD1 regulation sustains polyamine metabolism in prostate cancer. *Nature* **547**, 109-113 (2017). <https://doi.org:10.1038/nature22964>

1 INTRODUCCIÓN

1. Cáncer de Próstata

El cáncer de próstata (CaP) es el segundo cáncer más comúnmente diagnosticado y la principal causa de muerte por cáncer en hombres a nivel mundial¹, siendo la edad el principal factor de riesgo de aparición de la enfermedad.

La formación del tumor de próstata comienza con la aparición de una neoplasia prostática intraepitelial caracterizada por la proliferación de células luminales dentro de los conductos preexistentes⁷. A continuación, la enfermedad progresa hacia el desarrollo de adenocarcinoma *in situ*, que puede evolucionar hacia cáncer de próstata invasivo, el cual se diferencia por la invasión de la lámina basal que rodea la glándula. El proceso termina con la aparición del cáncer de próstata metastático, en el que el tumor metastatiza primero hacia los nódulos linfáticos y posteriormente a distintos órganos tales como hueso, hígado y pulmones^{8,9}.

El tratamiento estándar para pacientes con enfermedad localizada consiste en cirugía o radioterapia. En el caso de adenocarcinoma localizado, la principal línea de tratamiento es la deprivación androgénica (ADT) debido a la alta dependencia de testosterona que presenta la próstata²⁵. Sin embargo, una deprivación androgénica continuada resulta con frecuencia en la aparición de resistencias al tratamiento, progresando la enfermedad a CaP resistente a la castración (CRPC)²⁶. Esta fase de la enfermedad se caracteriza por una baja prognosis, siendo la primera línea de tratamiento el taxano Docetaxel, que supone una mejora de la supervivencia de tres meses.

Aunque en los últimos años se han desarrollado nuevos tratamientos para mCRPC, tales como Cabazitaxel o Abiraterone, el efecto en la supervivencia del paciente es muy reducido, lo que resalta la necesidad de desarrollar nuevos tratamientos^{23,30}. Por ello, recientes estudios genómicos a gran escala se han llevado a cabo con el objetivo de entender a mayor profundidad los mecanismos moleculares que subyacen a la enfermedad. Así, aunque el CaP se caracteriza por presentar una baja carga mutacional, mutaciones en *PTEN* presentan una alta frecuencia, estando relacionadas con tumores agresivos y un incremento de la metástasis. Asimismo, el 69% de los carcinomas *in situ* y el 86% de los mCRPC presentan alteraciones en *PTEN*⁵⁴. Además de alteraciones en algunas rutas esenciales como PI3K y rutas de reparación del ADN, los tumores de próstata también están enriquecidos en alteraciones de reguladores epigenéticos, tales como modificadores de histonas o remodeladores de cromatina⁵⁷. Esto implica que no solo las alteraciones genéticas juegan un papel clave en la progresión del CaP si no que alteraciones en la modificación del ADN también es decisiva.

En resumen, aunque ha habido importantes avances en la investigación del CaP, su elevada prevalencia, la alta tasa de desarrollo de resistencia al tratamiento y la gran heterogeneidad intratumoral constituyen los grandes obstáculos a superar. Por ello, la identificación de nuevos biomarcadores que permitan un

correcto diagnóstico de la enfermedad, así como el desarrollo de nuevos enfoques terapéuticos son esenciales para mejorar la calidad de vida de aquellos pacientes con tumores avanzados.

2. Epitranscriptómica

En los últimos años, numerosos estudios han resaltado la importancia de mecanismos no mutacionales, tales como marcas epigénéticas, en el desarrollo y progresión del cáncer de próstata (35). La baja carga mutacional del CaP hace que procesos como la epigenética o la epitranscriptómica surjan como un nuevo nivel de regulación de procesos biológicos esenciales y distintos eventos iniciadores de tumores (revisado en ¹⁰⁴⁻¹⁰⁷).

La epitranscriptómica surge como el estudio de los cambios a los que se ve sometido el ARN tras la transcripción, bien debido a modificaciones químicas o a alteraciones en la secuencia (que es lo que se conoce como edición del ARN)¹⁰⁸. En la actualidad, más de 170 modificaciones de ARN diferentes se han identificado, estando presentes bien en las cuatro bases del ARN o en el azúcar ribosa¹⁰⁸. Esta área presenta una alta complejidad regulatoria, existiendo enzimas encargadas de la deposición de estas modificaciones, conocidas como “*writers*”. También se han descrito “*erasers*” o proteínas que eliminan estas modificaciones, y los “*readers*”¹¹⁴, que reconocen selectivamente las marcas y se unen al ARN modificado para desempeñar distintas funciones¹¹⁵.

Se han detectado modificaciones epitranscriptómicas en todas las especies de ARN, sin embargo, los ARNs de transferencia o ARNts son los que se encuentran más extensamente modificados¹⁰⁸. Así, se han identificado más de 90 modificaciones diferentes que decoran alrededor del 20% de los nucleótidos que componen un ARNt¹²³. Los ARNts pueden presentar modificaciones tanto en los dominios estructurales (bucle D o T, bucle variable o brazo aceptor) o en la zona del anticodón. Las modificaciones que afectan al anticodón son complejas y regulan la fuerza y especificidad de reconocimiento del codón así como el mantenimiento del marco de lectura y la velocidad de traducción^{104,125,126}. Por su parte, las modificaciones que afectan al esqueleto estructural son necesarias para la estabilidad del ARNt y el plegamiento adecuado¹²⁸, estando su ausencia relacionada con degradación e inadecuado procesamiento de la molécula^{110,129,130}. Además, las modificaciones que decoran la estructura del ARNt están emergiendo como reguladores clave de la formación de fragmentos derivados de ARNt¹¹⁰, pequeñas moléculas de ARN no codificantes que se producen como producto de la escisión del ARNt¹³¹.

Inicialmente, estos fragmentos derivados de ARNts se consideraban meros productos de degradación sin ninguna función específica, sin embargo, en los últimos años se ha demostrado que pueden actuar regulando la expresión génica tanto a nivel transcripcional como traduccional^{110,130}. Existe una compleja clasificación en función de su tamaño, la zona de origen dentro del ARNt y la causa de su biogénesis¹⁵⁰. Su formación puede producirse de manera constitutiva o bien inducida bajo distintas condiciones, como el estado de desarrollo, de proliferación, o bien situaciones de estrés o infección viral^{147,148} o bien por la presencia o ausencia de determinadas modificaciones epitranscriptómicas. Así, algunas modificaciones

como 5-metilcitosine (m⁵C), queosina (Q) o 2'-O-metilación (Nm) se han descrito por proteger el ARNt de la formación de fragmentos-dependientes de endonucleasas¹⁵⁹⁻¹⁶¹. Por otra parte, otras modificaciones como la pseudouridilación mediada por PUS7, se han demostrado que marcan a los ARNts para su fragmentación¹³¹.

Como se ha mencionado anteriormente, se ha visto que estos fragmentos son capaces de regular procesos biológicos esenciales como la traducción de proteínas. Uno de los mecanismos más recientemente descritos está basado en la presencia de fragmentos de ARNt que presentan 4 o 5 residuos de guanina en el extremo 5' (oligoguanina 5' terminal or TOG). Fragmentos derivados del 5' de 35nt y otros de 18 nt de longitud derivados de los ARNts^{Ala} and ARNt^{Cys} se encuentran dentro de este grupo^{131,166}. La presencia de estas múltiples guaninas en el extremo 5' terminal les confiere una estructura tridimensional de horquilla que se ha descrito que interfiere con el ensamblaje del complejo de iniciación de la traducción¹⁶⁶. Así, los TOGs causan una inhibición global de la síntesis de la traducción desplazando los factores eIF4G/eIF4A o PABPC1 de los ARNm activamente traducidos^{131,166,167}, fenómeno que se ve enriquecido bajo condiciones de estrés.

Así, bien ya sea por proteger o marcar a los ARNts para su degradación o bien mediante regulando la capacidad de reconocimiento de los codones específicos, las modificaciones el ARNts juegan un papel esencial en el proceso de síntesis proteica, siendo esencial su correcta deposición para mantener la proteostasis de la célula.

2.1. METTL1 regula la deposición de m⁷G

La N-7-metilguanósina (m⁷G) es una de las modificaciones de ARNts más comunes en humanos, observándose también en distintas especies de procariotas, arqueas y eucariotas²⁰⁶. Su deposición en humanos es llevada a cabo por la subunidad catalítica metiltransferasa-1 (METTL1) que actúa junto con la unidad reguladora WDR4, en la posición 46 del bucle variable de varias isoformas de ARNts. Este proceso utiliza S-adenosil-metionina (SAM) como molécula donante del grupo metilo^{209,210}.

A nivel funcional, se ha demostrado que la marca m⁷G es esencial para mantener la estabilidad de los ARNts y una óptima traducción de proteínas, además de jugar un papel crucial en la capacidad de autorrenovación y diferenciación de células madre embrionarias murinas^{210,219-222}. Desde el punto de vista patológico, la sobreexpresión de *METTL1* se ha visto que está conectada con una mayor agresividad tumoral en distintos tipos de cáncer como sarcoma, pulmón, colon, hígado, gástrico, vejiga, esófago y glioma^{211,219-221,224-228}. De manera general, el mecanismo identificado se basa en una reducida eficiencia de traducción de aquellos ARNms con mayor dependencia en codones codificados por ARNts modificados con m⁷G²¹⁹, si bien los procesos moleculares que subyacen a la regulación tumorigénica varía entre tumores. Además, la inhibición conjunta de METTL1 junto con la metiltransferasa de ARNts NSUN2 ha demostrado que incrementa la sensibilidad de células HeLa al tratamiento quimioterapéutico 5-fluorouracilo (5FU)²²⁹. Así, estos datos sugieren que las metiltransferasas de ARNts y, especialmente

METTL1, desempeñan un papel esencial en la iniciación y progresión tumoral. Si bien, el papel de esta enzima en el CaP todavía no se ha descrito.

2 OBJETIVOS

Debido a la alta incidencia del cáncer de próstata en hombres a nivel mundial junto con la falta de terapias efectivas para el tratamiento de las fases más agresivas de la enfermedad, hay una necesidad acuciante de desarrollar nuevas terapias que mejoren la prognosis y la calidad de vida en estos pacientes. Basándonos en la baja carga mutacional que presentan los tumores de próstata junto con la evidencia creciente de la importancia de las modificaciones químicas del ARN en la regulación de la capacidad de proliferación y supervivencia de las células tumorales, hipotetizamos que las alteraciones epitranscriptómicas pueden jugar un papel clave en la iniciación y progresión del CaP, así como en la respuesta a tratamientos. Por ello, los objetivos específicos de esta tesis son:

1. Descifrar el epitranscriptoma del CaP para identificar las proteínas modificadoras del ARN que se encuentran alteradas durante la progresión de la enfermedad, y que así puedan ser empleados como potenciales biomarcadores y dianas terapéuticas.
2. Determinar el papel de la modificación m⁷G dependiente de METTL1 en la iniciación y progresión del CaP mediante la manipulación genética de la metiltransferasa en distintos modelos *in vitro* e *in vivo* de CaP. Además, se persigue evaluar la capacidad tumorigénica de los modelos deficientes para METTL1 así como desentrañar los mecanismos moleculares que lo gobiernan.
3. Evaluar el potencial terapéutico de la modificación m⁷G-dependiente de METTL1 en CaP mediante la combinación de la inhibición de la enzima junto con agentes quimioterapéuticos tradicionales del CaP, y analizando el efecto de los mismo en la iniciación y progresión del tumor en distintos modelos pre-clínicos murinos y humanos.

3 RESULTADOS

1. *METTL1* está sobreexpresado en CaP humano y murino y asociado con una peor prognosis

Con el fin de identificar alteraciones epitranscriptómicas que pudieran estar relacionadas con la tumorigénesis del CaP, se realizó un análisis *in silico* de la expresión génica de 132 proteínas modificadoras del ARN en colaboración con el Prof. Arkaitz Carracedo (CIC bioGUNE, Bilbao) y utilizando el software online CANCEERTOOL²⁸⁷. De igual manera, se realizó el mismo análisis con muestras de RNA-seq provenientes del modelo murino del CaP *Pten*KO⁷⁹ de ratones de tres y seis meses de edad, representando las fases de PIN y CaP invasivo, respectivamente (Figura 12A). Como resultado, ambos análisis identificaron *METTL1* como el gen más transcripcionalmente sobreexpresado en CaP (Figura 12B), siendo esta sobreexpresión mayor durante la progresión de la enfermedad (Figura 12C).

Asimismo, incremento en la expresión de *METTL1* se correlacionó directamente con una peor prognosis de la enfermedad y una mayor recurrencia tumoral (Figura 12D,E). Estos datos fueron validados con muestras de pacientes con CaP invasivo del Hospital de Basurto, observándose niveles más elevados de la proteína en muestras tumorales en comparación con hiperplasias benignas (Figura 14A).

Además, se observó una correlación directa entre la expresión de *METTL1* y la activación de la ruta PI3K, sugiriendo una regulación de la metiltransferasa mediada por esta ruta en algún punto *downstream* AKT (Figura 15E-H). La importancia de este resultado radica en que la ruta de PI3K es uno de los principales drivers del CaP y además, su alteración es la base genética del modelo de ratón empleado durante el estudio. Así, análisis de proteína, RNA y niveles de metilación corroboraron un incremento de los niveles de *METTL1* en las distintas fases de la enfermedad del modelo murino (Figura 16A,B) demostrando su validez como reflejo de la enfermedad humana.

2. La delección de *METTL1* produce la acumulación de fragmentos derivados de ARNts que inhiben la síntesis global de proteínas mediante el desplazamiento de los factores del complejo de inicio de la traducción

Para descifrar la función molecular de *METTL1* en CaP, se realizó manipulación genética en las líneas tumorales de CaP PC3 y DU145 con el objeto de producir una delección total (*knock out* o KO) o parcial (*knock down* o KD) de la enzima (Figura 20A-H). Estudios previos han descrito que la pérdida de la marca m⁷G mediada por *METTL1* resulta en una disminución de la estabilidad del ARNt, lo que conduce a una menor eficiencia de traducción de aquellos ARNm enriquecidos en codones que decodificados por ARNts marcados por m⁷G^{210,211,219,224,231}. Para comprobar si este efecto se recapitulaba en líneas de CaP, se llevó a cabo secuenciación de alto rendimiento de librerías de ARNts y análisis por Northern blot para identificar la abundancia de ARNts maduros. Sin embargo, no se identificaron diferencias entre las líneas PC3 wild type (WT) y *METTL1* KO (Figuras 23A,B), indicando que la delección de la metiltransferasa no afecta a la disponibilidad de los ARNts maduros.

Sin embargo, los datos de secuenciación mostraron una acumulación de fragmentos derivados de ARNt en las líneas PC3 *METTL1* KO en comparación con las WT. Así, se identificaron fragmentos cortos derivados del extremo 5' (5' tRFs), y 3' (3' tRFs), mitades de ARNt y fragmentos internos (int-tRFs) (Figura 23C). Debido al enriquecimiento significativo de fragmentos derivados del extremo 5' se llevó a cabo una análisis más detallado de este tipo de fragmentos, observándose que las células *METTL1* KO presentaban una acumulación de un tipo específico caracterizado por presentar un dominio de oligguanina en el extremo 5' denominados como 5'TOG (Figure 23D,E) que entre todos los 5'tRFs detectados. Estos fragmentos presentaban una longitud de unos 20 a 35 nt y derivaban de la fragmentación del ARNt a la altura del anticodón o del bucle D (Figura 23F). Estos resultados se validaron por Northern Blot, demostrando su formación en ARNts modificados por *METTL1*, como cisteína (Figura 23G). Además, se observó que su biogénesis se veía aumenta bajo condiciones de estrés

oxidativo (Figura 24A,C), pero de una manera independiente de la ribonucleasa angiogenina (Figura 24D), previamente descrita por regular la formación de fragmentos dependientes de estrés^{151,156}.

Los fragmentos de ARNts han sido previamente descritos por producir una inhibición de la síntesis de proteína global^{131,151,166}, especialmente los 5'TOG, los cuales han sido definidos por producir un desplazamiento específico de los factores del complejo de inicio de la traducción de los ARNm activamente traducidos^{131,308}. Para comprobar si este efecto se producía en las células deficientes para METTL1 con acumulación de fragmentos de ARNts, evaluamos la tasa global de traducción en células mediante el análogo de la puromicina O-propargil-puromicina (OP-puro). En consecuencia, se observó una disminución de la síntesis de proteínas tanto en células PC3 *METTL1* KO (Figura 25A) como DU145 *METTL1* KD (Figura 25B) en comparación con las WT, indicando que el efecto no es dependiente de la línea celular y que la falta parcial de la enzima es suficiente para causarlo. Para comprobar si este resultado era 5'TOG-dependiente, se realizó un *pulldown* de los ARNm activamente traducidos y se analizó los factores a los que estaban unidos. Detectando que las células PC3 *METTL1*-delecionadas mostraban una reducción de unión de los factores eIF4G, PAPBC1, YB1 y eIF4E a los ARNm activamente traducidos (Figura 25E). Además, se comprobó que la disminución de la eficiencia era mediada por los 5'TOG, ya que la transfección de células PC3 WT con 5'TOG sintéticos recapituló el efecto observado en las líneas *METTL1* KO. De igual manera, la transfección de una secuencia complementaria a la de los 5'TOG o antiTOG en las células PC3 *METTL1* KO rescató parcialmente la unión de los factores (Figura 25G), confirmando que los fragmentos eran los responsables de su desplazamiento del complejo de traducción.

3. La pérdida de la capacidad metiltransferasa de METTL1 en células del CaP produce una disminución de la capacidad tumorigénica

A continuación, se estudió el efecto de la deleción de *METTL1* en la progresión del CaP. Para ello, se evaluó la capacidad proliferativa en condiciones adherentes y en suspensión, así como *in vivo* e *in vitro*. En consecuencia, se observó una disminución significativa de la capacidad de proliferación de las células deficientes para *METTL1* tanto en líneas PC3 como DU145 (Figura 26A,B). Además, se detectó un incremento de la apoptosis, así como una deficiencia de la capacidad de autorrenovación mediante la generación de esferoides de célula única y ensayos de colonias en *soft agar* tras la depleción de la enzima (Figura 26D,F,G), sugiriendo que la esencialidad de la metiltransferasa en la regulación de estos procesos. Notablemente, este efecto se vio recapitulado *in vivo* mediante la generación de xenotransplantes de células PC3 WT y *METTL1* KO y DU145 WT y *METTL1* KD en ratones inmunodeficientes. En consecuencia, los tumores formados a partir de células deficientes para *METTL1* mostraron un tamaño significativamente menor que aquellos formados con células con expresión de la enzima (Figure 27A,C). siendo el efecto más evidente en aquellos tumores con deleción completa de *METTL1*. Así, la inhibición de la metiltransferasa previene tanto la iniciación como la progresión tumoral, siendo por tanto una potencial diana terapéutica.

Por otro lado, con el fin de entender el mecanismo molecular por el que METTL1 regula esta capacidad tumorigénica, generamos mutantes catalíticos en un plásmido que contiene una versión marcada de la enzima (HA-METTL1) mediante mutagénesis dirigida (Figura 28A-C). A continuación, las líneas PC3 *METTL1* KO se infectaron bien con el plásmido que expresa la versión wild type (WT) o bien el mutante catalítico (AFPA), además del vector vacío como control de la infección (eV) (Figura 28C,F). Así, se observó que las células *METTL1* KO AFPA recuperaban la expresión de la proteína, pero no su capacidad metiltransferasa, corroborando la generación del mutante catalítico. Asimismo, pudimos confirmar la dependencia de los fenotipos observados en la actividad metiltransferasa de METTL1, ya que la capacidad proliferativa en condiciones de suspensión y adherencia se rescató con la expresión exógena de la versión WT, pero no con el mutante catalítico (Figura 28D,E,G,H). Sin embargo, la mayor novedad supuso demostrar la dependencia de estos mismos fenotipos en los fragmentos 5'TOG acumulados en ausencia de la enzima. Así, la transfección exógena de 5'TOGs sintéticos en células *METTL1* WT produjo una disminución significativa de la capacidad de proliferación y un incremento de la apoptosis celular, mientras que la transfección de antiTOGs en células *METTL1* KO tuvo el efecto contrario (Figura 28I-K). Esto demuestra que la regulación de la tumorigénesis del CaP mediada por METTL1 es dependiente de la formación de estos fragmentos.

4. METTL1 regula la traducción de proteínas involucradas en respuestas a estrés y es necesaria para un correcto flujo autofágico

Además de su papel en inhibir la síntesis global de proteínas, los fragmentos derivados de ARNts también han sido descritos por fomentar la traducción de transcritos específicos. Para comprobar si este efecto se observaba en nuestros modelos de CaP, se realizó un análisis del proteoma naciente utilizando la capacidad del OP-puro de unirse a proteínas activamente traducidas (Figura 29A). Como resultado, se obtuvo que las células con deficiencia de METTL1 mostraban una traducción reducida de proteínas relacionadas con ciclo celular y proliferación, pero también una mayor traducción de proteínas implicadas en respuestas a estrés (Figura 29B). Además, análisis del transcriptoma mostró que los cambios del proteoma no se correspondían a cambios transcripcionales (Figura 29D), demostrando que las diferencias observadas se deben a cambios traduccionales. Estos resultados se demostraron mediante amplificación de ARNm activamente traducidos aislados mediante *polysome profiling* (Figura 30).

Por otro lado, se identificó que la inhibición de METTL1 producía una acumulación de agregados de proteínas en las células PC3 (Figura 31A), lo que sugiere desregulación de algunos de los mecanismos implicados en su eliminación. Si bien no se detectaron alteraciones en la respuesta de proteínas mal plegadas (UPR, Figura 31B,C), sí que se observó un incremento del flujo autofágico en células PC3 *METTL1* KO (Figura 32A). Curiosamente, este efecto se vio incrementado ante el tratamiento con CQ, un inhibidor de la fusión autofagosoma-lisosoma, pero no tras el tratamiento con Rapamicina, un inductor de la activación de la autofagia (Figura 32A,B, Figura 33A,B,C). Esto sugiere METTL1 es necesario para una correcta terminación de la autofagia y que su ausencia resulta en una acumulación

de vesículas autofágicas en el citoplasma de las células. Como consecuencia, las células deficientes para la metiltransferasa presentan una acumulación de especies reactivas de oxígeno (ROS) (Figura 34A), que a su vez conlleva a una acumulación a daño al ADN (Figura 34B,C) en células PC3 y DU145. Esto, a su vez, se traduce en una menor capacidad de las células *METTL1* KO para adaptarse a situación de estrés, resultando a hipersensibilidad a estrés oxidativo (Figura 34D,E) y agentes quimioterapéuticos como Rapamicina, Docetaxel y Etopósido (Figura 34A-D). Por lo tanto, *METTL1* es necesaria para una correcta respuesta de las células tumorales a situaciones de estrés.

5. Deleción de *Mettl1* en el epitelio prostático de un modelo murino de CaP disminuye la capacidad tumorigénica

Para evaluar el efecto de la ausencia de la metiltransferasa en el proceso de formación del tumor de próstata en un ambiente *in vivo*, se generó un modelo con deleción condicional de *Mettl1* en el epitelio prostático al estar la recombinasa Cre bajo el control del promotor de la probasina (Pb) (Figura 34A). Mediante el cruce con el modelo de próstata previamente establecido (77), se obtuvo un modelo con cáncer de próstata deficiente en *Mettl1* (*Pten*KO/*Mettl1*^{flox/flox}). Además de la esperada reducción en los niveles de proteína y ARNm de *Mettl1*, estos ratones exhibieron una disminución de los niveles de metilación de ARNts y, más interesante, una acumulación de fragmentos derivados de ARNts identificados por Northern blot (Figura 36B-E). Así, el modelo generado recapitula fielmente los efectos de la deleción de la enzima observados *in vitro*.

Notablemente, los tumores de próstata delecionados para *Mettl1* mostraron una reducción significativa en tamaño y peso en comparación con aquellos con expresión de la enzima (Figura 37A,B). Además, los tumores derivados de ratones *Pten*KO/*Mettl1*^{flox/flox} mostraban una menor capacidad proliferativa, así como un incremento de la apoptosis, del flujo autofágico y del daño al ADN, tal y como se observaba en las células (Figura 37C-D). Esto implica que los tumores de próstata con deleción de *Mettl1* presentan la misma acumulación de marcadores de estrés observados *in vitro*, lo que sugiere que también mostrarán la misma hipersensibilidad a tratamientos quimioterapéuticos, emergiendo la metiltransferasa como una potencial diana terapéutica.

Además, análisis del porcentaje de las poblaciones celulares que componen las próstatas de ratones *Pten*KO y *Pten*KO/*Mettl1*^{flox/flox} mostraron que en ausencia de la enzima la composición celular de la próstata se asemejaba en más medida a una próstata sana (Figura 38), indicando que la inhibición de la enzima reduce significativamente la agresividad del tumor.

6. *METTL1* regula la respuesta a tratamientos del CaP *in vivo* y determina la capacidad de formación de organoides en un modelo humano pre-clínico

Debido a que la deleción de *Mettl1* en próstatas de ratón resultó en la activación de rutas de estrés, así como en una acumulación de estrés genotóxico de manera similar a lo observado *in vitro*, se evaluó si la deleción de la metiltransferasa podría afectar a la respuesta a quimioterapia.

Para ello, se estudió el efecto del tratamiento con los fármacos quimioterapéuticos Docetaxel y Etopósido en la formación de xenotransplantes de células de próstata PC3 WT y *METTL1* KO. Como resultado, se obtuvo no solo un menor crecimiento del tumor si no también una disminución del tamaño del mismo, efecto que no se observó en los tumores sin tratamiento ni en los tumores de células *METTL1* WT tratados (Figura 39A). Así, la acción conjunta de la inhibición de *METTL1* junto con el tratamiento incrementa la efectividad de éste hasta el punto de producir una muerte celular tan alta (Figura 39C) que disminuye el tamaño tumoral. Esto indica que el doble tratamiento de tumores agresivos con un inhibidor de *METTL1* combinado con tratamientos tradicionales de CaP es una opción atractiva para mejorar la respuesta a la terapia.

Además, también se evaluó el efecto de la depleción de *METTL1* en un modelo preclínico humano de organoides derivados de xenotransplantes derivados de pacientes (PDXs), los cuales son modelos tridimensionales y multicelulares del tumor humano. Así, mediante infección de un plásmido con expresión inducible de shARNs específicos para *METTL1*, se generó un modelo con reducida expresión de la enzima y se evaluó su capacidad de formación de organoides. Así, se vio que, aunque la falta de la enzima permitía la obtención de organoides viables, la capacidad de formación de éstos se veía disminuida (Figura 40C). Esto confirma el papel esencial de la metiltransferasa para la formación de tumores tanto *in vitro* como *in vivo*.

4 CONCLUSIONES

En conclusión, nuestros resultados destacan la dependencia que tiene la progresión y supervivencia de los tumores de próstata en una anormal metilación de ARNts. Este trabajo esclarece el mecanismo subyacente al procesamiento de los ARNts que tiene lugar en células tumorales, así como su conexión con mecanismos de respuesta a estrés.

Así, los datos obtenidos durante esta tesis doctoral conducen a las siguientes conclusiones:

- I. La metiltransferasa de ARNts *METTL1* está sobreexpresada en CaP, especialmente en tumores metastáticos, estando los altos niveles de la enzima asociados con una peor prognosis de los pacientes.
- II. La sobreexpresión de *METTL1* en CaP es dependiente de la sobreexpresión de *PTEN*, estando su transcripción regulada por la ruta PI3K en algún punto *downstream* AKT. Este efecto se refleja en el modelo de ratón de CaP *Pten*KO.
- III. *METTL1* metila preferencialmente ARNts en la guanina-7 localizada en la posición 46 del bucle variable de aproximadamente el 50% de las distintas isoformas de ARNts.
- IV. La pérdida de la marca m⁷G dependiente de *METTL1* no afecta a la disponibilidad de los ARNts maduros pero incrementa la acumulación de fragmentos derivados de ARNts, particularmente la biogénesis de 5'TOG de 30+40 nt de longitud.

- V. La acumulación de los fragmentos 5'TOG altera de manera simultánea el programa traduccional de las células de próstata así como inhibe la síntesis global de proteínas mediante el desplazamiento de los factores del complejo de inicio de la traducción de los ARNms que están siendo activamente traducidos.
- VI. La delección de *METTL1* resulta en una disminución de la capacidad de proliferación y autorrenovación de células del CaP *in vitro* e *in vivo* de una manera dependiente de la actividad metiltransferasa.
- VII. La incorporación exógena de 5'TOGs sintéticos recapitula el fenotipo observado tras la delección de *METTL1*.
- VIII. *METTL1* se expresa principalmente en células lumbinales prostáticas y su delección resulta en una menor proliferación tumoral así como una remodelación de las poblaciones celulares del tumor a una composición más similar a no-tumoral.
- IX. La modificación m⁷G de ARNts dependiente de METTL1 es esencial para una correcta terminación de la autofagia, y su pérdida conduce a la acumulación de agregados de proteínas, ROS y daño al ADN que en última instancia resulta en un incremento de la sensibilidad a condiciones de estrés y a tratamientos tradicionales del CaP tanto *in vitro* como *in vivo*.